ADVANCED TOPOLOGY OPTIMIZATION IN CYBER-PHYSICAL DISTRIBUTION SYSTEMS FOR MULTI-SECURITY AND OPERATIONAL FLEXIBILITY ENHANCEMENT

LEI CHAO

PhD

The Hong Kong Polytechnic University

2024

The Hong Kong Polytechnic University

Department of Electrical and Electronic Engineering

Advanced Topology Optimization in Cyber-Physical Distribution Systems for Multi-Security and Operational Flexibility Enhancement

Lei Chao

A thesis submitted in partial fulfillment of the requirements for the degree of Doctor of Philosophy

April 2024

CERTIFICATE OF ORIGINALITY

I hereby declare that this thesis is my own work and that, to the best of my knowledge and belief, it reproduces no material previously published or written, nor material that has been accepted for the award of any other degree or diploma, except where due acknowledgment has been made in the text.

_______________________________________(Signed)

_________LEI Chao_______(Name of student)

Abstract

The distribution grids evolve from the passive network with having the goal of supplying reliably and efficiently the end users, gradually to active networks with integrating distributed energy resources (DERs). With the extensive use of operational technologies (OT) and information and communication technologies (ICT) networks, the transition to cyber-physical distribution systems enables the complete observability enhancement of measurements and smartization of control components. Under this background, an effective distribution network reconfiguration (DNR) scheme plays a key role in smart energy management of today's active distribution networks (ADNs) for substantial cost reductions and operational flexibility enhancements subject to system observability and privacy concerns of different stakeholders.

Firstly, we propose a disjunctive convex hull relaxation (DCHR) to tackle with the classical DNR problem. This classic DNR problem is a mixed integer second order conic programming (MISOCP) problem which is non-convex and nonlinear. However, our proposed DCHR approach can perfectly addresses this problem and it is proven to be a tighter relaxation than the existing relaxation techniques for DNR problems, such as the Big-M and McCormick linearization methods.

Secondly, the system observability enabled by distribution-level PMUs becomes increasingly crucial for cyber-physical security enhancement. We formulate this

system observability as a disjunctive relaxed connected dominating set problem for reconfigurable ADNs with the least defense cost in theory. For the benefits of system observability, an observability defense-constrained DNR model has been proposed.

Thirdly, the topology switch for the loss minimization may expose the private load change information of an agent, e.g., transition from a light load to a heavy load, in interconnected ADNs managed by multiple agents. To address this issue, this paper proposes a differentially private distribution network reconfigu-ration (DP-DNR) mechanism based on a consensus alternating direction method of multipliers (C-ADMM) algorithm. This can tackle privacy leakage challenges on the agent's and customer's levels. To suppress private load change leakage as an agent's concern, this DP-DNR mechanism provides a mixture output of realistically optimal topology switch status and corresponding obfuscated-but-feasible load flows, part of which may have reverse load flow directions. On the customer's level, the C-ADMM-based decentralized DP-DNR approach can seek the optimal topology switch without customer's load datasets of agents, whilst exchanged communication signals in C-ADMM algorithm are also synthetic based on the proposed DP-DNR mechanism.

Lastly, a distribution-level topology optimization contributes to the flexibility enhancement of a look-ahead rolling economic dispatch of wind-thermal-bundled power system (WTBPS), which offsets the insufficient ramping margins of retrofitted coal-fired units. Since WTBPS connects to high voltage distribution networks (HVDNs), graph characterization of typical HVDNs is summarized, and then the simplified voltage-constrained load transfer strategy via topological structures can be developed. This proposed look-ahead economic dispatch model is cast as a MISOCP problem. For this established MISOCP-based model, it is highly desirable to combine the Multi-cut Benders Decomposition (MBD) and Generalized Benders Decomposition (GBD) as the devised Multi-cut GBD (MGBD) to tackle this MISOCP problem, which can enhance overall computational efficiency and be suitable for online rolling economic dispatch.

List of Publications

Journal papers

1. **C. Lei**, S. Bu, Q. Wang, N. Zhou, L. Yang, and X. Xiong, "Load transfer optimization considering hot-spot and top-oil temperature limits of transformers," *IEEE Transactions on Power Delivery*, vol. 37, no. 3, pp. 2194-2208, June 2022. DOI: https://doi.org/10.1109/TPWRD.2021.3106709. (Chapter 2 & 6)

2. **C. Lei,** S. Bu, J. Zhong, Q. Chen and Q. Wang, "Distribution Network Reconfiguration: A Disjunctive Convex Hull Approach," *IEEE Transactions on Power Systems*, vol. 38, no. 6, pp. 5926-5929, Nov. 2023. DOI: 10.1109/TPWRS. 2023.3304132. (Chapter 3)

3. **C. Lei**, S. Bu, Q. Wang, L. Liang and F. Wen, "Observability Defense-Constrained Distribution Network Reconfiguration for Cyber-Physical Security Enhancement," *IEEE Transactions on Smart Grid*, vol. 15, no. 2, pp. 2379-2382, March 2024. DOI: 10.1109/TSG.2023.3334078. (Chapter 4)

4. **C. Lei**, S. Bu, Q. Wang, Q. Chen, L. Yang and Y. Chi, "Look-Ahead Rolling Economic Dispatch Approach for Wind-Thermal-Bundled Power System Considering Dynamic Ramping and Flexible Load Transfer Strategy," *IEEE Transactions on Power Systems*, vol. 39, no. 1, pp. 186-202, Jan. 2024. DOI: 10.1109/TPWRS.2023.3238035. (Chapter 6)

5. **C. Lei**, S. Bu and Q. Wang, "A Consensus ADMM-based Differentially Private Reconfiguration Approach for Multi-Agent Active Distribution Networks," *IEEE Transactions on Smart Grid*, 2024 (Under Review). (Chapter 5)

6. **C. Lei**, S. Bu, Q. Chen, Q. Wang and D. Srinivasan, " Decentralized Optimal Power Flow for Multi-Agent Active Distribution Networks: A Differentially

Private Consensus ADMM Algorithm," *IEEE Transactions on Power Systems*, 2024 (Early Access).

7. **C. Lei**, S. Bu, Q. Wang, Z. Ren and D. Srinivasan, “Battery Dispatch Optimization for Electric Vehicle Aggregators: A Decomposition-Coordination-based Least Squares Approach with Disjunctive Cuts," *IEEE Transactions on Power Systems*, 2024 (Under Review).

8. **C. Lei**, S. Bu and Q. Wang, "Load Transfer Optimization with Graph Characterizations on Different Time-Scales for Multi-Voltage Distribution Networks Against Overload Cascades," *IEEE Transactions on Power Delivery*, 2024 (Under Review)

9. **C. Lei**, S. Bu, Q. Wang and D. Srinivasan, "Aging-Aware Vehicle Battery Dispatch for Aggregators: A Digital-Twin-enabled Rolling Optimization Framework," *IEEE Transactions on Power Systems*, 2024 (Ready for Submission).

10. Y. Zou, Q. Wang, Y. Chi, J. Wang, **C. Lei** and N. Zhou, "Electric Load Profile of 5G Base Station in Distribution Systems Based on Data Flow Analysis," *IEEE Transactions on Smart Grid*, vol. 13, no. 3, pp. 2452-2466, Feb 2022. DOI: 10.1109/TSG.2022.3150074.

11. H.Wang, F. Gao, Q. Chen, S. Bu and **C. Lei**, "Instability Pattern-guided Model Updating Method for Data-driven Transient Stability Assessment," *IEEE Transactions on Power Systems*, 2024 (Early Access).

12. Y. Zou, Q. Wang, Q. Xia, Y. Chi, **C. Lei**, N. Zhou, " Federated reinforcement learning for Short-Time scale operation of Wind-Solar-Thermal power network with nonconvex models," *International Journal of Electrical Power & Energy Systems*, vol. 158, 2024.

Conference papers

1. **C. Lei**, S. Bu, Q. Wang and Q. Chen, "Dynamic Ramping of Retrofitted Coal-Fired Power Plants: Basic Formulation and Tightened Approximation," *in the 2023 IEEE Power & Energy Society General Meeting (PESGM)*, Orlando, Florida, USA, 2023. DOI: 10.1109/PESGM52003.2023.10253043.

Patents

1. S. Bu, G. Lu, E. Yim and **C. Lei**, "A Health Index System and Method of Predicting Health Condition in Underground Cables," HK30064886, July. 8th, 2022. Available: https://esearch.ipd.gov.hk, Accessed on: July. 8th, 2022.

Book and Book Chapters

1. **C. Lei**, Q. Wang and N. Zhou, "Load Transfer Optimization in Smart Distribution Networks," Publisher: China Electric Power Press, 2024. (Accepted)
2. **C. Lei** and Q. Wang, "Look-ahead Rolling Economic Dispatch Approach for Wind-Thermal-bundled Power System with Operational Flexibility Enhancement", *Modelling and Optimization of Power and Energy Resources*, edited by Farhad Shahnia and Fushuan Wen, Publisher: Springer Press, 2024. (Accepted)
3. **C. Lei** and S. Bu, " Distribution Network Reconfiguration: A Disjunctive Convex Hull Approach", *Modelling and Optimization of Power and Energy Resources*, edited by Farhad Shahnia and Fushuan Wen, Publisher: Springer Press, 2024. (Accepted)

Acknowledgments

First and foremost, I would like to express my most sincere gratitude to my chief supervisor Dr. Siqi. Bu. He is one of the top-tier scholars in the field of power system stability and control. It is truly a great honor to be able to pursue my Ph.D. under his guidance. His attitude and enthusiasm for scientific research has always been a role model for me to follow. From academic research to life value, he has given me countless suggestions for thoughts shaping and paper writing. His research integrity, academic guidance and great support in my research is really a valuable treasure in my life.

Moreover, I am eternally grateful to my co-supervisors, Professor C. Y. Chung, Professor Edward Chung from The Hong Kong Polytechnic University and Professor Dipti Srinivasan from National University of Singapore, for their insightful suggestions on my research and advice in polishing my journal papers. Besides, I owe my special thanks to my thesis committee members for their precious time in reading my thesis and giving me valuable suggestions for improvement. I would like to acknowledge the support from Centre for Advances in Reliability and Safety (CAiRS) for offering me the research associate position to support my PhD study, without which this PhD research would not have been possible.

Besides, my appreciation also goes to Dr. Jiaxin Wen, Mr. Qifan Chen, Mr. Chao Huang, and Mr. Shu Wa Kong for the patient support throughout my entire PhD study. They have given me much valuable advice and practical helps on my life and research.

I will never forget this marvelous research journey in Hong Kong.

Last but not least, I would like to thank the support from The Hong Kong Polytechnic University.

Table of Contents

List of Abbreviations

DERs	Distributed energy resources
DSR	Demand-side response
BESSs	Battery energy storage systems
MGs	Microgrids
EVs	Electric vehicles
OT	Operational technologies
ICT	Information and communication technologies
CPDS	Cyber-physical distribution systems
DSO	Distribution system operator
CBs	Circuit breakers
DNR	Distribution network reconfiguration
CH	Convex hull
DCHR	Disjunctive convex hull relaxation
DP	Differential privacy
WTBPS	Wind-thermal-bundled power system
HVDNs	High voltage distribution networks
MISOCP	Mixed-integer second-order conic programming
MGBD	Multi-cut Generalized Benders Decomposition
ADNs	Active Distribution networks
IBRs	Inverter-based resources
BFM	Branch flow model
AVC	Automatic voltage control
LMI	Linear matrix inequality
SCF	Single commodity flow

ST	Spanning tree
PCC	Point of common coupling
SOCP	Second-order conic programming
SDP	Semi-definite programming
MISDP	Mixed integer semi-definite programming
SOC	Second-order conic
D-PMU	Distribution-level phasor measurement unit
RCDS	Relaxed connected dominating set
FDIAs	False data injection attacks
MIQP	Mixed-integer quadratic programming
DSC	Direct supply connection
SSC	Serial supply connection
ED	Economic dispatch
WPTs	Wind power turbines
TMP	Master problem
TSP	Sub-problems
OPF	Optimal power flow
DP-DNR	Differentially private DNR
ADMM	Alternating direction method of multipliers
C-ADMM	Consensus ADMM
KKT	Karush–Kuhn–Tucker conditions
MVDNs	Medium-voltage distribution networks
LVDNs	Low-voltage distribution networks

List of Notations

t, i	Indices for time and node number.
m, n, l_t, l_b, l	Tie-line l_t and an internal branch l_b in an agent, and arbitrary branch l between nodes (m, n) for an agent.
$\mathcal{G}$, $\mathcal{N}$, $\mathcal{E}$	Undirected tree $\mathcal{G}$ with the sets of nodes $\mathcal{N}$ and branches $\mathcal{E}$.
$\boldsymbol{A}$	Branch-node incidence matrix in tree graph $\mathcal{G}$.
$\dot{U}_m$, $(I^l_{mn})^*$	Voltage phasor at node m and conjugate of current phasor between nodes m and n.
$\boldsymbol{D}_r$, $\boldsymbol{D}_x$	Diagonal matrices of resistances and reactances.
$\boldsymbol{P}^d$, $\boldsymbol{Q}^d$	Nodal active/reactive load [p.u.].
$\boldsymbol{z}^l$	Diagonal matrix of impedance [p.u.].
$\boldsymbol{D}_v$	Diagonal matrix of $\boldsymbol{v}$ of the sending nodes for all branches [p.u.].
M, B	Large-enough positive scalar and rated branch capacity.
$\underline{v}$, $\overline{v}$, $\underline{U}$, $\overline{U}$	Lower and upper boundaries of nodal squared and normal voltage profiles [p.u.].
$\boldsymbol{\ell}^l$	Vector of squared current on branches [p.u.].
$\boldsymbol{P}^l$, $\boldsymbol{Q}^l$, $\boldsymbol{Q}^{cr}$	Vector of active and reactive power flow variables, and reactive power compensation variables [p.u.].
$\boldsymbol{u}^l$	Status of switches with $ul = 0$ for open and 1 if closed.
$\boldsymbol{v}$	Nodal squared voltage profiles [p.u.].
$\boldsymbol{P}^g$, $\boldsymbol{Q}^g$	Nodal active/reactive power injections [p.u.].
$\boldsymbol{Q}^{cr}$	Vector of nodal reactive power compensation [p.u.].
$\boldsymbol{\beta}^l$	Vector of continuous parent-child relationship variables.
$\mathcal{F}$, $\mathcal{F}_\varepsilon$	Feasible set of a SOCP and associated polyuhedral set.
L^2	Lorentz cone.
$\boldsymbol{\Omega}^l$	Feasible set of the DNR problem.
P^l_0, P_{loss}	Active power injection at the root node 0 and active power loss.

$\boldsymbol{\Omega}_1$, $\boldsymbol{\Omega}_2$	Sets of DCHR formation.
$\mathcal{D}, \mathcal{D}^*, \widetilde{\mathcal{D}}$	RCDS, optimal RCDS solution and optimal solution of maximum leaf spanning tree problem.
ψ, h	Radiality constraints and system-wide operational constraints.
$\mathcal{M}^P$	Set of all nodes of D-PMUs other than the root node.
$\mathcal{M}^l$, $\mathcal{M}^k$	Sets of zero injection nodes for non-leaf nodes and leaf nodes, respectively.
$\boldsymbol{z}$, z^g	Decision vector for D-PMUs and associated lower bound number.
$\boldsymbol{y}$	Auxiliary binary-based decision variable vector for zero injection nodes.
$\boldsymbol{I}$, $\boldsymbol{P}$	Sets of all zero injection nodes and associated dominated nodes and all D-PMU nodes, and associated dominated nodes.
w_{ij}^l, m_{ij}^l, e_k	Auxiliary binary variables.
c_1, c_2	Coefficients for defense cost and power loss.
$\boldsymbol{f}^t$	Vector of virtual flows.
$\boldsymbol{d}$	Nodal active/reactive load [p.u.].
$\mathcal{A}$	Set of agents.
$\mathcal{C}_i$	Closed convex set for variables.
$\mathcal{T}_i$	Set of tie-lines for the i-th agent, and T refers to the set of all tie-lines.
$\mathcal{X}, \mathcal{X}_{\mathrm{I}}, \mathcal{X}_{\mathrm{II}}$	Sets of feasibility spaces.
$\mathcal{V}_i$	Set of feasibility space.
c	Coefficient matrix for the objective function.
k_{max}	Maximum iteration number.
$n_{\mathcal{A}}$	Number of agents.
$\underline{x}^l, \overline{x}^l$	Lower and upper bounds of optimization variable vector $\boldsymbol{x}^l$.
$\boldsymbol{\xi}^l$	Vector of random perturbations [p.u.].
$\boldsymbol{\alpha}^l$, $\boldsymbol{g}$	Upper bounds of $\boldsymbol{\alpha}^l$ and $\boldsymbol{g}$.
ϑ, λ	Given constants.
ε, $\Delta\rho$, ρ	Privacy parameter, $\ell 2$-sensitivity and measurable quantity.
τ_i	$\tau_i = 1$ if the i-th agent has an obfuscation request for tie-line load flow directions; otherwise $\tau_i = 0$.

$\boldsymbol{f}$	Vector of auxiliary binary variables.
$\boldsymbol{g}$	Vector of virtual power injection/ejections at boundary nodes [p.u.].
$\boldsymbol{V}_{i,b}$	Incorporated variables for squared voltage profile variables at boundary nodes [p.u.].
$\boldsymbol{W}_{v}$	Consensus variables of squared voltage profiles at boundary nodes [p.u.].
$\boldsymbol{x}^{l}$, $\boldsymbol{x}^{lt}$	Vector of operational variables and an operational variables for tie-line l_t; and $\hat{x}^{l}$ and $\boldsymbol{x}^{l*}$ are optimal solutions [p.u.].
$\boldsymbol{X}_{i}$, $\boldsymbol{X}_{i,b}$	Block variables and boundary variables of the i-th agent, $\boldsymbol{X}^{*}_{i}$ is the corresponding optimal solution [p.u.].
$\boldsymbol{Z}_{x}$	Vector of consensus variables [p.u.].
$\boldsymbol{\alpha}^{l}$	Vector of recourse variables.
$\boldsymbol{\mu}_{i,b}$, $\boldsymbol{\gamma}_{i,b}$	Vectors of dual variables.
$\mathcal{L}_{\lambda}$	Augmented lagrangian function.
a, b, c, d	Parameters of dynamic ramp rate.
$a_{f,\text{upper}}$, $b_{f,\text{upper}}$, $c_{f,\text{upper}}$, $a_{f,\text{lower}}$, $b_{f,\text{lower}}$, $c_{f,\text{lower}}$	Coefficients of quadratic ramping margin functions.
A_{upper}, B_{upper}, A_{lower}, B_{lower}	Coefficients of linear ramping constraints.
$c_{2i,u}$, $c_{1i,u}$, $c_{0i,u}$	Production cost coefficients for the i-th retrofitted coal-fired unit in the u-th agent of WTBPS.
A_l, B_l, b_l, $D^{y}_{q_1}$, $D^{y}_{q_2}$, $D^{y}_{l_1}$, $D^{y}_{l_2}$, D^{x}_{q}, D^{x}_{l}, E_l, h_l, F_l, r_{le}, G_l, r_{ls}, Q_r, l_r, g_r	Matrix symbols of rolling economic dispatch models with MGBD.
F_{o}, F_{o1}, F_{o2}	Cost functions of rolling economic dispatch.
$f(x)$, $g(x)$	Ramp-up/down margin functions.
$f_U(x)$, $g_L(x)$	Quadratic functions for $f(x)$ and $g(x)$.

h_U	Distance at point U between $f(x)$ and $f_U(x)$.
i, j, t, u	Indices for retrofitted coal-fired units, circuit switches or stations, time, and agent numbers.
$\boldsymbol{L}_j^t$, $\boldsymbol{b}_j^t$	Vectors of load coefficients for specific topological networks for the j-th station at time t.
$N_{\mathrm{G},u}$	Number of retrofitted coal-fired units in the u-th agent of WTBPS.
N_{Ts}	Number of time horizons in a look-ahead window.
$n_{\mathrm{s},j}$, N_{s}, N_{T}	Number of transformers in the j-th station, number of circuit breakers, and number of 220kV stations in HVDNs.
N_u	Number of agents of WTBPS.
N_w	Number of allowable switching actions.
$P_{\mathrm{T},u}^t$	Transmission power on tie-lines for the u-th agent of WTBPS at time t.
$P_{\mathrm{G},u}^t$,$P_{\mathrm{G}i,u,\max}$	Active power and rated capacity of the i-th retrofitted coal-fired unit in the u-th agent of WTBPS at time t.
$P_{\mathrm{D},u}^t$	Dispatchable loads for the u-th agent of WTBPS at time t.
P_{base}	Scheduled power on tie-lines.
P_u^{spin}	System spinning reserve capacity for the u-th agent of WTBPS.
$P_{\mathrm{W},u}^t$, P_{wind}	Wind power for the u-th agent of WTBPS at time t and rated wind power capacity.
$P_{\mathrm{c}}^t / Q_{\mathrm{c}}^t$, $P_{\mathrm{d}}^t / Q_{\mathrm{d}}^t$	Active/reactive loads at 110kV substations C and D at time t.
P_{A1}^t , P_{A2}^t	Total active power on transformers in 220kV stations A1 and A2 at time t.
P_{mk}^t , Q_{mk}^t	Real power and reactive power to branch (m,k) for time t.
q_u	Variable from the u-th sub-problem ($\boldsymbol{SP_u}$) for the relaxed master problem of MGBD.
$\boldsymbol{P}_{\mathrm{S}}^t$	Vector of active power on transformers in 220kV stations at time t.
$r_{i,u}^t$	Percentage of $P_{\mathrm{G}i,u}^t / P_{\mathrm{G}i,u,\max}$ at time t.
R_{mk}, X_{mk}	Resistance and reactance of branch (m,k).
$S_{\mathrm{N},j}$	Single transformer rated capacity in the j-th station.
$S_{\mathrm{L},j}$	Capacity of the branch connecting to the j-th station.

$\boldsymbol{S}^t$	Vector of binary states of circuit breakers with 0-OFF and 1-ON at time t.
T_s	Set of time-horizons in a rolling look-ahead, $T_s=\{t\}$, and t=1,2,…, N_{Ts}.
$v_{i,u}^t$	Ramp rate for the i-th retrofitted coal-fired unit in the u-th agent of WTBPS at time t.
x_-^*, x_+^*	Roots of maximum inner-approximated errors.
x_B, x_C, x_D, x_U, y_B, y_C, y_D, y_U	x-coordinates and y-coordinates of points B, C, D and U.
$\boldsymbol{X}$,$\boldsymbol{Y}_1$,$\boldsymbol{Y}_2$	Optimization variable sets for the u-th agent of WTBPS.
$\hat{y}_u^k$, $\hat{y}_u^{f,k}$, $\hat{x}^{k-1}$	Given continuous variables for $\boldsymbol{SP_u}$ and feasibility check problem of MBGD at the k-th iteration, and given discrete variables at the (k-1)-th iteration.
z_j^t	Auxiliary binary variable for binary variables of circuit breakers at time t.
$\Delta r_{i,u}^t$	Percentage of maximum active power variation.
Δe_U, Δe_L	Maximum inner-approximated errors between linear and untightened ramp-up/down margins.
Δs_U, Δs_L	Maximum inner-approximated errors between SOC and untightened ramp-up/down margins.
Δv_{mk}^t, $\Delta \bar{v}$,	Voltage profile drop and allowable voltage drop for branch (m,k) at time t.
$\bar{v}$, $\Delta\bar{V}$	Maximum voltage profile and allowable squared voltage drop.
σ_u	Relaxed variable for $\boldsymbol{SP_u}$ of MGBD.
δ%	Specified range of power on tie-lines by percentage.
$\boldsymbol{\Gamma}$	Coefficient matrix of $f_U(x)$.
μ_1, μ_2	Weighting coefficients.
ΔT	Dispatch period.
$\hat{\lambda}_{u,1}^k$, $\hat{\lambda}_{u,2}^k$, $\hat{\lambda}_{u,3,i}^k$, $\hat{\gamma}_{u,1}^k$, $\hat{\gamma}_{u,2}^k$, $\hat{\gamma}_{u,3,i}^k$	Lagrange multiplier vectors of relaxed master problem and sub-problems of MGBD at the k-th iteration.
$\eta_{i,u}$, $\omega_{i,u}$, $\chi_{i,u}$, $\xi_{i,u}$	Variables of ramping constraints at time t.
m_{upper}, J_{upper}, m_{lower}, J_{lower}	Auxiliary variables for SOC constraints.

Chapter 1

Introduction

1.1 Backgrounds

The distribution grids evolves from the passive network with having the goal of supplying reliably and efficiently the end users, gradually to active networks with integrating distributed energy resources (DERs), demand-side response (DSR), battery energy storage systems (BESS), microgrids (MGs) and electric vehicles (EVs). This new electricity generation mix is causing a dramatic revolution of active distribution systems [1]. Nowadays, active distribution networks (DNs) are increasingly dependent on operational technologies (OT) and information and communication technologies (ICT) networks for real-time monitoring and control of physical facilities [2, 3]. Distribution systems including power networks and associated information devices are tightly coupled with ICT and OT systems together with applied intelligent network components, e.g., reliably wireless/wired communication, sophisticated control devices. This gradually transits active distribution systems to an interdependent and complex cyber-physical distribution systems integrated with big data, block chain, cloud computing, edge computing and IoT systems [4, 5].

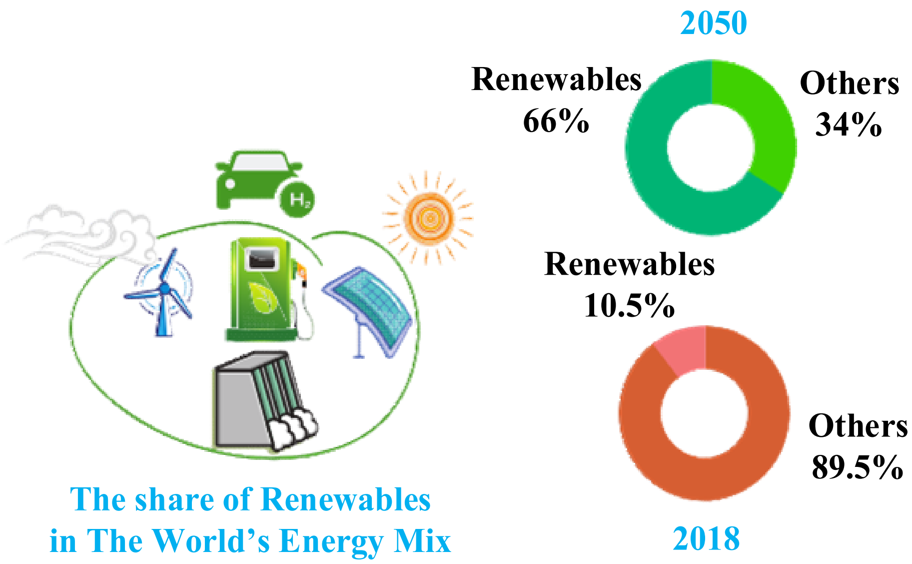

Fig. 1.1 Share of renewables in the world's energy mix in 2050 [6].

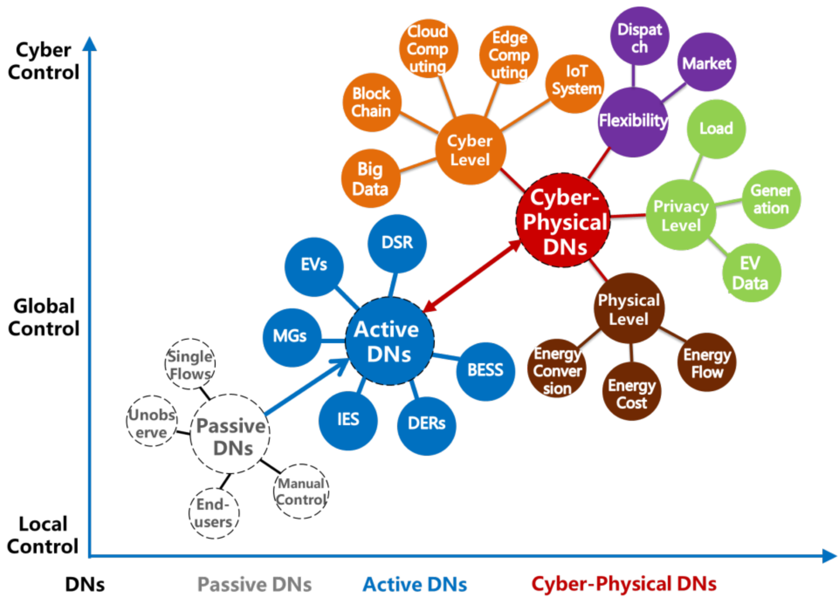

Fig. 1.2 Diagram of distribution system evolutions

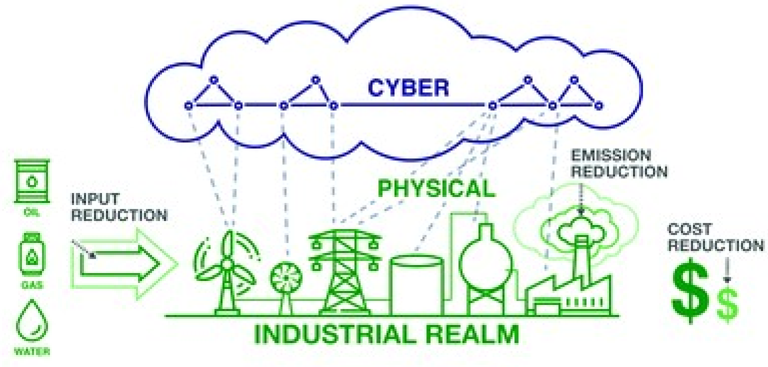

Fig. 1.3 Cyber-physical systems on the decarbonization of energy [2].

From the distribution system operator (DSO) point of view, a high penetration of active resources and an extensive use of intelligent devices will closely interact with system operational actions, which plays a key role in smart energy management of today's DNs for substantial cost reductions [5]. Under this background, the evolution toward cyber-physical distribution systems enables the complete observability enhancement of measurements and smartization of control components via optic fiber communications systems. Plus, circuit breakers (CBs) or reclosers, instead of usual sectionalizers, are deployed for remote control and frequent operational switching in recent years. Thus, it is clear that real-time topology reconfiguration via distribution network reconfiguration (DNR) can be realizable and adaptive to system operational requirements [7]. In terms of DNR problems in cyber-physical environment, the real-time topology optimization follows the dynamic balance between supply and demand on multiple facets of security levels, i.e., physical level, cyber level and privacy level. As an alternative, DNR can achieve operational flexibility enhancement for economic dispatch tasks.

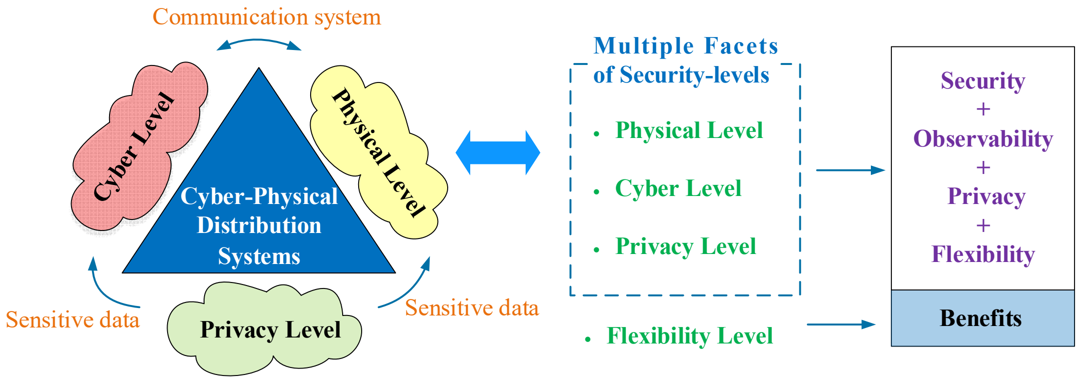

Fig. 1.4 Three concerned levels of cyber-physical distribution systems and associated benefits

1.2 Research Motivations

Distribution network reconfiguration (DNR) is a classical optimal operation problem of DNs over decades. It is a specific topology optimization about choosing the optimal switch status of sectionalizing switches (normally closed), tie-switches (normally open), and/or controllable power flows by soft open points (SOPs) [8]. In contrast to passive DNs, two objectives are achievable from performing DNR actions: (*i*) maintaining real-time load balancing and loss reduction for DNs with the growing penetration of DERs; and (*ii*) coordinating real-time transactive dispatch tasks between supply and demand at the market level of DNs. At present, these two objectives can be realizable due to the upgraded applications of high-speed switching devices. Therefore, this DNR research is the fundamental for the transition to active DNs involved with various requirements for the quick solvability, cyber-physical system security, privacy-preserving ability and dispatch flexibility enhancement.

1.2.1 Primary Approaches for Topology Optimization of ADNs

To address the quick solvability of DNR problems, heuristic methods and convex relaxations are two primary effective solving approaches for ADNs.

In terms of heuristic methods, there is a rich set of optimization approaches in the power systems literature that tries to circumvent these problems. In fact, the non-linearity of AC power flow complicate solving a DNR problem. To handle this problem, researchers used DC power flow, a *DistFlow* model [10] that is a second-order mathematical programming model, and full AC power flow [11]. However, the DC power flow model is inaccurate while the *DistFlow* and the full AC power flow models are accurate but very time-consuming for a large system. Black-box heuristic methods, which push power flow calculations outside the optimization solver, have become very popular, owing to their broad applicability [12]. In summary, heuristic methods perform well in small systems but might converge slowly, especially in large-scale systems [13]. And the results obtained by heuristic methods for different runs might not be the same, which prevents them from being widely used in power system applications.

Regarding convex relaxations, efficacious convex relaxation approaches in existing studies for DNR are effective for fast solving. It mainly adopted the Big-M method [14], or McCormick linearization method [15], [16] to slack power flow constraints by switch status indicators, or construct relaxation constraints with variables automatically satisfied for a disconnected line [17]. However, these convex relaxation methods suffer from loosened relaxation bounds, which renders a large amount of computational time. Moreover, a DNR problem is cast as a combinatorial explosion in the number of total possible solutions as the number of branches increases, if the open/closed status of each branch is regarded as a binary variable. For instance, the number of total possible solutions is 2136 for a DN has 136 circuit breakers. This induces that a DNR problem becomes high-dimensional, thus spending significant amounts of computational time [18]. To reduce the computational time caused by high-dimension binary variables, it is essential to exploit the DNR model characterization that can be used to accelerate this entire computation. On top of that, with a high penetration of DERs into DNs, the fluctuated power injections intricately trigger a complicated DNR decision-making process due to bi-directional power flows [19], [20]. This suggests that today's active DNs increases the difficulty level of quick solvability. In the light of loosened relaxation bounds, high-dimensional space of binary variables and integrations of enrichable DERs, there is a research gap to explore the efficient and tight relaxation approach for DNR problems in large-scale active DNs.

Based on the convex hull (CH) of *DistFlow* equations [21], a disjunctive convex hull relaxation (DCHR) [22] can be further constructed to deal with these on/off constraints caused by switch status indicators. In this thesis, we are stimulated to study the DCHR approach for the classic DNR problem, which can be designed to tighten the voltage drop equation and quadratic equality of *DistFlow* equations with continuous parent-child relationship variables in spanning tree constraints.

1.2.2 Cyber-Physical Security Enhancement for Topology Optimization of ADNs

Apart from the fast computation methods for DNR problems, we have to consider the cyber-physical security enhancement for topology optimization of ADNs. The deployment of cyber-physical systems with ADNs has led to an increase in efficiency, observability, and flexibility to facilitate the real-time operation of ADNs. However, some security threats from the inter dependency of the cyber and physical components of CPDS cannot be sufficiently tackled only with the simplest protection measures such as data encryption [23], [24]. Protecting DNs against cyber–physical threats typically is simply to eliminate the threat of false data injection attacks (FDIAs) on state estimation [25]–[28], where the data integrity of state estimation is greatly relevant to limited security resources, e.g., distribution-level phasor measurement units (D-PMUs) [29] and communication networks.

Against these possible cyber-physical threats, the defense level of cyber-physical distribution system security for the real-time DNR has not been widely concerned to date. In existing studies, K. C. Sou [30], [31] constructs a minimum cost placement of PMUs such that no FDIA is possible. However, this work is a D-PMU planning issue with the corresponding minimal encrypted device investment for a fixed grid topology, which model is not suitable to solve operational issues. For the operational issues regarding D-PMUs, the measurements of D-PMUs can be employed to address physical DNR problems in DNs [32], [33]. However, since any measurements of D-PMUs can be attackable, corrupted measurements and/or load data on state estimation [34] can render improper DNR actions, then probably inducing physical security issues that cannot be observed. To migrate this issue, we are focused on the full system observability of DNs that is crucial to understand the physical system states [35].

With the full system observability of ADNs, the various grid operations depending on the physical system's behaviors, e.g., generator redispatch, fault location, can be under monitoring and control. For example, the DSOs can observe the voltage excursion and overloading power flows as soon as early, and then can remove these insecurity problems in time [36]. Accordingly, the effective cyber-physical system security defense, e.g., the full system observability guarantees, cannot be neglected [37]. At present, few studies deal with this defense issue at the lowest expense of different topology schemes from the perspective of full system observability.

1.2.3 Privacy-Preserving Enhancement for Topology Optimization of ADNs

Even though cyber-physical security of ADNs can be guaranteed, privacy-preserving data sharing should be also crucial for distribution-level agents, especially for those with conflicting interests. At the operation level, DSOs maintain load balancing and loss reduction via the ADNs reconfiguration by the optimal status of sectionalizing switches and tie-switches [9]. This is very common for interconnected ADNs, which are energized by two or more substations to coordinate the use of both resources to meet the load demands, and also helps to reduce new utility investments and operating costs effectively [38]. In this chapter, the interconnected ADNs are supposed to be managed by different agents who are also stakeholders, e.g., load aggregators. And their network connections are tie-lines across different agents.

For interconnected multi-agent ADNs, tie-line load flow information and topology switch status are generally shared with different agents for interconnected operational and/or marketing purposes, which energy data-sharing may evoke privacy-related complications, i.e., inference of sensitive information [39]. In the future energy data asset market, the energy data-sharing mechanisms has drawn extensive attention [40], especially for the auction market with fair commercial competition [41]. Under this background, we specifically focus on the privacy-related information leakage issue of loads caused by the DNR operation on two load levels, i.e., agent's and customer's levels. For agent's privacy concerns, sharing tie-line load flow information may suffer from leaking the private load change information of an agent, i.e., transition from a light load to a heavy load. This information can be acknowledged by other agents who are stakeholders with conflicting interests, e.g., bidding for grid services in energy market [41]. On the customer's load privacy level, all customer's load datasets from smart meters are obliged to be uploaded to the distribution dispatch center, which is used for centralized DNR operations by the DSO. This may possibly expose the sensitive load consumption of individual customers to adversaries, i.e., further inferring commercial behaviors [42] or performing cyber-physical attacks [43], [44].

To cope with agent's privacy leakage challenge, homomorphic encryption [45], or differential privacy [46] can be constructed to preserve these sensitive datasets, e.g., tie-line load flows. Homomorphic encryption protects exchanged data via encryption and decryption operation by a trusted third party who should own a large amount of available computational resources in [45] and [47]. However, finding an authorized and high-performance computing third party for this job is also very costly for real-time DNR operations. Therefore, we concentrate on a differential privacy mechanism to increase the data privacy and it can be used to share sensitive data without a trusted third party. Regarding differential privacy mechanism in power systems, it can quantify and bound privacy risks through the randomization of sensitive datasets, e.g., leveraging a carefully calibrated noise to solve the private-preserving optimal power flow (OPF) problems in ADNs [48] and transmission systems [49], or obfuscating power grid parameters for network privacy preservation [50]. Recently, the program perturbation strategy [51], [52] is created to ensure the feasibility of privacy-preserving optimal solutions with the high probability via a stochastic chance-constrained optimization reformulation. This is superior to the bi-level optimization based on the output/objective perturbation strategy used in [49]. Nevertheless, this program perturbation strategy fails to output a mixture of the realistically optimal topology solution and obfuscated-but-feasible load flow solutions in the query answers. To explore this mixture query, it is essential to construct a tailored differentially private DNR (DP-DNR) mechanism to provide the optimal topology solution for the entire interconnected ADNs, whilst the sensitive information of agent's load changes can be preserved via obfuscated-but- feasible load flow solutions.

Regarding the customer's privacy, since this privacy leakage may be caused by uploading sensitive load datasets to the distribution dispatch center, a decentralized framework is well suited for the DSO to deal with this DNR problem [53] and the resilience enhancement of ADNs in recent years [54], [55], [56], [57]. This also contributes to relieving the communication burden and preserving the privacy of customers' load datasets. In terms of decentralized frameworks, the alternating direction method of multipliers (ADMM) approach and its variants [58], are typical decentralized solutions for such privacy-preserving concerns [59]. Recently, it can be used in mixed-integer quadratic programming (MIQP) problems with good performance as reported in [56], [57], [60]. To be specific, the DNR problem can be approximated as a MIQP problem. Thus, the consensus ADMM (C-ADMM) approach can be adopted to deal with this DNR problem by breaking the complex computational DNR tasks into much smaller ones. Each smaller computational task is performed by an individual agent who only communicates and works collectively with the DSO by exchanging their tie-switch states and tie-line load flows. However, the explicit communication exchanging signals of realistic tie-line load flows are also potentially risky to leak the sensitive information of agent's load changes. In this study, we consider integrating the proposed DP-DNR mechanism into the C-ADMM approach. Namely, the communication signals of tie-line load flows between neighbors and the DSO is differentially private subject to the realistic tie-switch status. In this regard, a decentralized DNR approach can be very satisfactory for the agent's and customer's privacy-preserving desires.

1.2.4 Operational Flexibility Enhancement by Topology Optimization of HVDNs

On top of that, growing penetration of renewable energy in power generation areas provides a green solution to the decarbonization of power systems [61]-[64]. To accommodate more renewable energy integration, the wind-thermal-bundled power system (WTBPS) is a suitable option to increase power system flexibility [65]. To explore an efficient economic dispatch of WTBPS, distribution-level topology optimization [66] and energy storage [67] can be used to increase the flexibility of WTBPS in which this generation system instantly accommodates the rapid growth of wind farms.

Since WTBPS can mitigate the uncertainty and variability of renewable resources, the transition of optimal generation dispatch is underway to multi-energy generation systems. Previous work has investigated the economic dispatch methods in bulk AC/DC hybrid WTBPS [68], combined generation system of multiple renewable energy resources and energy storage [69], multi-fuel [70], and integrated electricity and natural gas system [71]. Also, multi-energy generation systems can involve flexible demand-side resources such as energy hubs [72], electric vehicles [73], and controllable loads [74] into economic dispatch problems, which further eases the pressure on the power system. In view of these economic dispatch methods, they have not considered retrofitting flexibility measures on coal-fired power plants and d via HVDNs into economic dispatch problems.

On the one hand, retrofitted coal-fired plants are worldwide concerned, since coal-fired plants are not phased out, especially in middle-income countries [75]. Without retrofits, coal power plants can run at the minimum level of 50%, and the ramp rate for an inflexible unit is 0.6–2% per minute of rated power [76]. After retrofits, retrofitted power plants can enable sufficient flexibility [73], [77], the most beneficial advances of which are the reduction of minimum load levels to 15%-30% of rated capacities and the increase of ramp rate to 2–6% per minute of rated power. For example, the ramp rates of retrofitted power plants are generally raised to 2–6% in China, 2–6% in Poland, and 3-6% in Germany. The minimal load of coal-fired plant Bexbach has been reduced by 11%, and coal-fired plant Wes Weiler has increased the ramp rate by 10MW/min in Germany [77]. As reported in [78], ramping limits in practical applications should be a function of the unit's generating output. Thus, ramp rates are dynamic at different output power levels. Existing pieces of literature regarding dynamic ramp rates mainly fit into two categories, i.e., piecewise linear functions and stepwise linear representations [78]. Piecewise linear function models capture the dynamic ramp rates between two consecutive periods as a function of the output level [79]; whereas stepwise linear function models select fixed ramp rates. Similar to a piecewise method, the dynamic ramping model in [80] by incorporating a status transition modeling approach is further improved. Retrofitted coal-fired units with molten-salt thermal energy storage [73], as a type of flexibility improvement, enable faster ramp rates to relieve the peak regulation stress.

On the other hand, storage energy response [81] or distribution-side load transfer actions [82] will be an alternative to offset the insufficient ramping margins of coal-fired units in WTBPS. Reference [83] adopts an adjustable heat storage strategy from solar power stations to shift excess wind power in combined wind-thermal generation systems. However, compared with solar power resources, the operation cost of stored energy is too expensive to be widely used in WTBPS. Load resources in distribution networks have instinctive flexibility, which has great potential to install with WTBPS in order to maximally avoid wind curtailment. As the desirable load provider, the distribution-level topology actions have been performed via reconfigurable HVDNs integrated with renewable resources under stability-constrained conditions [84]. HVDNs are sub-transmissions on 110kV voltage level [82] constructed in meshed topology (closed loop) but operated in radial structures (open loop), which network can be found in China [82], Spain [84] and Finland [85]. The HVDNs are composed of specific topological units, which can reduce the computational complexity of distribution-level topology optimization from conventional network reconfiguration. The proposed distribution-level topology optimization model in [82] adopts simplified *DistFlow* to embody voltage security constraints. However, this increases computational complexity and decreases the efficiency of many power flow variables. To this end, we aim to enhance this effective distribution-level topology optimization model with more simplified yet effective voltage security constraints.

1.3 Primary Contributions

Severe issues in facets of physical-oriented, cyber-oriented, and privacy-oriented security can be emerged in the topology reconfiguration of smart DNs, which should be considered for real-time operational actions. This thesis aims to enhance different facets of security using the advanced topology optimization, and then explores a distribution-level topology optimization for flexibility enhancement in economic dispatch of wind-thermal-bundled power system.

1) To avoid worldwide climate change effects, decarbonization initiatives transit the conventional DNs to be smart DNs mixed with a high penetration of DERs. This paper theoretically reformulates the DNR model with enrichable DERs using the disjunctive convex hull approach. Continuous parent-child relationship variables in spanning tree constraints can be regarded as disjunctive variables to represent disjunctive convex hull of *DistFlow* equations. And this disjunctive convex hull relaxation (DCHR) is proven as a tighter relaxation than the existing relaxation techniques for DNR problems, such as the Big-M and McCormick linearization methods. Case studies also demonstrate that the DCHR's computing performance is superior to the prior relaxation methods.

2) The system observability enabled by D-PMUs becomes increasingly crucial for cyber-physical security enhancement. We formulate this system observability as a disjunctive relaxed connected dominating set problem for reconfigurable distribution networks with the least defense cost in theory. For the benefits of system observability, an observability defense-constrained DNR model has been proposed. This DNR

model is then converted to a mixed integer second-order conic programming problem, which can be solved with commercial solvers easily.

3) The topology switch for the loss minimization may expose the private information of light and heavy loads for interconnected DNs owned by different stakeholders with conflicting interests. For agent's privacy concerns, we propose the DP-DNR mechanism in this chapter. This DP-DNR mechanism provides a mixture output of realistically optimal tie-switch status and corresponding obfuscated-but-feasible load flows, part of which may have reverse load flow directions. This privacy-preserving mechanism is used to mitigate agent's privacy concerns against private load change leakage from DNR operations, which has not been concerned yet. On the customer's privacy-preserving level, the C-ADMM-based decentralized DP-DNR approach can seek the optimal DNR solution without customer's load datasets of agents. The exchanged communication signals are also synthetic based on the proposed DP-DNR mechanism, which perfectly protects the realistic communication messages between agents and the DSO. Thus, this proposed decentralized reconfiguration approach is applicable for interconnected multi-agent ADNs against the agent's and customer's privacy leakage, which has not been studied to date.

4) A distribution-level topology optimization contributes to the flexibility enhancement of a look-ahead rolling economic dispatch of WTBPS, which offsets the insufficient ramping margins of retrofitted coal-fired units. Since WTBPS connects to high voltage distribution networks (HVDNs), graph characterization of typical

HVDNs is summarized, and then the simplified voltage-constrained load transfer strategy via topological structures can be developed. Moreover, this proposed look-ahead economic dispatch model is cast as a mixed-integer second-order cone programming (MISOCP) problem. For this established MISOCP-based model, it is highly desirable to combine the Multi-cut Benders Decomposition (MBD) [86] and Generalized Benders Decomposition (GBD) [87] as the devised Multi-cut GBD (MGBD) to tackle this MISOCP problem, which can enhance overall computational efficiency and be suitable for online rolling economic dispatch.

Table 1.1 Highlights of contributions in this thesis

Items	Key characteristics of research problems	Weakness of existing references	Contributions
Computational challenges of DNR (Chapter 3)	● Mixed-integer second-order conic optimization problem ● Computationally challenging, especially for the large-scale networks	● Big-M method [14] ● McCormick linearization method [15], [16] ● Loosened relaxation techniques	DCHR with provably tightened relaxation
Cyber-physical security of DNR (Chapter 4)	● System observability cost can be optimized w.t.r. reconfiguration	● Conventional DNR model ● System observability cannot be guaranteed[37] ● RCDS formulation [30] ,[31]	Observability defense-constrained DNR
Privacy-preserving DNR (Chapter 5)	● Topology switch for the loss minimization may expose the private information of light and heavy loads	● Conventional DNR model ● Private information for agents cannot be guaranteed [39],[40]	DP-DNR mechanism
Flexibility enhancement of economic dispatch (Chapter 6)	● Look-ahead rolling economic dispatch of WTBPS ● Dispatchable load resources ● Mixed-integer	● Conventional ramping model of thermal power units [80] ● Conventional dispatch model of thermal-wind-bundled	Decentralized MGBD-based approach for rolling economic dispatch of WTBPS

	second-order conic optimization problem ● Computationally challenging, especially for the large-scale networks	generation system [104] ● Centralized optimization, e.g., GBD [87]	

1.4 Thesis Layout

The rest of this thesis consists of seven Chapters. Chapter 2 reviews the fundamentals of *DistFlow* equations and its convex relaxation formulations. Chapter 3 firstly proposes the disjunctive convex hull approach to deal with the reconfiguration of DNs. This approach is theoretically tighter than the McCormick linearization method and the Big-M method, and it is especially suitable for smart DNs with directional power flows. Chapter 4 develops the observability defense-constrained topology optimization of DNs, which perfectly enables an observable DNR solution just with the cyber–physical security enhancement. Chapter 5 presents a differentially private topology optimization of ADNs, which provides a pair of realistic optimal topology variables and obfuscated-but-feasible power flow variables simultaneously. This is applicable for shared data access with agent’s and customer’s privacy protection. Chapter 6 deals with distribution-level topology optimization for flexibility enhancement in economic dispatch of wind-thermal-bundled power system. This distribution-level topology optimization offsets the insufficient ramping margins of retrofitted coal-fired units. Finally, the conclusions and future work of the thesis are drawn in Chapter 7.

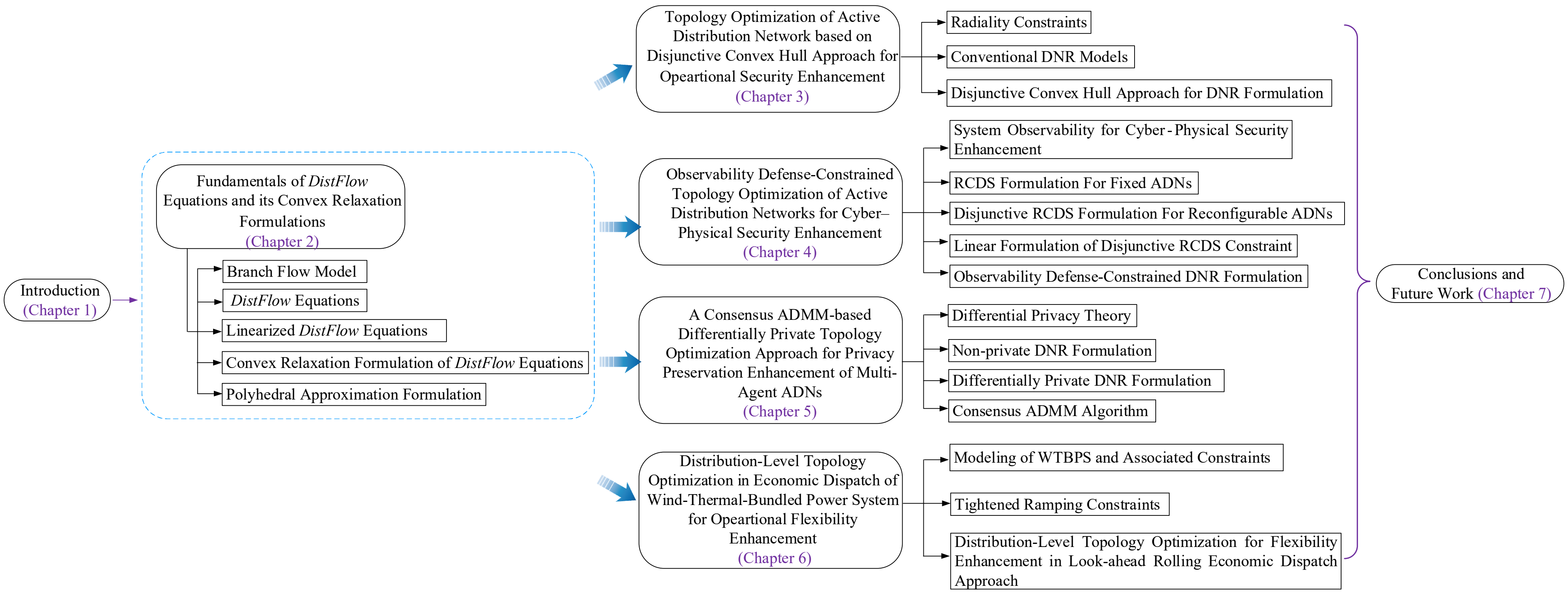

Fig. 1.5 Illustration of overall organizational structure of the thesis.

Chapter 2

Fundamentals of *DistFlow* Equations and its Convex Relaxation Formulations

In view of distribution networks (DNs) highly penetrated by enrichable distributed energy resources (DERs) and inverter-based resources (IBRs), a fast power flow calculation method is essential not only for the load balancing and loss reduction at the voltage security-constrained level, but also for real-time transactive dispatch tasks between supply and demand at the market level of DNs.

This chapter lays the theoretical foundation of *DistFlow* equations and its convex relaxation formulations. Initially, *DistFlow* equations can be derived from the branch flow model, and then a linearized *DistFlow* equations can be obtained if the non-convex terms are negligible. Subsequently, the SOCP and SDP form of *DistFlow* equations are formulated according to SOCP and SDP convex relaxation techniques. Additionally, the polyhedral approximation formulation is included for linearizing the SOC constraints in SOCP-based reactive power optimization model. The results of case studies prove the effectiveness of the variations of *DistFlow* equations.

2.1 Branch Flow Model

The steady-state network power flow status can be described by branch flow model (BFM) proposed in [10]. A arbitrary branch l:= (m, n) in single-phase radial DNs (i.e., networks with a tree topology) is illustrated in Fig. 2.1. For this branch l, P_n^d and Q_n^d

are fixed active and reactive power demands with $\tilde{S}_n^d = P_n^d + jQ_n^d$; z_{mn}^l refers to the impedance with $(z_{mn}^l)^2 = (r_{mn}^l)^2 + (x_{mn}^l)^2$; P_n^g and Q_n^g are active and reactive power generation at node n with $\tilde{S}_n^g = P_n^g + jQ_n^g$, respectively; P_{mn}^l and Q_{mn}^l are active and reactive power flows with $\tilde{S}_{mn}^l = P_{mn}^l + jQ_{mn}^l$, respectively.

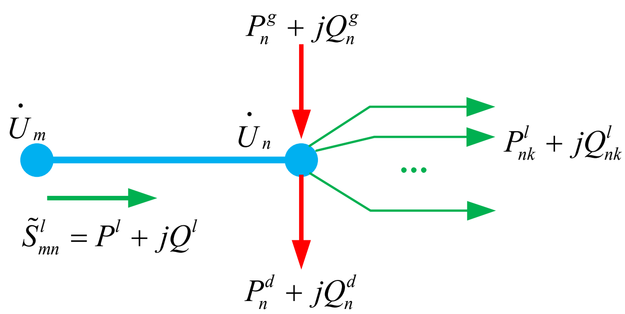

Fig. 2.1 Typical connection of a branch in DNs.

In practice, we have one assumption that the shunt elements in DNs are assumed zero, namely $b_{mn}/2=0$. This assumption is reasonable for realistic DNs due to short distances of branches. Under this assumption, we can express the apparent power flow for this branch l as $\tilde{S}_{mn}^l = \dot{U}_m (I_{mn}^l)^*$, where $\dot{U}_m$ refers to the voltage phasor at node m and $(I_{mn}^l)^*$ refers to the conjugate of current phasor between nodes m and n. However, if this branch is modeled by a series admittance y_{mn} with shunt elements, i.e. $b_{mn}/2\neq 0$, then a shunt admittance $b_{mn}/2$ is included on each end of line (m, n) in the π model. Accordingly, the apparent power flow should be rearranged as $\tilde{S}_{mn}^l - j\frac{b_{mn}U_m^2}{2} = \dot{U}_m (I_{mn}^l)^*$. Moreover, the voltage drop equation can be written as $\dot{U}_n = \dot{U}_m - z_{mn}^l \cdot I_{mn}^l$, where z_{mn}^l denotes the impedance of branch l. Therefore, when formulating distribution power flow equations in phasor form, we can achieve the BFM-based power flow equality, yielding

$$\begin{cases} \dot{U}_n = \dot{U}_m - z_{mn}^l \cdot I_{mn}^l \\ \tilde{S}_{mn}^l = \dot{U}_m (I_{mn}^l)^* \\ \tilde{S}_{mn}^l + \tilde{S}_n^g - z_{mn}^l |I_{mn}^l|^2 = \sum\limits_{k \in \pi(n)} \tilde{S}_{nk}^l + \tilde{S}_n^d \end{cases}, \quad \forall l \in \mathcal{E}, \forall m, n \in \mathcal{N} \tag{2.1}$$

where $\pi(n)$ refers to the set of branches that connect the node n.

As observed in (2.1), distribution power flow equations are non-convex due to non-convex terms $\dot{U}_m (I_{mn}^l)^*$. And $\tilde{S}_{mn}^l + S_n^g - z_{mn}^l |I_{mn}^l|^2 = \sum\limits_{k \in \pi(n)} \tilde{S}_{nk}^l + S_n^d$ is a nonlinear equation caused by $|I_{mn}^l|^2$. In other words, BFM-based power flow equality is not suitable for tractable computation, and thus we need to reformulate this BFM-based power flow equality.

2.2 *DistFlow* Equations

Due to this voltage drop equation in phasor form, we solve this equation with squares on both sides as $|\dot{U}_n|^2 = |\dot{U}_m - z_{mn}^l \cdot I_{mn}^l|^2$. After multiplying both sides by complex conjugate, the right hand side (RHS) of this voltage drop equation can be rearranged as

$$\begin{aligned} |\dot{U}_m - z_{mn}^l \cdot I_{mn}^l|^2 &= (\dot{U}_m - z_{mn}^l \cdot I_{mn}^l)(\dot{U}_m - z_{mn}^l \cdot I_{mn}^l)^* \\ &= |U_m|^2 + |z_{mn}^l \cdot I_{mn}^l|^2 - 2\,\mathrm{Re}(\dot{U}_m (z_{mn}^l \cdot I_{mn}^l)^*) \\ &= |U_m|^2 + |z_{mn}^l|^2 \cdot |I_{mn}^l|^2 - 2\,\mathrm{Re}(\dot{U}_m \cdot z_{mn}^{l*} \cdot I_{mn}^{l*}) \\ &= |U_m|^2 + |z_{mn}^l|^2 \cdot |I_{mn}^l|^2 - 2\,\mathrm{Re}(z_{mn}^{l*} \cdot \tilde{S}_{mn}^l) \\ &= |U_m|^2 + |z_{mn}^l|^2 \cdot |I_{mn}^l|^2 - 2 r_{mn}^l \cdot P_{mn}^l - 2 x_{mn}^l \cdot Q_{mn}^l \end{aligned} \tag{2.2}$$

where r_{mn}^{l} and x_{mn}^{l} indicate the resistance and reactance of branch *l*. $|U_m|$ and $|I_{mn}^{l}|$ denote the voltage magnitude of voltage phasor $\dot{U}_m$ and current modulus of current phasor I_{mn}^{l}, respectively. Note that for any vector *x*, Re(*x*) refers to the real part of *x*.

It should be noted that (2.1) is actually a phase angle free equation, since all variables $|U_m|$, $|I_{mn}^{l}|$, P_{mn}^{l} and Q_{mn}^{l} are real-valued numbers. In mathematics, we call this equation as the angle relaxation. Indeed, we can consider the real-valued ($|U_m|, |I_{mn}^{l}|, P_{mn}^{l}, Q_{mn}^{l}$)-space as a projection of complex-valued ($\dot{U}_m, I_{mn}^{l}, \tilde{S}_{mn}^{l}$)-space. This implies that each variable $|I_{mn}^{l}|$ or $|U_m|$ is relaxed from a point in the complex plane to a circle with a radius equal to the distance of the point from the origin. The intuitive explanation for this angle relaxation can be taken $\dot{U}_m = |U_m| e^{i\theta}$ as shown in Fig. 2.2. Suppose that $\dot{U}_m$ on the complex coordinate space is a point. Then, a circle with a radius equal to $|U_m|$ is the set of solutions for any real-valued variable $|U_m|$. By $|\dot{U}_m|^2 = |U_m|^2$, a point is clearly relaxed to a circle.

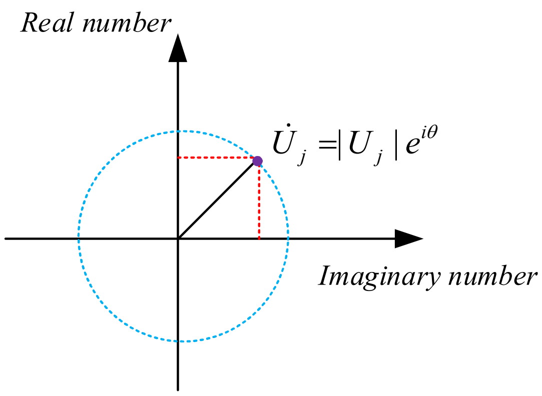

Fig. 2.2 Illustration of angle relaxation for (2.1).

Similarly, we take the modulus with squares on both side of $\tilde{S}^{l}_{mn} = \dot{U}_{m}(I^{l}_{mn})^{*}$, yielding

$$|\dot{U}_{m}(I^{l}_{mn})^{*}|^{2} = |\tilde{S}^{l}_{mn}|^{2} \quad \Leftrightarrow \quad |U_{m}|^{2} \cdot |I^{l}_{mn}|^{2} = (P^{l}_{mn})^{2} + (Q^{l}_{mn})^{2} \tag{2.3}$$

As mentioned above, if a shunt admittance $b_{mn}/2$ is included, then $|\tilde{S}^{l}_{mn} - j\frac{b_{mn}U^{2}_{m}}{2}|^{2} = |\dot{U}_{m}(I^{l}_{mn})^{*}|^{2}$ is a complicated quadratic equation that cannot be converted to this SOC form. In summary, it can be seen that (2.1) and (2.2) are two angle free equations after applying angle relaxation. According to the reference direction of power flow shown in Fig. 2.1, the left-hand (right-hand) side gathers total active and reactive power injected (withdrawn) in (from) node n. We can express the corresponding ***DistFlow*** equations with respect to unknown variables $(|U_{m}|, |I^{l}_{mn}|, P^{l}_{mn}, Q^{l}_{mn})$ based on nodal power flow balance equations and (2.1)-(2.2). In this study, the radial DNs are considered as a connected undirected tree $\mathcal{G} = (\mathcal{N}, \mathcal{E})$, where $\mathcal{N} = [1,\ 2,\ ...,|\mathcal{N}|]$ is the set of nodes and $\mathcal{E}$ is the set of branches in the dimension $|\mathcal{E}| = (|\mathcal{N}| - 1) \times 1$. The branch l:= (m, n), $l \in \mathcal{E}$ is between nodes (m, n) where $m, n \in \mathcal{N}$ and we assume that the point of common connection (PCC) node is 0. Therefore, *DistFlow* equations [10] are expressed as

$$P^{l}_{mn} + P^{g}_{n} - r^{l}_{mn}\ell^{l}_{mn} = \sum_{k \in \pi(n)} P^{l}_{nk} + P^{d}_{n} \quad \forall l \in \mathcal{E}, \forall m, n \in \mathcal{N} \tag{2.4}$$

$$Q^{l}_{mn} + Q^{g}_{n} - x^{l}_{mn}\ell^{l}_{mn} = \sum_{k \in \pi(n)} Q^{l}_{nk} + Q^{d}_{n} \quad \forall l \in \mathcal{E}, \forall m, n \in \mathcal{N} \tag{2.5}$$

$$v_{n} = v_{m} - 2(r^{l}_{mn}P^{l}_{mn} + x^{l}_{mn}Q^{l}_{mn}) + |z^{l}_{mn}|^{2}\ell^{l}_{mn} \quad \forall l \in \mathcal{E}, \forall m, n \in \mathcal{N} \tag{2.6}$$

$$\ell^{l}_{mn} \cdot v_{m} = (P^{l}_{mn})^{2} + (Q^{l}_{mn})^{2} \quad \forall l \in \mathcal{E}, \forall m, n \in \mathcal{N} \tag{2.7}$$

where $\ell^{l}_{mn} = |I^{l}_{mn}|^{2}, v_{m} = |U_{m}|^{2}$ and $v_{n} = |U_{n}|^{2}$.

In this set of ***DistFlow*** equations, (2.4)-(2.5) are nodal active power and reactive power balancing conditions. (2.6) describes forward voltage drop on each branch obtained by (2.2) and (2.7) is derived from (2.3) which defines apparent power flow injection at the head node m of each branch. The squared voltage magnitude $v_0 = |U_0|^2$ at the PCC is a constant. In this regard, we can define a vector of variables as $\boldsymbol{x}$:=($\boldsymbol{v}$, ℓ^l , $\boldsymbol{P}^l$, $\boldsymbol{Q}^l$) for $\forall l \in \mathcal{E}$,the key feature of which is that $\boldsymbol{x}$ does not involve angles of voltage and current phasors. Most importantly, (2.4)-(2.7) in BFM are linear, and non-convexity only appears in branch flow equality (2.7). This BFM-based power flow equation is much different from bus injection model in which power balancing conditions render non-convex quadratic equalities.

It should be also noted that:

- **Uniqueness of solutions for *DistFlow* equations**

There are $2|\mathcal{E}|+2|\mathcal{E}|=4|\mathcal{N}|-4$ equations in $|\mathcal{N}|-1+3|\mathcal{E}|=4|\mathcal{N}|-4$ real variables. It is clear that the number of variables is equal to the number of equations, which means that this ***DistFlow*** equations would have a unique solution or multiple solution. It is shown in [88], [89] that this set of equations have generally multiple solutions, but for radial distribution networks with $|U| \approx 1$ p.u. and small r_{mn}^l and x_{mn}^l , the solution of (2.4)-(2.7) is unique and same to the one produced by the traditional bus injection model in rectangle coordinate. It should be noted that for a connected mesh network ($|\mathcal{E}|=|\mathcal{N}|$), this set of (2.4)-(2.7) equations have $2|\mathcal{E}|+2|\mathcal{E}|=4|\mathcal{N}|$ equations in which the number of variables is $|\mathcal{N}|-1+3|\mathcal{E}|=4|\mathcal{N}|-1$. Therefore, the solution is generally nonunique. Some of these solutions may be spurious, i.e., they do not correspond to a solution of the original branch flow equations.

- **Application to general networks (loop networks)**

The ***DistFlow*** equations can be extended to be used for general networks that may contain cycles by introducing a cycle condition. We define the angle difference across for branch l as

$$\beta_{mn}(x) := \angle(\dot{U}_m - z^l_{mn} \cdot I^l_{mn}) \tag{2.8}$$

For convenience, we let $\beta(x) := (\beta_{mn}(x), l := (m,n), \forall l \in \mathcal{E})$. Thus, the ***DistFlow*** equations are extended to general networks as:

$$(2.4)-(2.7), \exists \theta \in \mathbb{R}, s.t. \beta\ (x) = A \cdot \theta \tag{2.9}$$

where A is a $|\mathcal{E}|$ by $|\mathcal{N}|$ branch-node incidence matrix in tree graph $\mathcal{G}$ with A_{ml}=1 if $l = m \to n$ for some n, A_{ml}=-1 if $l = n \to m$ for some m, and 0 otherwise. This branch-node incidence matrix A will be discussed later. We refer to the condition $\beta\ (x) = A \cdot \theta$ on x in (2.9) as the cycle condition, which can be enforced by introducing θ as additional variables. For general networks (2.4)-(2.7) can thus be interpreted as a relaxation of (2.9) where the cycle condition is ignored. When a network is radial, the cycle condition is vacuous and (2.9) reduces to (2.4)-(2.7).

- **Compact matrix-vector form**

For brevity, l refers to a vector of branches if sending end nodes m, n are omitted; otherwise, l denotes an arbitrary branch l: =(m,n), $l \in \mathcal{E}$ is between nodes (m, n) where $m,n \in \mathcal{N}$. In this study, we assume that the root node is 0. v_m and v_n are the squared voltage profiles at node m and n. It should be noted that $\boldsymbol{A}^l \cdot v = v_m - v_n$ holds where $\boldsymbol{A}$ is a $|\mathcal{E}|$ by $|\mathcal{N}|$ branch-node incidence matrix in tree graph $\mathcal{G}$ and $\boldsymbol{A}^l$ refers to the l-th row. Expressing with $A \cdot v$ is generally formulated in the matrix-vector form. To avoid heavy notations, the following steady-state network power flow equality (2.10)-(2.13) can be derived by the real-valued ***DistFlow*** equations for $\forall l \in \mathcal{E}$ in the compact matrix vector form.

$$-\boldsymbol{P}^g + \boldsymbol{P}^d = \boldsymbol{A}^T \boldsymbol{P}^l - \boldsymbol{D}_r \ell^l \tag{2.10}$$

$$-\boldsymbol{Q}^g + \boldsymbol{Q}^d = \boldsymbol{A}^T \boldsymbol{Q}^l - \boldsymbol{D}_x \ell^l \tag{2.11}$$

$$\boldsymbol{A}\boldsymbol{v} - 2\boldsymbol{D}_r \boldsymbol{P}^l - 2\boldsymbol{D}_x \boldsymbol{Q}^l + \boldsymbol{D}_z \ell^l = 0 \tag{2.12}$$

$$\ell^l \cdot \boldsymbol{D}_v = |\boldsymbol{P}^l|^2 + |\boldsymbol{Q}^l|^2 \tag{2.13}$$

where P^l and Q^l refer to the vectors of sending-end active and reactive power flows with the moduli equal to $|P^l|$ and $|Q^l|$. P^g, Q^g and P^d, Q^d indicate the vectors of given nodal active and reactive power injections and active and reactive loads at nodes. Q^{cr} is the vector of nodal reactive power compensation. ℓ^l is the vector of squared current on branches. $\boldsymbol{D}_r$ and $\boldsymbol{D}_x$ indicate the diagonal matrices whose diagonal elements are the resistance vector and the reactance vector, respectively. $\boldsymbol{D}_z$ is the diagonal matrix whose diagonal elements are $|\boldsymbol{z}^l|=|\boldsymbol{r}^l|^2+|\boldsymbol{x}^l|^2$. $\boldsymbol{D}_v$ is the diagonal matrix whose diagonal elements are squared voltage profiles of the sending nodes for all branches.

Let us illustrate more about branch-node incidence matrix $\boldsymbol{A}$. For instance, the topology of a radial DN is displayed in Fig. 2.3, where $|\mathcal{N}|=10$, $|\mathcal{E}|=9$ and $|\mathcal{N}|=|\mathcal{E}|+1$. The line feeding node n is indexed as line n-th, e.g. the second branch is brn#2 where the ending node is 2.

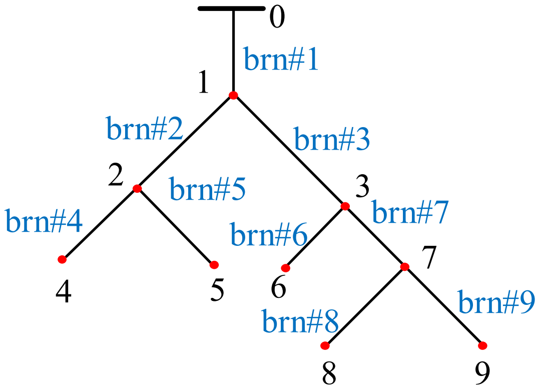

Fig. 2.3 Topology of a radial DN.

For (2.12) and (2.13), we present the branch-node incidence matrix A as

$$
\boldsymbol{A} = \begin{array}{r} \\ brn\#1: \\ brn\#2: \\ brn\#3: \\ brn\#4: \\ brn\#5: \\ brn\#6: \\ brn\#7: \\ brn\#8: \\ brn\#9: \end{array}
\begin{array}{c}
\begin{array}{cccccccccc} node:0 & 1 & 2 & 3 & 4 & 5 & 6 & 7 & 8 & 9 \end{array} \\
\begin{bmatrix}
1 & -1 & & & & & & & & \\
 & 1 & -1 & & & & & & & \\
 & 1 & & -1 & & & & & & \\
 & & 1 & & -1 & & & & & \\
 & & 1 & & & -1 & & & & \\
 & & & 1 & & & -1 & & & \\
 & & & 1 & & & & -1 & & \\
 & & & & & & & 1 & -1 & \\
 & & & & & & & 1 & & -1
\end{bmatrix}
\end{array}
\tag{2.14}
$$

As for (2.12), we substitute the given voltage magnitude of PCC at node 0 for the first brn #1. We can further simplify A as below:

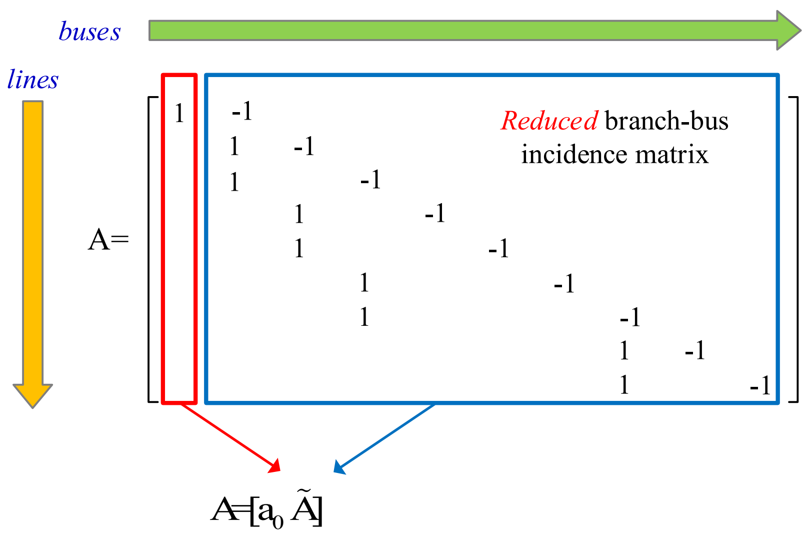

where $\tilde{\mathbf{A}}$ refers to the reduced branch-node incidence matrix. Thus, (2.13) can be further rearranged as

$$-\tilde{\boldsymbol{A}}v - 2D_r P^l - 2D_x Q^l + D_z \ell^l = a_0 v_0 \tag{2.15}$$

According to Ohm's law, when each node is injected by the current in one unit, we can obtain

$$\boldsymbol{A} \cdot 1_{|\varepsilon|+1} = 0 \Rightarrow a_0 + \tilde{\boldsymbol{A}} \cdot 1_{|\varepsilon|} = 0 \Rightarrow 1_{|\varepsilon|} = -a_0 \cdot \tilde{\boldsymbol{A}}^{-1}$$

where $-a_0 \cdot \tilde{\boldsymbol{A}}^{-1}$ can be defined as the branch-branch incidence matrix and a_0 is a scalar. Given this branch-branch incidence matrix, we can obtain the current for any branches by the measured current from the PCC. For example, the branch-branch incidence matrix $-a_0 \cdot \tilde{\boldsymbol{A}}^{-1}$ can be equal to

$$\begin{array}{r c}
 & \begin{array}{ccccccccc} brn: 1 & 2 & 3 & 4 & 5 & 6 & 7 & 8 & 9 \end{array} \\
\begin{array}{r} brn\#1: \\ brn\#2: \\ brn\#3: \\ brn\#4: \\ brn\#5: \\ brn\#6: \\ brn\#7: \\ brn\#8: \\ brn\#9: \end{array} &
\begin{bmatrix}
1 & & & & & & & & \\
1 & 1 & & & & & & & \\
1 & & 1 & & & & & & \\
1 & 1 & & 1 & & & & & \\
1 & 1 & & & 1 & & & & \\
1 & & 1 & & & 1 & & & \\
1 & & 1 & & & & 1 & & \\
1 & & 1 & & & & 1 & 1 & \\
1 & & 1 & & & & 1 & & 1
\end{bmatrix}
\end{array} \tag{2.16}$$

where a_0=1.

2.3 Linearized *DistFlow* Equations

The compact matrix-vector form of ***DistFlow*** equations can be simplified if dropping terms related to losses and quadratic equations are negligible. We can express the real-valued LDF equations for $\forall l \in \mathcal{E}$ in the compact matrix-vector notation using the LDF method

$$-\boldsymbol{P}^g + \boldsymbol{P}^d = \boldsymbol{A}^T \tilde{\boldsymbol{P}}^l \tag{2.17}$$

$$-\boldsymbol{Q}^g + \boldsymbol{Q}^d = \boldsymbol{A}^T \tilde{\boldsymbol{Q}}^l \tag{2.18}$$

$$-\boldsymbol{A}\tilde{\boldsymbol{v}} - 2\boldsymbol{D}_r \tilde{\boldsymbol{P}}^l - 2\boldsymbol{D}_x \tilde{\boldsymbol{Q}}^l = 0 \tag{2.19}$$

where $\tilde{P}^l$ and $\tilde{Q}^l$ refer to the vector of sending-end active and reactive power flows; $\tilde{v}$ denotes the vector of squared voltage profiles.

Equivalently, we rearrange this set of LDF equations as

$$\tilde{\boldsymbol{P}}^l = \boldsymbol{A}(-\boldsymbol{P}^g + \boldsymbol{P}^d) \tag{2.20}$$

$$\tilde{\boldsymbol{Q}}^l = \boldsymbol{A}(-\boldsymbol{Q}^g + \boldsymbol{Q}^d) \tag{2.21}$$

$$-\boldsymbol{A}\tilde{\boldsymbol{v}} - 2\boldsymbol{D}_r \boldsymbol{A}(-\boldsymbol{P}^g + \boldsymbol{P}^d) - 2\boldsymbol{D}_x \boldsymbol{A}(-\boldsymbol{Q}^g + \boldsymbol{Q}^d) = 0 \tag{2.22}$$

It should also be noted that there are several characteristics for this set of LDF equations

(*i*) All equations are linear and are only with respect to a vector of variables $\tilde{\boldsymbol{x}}$:=($\tilde{\boldsymbol{v}}$, $\tilde{\boldsymbol{P}}^l$, $\tilde{\boldsymbol{Q}}^l$), which is smaller than the size of $\boldsymbol{x}$ in ***DistFlow*** equations.

(*ii*) Voltage drop and line power flows are approximately linearly related to power injections.

(*iii*) LDF gives an over-estimator for squared voltage magnitudes.

Proof: According to (2.22), we can formulate

$$-\tilde{\boldsymbol{A}}\boldsymbol{v} - 2\boldsymbol{D}_r \boldsymbol{P}^l - 2\boldsymbol{D}_x \boldsymbol{Q}^l + \boldsymbol{D}_z \ell^l = a_0 v_0 \tag{2.23}$$

Rearranging (2.23) as

$$\boldsymbol{v} = -(\tilde{\boldsymbol{A}})^{-1} \cdot [a_0 v_0 + 2\boldsymbol{D}_r \boldsymbol{P}^l + 2\boldsymbol{D}_x \boldsymbol{Q}^l] + (\tilde{\boldsymbol{A}})^{-1} \boldsymbol{D}_z \ell^l \tag{2.24}$$

Then, due to $(\tilde{\boldsymbol{A}})^{-1} \boldsymbol{D}_z \ell^l < 0$ and $-(\tilde{\boldsymbol{A}})^{-1} \cdot [a_0 v_0 + 2\boldsymbol{D}_r \boldsymbol{P}^l + 2\boldsymbol{D}_x \boldsymbol{Q}^l] > 0$, we can obtain this inequality as

$$\boldsymbol{v} < -(\tilde{\boldsymbol{A}})^{-1} \cdot [a_0 v_0 + 2\boldsymbol{D}_r \boldsymbol{P}^l + 2\boldsymbol{D}_x \boldsymbol{Q}^l] \tag{2.25}$$

The RHS of (2.25) is equal to $\tilde{\boldsymbol{v}} = -(\tilde{\boldsymbol{A}})^{-1} \cdot [a_0 v_0 + 2\boldsymbol{D}_r \boldsymbol{P}^l + 2\boldsymbol{D}_x \boldsymbol{Q}^l]$, which can be achieved by LDF. Thus, we prove that $\tilde{\boldsymbol{v}} > \boldsymbol{v}$.

(*iv*) LDF gives an under-estimator for line flows.

Proof: According to (2.22), we can directly derive the following inequality

$$\boldsymbol{P}^l = \boldsymbol{A}(-\boldsymbol{P}^g + \boldsymbol{P}^d + \boldsymbol{D}_r \ell^l) > \boldsymbol{A}(-\boldsymbol{P}^g + \boldsymbol{P}^d) = \tilde{\boldsymbol{P}}^l \tag{2.26}$$

$$\boldsymbol{Q}^l = \boldsymbol{A}(-\boldsymbol{Q}^g + \boldsymbol{Q}^d + \boldsymbol{D}_x \ell^l) > \boldsymbol{A}(-\boldsymbol{Q}^g + \boldsymbol{Q}^d) = \tilde{\boldsymbol{Q}}^l \tag{2.27}$$

Thus, we prove that $\boldsymbol{P}^l > \tilde{\boldsymbol{P}}^l$ and $\boldsymbol{Q}^l > \tilde{\boldsymbol{Q}}^l$.

(*v*) Approximation accuracy by LDF depends on loading conditions. The approximation error of this LDF can be acceptable if

- Voltage magnitudes close to unity, namely $|\boldsymbol{v}| = 1 + \varepsilon$ with $|\varepsilon| \simeq 0$;
- Voltage angle differences across lines close to zero, i.e., $\theta_{nm} = \theta_n - \theta_m \simeq 0$
- Ignoring line resistances and shunt elements.

In industrial applications, DNs generally have relatively flat voltage profiles maintaining by automatic voltage control (AVC) system. Due to flat voltage profiles, the small approximation error of LDF can only be about ±1% [90]. Note that the squared voltage profile $|v_i|$ can be approximated from first-order Taylor series expansion around the normal voltage profile $|U_0| = 1$.

2.4 Convex Relaxation Formulation of *DistFlow* Equations

2.4.1 Second-order Conic Programming Formulation

In the sake of realizing minimum power losses, we discuss the reactive power optimization problem for the fixed typology of DNs. The two convex relaxations of ***DistFlow*** equations are discussed in the section. Before incorporating convex relaxations, we at first discuss the conventional reactive power optimization model for DNs:

$$\min_{\tilde{S}^l, I^l, \dot{U}, Q^{cr} \in \mathbb{C}} \quad \mathrm{Re}(\tilde{S}_0^l)$$
$$s.t. \begin{cases} \dot{U}_n = \dot{U}_m - z_{mn}^l \cdot I_{mn}^l, \quad \forall l \in \mathcal{E}, \forall m,n \in \mathcal{N} \\ \tilde{S}_{mn}^l = \dot{U}_m (I_{mn}^l)^*, \quad \forall l \in \mathcal{E}, \forall m,n \in \mathcal{N} \\ \tilde{S}_{mn}^l + \tilde{S}_n^g - z_{mn}^l |I_{mn}^l|^2 = \sum_{k \in \pi(n)} \tilde{S}_{nk}^l + \tilde{S}_n^d, \quad \forall l \in \mathcal{E}, \forall m,n \in \mathcal{N} \\ \underline{Q}_{inj}^l \le \mathrm{Im}(\tilde{S}_{inj}^l) \le \overline{Q}_{inj}^l \\ \underline{Q}^{cr} \le Q^{cr} \le \overline{Q}^{cr} \\ \underline{U} \le |\dot{U}| \le \overline{U} \end{cases} \tag{2.28}$$

where $\tilde{S}_0^l$ refers to the complex power on the first branch between the PCC and a PQ bus; $\mathrm{Re}(\tilde{S}_0^l)$ and $\mathrm{Im}(\tilde{S}_0^l)$ refer to the real part and imaginary part of $\tilde{S}_0^l$, respectively. Other symbols are illustrated in Section 1.

Recall that the conventional reactive power optimization model (2.28) is non-convex, we can further modify this conventional model based on *DistFlow* equations for the preparation of convex relaxations:

$$\min_{x^l \in \mathbb{R}} \quad P_0^l$$

$$s.t. \begin{cases} P_{mn}^l + P_n^g - r_{mn}^l \ell_{mn}^l = \sum\limits_{k \in \pi(n)} P_{nk}^l + P_n^d, \forall l \in \mathcal{E}, \forall m, n \in \mathcal{N} \\ Q_{mn}^l + Q_n^g - x_{mn}^l \ell_{mn}^l = \sum\limits_{k \in \pi(n)} Q_{nk}^l + Q_n^d, \forall l \in \mathcal{E}, \forall m, n \in \mathcal{N} \\ v_n = v_m - 2(r_{mn}^l P_{mn}^l + x_{mn}^l Q_{mn}^l) + |z_{mn}^l|^2 \ell_{mn}^l, \forall l \in \mathcal{E}, \forall m, n \in \mathcal{N} \\ \ell_{mn}^l \cdot v_m = (P_{mn}^l)^2 + (Q_{mn}^l)^2, \forall l \in \mathcal{E}, \forall m, n \in \mathcal{N} \\ \underline{Q}_{inj}^l \le Q_{inj}^l \le \overline{Q}_{inj}^l \\ \underline{Q}^{cr} \le Q^{cr} \le \overline{Q}^{cr} \\ \underline{v} \le v \le \overline{v} \end{cases} \tag{2.29}$$

where P_0^l refers to the active power injection of the first branch between the PCC and a PQ bus.

For (2.29), all constraints are linear only except for $\ell_{mn}^l \cdot v_m = (P_{mn}^l)^2 + (Q_{mn}^l)^2$. Here, we equivalently slack this quadratic equalities to a pair of two inequalities below:

$$\ell_{mn}^l \cdot v_m \ge (P_{mn}^l)^2 + (Q_{mn}^l)^2 \quad \forall l \in \mathcal{E}, \forall m, n \in \mathcal{N} \tag{2.30}$$

$$\ell_{mn}^l \cdot v_m \le (P_{mn}^l)^2 + (Q_{mn}^l)^2 \quad \forall l \in \mathcal{E}, \forall m, n \in \mathcal{N} \tag{2.31}$$

After dropping (2.31), we can relax the non-convex quadratic equalities as an inequality below:

$$\ell_{mn}^l \cdot v_m \ge (P_{mn}^l)^2 + (Q_{mn}^l)^2 \quad \forall l \in \mathcal{E}, \forall m, n \in \mathcal{N} \tag{2.32}$$

We can arrange this inequality by multiplying 4 on the both sides of (2.32)

$$(2P_{mn}^l)^2 + (2Q_{mn}^l)^2 - 2\ell_{mn}^l \cdot v_m \le 2\ell_{mn}^l \cdot v_m \quad \forall l \in \mathcal{E}, \forall m, n \in \mathcal{N} \tag{2.33}$$

After adding $(\ell_{mn}^l)^2 + (v_m)^2$ on both sides of (2.33), (2.33) can be rearranged as

$$(2P_{mn}^l)^2 + (2Q_{mn}^l)^2 + (\ell_{mn}^l - v_m)^2 \le (\ell_{mn}^l + v_m)^2 \quad \forall l \in \mathcal{E}, \forall m, n \in \mathcal{N} \tag{2.34}$$

Therefore, this inequality (2.34) is converted to a standard SOC form by

$$\begin{Vmatrix} 2P_{mn}^{l} \\ 2Q_{mn}^{l} \\ \ell^{l}_{mn} - v_m \end{Vmatrix}_2 \leq (\ell^{l}_{mn} + v_m) \quad \forall l \in \mathcal{E}, \forall m,n \in \mathcal{N} \tag{2.35}$$

Note that (2.32) also refers to a rotated SOC inequality. The standard SOCP-based formulation of *DistFlow* equations is

$$P_{mn}^{l} + P_n^{g} - r_{mn}^{l}\ell^{l}_{mn} = \sum_{k \in \pi(n)} P_{nk}^{l} + P_n^{d} \quad \forall l \in \mathcal{E}, \forall m,n \in \mathcal{N} \tag{2.36}$$

$$Q_{mn}^{l} + Q_n^{g} - x_{mn}^{l}\ell^{l}_{mn} = \sum_{k \in \pi(n)} Q_{nk}^{l} + Q_n^{d} \quad \forall l \in \mathcal{E}, \forall m,n \in \mathcal{N} \tag{2.37}$$

$$v_n = v_m - 2(r_{mn}^{l}P_{mn}^{l} + x_{mn}^{l}Q_{mn}^{l}) + |z_{mn}^{l}|^2 \ell^{l}_{mn} \quad \forall l \in \mathcal{E}, \forall m,n \in \mathcal{N} \tag{2.38}$$

$$\begin{Vmatrix} 2P_{mn}^{l} \\ 2Q_{mn}^{l} \\ \ell^{l}_{mn} - v_m \end{Vmatrix}_2 \leq (\ell^{l}_{mn} + v_m) \quad \forall l \in \mathcal{E}, \forall m,n \in \mathcal{N} \tag{2.39}$$

According to SOCP-based *DistFlow* equations, we define the vector of optimization variables $\boldsymbol{x}^{l}$ for the minimization of real power loss. This is also called reactive power optimization problem for the fixed typology of DNs. The set of optimization variables involves a set of state variables $\left[P^{l},\, Q^{l},\, \ell^{l},\, v_{PQ}\right]^{T}$ and a vector of controllable variables $\left[v_{PCC}, Q^{cr}\right]^{T}$. Here, v_{PQ} refers to squared voltage profiles at PQ nodes and v_{PCC} is the adjustable squared voltage profile at PCC node; and Q^{cr} is a vector of the reactive power compensation sources. In addition, as observed in (2.39), two auxiliary variables can be incorporated to represent:

$$\begin{cases} w^{l} = \ell^{l}_{mn} - v_m \\ m^{l} = \ell^{l}_{mn} + v_m \end{cases} \tag{2.40}$$

Consequently, the vector of optimization variables $\boldsymbol{x}^{l}$ can be defined as

$$\boldsymbol{x}^{l} := [P^{l},\, Q^{l},\, \ell^{l},\, v,\, Q^{cr}, w^{l}, m^{l}]^{T} \tag{2.41}$$

The constraints are composed of *Distflow* equations and reactive power injection constraint of the first branch between the PCC and a PQ bus, reactive power capacity compensation constraints for all reactive power compensation sources as well as voltage security constraints for all nodes.

$$\underline{Q}^{cr} \le Q^{cr} \le \overline{Q}^{cr} \tag{2.42}$$

$$\underline{v} \le v \le \overline{v} \tag{2.43}$$

where $\underline{Q}^{cr}$ and $\overline{Q}^{cr}$ indicate the lower and upper limits of reactive power compensation sources. $\underline{v}$ and $\overline{v}$ denote the lower and upper squared voltage profile limits of PQ nodes.

The objective function of this minimization of real power loss can be converted to the minimal real power injection at PCC node. Thus, the reactive power optimization model is formulated as

$$\begin{aligned}
&\min_{\boldsymbol{x}^l \in \mathbb{R}} \quad P_0^l \\
&s.t. \begin{cases}
P_{mn}^l + P_n^g - r_{mn}^l \ell_{mn}^l = \sum_{k \in \pi(n)} P_{nk}^l + P_n^d, \forall l \in \mathcal{E}, \forall m,n \in \mathcal{N} \\
Q_{mn}^l + Q_n^g - x_{mn}^l \ell_{mn}^l = \sum_{k \in \pi(n)} Q_{nk}^l + Q_n^d, \forall l \in \mathcal{E}, \forall m,n \in \mathcal{N} \\
v_n = v_m - 2(r_{mn}^l P_{mn}^l + x_{mn}^l Q_{mn}^l) + |z_{mn}^l|^2 \ell_{mn}^l, \forall l \in \mathcal{E}, \forall m,n \in \mathcal{N} \\
\left\| \begin{matrix} 2P_{mn}^l \\ 2Q_{mn}^l \\ w^l \end{matrix} \right\|_2 \le m^l, \forall l \in \mathcal{E}, \forall m,n \in \mathcal{N} \\
w^l = \ell_{mn}^l - v_m,\ m^l = \ell_{mn}^l + v_m, \quad \forall l \in \mathcal{E}, \forall m,n \in \mathcal{N} \\
\underline{Q}^{cr} \le Q^{cr} \le \overline{Q}^{cr}, \underline{v} \le v \le \overline{v}
\end{cases}
\end{aligned} \tag{2.44}$$

where P_0^l is the active power injection at the root node 0.

Exactness of SOCP convex relaxation

However, is the optimal solution of (2.44) the same as the one solved by (2.1)? If and only if the convex relaxation techniques are exact, the obtained solution is the same as the optimal solution of original non-convex nonlinear optimization. This section we discuss whether SOCP relaxations for reactive power optimization problems are exact or not. Looking from case studies in previous subsections, it seems that all optimal solutions are satisfied with SOC equality. This suggests that the SOC relaxation is exact. Now, let us give the exactness of SOCP convex relaxation and its associated proof by contradiction [88], [89].

Theorem: The SOCP-based reactive power optimization formulation (2.44) is convex. Moreover, it is exact, i.e., an optimal solution of (2.44) is also optimal for the original reactive power optimization problem (2.1).

Proof: For this SOCP-based model (2.44), we rewrite the objective function $\min P_{inj}^{l}$ as $\min \sum_{l\in\mathcal{E}} r_{mn}^{l}\ell_{mn}^{l}$. To prove that the relaxation is exact, it suffices to show that any optimal solution of (2.1) has equality in $\ell_{mn}^{l}\cdot v_{m}=(P_{mn}^{l})^{2}+(Q_{mn}^{l})^{2}$. Assume for the sake of contradiction that $x^{l\star}:=(P_{ij}^{l\star},Q_{ij}^{l\star},\ell^{l\star},v^{\star},Q^{cr\star})$ is optimal but has strict inequality, i.e.,

$$\ell_{mn}^{l\star}\cdot v_{m}^{\star}>(P_{mn}^{l\star})^{2}+(Q_{mn}^{l\star})^{2},\forall l\in\mathcal{E} \tag{2.45}$$

Now for some $\varepsilon>0$, consider another point $\tilde{x}^{l}:=(\tilde{P}_{ij}^{l},\tilde{Q}_{ij}^{l},\tilde{\ell}^{l},\tilde{v},\tilde{Q}^{cr})$, which is defined by

$$\begin{cases} \tilde{v}=v^{\star}, \tilde{Q}^{cr}=Q^{cr\star} \\ \tilde{P}^{l}_{mn}=P^{l\star}_{mn}-r^{l}_{mn}\varepsilon/2, \quad \tilde{P}^{l}_{-mn}=P^{l\star}_{-mn} \\ \tilde{Q}^{l}_{mn}=Q^{l\star}_{mn}-x^{l}_{mn}\varepsilon/2, \quad \tilde{Q}^{l}_{-mn}=Q^{l\star}_{-mn} \\ \tilde{\ell}^{l}_{mn}=\ell^{l\star}_{mn}-\varepsilon, \quad \tilde{\ell}^{l}_{-mn}=\ell^{l\star}_{-mn} \\ \tilde{P}^{d}_{n}=P^{d}_{n}+r^{l}_{mn}\varepsilon/2, \quad \tilde{P}^{d}_{m}=P^{d}_{m}+r^{l}_{mn}\varepsilon/2, \\ \tilde{Q}^{d}_{n}=Q^{d}_{n}+x^{l}_{mn}\varepsilon/2, \quad \tilde{Q}^{d}_{m}=Q^{d}_{m}+x^{l}_{mn}\varepsilon/2, \\ \tilde{P}^{d}_{-n}=P^{d}_{-n}, \tilde{P}^{d}_{-m}=P^{d}_{-m}, \tilde{Q}^{d}_{-n}=Q^{d}_{-n}, \tilde{Q}^{d}_{-m}=Q^{d}_{-m} \end{cases} \tag{2.46}$$

where the negative indices mean excluding elements from a vector.

When $\tilde{\ell}^{l}_{mn}\cdot\tilde{v}_{m}=(\tilde{P}^{l}_{mn})^{2}+(\tilde{Q}^{l}_{mn})^{2}$ holds for certain $\varepsilon>0$, it can be verified that $\tilde{x}^{l}$ can satisfy

$$\begin{aligned} \tilde{v}_{n} &= \tilde{v}_{m}-2(r^{l}_{mn}\tilde{P}^{l}_{mn}+x^{l}_{mn}\tilde{Q}^{l}_{mn})+|z^{l}_{mn}|^{2}\tilde{\ell}^{l}_{mn} \\ &= \tilde{v}_{m}-2(r^{l}_{mn}P^{l\star}_{mn}+x^{l}_{mn}Q^{l\star}_{mn})+|z^{l}_{mn}|^{2}\ell^{l\star}_{mn}+(r^{l}_{mn})^{2}\varepsilon+(x^{l}_{mn})^{2}\varepsilon-|z^{l}_{mn}|^{2}\varepsilon \\ &= \tilde{v}_{m}-2(r^{l}_{mn}P^{l\star}_{mn}+x^{l}_{mn}Q^{l\star}_{mn})+|z^{l}_{mn}|^{2}\ell^{l\star}_{mn} \end{aligned} \tag{2.47}$$

For $\tilde{P}^{l}_{mn}+P^{g}_{n}-r^{l}_{mn}\tilde{\ell}^{l}_{mn}=\sum_{k\in\pi(n)}\tilde{P}^{l}_{nk}+\tilde{P}^{d}_{n}$, we can find $P^{l\star}_{mn}-r^{l}_{mn}\varepsilon/2+P^{g}_{n}-r^{l}_{mn}\ell^{l\star}_{mn}+r^{l}_{mn}\varepsilon=\sum_{k\in\pi(n)}P^{l\star}_{nk}+P^{d}_{n}+r^{l}_{mn}\varepsilon/2$ holds and for $Q^{l}_{mn}+Q^{g}_{n}-x^{l}_{mn}\ell^{l}_{mn}=\sum_{k\in\pi(n)}Q^{l}_{nk}+Q^{d}_{n}$, this point $\tilde{x}^{l}$ still holds under this over-satisfaction of load. Please note that this over-satisfaction of load is needed because we have increased the loads $\tilde{P}^{d}_{n}$ and $\tilde{Q}^{d}_{n}$ on buses and to obtain the alternative feasible solution $\tilde{x}^{l}$.

This means that $\tilde{x}^{l}$ satisfies all constraints (2.1) and hence is a feasible point. Since $\tilde{\ell}^{l}_{mn}=\ell^{l\star}_{mn}-\varepsilon$, the $\tilde{x}^{l}$ has a strictly smaller objective value $\sum_{l\in\mathcal{E}}r^{l}_{mn}\ell^{l}_{mn}$ than $x^{l\star}$. This contradicts the optimality of $x^{l\star}$. This theorem indicates that the optimal solution satisfies SOC with equality and yield lower loss cost, if the objective function is strictly increasing in the power injections. Once there is an inverse power flow in DNs, i.e. DGs to generate power to grids, this relaxation may be inexact. So this exact SOCP relaxation condition holds under a load oversatisaction assumption (i.e., for a node n, $\tilde{P}_n^d - P_n^d \geq 0$) and radial networks, while the objective is to minimize losses or minimize the total cost with respect to power injections. ■

2.4.2 Semi-Definite Programming Formulation

We firstly recall the general mathematic conversion between inequality constraints and semi-definite formulation. For example, we can find the following two formulations are equivalent:

$$\left\{(x,y)\in\mathbb{R}^2 : \boldsymbol{X}=\begin{bmatrix} x & 0 & y \\ 0 & 1 & -x \\ y & -x & 1 \end{bmatrix}\succeq 0, \operatorname{rank}(\boldsymbol{X})=1\right\} \Leftrightarrow \left\{(x,y)\in\mathbb{R}^2 : \begin{array}{c} 0\leq x\leq 1 \\ x\geq y^2 \\ x-x^3-y^2\geq 0 \end{array}\right\} \quad (2.48)$$

Similarly, we can apply this equivalent conversion for the quadratic constraints in *DistFlow* equations. The alternative formulation of non-convex quadratic equalities (1.7) can be expressed in SDP form. We establish $\boldsymbol{X}^l = \begin{bmatrix} \dot{U}_m \\ I_{mn}^l \end{bmatrix}\begin{bmatrix} \dot{U}_m^* & (I_{mn}^l)^* \end{bmatrix} = \begin{bmatrix} v_m & \tilde{S}_{mn}^l \\ \tilde{S}_{mn}^{l*} & \ell_{mn}^l \end{bmatrix}$ that satisfies $\det(\boldsymbol{X}^l) = \ell_{mn}^l \cdot v_m - \tilde{S}_{mn}^l \tilde{S}_{mn}^{l*}$. If $\boldsymbol{X}^l$ is semi-definite as $\boldsymbol{X}^l \succeq 0$ and rank($\boldsymbol{X}^l$)=1, then $\ell_{mn}^l \cdot v_m - \tilde{S}_{mn}^l \tilde{S}_{mn}^{l*} \geq 0$.

The non-convex quadratic equalities (1.7) is converted to

$$X^l = \begin{bmatrix} v_m & \tilde{S}_{mn}^l \\ \tilde{S}_{mn}^{l*} & \ell_{mn}^l \end{bmatrix} \succeq 0 \quad (2.49)$$

$$\operatorname{rank}(\boldsymbol{X}^l)=1 \quad (2.50)$$

However, $\mathrm{rank}(\boldsymbol{X}^{l})=1$ is a non-convex constraint, and thus the standard SDP-based formulation omits this constraint. Therefore, the standard SDP-based formulation of *DistFlow* equations [89] is

$$P_{mn}^{l}+P_{n}^{g}-r_{mn}^{l}\ell_{mn}^{l}=\sum_{k\in\pi(n)}P_{nk}^{l}+P_{n}^{d}\quad\forall l\in\mathcal{E},\forall m,n\in\mathcal{N}\tag{2.51}$$

$$Q_{mn}^{l}+Q_{n}^{g}-x_{mn}^{l}\ell_{mn}^{l}=\sum_{k\in\pi(n)}Q_{nk}^{l}+Q_{n}^{d}\quad\forall l\in\mathcal{E},\forall m,n\in\mathcal{N}\tag{2.52}$$

$$v_{n}=v_{m}-2\left(r_{mn}^{l}\frac{\tilde{S}_{mn}^{l}+\tilde{S}_{mn}^{l*}}{2}+x_{mn}^{l}\frac{\tilde{S}_{mn}^{l}-\tilde{S}_{mn}^{l*}}{2}\right)+|z_{mn}^{l}|^{2}\ell_{mn}^{l}\quad\forall l\in\mathcal{E},\forall m,n\in\mathcal{N}\tag{2.53}$$

$$\boldsymbol{X}^{l}=\begin{bmatrix}v_{m} & \tilde{S}_{mn}^{l}\\ \tilde{S}_{mn}^{l*} & \ell_{mn}^{l}\end{bmatrix}\succeq 0\tag{2.54}$$

For the 2×2 complex-valued matrix $\boldsymbol{X}^{l}$, we can decompose it as a linear matrix inequality (LMI) constraint

$$\begin{aligned}\boldsymbol{X}^{l}&=\begin{bmatrix}v_{m} & \tilde{S}_{mn}^{l}\\ \tilde{S}_{mn}^{l*} & \ell_{mn}^{l}\end{bmatrix}\\ &=v_{m}\begin{bmatrix}1&0\\0&0\end{bmatrix}+(P_{mn}^{l}+jQ_{mn}^{l})\begin{bmatrix}0&1\\0&0\end{bmatrix}+(P_{mn}^{l}-jQ_{mn}^{l})\begin{bmatrix}0&0\\1&0\end{bmatrix}+\ell_{mn}^{l}\begin{bmatrix}0&0\\0&1\end{bmatrix}\\ &=v_{m}\begin{bmatrix}1&0\\0&0\end{bmatrix}+P_{mn}^{l}\begin{bmatrix}0&1\\1&0\end{bmatrix}+Q_{mn}^{l}\begin{bmatrix}0&j\\-j&0\end{bmatrix}+\ell_{mn}^{l}\begin{bmatrix}0&0\\0&1\end{bmatrix}\succeq 0\end{aligned}\tag{2.55}$$

According to SDP-based *DistFlow* equations, we define the vector of optimization variables $\boldsymbol{x}^{l}$ for the minimization of real power loss. By applying LMI constraint, the complex-valued matrix $\boldsymbol{X}^{l}$ is rearranged to a constraint with respect to variables P_{mn}^{l}, Q_{mn}^{l}, ℓ_{mn}^{l}, and v_{m}. Therefore, the vector of optimization variables $\boldsymbol{x}^{l}$ can be defined as

$$\boldsymbol{x}^{l}:=[\boldsymbol{P}^{l},\boldsymbol{Q}^{l},\ \ell^{l},\ \boldsymbol{v},\boldsymbol{Q}^{cr}]^{T}\tag{2.56}$$

Consequently, the complete reactive power optimization model is formulated as

$$
\min_{\boldsymbol{x}^l \in \mathbb{R}} \quad P_0^l
$$

$$
s.t.\begin{cases}
P_{mn}^l + P_n^g - r_{mn}^l \ell^l{}_{mn} = \sum\limits_{k\in\pi(n)} P_{nk}^l + P_n^d, \forall l \in \mathcal{E}, \forall m,n \in \mathcal{N} \\
Q_{mn}^l + Q_n^g - x_{mn}^l \ell^l{}_{mn} = \sum\limits_{k\in\pi(n)} Q_{nk}^l + Q_n^d, \forall l \in \mathcal{E}, \forall m,n \in \mathcal{N} \\
v_n = v_m - 2(r_{mn}^l P_{mn}^l + x_{mn}^l Q_{mn}^l) + |z_{mn}^l|^2 \ell^l{}_{mn}, \forall l \in \mathcal{E}, \forall m,n \in \mathcal{N} \\
v_m \begin{bmatrix} 1 & 0 \\ 0 & 0 \end{bmatrix} + P_{mn}^l \begin{bmatrix} 0 & 1 \\ 1 & 0 \end{bmatrix} + Q_{mn}^l \begin{bmatrix} 0 & j \\ -j & 0 \end{bmatrix} + \ell^l{}_{mn} \begin{bmatrix} 0 & 0 \\ 0 & 1 \end{bmatrix} \succeq 0, \forall l \in \mathcal{E}, \forall m,n \in \mathcal{N} \\
\underline{Q}^{cr} \le Q^{cr} \le \overline{Q}^{cr}, \underline{v} \le v \le \overline{v}
\end{cases}
\tag{2.57}
$$

Note that there is another formulation of this model with respect to complex-valued vector $\boldsymbol{x}^l := [\tilde{S}^l,\ \ell^l,\ v,\ Q^{cr}]^T$. In this vein, we formulate this complex-valued reactive power optimization model below:

$$
\min_{\boldsymbol{x}^l \in \mathbb{C}} \quad \frac{\mathrm{Tr}(S_0^l + S_0^{l*})}{2}
$$

$$
s.t.\begin{cases}
P_{mn}^l + P_n^g - r_{mn}^l \ell^l{}_{mn} = \sum\limits_{k\in\pi(n)} P_{nk}^l + P_n^d, \forall l \in \mathcal{E}, \forall m,n \in \mathcal{N} \\
Q_{mn}^l + Q_n^g - x_{mn}^l \ell^l{}_{mn} = \sum\limits_{k\in\pi(n)} Q_{nk}^l + Q_n^d, \forall l \in \mathcal{E}, \forall m,n \in \mathcal{N} \\
v_n = v_m - 2(r_{mn}^l \dfrac{\tilde{S}_{mn}^l + (\tilde{S}_{mn}^l)^*}{2} + x_{mn}^l \dfrac{\tilde{S}_{mn}^l - (\tilde{S}_{mn}^l)^*}{2}) + |z_{mn}^l|^2 \ell^l{}_{mn}, \forall l \in \mathcal{E}, \forall m,n \in \mathcal{N} \\
v_m \begin{bmatrix} 1 & 0 \\ 0 & 0 \end{bmatrix} + S_{mn}^l \begin{bmatrix} 0 & 1 \\ 0 & 0 \end{bmatrix} + S_{mn}^{l*} \begin{bmatrix} 0 & 0 \\ 1 & 0 \end{bmatrix} + \ell^l{}_{mn} \begin{bmatrix} 0 & 0 \\ 0 & 1 \end{bmatrix} \succeq 0, \forall l \in \mathcal{E}, \forall m,n \in \mathcal{N} \\
\underline{Q}^{cr} \le Q^{cr} \le \overline{Q}^{cr}, \underline{v} \le v \le \overline{v}
\end{cases}
\tag{2.58}
$$

where $\mathrm{Tr}(S_0^l + S_0^{l*})$ refers to the trace of $S_0^l + S_0^{l*}$.

2.5 Polyhedral Approximation Formulation

It is evident that the quadratic equality of *DistFlow* equations can be relaxed in a SOC formulation according to Subsection 2.4.1. In this subsection, we investigate how can a SOC cone can be approximated into a set of linearizations. Mathematically, the second-order cone is also called a Lorentz cone or an ice-cream cone. The general mathematical definition is cast as

$$L^n := \{(x,t) \in \mathbb{R}^n \times \mathbb{R} \,|\, \| x \|_2 \leq t\} \tag{2.59}$$

For instance, if n=2, then the geometry of a Lorentz cone L^2 is displayed in Fig. 2.4.

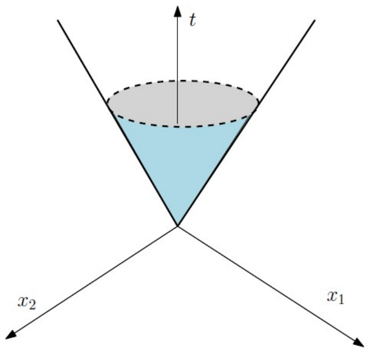

Fig. 2.4 Geometry of a Lorentz cone L^2.

The feasible region of a second-order cone can be well-approximated by a polyhedral cone, as presented in Fig. 2.5. This polyhedral approximation makes a SOC constraint become a series of linear constraints. The approximation accuracy depends on the number of outer polyhedral linearizations.

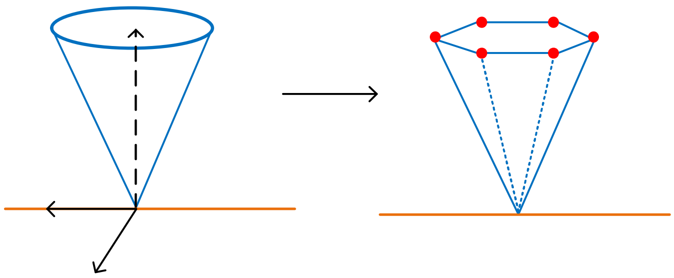

Fig. 2.5 Approximation of a Lorentz cone as a polyhedral cone.

Definition. Let $\mathcal{F}$ be a feasible region of a SOCP, i.e. $\mathcal{F} := \{x : Ax \geq b, \| Ax - b \|_2 \leq cx - d\}$ and let $\mathcal{F}_\varepsilon := \{x : Ax \geq b, \| Ax - b \|_2 \leq (cx - d)(1 + \varepsilon)\}$. A polyhedral cone $\boldsymbol{P}$ is an ε-approximation of $\mathcal{F}$ if $\mathcal{F} \subseteq \mathrm{P} \subseteq \mathcal{F}_{\varepsilon}$.

Next, we seek to find an ε-approximation of $\mathcal{F}$. Recall that a 3-dimensional Lorentz cone $L^2 = \{(x,t) \in \mathbb{R}^2 \times \mathbb{R} : \| x \| \le t\}$. Given $\tilde{x} = (\tilde{x}_1, \tilde{x}_2, \overline{t}) \in \mathbb{R}^3$, how can determine this any point lies in L^2. Assume w.l.o.g. $\overline{t} = 1$, $\tilde{x} \ge 0$. Ideally, rotating the point $(\tilde{x}_1, \tilde{x}_2, 1)$ to $(\tilde{x}_1^{'}, 0, 1)$ is shown in Fig. 2.6. It is clear that $\tilde{x} \in L^2$ iff $\tilde{x}_1^{'} \le 1$. If this angle is arbitrarily small, then we can check whether the rotated point $\tilde{x}_1^{'} \in L_{\varepsilon}^2$ for an appropriate small ε, since the component $\tilde{x}_2^{'}$ is very close to 0.

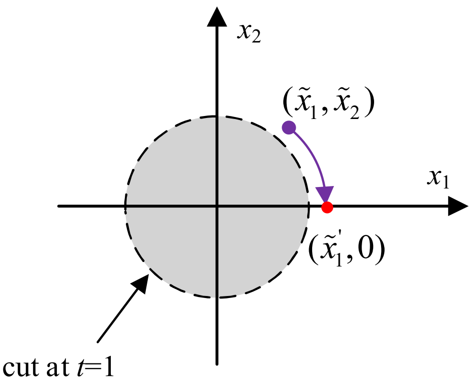

Fig. 2.6 ε-approximation of a Lorentz cone L^2.

This polyhedral approximation method is proposed by Ben-Tal and Nemirovski [91]. For $\sqrt{x_1^2 + x_2^2} \le t$ can be approximated by a system of linear homogeneous equalities and inequalities in terms of x_1, x_2, t, and $2(v+1)$ variables ς^j, η^j for $j = 0,1,2,\ldots v$ where v is a parameter of the polyhedral $\varepsilon(v)$ relaxed approximation such that

$$\varepsilon(v) = \frac{1}{\cos(\frac{\pi}{2^{v+1}})} - 1 \tag{2.60}$$

This gives $\varepsilon(v) \approx 3 \times 10^{-7}$ when $v = 11$; the relaxed approximation in $(1+\varepsilon)t \ge \sqrt{x_1^2 + x_2^2}$ will have $(1+\varepsilon(v))^2 - 1 \approx 6 \times 10^{-7}$. The system of linear homogeneous equations is given by the following polyhedron *T*.

$$
\begin{aligned}
T := \{(x_1, x_2, \varsigma^0, \eta^0, \ldots, \varsigma^v, \eta^v, t) : & \ \varsigma^0 \geq |x_1| \\
& \eta^0 \geq |x_2| \\
& \varsigma^j = \cos(\tfrac{\pi}{2^{j+1}})\varsigma^{j-1} + \sin(\tfrac{\pi}{2^{j+1}})\eta^{j-1}, \quad j = 1, \ldots, v \\
& \eta^j \geq -\sin(\tfrac{\pi}{2^{j+1}})\varsigma^{j-1} + \cos(\tfrac{\pi}{2^{j+1}})\eta^{j-1}, \quad j = 1, \ldots, v \\
& \eta^j \geq \sin(\tfrac{\pi}{2^{j+1}})\varsigma^{j-1} - \cos(\tfrac{\pi}{2^{j+1}})\eta^{j-1}, \quad j = 1, \ldots, v \\
& \varsigma^v \leq t \\
& \eta^v \leq \tan(\tfrac{\pi}{2^{v+1}})\varsigma^v
\end{aligned}
\tag{2.61}
$$

where (ξ_0, η_0) rotates (x_1, x_2) so that $x_1, x_2 \geq 0$, and we have two additional variables ξ_j, η_j for each iteration j=1, ⋯, v.

The polyhedral approximation given by (2.61) can be reduced by using the linear equality constraints in $\varsigma^j = \cos(\frac{\pi}{2^{j+1}})\varsigma^{j-1} + \sin(\frac{\pi}{2^{j+1}})\eta^{j-1}$, j=1,…,v to solve for ς^j, $j = 1, \ldots, v$ in terms of ς^0, η^{j-1}, j=1,…,v and then substitute ς^j out of the system (2.61) by this linear equality constraint. The resulting system will only have linear inequality constraints in terms of the variables $x_1, x_2, x_3, \varsigma^0$ and the $(v+1)$ variables for η^j for j=0,…,v.

The system of linear homogeneous equalities and inequalities (2.61) is known as the polyhedral approximation for a Lorentz cone L^2. Inspired by this idea, we can extend this polyhedral approximation for an arbitrary Lorentz cone L^n. Assume w.l.o.g $n = 2^k$ for some $k \in \mathbb{Z}$. We show that we can give an extended formulation for

$$
L^n := \left\{(x_{0,1}, \cdots, x_{0,n}, t) \in \mathbb{R}^n \times \mathbb{R} \big| \|(x_{0,1}, \cdots, x_{0,n})\|_2 \leq t\right\} \tag{2.62}
$$

We split all the original variables into pairs $(x_{0,2j-1}, x_{0,2j})$ for $j \in [n/2]$ and associate to each pair to a new "1st level" variable $x_{1,j}$ such that

$\|(x_{0,2j-1}, x_{0,2j})\|_2 \le x_{1,j}$, where $x_{1,j}$ is a new introduced variable for a pair $(x_{0,2j-1}, x_{0,2j})$. Then, introducing "2nd" level variables $x_{2,j}$ is subject to $\|(x_{1,2j-1}, x_{1,2j})\|_2 \le x_{2,j}$ in a similar way. We therefore construct a binary tree, where each *i*-th level variable has as children two (*i*-1)-th level variables. The same structure is preserved up to the level $\log_2(n)$, which has a single node $x_{\log_2(n)} = t$. At each level of the tree, we have an ε-approximation of the L^2 cones with the construction from the previous section. This gives in total a $((1+\varepsilon)^{\log_2(n)} - 1)$-approximation for L^n.

For explanation, let us exemplify this idea by

$$L^4 := \left\{ (x_{0,1}, x_{0,2}, x_{0,3}, x_{0,4}, t) \in \mathbb{R}^4 \times \mathbb{R} \middle| \|(x_{0,1}, x_{0,2}, x_{0,3}, x_{0,4})\|_2 \le t \right\} \tag{2.63}$$

The approximation process can be summarized in Fig. 2.7.

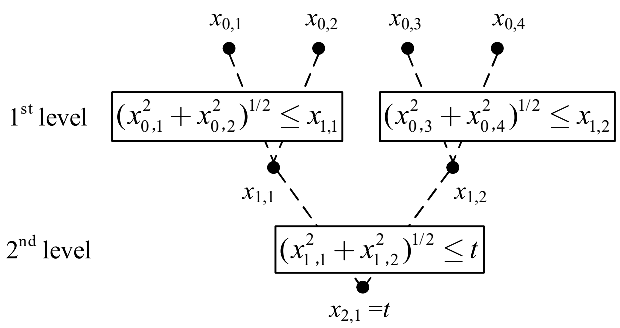

Fig. 2.7 ε-approximation flowchart of a Lorentz cone L^2.

Consider the following SOCP problem by the polyhedral approximation method.

$$\begin{aligned} \min \quad & x_1 + x_2 + 3x_3 \\ s.t. \quad & x_1 + x_2 + 2x_3 = 3 \\ & x_3 \ge \sqrt{x_1^2 + x_2^2} \\ & 0 \le x_1, x_2, x_3 \le 1 \end{aligned} \tag{2.64}$$

This SOCP-based model can obtain the exact optimum. The minimum objective value is 3.8787 and the optimal vector $x=(0.6213, 0.6213, 0.8787)^T$ is achieved. The

SOC constraint satisfies with equality as observed by the gap error 3.1666×10^{-7}.

Subsequently, we linearize this SOC constraint with respect to x_1, x_2, x_3 and 2(3+1)=8 variables $\varsigma^0, \varsigma^1, \varsigma^2, \varsigma^3, \eta^0, \eta^1, \eta^2, \eta^3$. The system of polyhedral approximation constraints is expressed below

$$\begin{cases} -\varsigma^0 \le x_1 \le \varsigma^0 \\ -\eta^0 \le x_2 \le \eta^0 \\ \varsigma^1 - \cos(\frac{\pi}{2^2})\varsigma^0 - \sin(\frac{\pi}{2^2})\eta^0 = 0 \\ \varsigma^2 - \cos(\frac{\pi}{2^3})\varsigma^1 - \sin(\frac{\pi}{2^3})\eta^1 = 0 \\ \varsigma^3 - \cos(\frac{\pi}{2^4})\varsigma^2 - \sin(\frac{\pi}{2^4})\eta^2 = 0 \end{cases}$$

$$\begin{cases} -\sin(\frac{\pi}{2^2})\varsigma^0 + \cos(\frac{\pi}{2^2})\eta^0 - \eta^1 \le 0 \\ \sin(\frac{\pi}{2^2})\varsigma^0 - \cos(\frac{\pi}{2^2})\eta^0 - \eta^1 \le 0 \\ -\sin(\frac{\pi}{2^3})\varsigma^1 + \cos(\frac{\pi}{2^3})\eta^1 - \eta^2 \le 0 \\ \sin(\frac{\pi}{2^3})\varsigma^1 - \cos(\frac{\pi}{2^3})\eta^1 - \eta^2 \le 0 \\ -\sin(\frac{\pi}{2^4})\varsigma^2 + \cos(\frac{\pi}{2^4})\eta^2 - \eta^3 \le 0 \\ \sin(\frac{\pi}{2^4})\varsigma^2 - \cos(\frac{\pi}{2^4})\eta^2 - \eta^3 \le 0 \end{cases} \quad \begin{cases} \varsigma^3 \le x_3 \\ \eta^3 \le \tan(\frac{\pi}{2^4})\varsigma^3 \end{cases} \tag{2.65}$$

The vector of optimization variables is ***x***=[$x_1, x_2, x_3, \varsigma^0, \varsigma^1, \varsigma^2, \varsigma^3, \eta^0, \eta^1, \eta^2, \eta^3$]^T, the total of which is 3+2(3+1)=11. By solving this linear programming model, the minimum objective value is 3.8787 and the optimal vector *x*=(0.6213, 0.6213, 0.8787)^T is achieved. The SOC constraint satisfies inequality by the gap error -0.0301. Improving the approximation accuracy is just to set a larger linearization segments, e.g. *n*=10. Thus, a more accurate solution with a gap error equal to -1.8167×10^{-6} can be provided.

2.6 Case Study

2.6.1 Simple 6-node DN

The following simple 6-node DN is used to exemplify this SOCP-based formulation of *DistFlow* equations. The network topology is shown in Fig. 2.8. The node 1 is the PCC bus, while nodes 2-6 are PQ buses. In other words, $\mathcal{N}$ ={1,2,3,4,5,6} and $\mathcal{E}$ ={1,2,3,4,5}, where branch labels are displayed in yellow-filled square boxes. The impedance of each branch, the load demand of each node and the reactive power compensation capacity of installed capacitors are labeled in this figure. The voltage allowance band of each node is set to 0.97–1.07 p.u. For this fixed topology, we focus on the reactive power optimization on the active branches for the minimization of real power loss.

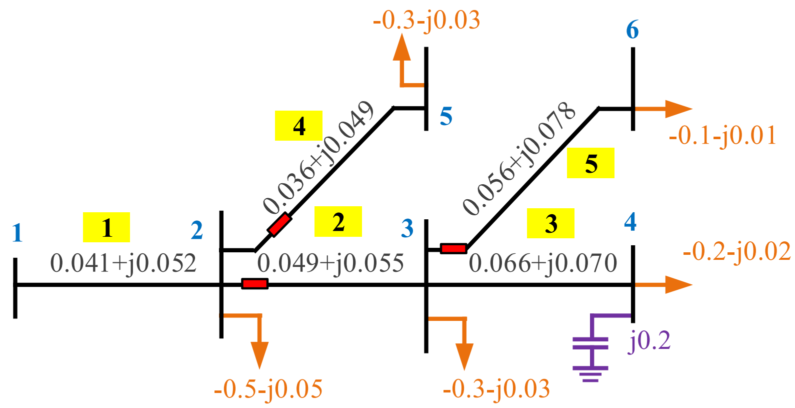

Fig. 2.8 Topology of a radial DN.

According to this SOCP-based reactive power optimization model (2.18), the operational constraints are composed of 4 × 5=20 *Distflow* equations and 1 reactive power capacity compensation constraint as well as 6 voltage security constraints. To validate the effectiveness of optimal solutions, we have provided the Matlab function in our designed MATDNR Toolbox v1.0 [92] to run this SOCP-based reactive power optimization model (2.18) with commercial solvers MOSEK [93], Baron [94] and SDP-based reactive power optimization model (2.57) by the commercial solver SeduMi [95]. Please note that no overlapping variables are allowed for all SOC constraints, and thus more new variables are included for the solver MOSEK. More information can be found at the handbook of MOSEK online. We also employ the reactive power optimization solver based on conventional power flow equations in polar coordinates (Varopt) [96], and the solving algorithm is interior point algorithm. To compare the accuracy of the polyhedral method, we solve this reactive power optimization model with polyhedral approximations with 32 segments of linearizations by commercial SOCP solvers MOSEK and Baron. The solution can be found in Table 2.1. The nodal voltage profiles by SOCP-based and polyhedral approximation formulations of reactive power optimization models can be presented in a tree-shaped Fig. 2.9, where x-axis refers to branches. For instance, node (1,2) refers to branch 1, node (2,3) refers to branch 2, node (3,4) refers to branch 3 in this figure.

Table 2.1 Optimal solutions of the 6-node DN.

Models	Solvers	Minimal injected real power at PCC node (p.u.)	Real Power Loss (p.u.)	Algorithm Iterations	Computational Time (seconds)
SOCP	MOSEK	1.501	0.101453	10	0.2030
	Baron	1.501	0.101453	10	0.1895
	Varopt	1.501	0.101453	7	0.0469
SDP	SeduMi	1.501	0.101453	16	0.6406
Polyhedral	MOSEK	1.5005	0.1005	16	0.3280

Baron	1.5005	0.1005	14	0.3195

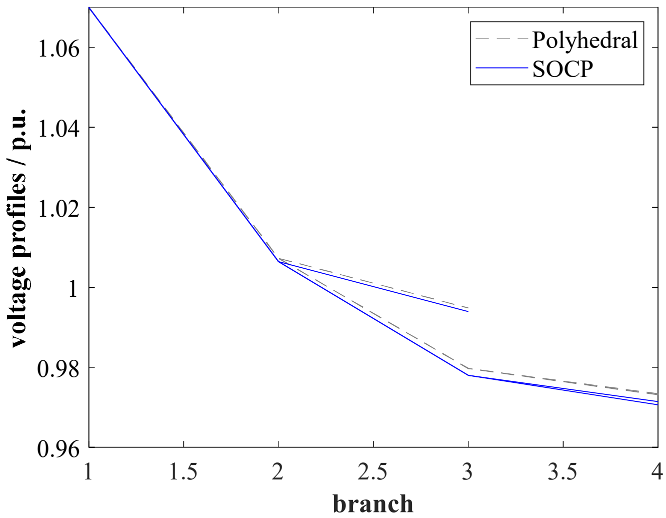

Fig. 2.9 Tree-shaped voltage profile of this simple 6-node DN.

Observing Table 2.1 tells us that the commercial solvers MOSEK, Baron and SeduMi can be effective to solve the SOCP-based/semi-definite-based reactive power optimization model, since the optimal solutions including power loss and voltage profiles are the same with ones by Varopt that is based on the conventional nonlinear power flow equations. Moreover, the optimal solution is converged at the equality of SOC constraints. This means that this optimal solution is feasible for power flow equations and thus convex relaxations are exact. For the polyhedral model, the optimal solution is extremely close to the exact ones, where the maximum error of voltage profiles is less than 0.01%, as observed in Fig. 2.9.

2.6.2 Large-scale DNs

We validate the computational performance of this SOCP-based formulation of reactive power optimization model with different scalability of systems. i.e., *IEEE*

16-node, 33-node, 123-node and 1060-node DNs with DERs that are used for tests. The switch-off circuit breakers for these benchmark systems are shown in Table 2.2, while other circuit breakers are switched on.

Table 2.2 Switch-off circuit breakers for these benchmark systems

DNs	switch-off circuit breakers	
	start node	end node
16-node	6	12
	11	15
	8	17
33-node	9	8
	32	31
	28	29
	15	14
	8	21
123-node	76	72
	105	101
1060-node	80	102
	17	111
	54	117
	45	143
	73	134
	97	76
	28	56

The computational performance in terms of CPU time in seconds and algorithm iterations are given in Table 2.3. The nodal voltage profiles by SOCP-based and polyhedral approximation formulations of reactive power optimization models can be presented in a tree-shaped is presented in Fig. 2.10 (a) –(d).

Table 2.3 Optimal solutions of different scalability of DNs

DNs	Models	Solvers	Minimal injected real power at PCC node (p.u.)	Real Power Loss (p.u.)	Algorithm Iterations	Computational Time (seconds)
16 node	SOCP	MOSEK	2.972	0.042	17	0.219
		Baron	2.972	0.042	15	0.201

		Varopt	2.972	0.042	8	0.078
	SDP	SeduMi	2.972	0.042	21	0.542
	Polyhedral	MOSEK	2.967	0.042	19	0.235
33 node	SOCP	MOSEK	3.830	0.115	14	0.201
		Baron	3.830	0.115	11	0.183
		Varopt	3.830	0.115	7	0.065
	SDP	SeduMi	3.830	0.115	24	0.635
	Polyhedral	MOSEK	3.811	0.113	22	0.275
123 node	SOCP	MOSEK	3.667	0.1776	28	0.221
		Baron	3.667	0.1776	21	0.218
		Varopt	3.667	0.1776	9	0.318
	SDP	SeduMi	3.667	0.1776	38	0.321
	Polyhedral	MOSEK	3.658	0.1772	39	0.346
1060 node	SOCP	MOSEK	4.508	0.163	26	0.203
		Baron	4.508	0.163	24	0.201
		Varopt	4.508	0.163	12	0.098
	SDP	SeduMi	4.508	0.163	31	0.368
	Polyhedral	MOSEK	4.461	0.162	44	0.344

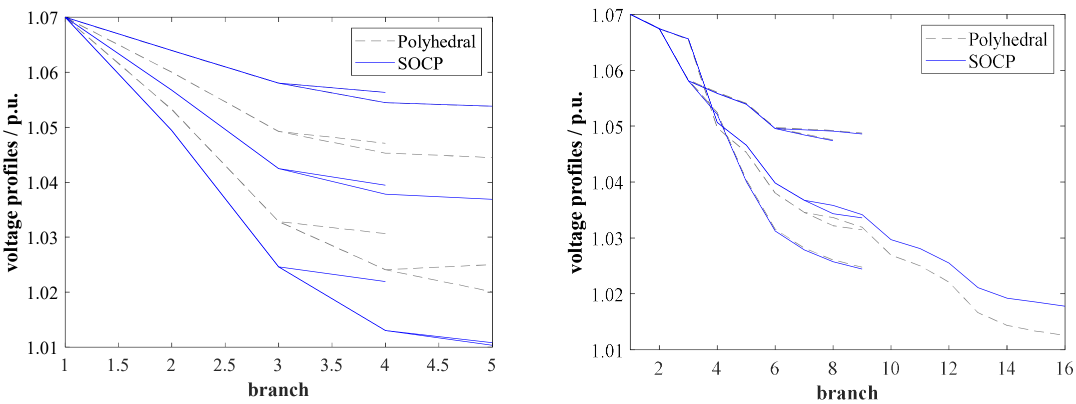

(a) (b)

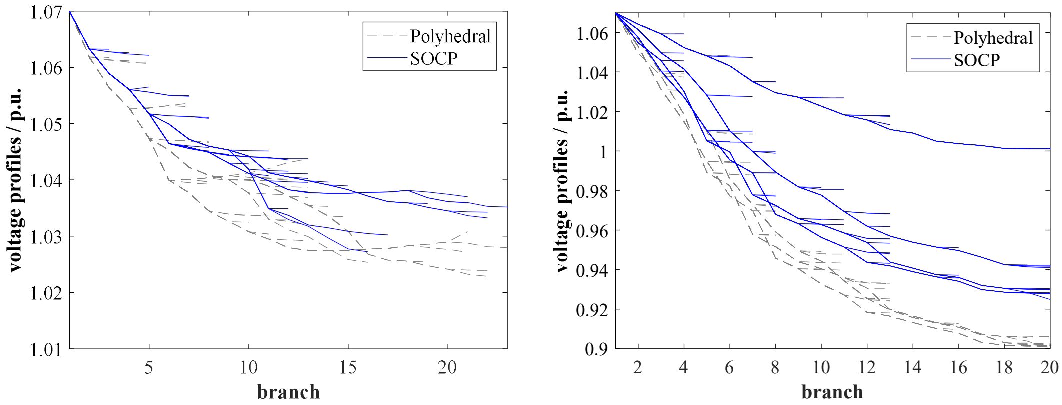

(c) (d)

Fig. 2.10 Tree-shaped voltage profiles of different DNs: (a) 16-node; (b) 33-node; (c) 123-node and (d) 1060-node.

Table 2.2 shows that the above-mentioned solvers can be effective to solve the reactive power optimization problem formulated in the SOCP-based and SDP-based *DistFlow* form. Fig.2.10 (a)-(d) display that the nodal voltage profiles by SOCP-based and polyhedral approximation formulations are very close. The maximum errors of *IEEE* 16-node, 33-node, 123-node and 1060-node DNs are 0.286%, 0.510%, 1.005% and 4.211%, respectively. This demonstrates that *DistFlow* equations have advantageous properties that can be reformulated in the SOCP and SDP form, and the polyhedral approximation formulation of SOC constraints can be also accurate and effective for quick convergence.

2.7 Summary

This chapter summarizes the fundamentals of *DistFlow* equations. As demonstrated in case studies, *DistFlow* equations have advantageous properties that can be reformulated in the SOCP and SDP form. The polyhedral approximation formulation of SOC constraints can be also accurate and effective for quick convergence. This *DistFlow* equations and its convex relaxation formulations lays the theoretical foundation for the following DNR problems with convex optimization solvers.

Chapter 3

Topology Optimization of Active Distribution Network based on Disjunctive Convex Hull Approach for Operational Security Enhancement

Distribution network reconfiguration (DNR) is a classical optimal operation problem over decades. It aims to maintain load balancing and loss reduction at the voltage security-constrained operation level, and to coordinate real-time transactive dispatch tasks between supply and demand at the market level of DNs. However, the computing performance of existing methods in terms of running time and iterations is not satisfactory for a large-scale network. This chapter investigates the convex hull (CH) of *DistFlow* equations for the superior numerical performance.

This chapter proposes the disjunctive convex hull relaxation (DCHR) approach, which can be further used to deal with these on/off constraints caused by switch status indicators. In this chapter, we are stimulated to study the DCHR approach for the classic DNR problem, which can be designed to tighten the voltage drop equation and quadratic equality of *DistFlow* equations with continuous parent-child relationship variables in spanning tree constraints. The results of case studies prove the effectiveness of the proposed DCHR for DNR problems.

3.1 Radiality Constraints

In this thesis, we suppose that each branch of DNs has a sectionalizing switch or tie switch. Each bus in DNs is connected by a branch with a switch, and one tie switch can form a loop with other sectionalizing switches. The DNR problem can be deemed as a combinatorial issue about choosing optimal switch status of sectionalizing switches (normally closed) and tie-switches (normally open). The DNR provides an optimal network structure to realize minimum power losses and achieve better load balancing; or to be used for post-outage restoration and planned maintenance, etc. In this section, we discuss the relaxation techniques for DNR problems based on *DistFlow* equations.

3.1.1 Virtual Commodity Flow Constraints

In the traditional DNs, DNR is not a frequent operation. However, with the application of high-speed switching devices in DNs, the DNR is developing toward real-time reconfiguration for maintaining the optimal operation condition of DNs. The ability to switch between different topologies enables a class of radial grids subject to single commodity flow (SCF) constraints. Let u^l be the binary state vector of circuit breakers, which is zero if the switch is open and one if closed, namely $u^l \in \{0,1\}, u^l \in \mathbb{Z}$.

One of the most popular radiality model ensures connectivity of loads to DERs via the power flow equations, and connects DERs to the substation via flows of a virtual commodity [97]. The tightness of a linear programming relaxation for this model has also been recently. In this section, we advance upon the commodity flow approach and propose a more succinct model with fewer variables and constraints. We consider a virtual single commodity flowing on the network graph $\mathcal{G}$ and set a demand of one unit on all non-substation buses. This is to say, all load nodes to have nonzero power injection (no transfer nodes in DNs). Consequently, all demands supplied by substation and all nodes have a path to substation ensuring connectivity. Virtual commodity flow constraints can be expressed with respect to the branch-bus incidence matrix **A**, by forcing the virtual flows in f^l to be zero for open lines:

$$\boldsymbol{A}^T f = 1 \tag{3.1}$$

$$-N \cdot u^l \leq f^l \leq N \cdot u^l, \quad \forall l \in \mathcal{E} \tag{3.2}$$

$$1^T u^l = |\mathcal{N}| - 1 \tag{3.3}$$

where f^l refers to the vector of virtual flows on each branch.

In this set of virtual commodity flow constraints, the virtual flow variable f^l does not relate to the actual line flows and is introduced only to enforce connectivity. Given that flows are allowed only on active lines, enforcing flow balance (KCL) on a node with only one unit flow injection, which results in $\boldsymbol{A}^T f = 1$. Moreover, $-N \cdot u^l \leq f^l \leq N \cdot u^l$ can be used to maintain radiality of DNs by linking f^l and u^l. Lastly, $1^T u^l = |\mathcal{N}| - 1$ guarantees that the network reconfiguration solution will be an acyclic network. It should be worthwhile to note that when there are no transfer nodes in DNs, $1^T u^l = |\mathcal{N}| - 1$ and power flow equations can be effective to maintain radiality of DNs; otherwise, virtual commodity flow constraints should be considered.

3.1.2 Spanning Tree Constraints

The spanning tree (ST) constraints are used to formulate a linear program of the minimum spanning tree problem [98]. For a DNR problem, we can encode every branch as a directed arc with respect to an acyclic network rooted at node, which ST constraints can be applied for network reconfiguration. To enforce a radial typology, a pair of variables β_{mn}^{l} and β_{nm}^{l} for branch l is ranged in [0, 1], indicating the parent-child relationship between nodes m and n for the radiality of networks. For instance, $\beta_{mn}^{l}=1$ and $\beta_{nm}^{l}=0$ means that n is the parent node of m, otherwise $\beta_{mn}^{l}=0$ and $\beta_{nm}^{l}=1$ implies that m is the parent node of n.

$$\beta_{mn}^{l}+\beta_{nm}^{l}=u^{l} \tag{3.4}$$

$$\beta_{mn}^{l}=0, \quad if\ m=S \tag{3.5}$$

$$\sum_{n:(m,n)\in E}\beta_{mn}^{l}=1, \quad \forall\, m\in N\setminus S \tag{3.6}$$

$$\beta_{mn}^{l}\in[0,1] \tag{3.7}$$

where S is the set of source nodes.

Flowing on the branch with nodes (m,n) can only in one direction, which explicitly is set to a combination of variables β_{mn}^{l} and β_{nm}^{l}. The parent-child relationship variables β^{l} are continuous, i.e., $\beta^{l}\in\mathbb{R}^{n}$. After applying this set of ST constraints, β^{l} can be proved to get converged as 0 or 1. Reference [14] proves that any feasible β_{mn}^{l} must be zeros and ones, and for each source node, it describes the edges of an unweighted, directed tree graph with a source node.

Please note that if only ST constraints are considered in the DNR model, then ST constraints are inadequate to represent the radiality. Take the following Fig. 3.1 as an example from reference [99] where we suppose that node 1 is a point of common coupling (PCC) node.

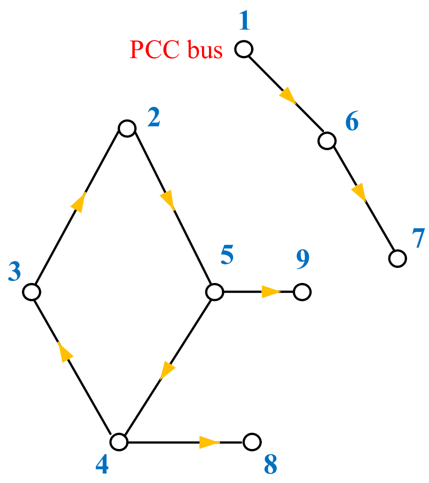

Fig. 3.1 An example of inadequate ST constraints.

By ST constraints, we give the following β^l values for this figure in Table. 3.1.

Table 3.1 Values of parent-child relationship variable β^l.

Connected Branches		β^l_{mn}	β^l_{nm}	Parent-child relationship
Node m	Node n			
6	1	1	0	1-parent, 6-child
7	6	1	0	6-parent, 7-child
3	**2**	0	1	3-parent, 2-child
4	**3**	0	1	4-parent, 3-child
5	**4**	0	1	5-parent, 4-child
5	**2**	1	0	2-parent, 5-child
9	5	1	0	5-parent, 9-child
8	4	1	0	4-parent, 8-child

It can be inferred from Table. 3.1 that all β^l values satisfy ST constraints (2.25)-(2.28). Unfortunately, there is a cycle topology that is not a radial network. For a DNR problem, power flow equations are hard constraints in this DNR model. Clearly, this disconnected network in Fig. 3.1 leads to an infeasible power flow solution. In other words, the above-mentioned example cannot satisfy the nodal power flow balance at node 7 under assumed power flow directions in Fig. 3.1.

But from our perspective, the power flow equations are necessary but insufficient conditions for the connectivity constraint in DNR model. As displayed in Fig. 3.2, we can show this counter-example based on Fig. 3.1.

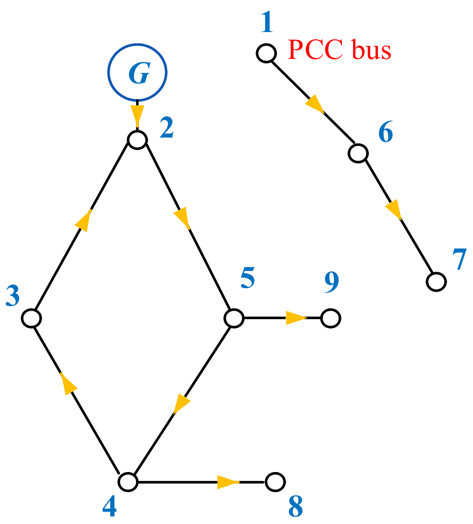

Fig. 3.2 An example of inadequate ST and power flow constraints.

In this case, we can find that ST and power flow equations constraints cannot guarantee a radial topology when there is a DG source at node 2 in this distribution system. It may result in an unconnected graph containing loops with nodes 2, 5, 4 and 3. This illustrates that power flow equations cannot entirely guarantee the connective topology. Thus, it is suggested in [98] that single-commodity flow constraints (SCF) and ST constraints can guarantee the radial topology.

3.2 Conventional DNR Models

By the angle relaxation, *DistFlow* equations can be cast as a second-order conic programming (SOCP) or a semi-definite programming (SDP) formulation for *DistFlow* equations. By these convex relaxations, the DNR model can be modeled as a mixed-integer second-order conic programming (MISOCP) or a mixed integer semi-definite programming (MISDP) problem in the following. These convex models exploit the optimal distribution topology with reduced computational complexity. In this subsection, we only discuss SOCP-based model of DNR problems with Big-M relaxation method.

3.2.1 MISOCP-based DNR Model with Big-M Relaxation Method

For the sake of the minimal power loss in reconfigurable DNs, the set of optimization variables involves a set of operational variables $\left[P^l,\ Q^l,\ \ell^l,\ v_{PQ}\right]^T$ and a vector of controllable variables $\left[v_0, Q^{cr}, f^l, \beta^l_{mn},\ \beta^l_{nm}, u^l\right]^T$. Here, v_0 refers to the squared voltage profile at the root node 0. Accordingly, once controllable variables are provided, operational variables can be automatically determined just by power flow equations. For this DNR optimization problem, we combine operational and controllable variables together as $x^l := [P^l, Q^l, \ell^l, v, Q^{cr}, w^l, m^l, f^l, \beta^l_{mn},\ \beta^l_{nm}, u^l]^T$ for all branches of DNs, where $(P^l, Q^l, \ell^l, v, Q^{cr}, w^l, m^l, f^l, \beta^l_{mn},\ \beta^l_{nm}) \in \mathbb{R}$ and $u^l \in \mathbb{Z}$.

With *DistFlow* equations, the big-M method is utilized to relax equality $v_n - v_m + 2(r^l_{mn}P^l_{mn} + x^l_{mn}Q^l_{mn}) - |z^l_{mn}|^2\ell^l_{mn} = 0$ as two inequalities with a large-enough positive scalar ***M***. The optimization variables are expressed as

$x^l := \left[P^l, Q^l, \ell^l, v, Q^{cr}, w^l, m^l, f^l, \beta^l_{mn}, \beta^l_{nm}, u^l\right]^T$, $\forall l \in \mathcal{E}$. Thus, the entire network reconfiguration model with the loss minimization is cast as

$$
\min_{x^l} \quad P_0^l
$$

$$
s.t. \begin{cases}
P^l_{mn} + P^g_n - r^l_{mn}\ell^l_{mn} = \sum\limits_{k \in \pi(n)} P^l_{nk} + P^d_n, \forall l \in \mathcal{E}, \forall m, n \in \mathcal{N} \\
Q^l_{mn} + Q^g_n - x^l_{mn}\ell^l_{mn} = \sum\limits_{k \in \pi(n)} Q^l_{nk} + Q^d_n, \forall l \in \mathcal{E}, \forall m, n \in \mathcal{N} \\
v_n - v_m + 2(r^l_{mn}P^l_{mn} + x^l_{mn}Q^l_{mn}) - |z^l_{mn}|^2\ell^l_{mn} - (1-u^l)M \le 0, \forall l \in \mathcal{E}, \forall m, n \in \mathcal{N} \\
v_n - v_m + 2(r^l_{mn}P^l_{mn} + x^l_{mn}Q^l_{mn}) - |z^l_{mn}|^2\ell^l_{mn} + (1-u^l)M \ge 0, \forall l \in \mathcal{E}, \forall m, n \in \mathcal{N} \\
\left\| \begin{matrix} 2P^l_{mn} \\ 2Q^l_{mn} \\ w^l \end{matrix} \right\|_2 \le m^l, \forall l \in \mathcal{E}, \forall m, n \in \mathcal{N} \\
w^l = \ell^l_{mn} - v_m, \; m^l = \ell^l_{mn} + v_m, \quad \forall l \in \mathcal{E}, \forall m, n \in \mathcal{N} \\
-\bar{Q}^l_0 \le Q^l_0 \le \bar{Q}^l_0 \\
-u^l\Gamma^l_{\max} \leqslant P^l, Q^l \leqslant u^l\Gamma^l_{\max} \\
\underline{Q}^{cr} \le Q^{cr} \le \bar{Q}^{cr} \\
\underline{v} \le v \le \bar{v} \\
\beta^l_{mn} + \beta^l_{nm} = u^l \\
\beta^l_{mn} = 0, \text{ if } m = S \\
\sum\limits_{n:(m,n) \in \mathcal{E}} \beta^l_{mn} = 1, \forall m \in \mathcal{N} \backslash S \\
\beta^l_{mn} \ge 0 \\
A^T f = 1 \\
-N \cdot u^l \le f^l \le N \cdot u^l, \quad \forall l \in \mathcal{E} \\
1^T u^l = |\mathcal{N}| - 1 \\
u^l \in \{0, 1\}
\end{cases} \tag{3.8}
$$

where P_0^l is the active power injection at the root node *S*.

3.2.2 MISOCP-based DNR Model using McCormick Linearization Method

In the previous subsection, the SOCP-based model of DNR problems can be formulated with Big-M relaxation method. However, we can further strengthen this bound relaxation using McCormick Linearization Method [100]. Let

$y^l = (v_n - v_m)\cdot u^l$. Then, the McCormick linearization method is utilized to relax equality $v_n - v_m + 2(r_{mn}^l P_{mn}^l + x_{mn}^l Q_{mn}^l) - |z_{mn}^l|^2 \ell^l_{mn} = 0$ as

$$y^l + 2(r_{mn}^l P_{mn}^l + x_{mn}^l Q_{mn}^l) - |z_{mn}^l|^2 \ell^l_{mn} = 0 \tag{3.9}$$

$$(\underline{v} - \overline{v})\cdot u^l \leqslant y^l \leqslant (\overline{v} - \underline{v})\cdot u^l \tag{3.10}$$

$$v_n - v_m - (\overline{v} - \underline{v})\cdot(u^l - 1) \leqslant y^l \leqslant v_n - v_m - (\underline{v} - \overline{v})\cdot(u^l - 1) \tag{3.11}$$

The optimization variables are expressed as $\boldsymbol{x^l} := \left[\boldsymbol{P^l}, \boldsymbol{Q^l}, \ell^l, \boldsymbol{v}, \boldsymbol{Q^{cr}}, \boldsymbol{w^l}, \boldsymbol{m^l}, \boldsymbol{y^l}, \boldsymbol{f^l}, \boldsymbol{\beta^l_{mn}}, \boldsymbol{\beta^l_{nm}}, \boldsymbol{u^l}\right]^T, \forall l \in \mathcal{E}$. Thus, the entire network reconfiguration model with the loss minimization is simply reformulated as

$$\min_{x^l} \quad P_0^l$$

$$s.t.\begin{cases}
P_{mn}^l + P_n^g - r_{mn}^l \ell_{mn}^l = \sum_{k\in\pi(n)} P_{nk}^l + P_n^d, \forall l\in\mathcal{E}, \forall m,n\in\mathcal{N} \\
Q_{mn}^l + Q_n^g - x_{mn}^l \ell_{mn}^l = \sum_{k\in\pi(n)} Q_{nk}^l + Q_n^d, \forall l\in\mathcal{E}, \forall m,n\in\mathcal{N} \\
y^l + 2(r_{mn}^l P_{mn}^l + x_{mn}^l Q_{mn}^l) - |z_{mn}^l|^2 \ell_{mn}^l = 0, \forall l\in\mathcal{E}, \forall m,n\in\mathcal{N} \\
(\underline{v}-\overline{v})\cdot u^l \leqslant y^l \leqslant (\overline{v}-\underline{v})\cdot u^l, \forall l\in\mathcal{E}, \forall m,n\in\mathcal{N} \\
v_n - v_m - (\overline{v}-\underline{v})\cdot(u^l-1) \leqslant y^l \leqslant v_n - v_m - (\underline{v}-\overline{v})\cdot(u^l-1) \\
\left\| \begin{matrix} 2P_{mn}^l \\ 2Q_{mn}^l \\ w^l \end{matrix} \right\|_2 \le m^l, \forall l\in\mathcal{E}, \forall m,n\in\mathcal{N} \\
w^l = \ell_{mn}^l - v_m,\ m^l = \ell_{mn}^l + v_m, \quad \forall l\in\mathcal{E}, \forall m,n\in\mathcal{N} \\
-\overline{Q}_0^l \le Q_0^l \le \overline{Q}_0^l \\
-u^l \Gamma_{\max}^l \leqslant P^l, Q^l \leqslant u^l \Gamma_{\max}^l \\
\underline{Q}^{cr} \le Q^{cr} \le \overline{Q}^{cr} \\
\underline{v} \le v \le \overline{v} \\
\beta_{mn}^l + \beta_{nm}^l = u^l \\
\beta_{mn}^l = 0, \text{ if } m = 0 \\
\sum_{n:(m,n)\in\mathcal{E}} \beta_{mn}^l = 1, \forall m \in \mathcal{N}\backslash 0 \\
\beta_{mn}^l \ge 0 \\
A^T f = 1 \\
-N\cdot u^l \le f^l \le N\cdot u^l, \quad \forall l\in\mathcal{E} \\
1^T u^l = |\mathcal{N}| - 1, \quad u^l \in \{0,1\}
\end{cases} \tag{3.12}$$

3.2.3 Quadratic DNR Model with Big-M and McCormick Linearization Methods

With LDF-based equations, the Big-M method is utilized to relax equality $v_n - v_m + 2(r_{mn}^l P_{mn}^l + x_{mn}^l Q_{mn}^l) = 0$ as two inequalities with a large-enough positive scalar $\boldsymbol{M}$. Therefore, a linearized DNR model with Big-M relaxation method is developed and firstly proposed in [14]. The optimization variables are expressed as $\boldsymbol{x^l} := \left[\boldsymbol{P^l}, \boldsymbol{Q^l}, \boldsymbol{v}, \boldsymbol{Q^{cr}}, \boldsymbol{f^l}, \boldsymbol{\beta_{mn}^l}, \boldsymbol{\beta_{nm}^l}, \boldsymbol{u^l}\right]^T$, $\forall l\in\mathcal{E}$. Since network loss is omitted in this LDF-based equations, we rewrite the objective function in the DNR model as

$\sum_{l\in\mathcal{E}} r_{mn}^{l}((P_{mn}^{l})^2+(Q_{mn}^{l})^2)$ where voltage profiles are all assumed as one unit. Due to this quadratic objective function, the entire linearized DNR model with the loss minimization is reformulated as a mixed integer quadratic programming problem.

$$\min_{x^l} \sum_{l\in\mathcal{E}} r_{mn}^{l}((P_{mn}^{l})^2+(Q_{mn}^{l})^2)$$
$$s.t.\begin{cases} P_{mn}^{l}+P_{n}^{g}=\sum\limits_{k\in\pi(n)} P_{nk}^{l}+P_{n}^{d}, \forall l\in\mathcal{E},\forall m,n\in\mathcal{N} \\ Q_{mn}^{l}+Q_{n}^{g}=\sum\limits_{k\in\pi(n)} Q_{nk}^{l}+Q_{n}^{d}, \forall l\in\mathcal{E},\forall m,n\in\mathcal{N} \\ v_n-v_m+2(r_{mn}^{l}P_{mn}^{l}+x_{mn}^{l}Q_{mn}^{l})-(1-u^l)M\le 0, \forall l\in\mathcal{E},\forall m,n\in\mathcal{N} \\ v_n-v_m+2(r_{mn}^{l}P_{mn}^{l}+x_{mn}^{l}Q_{mn}^{l})+(1-u^l)M\ge 0, \forall l\in\mathcal{E},\forall m,n\in\mathcal{N} \\ -\bar{Q}_0^l\le Q_0^l\le \bar{Q}_0^l \\ -u^l\Gamma_{\max}^{l}\leqslant P^l,Q^l\leqslant u^l\Gamma_{\max}^{l} \\ \underline{Q}^{cr}\le Q^{cr}\le \bar{Q}^{cr} \\ \underline{v}\le v\le \bar{v} \\ \beta_{mn}^{l}+\beta_{nm}^{l}=u^l \\ \beta_{mn}^{l}=0, \text{ if } m=S \\ \sum\limits_{n:(m,n)\in\mathcal{E}} \beta_{mn}^{l}=1, \forall m\in\mathcal{N}\backslash S \\ \beta_{mn}^{l}\ge 0 \\ A^T f=1 \\ -N\cdot u^l\le f^l\le N\cdot u^l, \quad \forall l\in\mathcal{E} \\ 1^T u^l=|\mathcal{N}|-1 \\ u^l\in\{0,1\} \end{cases} \tag{3.13}$$

3.2.4 Polyhedral Approximation of DNR Model using Big-M Relaxation Method

For SOC constraints in the DNR model, the polyhedral approximation can be used to simplify the SOC constraints to be a family of linear constraints. We can express $\left\|(2P_{mn}^{l} \quad 2Q_{mn}^{l} \quad w^l)^T\right\|_2\le m^l, \forall l\in\mathcal{E},\forall m,n\in\mathcal{N}$ as a polyhedral cone, which is visualized in Fig. 3.3. The error of approximation can be regarded as the distance between the exact optimal point ★ and the approximate optimal point ●.

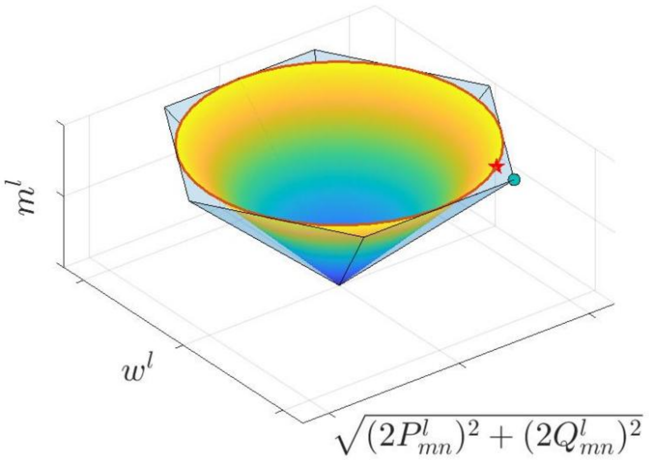

Fig. 3.3 Polyhedral cone for SOC constraint.

Moreover, the Big-M method is utilized to relax equality $v_n - v_m + 2(r^l_{mn}P^l_{mn} + x^l_{mn}Q^l_{mn}) - |z^l_{mn}|^2 \ell^l_{mn} = 0$ as two inequalities with a large-enough positive scalar *M*. Therefore, a polyhedral approximation DNR model with Big-M relaxation method is established [17]. The optimization variables are expressed as $\boldsymbol{x}^l := \left[\boldsymbol{P}^l, \boldsymbol{Q}^l, \boldsymbol{v}, \boldsymbol{Q}^{cr}, \boldsymbol{w}^l, \boldsymbol{m}^l, \boldsymbol{S}^l, \boldsymbol{\varsigma}, \boldsymbol{\eta}, \boldsymbol{\omega}, \boldsymbol{\kappa}, \boldsymbol{f}^l, \boldsymbol{\beta}^l_{mn}, \boldsymbol{\beta}^l_{nm}, \boldsymbol{u}^l\right]^T$, $\forall l \in \mathcal{E}$, where $\varsigma, \eta, \omega, \kappa$ are variables in the polyhedral approximation of SOC constraints. Thus, the entire DNR model with the polyhedral approximation of SOC constraints for the loss minimization is reformulated as

$$
\begin{aligned}
&\min_{x^l} \quad P_0^l \\
&s.t.\begin{cases}
P_{mn}^l + P_n^g - r_{mn}^l \ell^l{}_{mn} = \sum\limits_{k\in\pi(n)} P_{nk}^l + P_n^d, \forall l \in \mathcal{E}, \forall m,n \in \mathcal{N} \\
Q_{mn}^l + Q_n^g - x_{mn}^l \ell^l{}_{mn} = \sum\limits_{k\in\pi(n)} Q_{nk}^l + Q_n^d, \forall l \in \mathcal{E}, \forall m,n \in \mathcal{N} \\
v_n - v_m + 2(r_{mn}^l P_{mn}^l + x_{mn}^l Q_{mn}^l) - (1-u^l)M \le 0, \forall l \in \mathcal{E}, \forall m,n \in \mathcal{N} \\
v_n - v_m + 2(r_{mn}^l P_{mn}^l + x_{mn}^l Q_{mn}^l) + (1-u^l)M \ge 0, \forall l \in \mathcal{E}, \forall m,n \in \mathcal{N} \\
w^l = \ell^l{}_{mn} - v_m,\ m^l = \ell^l{}_{mn} + v_m, \quad \forall l \in \mathcal{E}, \forall m,n \in \mathcal{N} \\
\varsigma^0 \ge |2P_{mn}^l|, \forall l \in \mathcal{E} \\
\eta^0 \ge |2Q_{mn}^l|, \forall l \in \mathcal{E} \\
\varsigma^j = \cos(\frac{\pi}{2^{j+1}})\varsigma^{j-1} + \sin(\frac{\pi}{2^{j+1}})\eta^{j-1}, \quad j = 1,\ldots,\upsilon \\
\eta^j \ge |-\sin(\frac{\pi}{2^{j+1}})\varsigma^{j-1} + \cos(\frac{\pi}{2^{j+1}})\eta^{j-1}|, \quad j = 1,\ldots,\upsilon \\
\varsigma^\upsilon \le S_{mn}^l, \forall l \in \mathcal{E} \\
\eta^\upsilon \le \tan(\frac{\pi}{2^{\upsilon+1}})\varsigma^v \\
\omega^0 \ge |S_{mn}^l|, \forall l \in \mathcal{E} \\
\kappa^0 \ge |w^l|, \forall l \in \mathcal{E} \\
\omega^j = \cos(\frac{\pi}{2^{j+1}})\omega^{j-1} + \sin(\frac{\pi}{2^{j+1}})\kappa^{j-1}, \quad j = 1,\ldots,\upsilon \\
\kappa^j \ge |-\sin(\frac{\pi}{2^{j+1}})\omega^{j-1} + \cos(\frac{\pi}{2^{j+1}})\kappa^{j-1}|, \quad j = 1,\ldots,\upsilon \\
\omega^\upsilon \le m^l, \forall l \in \mathcal{E} \\
\kappa^\upsilon \le \tan(\frac{\pi}{2^{\upsilon+1}})\omega^\upsilon \\
-\overline{Q}_0^l \le Q_0^l \le \overline{Q}_0^l \\
\underline{Q}^{cr} \le Q^{cr} \le \overline{Q}^{cr} \\
\underline{v} \le v \le \overline{v} \\
\beta_{mn}^l + \beta_{nm}^l = u^l \\
\beta_{mn}^l = 0, \text{ if } m = 0 \\
\sum\limits_{n:(m,n)\in\mathcal{E}} \beta_{mn}^l = 1, \forall m \in \mathcal{N} \backslash 0 \\
\beta_{mn}^l \ge 0 \\
\boldsymbol{A}^T f = 1 \\
-N \cdot u^l \le f^l \le N \cdot u^l, \quad \forall l \in \mathcal{E} \\
1^T u^l = |\mathcal{N}| - 1 \\
u^l \in \{0,1\}
\end{cases}
\end{aligned}
\tag{3.14}
$$

where υ is the parameter of the polyhedral $\varepsilon(\upsilon)$ relaxed approximation in (2.60).

3.3 Disjunctive Convex Hull Approach for DNR Formulation

As stated the above, convex relaxation approaches in the conventional DNR models include Big-M method and McCormick linearization method. These two existing convex relaxation approaches are used to slack power flow constraints by switch status indicators, or construct relaxation constraints with variables automatically satisfied for a disconnected line. Since these convex relaxation methods suffer from loosened relaxation bounds, there is a research gap to explore the efficient and tight relaxation approach for DNR problems.

For the sake of the minimal power loss in reconfigurable DNs, the set of optimization variables involves a set of operation variables $\boldsymbol{x}^l := [\boldsymbol{P}^l, \boldsymbol{Q}^l, \ell^l, \boldsymbol{v}, \boldsymbol{Q}^{cr}]^T$, $\boldsymbol{x}^l \in \mathbb{R}^n$, the continuous parent-child relationship variable $\boldsymbol{\beta}^l \in \mathbb{R}^{2\varepsilon}$ in spanning tree constraints, and binary state vector of circuit breakers $\boldsymbol{u}^l \in \{0, 1\}$, $\boldsymbol{u}^l \in \mathbb{Z}^{\varepsilon}$, where $\boldsymbol{u}^l$ is zero if the switch is open and one if closed. The DNR model is to seek the loss minimization over *DistFlow* equations. In reconfigurable DNs, if a branch $l := (m, n)$ is unconnected, $v_n - v_m + 2(r^l_{mn}P^l_{mn} + x^l_{mn}Q^l_{mn}) - |z^l_{mn}|^2\ell^l_{mn} = 0$ in (1.6) can hold for $P^l_{mn} = Q^l_{mn} = 0$, $\ell^l = 0$ and $\underline{v} \le v \le \overline{v}$, but $v_n - v_m + 2(r^l_{mn}P^l_{mn} + x^l_{mn}Q^l_{mn}) - |z^l_{mn}|^2\ell^l_{mn} = 0$ may not stand with this solution due to $\boldsymbol{A}^l \cdot v \neq \boldsymbol{0}$. Suppose that no additional active/reactive power injections from reactive compensation or distributed energy resources (DERs) are available to this branch l, and as long as $\boldsymbol{A}^l \cdot v = v_m - v_n > 0$ holds, then it is inferred that m should be the parent node of n.

According to [14], continuous parent-child relationship variables β^l are proved to get converged as binary solutions from real-valued continuous numbers. Inspired by this characteristic, we can ideally link disjunctive parent-child relationship variables β_l with "on/off" equality (1.6) and (1.7) via the disjunctive convex hull relxations (DCHR) approach. In other words, if an arbitrary branch l := (m, n) with active/reactive power flow directions depending on parent-child relationship variables of DNs, then $v_m - v_n > 0$ is consistent with β^l_{nm}=1 and β^l_{mn}=0, or $v_m - v_n < 0$ is consistent with β^l_{mn}=1 and β^l_{nm}=0. Mathematically, we have

Theorem: Let Ω^l be the feasible set of the DNR problem with respect to optimization variables (x^l, β^l, u^l). For an arbitrary branch l := (m, n) for $\forall(m,n)\in\mathcal{N}$, if the signs of P^l_{mn} and Q^l_{mn} simultaneously depend on the combination of β^l_{nm} and β^l_{mn}, then Ω^l can be expressed as:

$$\Omega^l = \left\{ (\boldsymbol{x}^l, \boldsymbol{\beta}^l, \boldsymbol{u}^l) \in \mathbb{R}^{n+2|\varepsilon|} \times \mathbb{Z}^{2|\varepsilon|} \left| \begin{array}{l} (2.4)-(2.7) \\ (3.4)-(3.7) \\ (v_m - v_n)\cdot\beta^l_{nm} > 0 \\ \vee (v_m - v_n)\cdot\beta^l_{nm} < 0 \\ \vee (v_m - v_n)\cdot u^l_{mn} = 0 \end{array} \right. \right\} \tag{3.15}$$

where $\vee$ denotes the logic operator for disjunction.

Proof: Suppose that there exists a directional branch power flow from parent node n to child node m such that $v_m - v_n > 0$ for β^l_{mn}=1 and β^l_{nm}=0. Due to $\ell^l_{mn} > 0$, then we have $-|z^l_{mn}|^2\ell^l_{mn} < 0$. And directional branch power flow from n to node m means that P^l_{mn}<0 and Q^l_{mn}<0. Subsequently, it is derived that $v_m - v_n = 2R_{mn}P^l_{mn} + 2X_{mn}Q^l_{mn} - |z^l_{mn}|^2\ell^l_{mn} < 0$ where R_{mn} and X_{mn} refer to the resistance and reactance of branch l. This induces $v_m - v_n < 0$, which contradicts $v_m - v_n$>0 as the initial assumption. Similarly, this theorem can be also proven for which $v_m - v_n < 0$ is consistent with β^l_{mn}=1 and β^l_{nm}=0. If u^l_{mn}=0, then $\beta^l_{nm} = \beta^l_{mn} = 0$ by (3.15) and $v_m - v_n$ can be free. ■

With this theorem's framework, it is found that no additional disjunctive variables are incorporated for tighter relaxations, but it can guarantee a more rapid convergence than using Big-M and McCormick linearization method. Indeed, if there exists a DN without any reactive compensation or DERs injection, the enforced disjunctive constraint naturally holds for each branch since the voltage profile at the root node is the only highest. For a branch l:= (m, n) with additional reactive compensation or DERs injection at the ending node n, this theorem may not hold due to $v_m - v_n < 0$ and β^l_{mn} = 1, β^l_{nm} = 0. It is known that this l is a connected branch with parent node m and child node n, but $(v_m - v_n) \cdot u^l_{mn} \neq 0$, $(v_m - v_n) \cdot \beta^l_{mn}$=0 and $(v_m - v_n) \cdot \beta^l_{nm} < 0$ disobeys this **Theorem**. Therefore, if a branch has a bi-directional power flow caused by reactive compensation or DERs injection, any enforced disjunctive constraints between parent-child relationship variables and voltage drops in (3.15) should be relaxed. Otherwise, additional disjunctive variables should be incorporated to replace parent-child relationship variables in (3.15). Excluding branches with the possibility of bi-directional power flows, a disjunctive CH based on parent-child relationship variables can be utilized to construct tighter convex relaxations of (1.6) and (1.7) and disjunctive constraints in (3.15) for the rest of the branches. Please also note that the simple way is to estimate which is the farthest load node from the center of each reactive compensation and DERs injection node via calculating their capacity accommodation. Thus, we can easily find these possible branches and relax their corresponding disjunctive constraints between parent-child relationship variables and voltage drops in (1.6).

For (1.6), we define $\Omega_{1,\,mn}$ and $\Omega_{1,\,nm}$ as the disjunctive convex sets for (3.15) integrated with $\beta^l_{mn} = 1$ and $\beta^l_{nm} = 1$ for branch $l := (m, n)$, respectively. Subsequently, $\Omega_{1,\,mn}$ can be written as a union of two convex sets $\Omega^{0\,1,}_{mn}$ and $\Omega^{1\,1,}_{nm}$ corresponding to $\beta^l_{nm} =$ 1 and $\beta^l_{mn} = 0$. This is similar to $\Omega_{1,\,nm}$ under β^l_{nm}=1 and β^l_{nm}=0.

$$\Omega_{1,mn} = \mathrm{Conv}(\Omega^0_{1,mn} \cup \Omega^1_{1,mn}),\ \Omega_{1,mn} = \mathrm{Conv}(\Omega^0_{1,nm} \cup \Omega^1_{1,nm}) \tag{3.16}$$

$$\Omega^0_{1,mn}, \Omega^0_{1,nm} = \{\boldsymbol{x^l} \in \mathbb{R}^n \mid \underline{\boldsymbol{v}} \le \boldsymbol{v} \le \overline{\boldsymbol{v}}, \ell^l_{mn}, P^l_{mn}, Q^l_{mn} = 0\} \tag{3.17}$$

$$\Omega^1_{1,mn}, \Omega^1_{1,nm} = \{\boldsymbol{x^l} \in \mathbb{R}^n \mid (1.6), \underline{\boldsymbol{v}} \le \boldsymbol{v} \le \overline{\boldsymbol{v}}, 0 \le \ell^l_{mn} \le \overline{\ell}^l\} \tag{3.18}$$

In this vein, we sketch the geometry closure of $\Omega_{1,mn}$ and $\Omega_{1,nm}$ with a continuous variation of β^l_{nm}, β^l_{mn} $\in$ [0, 1] on (v_m−v_n, $2R_{mn}P^l_{mn}$ +$2X_{mn}Q^l_{mn}$ −$|z^l_{mn}|^2\ell^l_{mn}$, β^l)-space in Fig. 3.4 (a). The geometry closure of $\Omega_{1,\,mn}$ and $\Omega_{1,\,nm}$ are disjunctive polyhedral sets with vertexes V_1−V_4 and V_1, V_5−V_7 in blue and green CHs, respectively. Note that the former vertical coordinate axis is upward β^l_{nm} while the latter vertical axis is downward β^l_{mn}. Clearly, the hyperplane ψ_1 with vertexes V_1, V_2 and V_4 is at the bottom of the blue polyhedral hull, whereas hyperplane ψ_2 with vertexes V_4, V_5 and V_7 is at the top of the green polyhedral hull. With this definition of bi-directional vertical axis, ψ_1 and ψ_2 are bottom hyperplanes of blue and green polyhedral CHs, respectively. As a result, with the hyperplanes ψ_1 and ψ_2, we explicitly express two constraints in (3.19) that are obtained from the coordinates of vertexes V_1, V_2, V_4, V_5 and V_7, which are {$\overline{v}-\underline{v}$, $\overline{v}-\underline{v}$, 1}, {0, 0, 1}, {0, 0, 0}, {$\underline{v}-\overline{v}$, $\underline{v}-\overline{v}$, 1} and {0, 0, 1}. In terms of top hyperplane, both disjunctive CH $\Omega_{1,mn}$ and $\Omega_{1,nm}$ have the same upper bound.

Subsequently, the third constraint in (3.19) using $u^l_{mn} = \beta^l_{mn} + \beta^l_{nm}$ can represent the top hyperplane with vertexes V_1, V_2, V_3 or V_5, V_6, V_7. These linear constraints from equations of the above-mentioned hyperplane:

$$\begin{cases} \dfrac{1}{\overline{v}-\underline{v}}\cdot \boldsymbol{A}\cdot \boldsymbol{v} - \dfrac{1}{\overline{v}-\underline{v}}\cdot(2\boldsymbol{D}_r\boldsymbol{P}^l + 2\boldsymbol{D}_x\boldsymbol{Q}^l - |\boldsymbol{z}^l|^2\, \ell^l) - \beta^l_{nm} \geq \text{-}1 \\ \dfrac{1}{\overline{v}-\underline{v}}\cdot \boldsymbol{A}\cdot \boldsymbol{v} - \dfrac{1}{\overline{v}-\underline{v}}\cdot(2\boldsymbol{D}_r\boldsymbol{P}^l + 2\boldsymbol{D}_x\boldsymbol{Q}^l - |\boldsymbol{z}^l|^2\, \ell^l) - \beta^l_{mn} \geq \text{-}1 \\ \dfrac{1}{\overline{v}-\underline{v}}\cdot \boldsymbol{A}\cdot \boldsymbol{v} - \dfrac{1}{\overline{v}-\underline{v}}\cdot(2\boldsymbol{D}_r\boldsymbol{P}^l + 2\boldsymbol{D}_x\boldsymbol{Q}^l - |\boldsymbol{z}^l|^2\, \ell^l) + u^l_{mn} \leq 1 \end{cases} \tag{3.19}$$

As a DCHR formation via $u^l = \beta^l_{mn}+\beta^l_{nm}$, the disjunctive CH $\Omega_1 = \mathrm{Conv}(\Omega_{1,nm} \cup \Omega_{1,mn})$ of (1.6) and the enforced disjunctive constraint in (3.15) yields

$$\Omega_1 = \{(\boldsymbol{x}^l, \boldsymbol{\beta}^l, \boldsymbol{u}^l) \in \mathbb{R}^{n+2|\varepsilon|} \times \mathbb{Z}^{|\varepsilon|} \mid (3.19) \text{ and } (3.21)-(3.23)\} \tag{3.20}$$

where corresponding perspective linear cuts are imposed to improve bounds of v and ℓ^l by

$$(1-\beta^l_{nm})(\underline{v}-\overline{v}) \leq v_m - v_n \leq \beta^l_{nm}(\overline{v}-\underline{v}) \tag{3.21}$$

$$\beta^l_{mn}(\underline{v}-\overline{v}) \leq v_m - v_n \leq (1-\beta^l_{mn})(\overline{v}-\underline{v}) \tag{3.22}$$

$$\ell^l = \ell^l_+ + \ell^l_-,\ 0 \leq \ell^l_+ \leq \beta^l_{mn}\overline{\ell}^l, 0 \leq \ell^l_- \leq \beta^l_{nm}\overline{\ell}^l \tag{3.23}$$

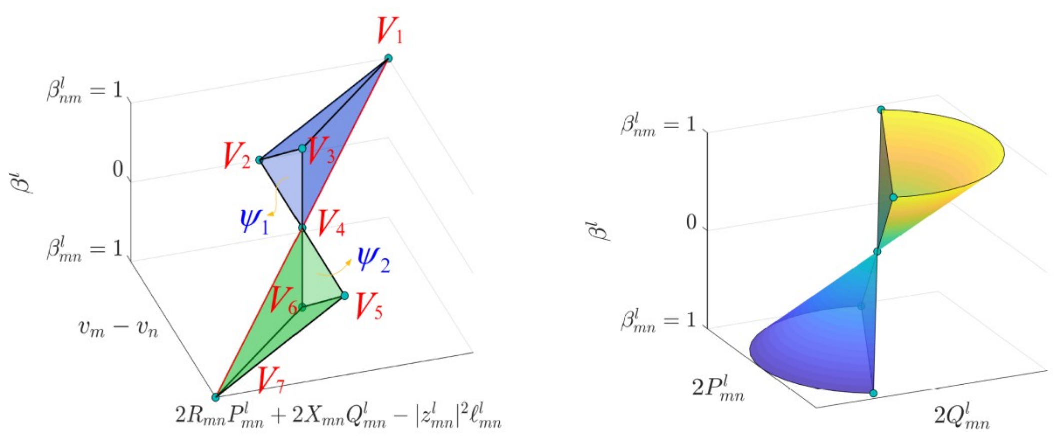

(a) (b)

Fig. 3.4 (a) Disjunctive closure of Ω_1; (b) disjunctive closure of Ω_2.

For (1.7) of the branch l := (m, n), the possible CH of both (1.7) and the enforced disjunctive constraint in (3.15) can be expressed as the union of two points (x^l,u^l)=(0, 0, 0, $\underline{v}$, 0, 0) and (0, 0, 0, $\overline{v}$, 0, 0) and a continuous second-order conic (SOC) set, where this SOC set is drawn from a continuous SOC relaxation of the quadratic equality (1.7), yielding

$$\|(2P_{mn}^l, 2Q_{mn}^l, v_m - \ell_{mn}^l)^T\|_2 \le v_m + \ell_{mn}^l, \forall m,n \in \mathcal{N} \tag{3.24}$$

With the above-mentioned theorem, we visualize the geometry closure of this SOC-representable set by (3.24) as a disjunctive CH on ($2P_{mn}^l$, $2Q_{mn}^l$, β^l)-space as shown in Fig. 3.4 (b). In this figure, the intersection between the second-order cone and a valid cutting plane by either $v_m - v_n = 2P_{mn}^l + 2Q_{mn}^l - |z_{mn}^l|^2\ell_{mn}^l \geqslant 0$ or $v_m - v_n \leqslant 0$ contributes to forming a nearly half second-order cone. Evidently, this disjunctive closure is tighter than a full second-order cone. Let Ω_2 be a DCHR formation with respect to β_{mn}^l and β_{nm}^l, which is expressed as

$$\Omega_2 = \{(\boldsymbol{x}^l, \boldsymbol{\beta}^l, \boldsymbol{u}^l) \in \mathbb{R}^{n+2|\varepsilon|} \times \mathbb{Z}^{|\varepsilon|} \mid (3.24) \text{ and } (3.26)\text{-}(3.27)\} \tag{3.25}$$

where corresponding perspective linear cuts are given as

$$0 \le 2\boldsymbol{D}_r\boldsymbol{P}^l + 2\boldsymbol{D}_x\boldsymbol{Q}^l - \boldsymbol{D}_z\ell^l \le (\overline{v} - \underline{v}) \cdot \boldsymbol{\beta}_{nm}^l \tag{3.26}$$

$$(\underline{v} - \overline{v}) \cdot \boldsymbol{\beta}_{mn}^l \le 2\boldsymbol{D}_r\boldsymbol{P}^l + 2\boldsymbol{D}_x\boldsymbol{Q}^l - \boldsymbol{D}_z\ell^l \le 0 \tag{3.27}$$

By the observation of Ω_1 and Ω_2, this DCHR approach is tighter than the McCormick linearization method and the Big-M method for any branch l under Theorem, which corresponding proof can be provided here.

Proof: For McCormick linearization method, we suppose $\boldsymbol{y}^l = \boldsymbol{u}^l \cdot \boldsymbol{A} \cdot \boldsymbol{v}$ and then $\boldsymbol{y}^l - 2\boldsymbol{D}_r\boldsymbol{P}^l - 2\boldsymbol{D}_x\boldsymbol{Q}^l + \boldsymbol{D}_z\ell^l = 0$ automatically holds also for connected and/or unconnected branches subject to $\boldsymbol{A} \cdot \boldsymbol{v} + (\overline{v} - \underline{v}) \cdot (\boldsymbol{u}^{l} - 1) \leq \boldsymbol{y}^{l} \leq \boldsymbol{A} \cdot \boldsymbol{v} - (\overline{v} - \underline{v}) \cdot (\boldsymbol{u}^{l} - 1)$. It is clear that, due to the large-enough positive scalar number $M \geq (\overline{v} - \underline{v})$, McCormick linearization method has tighter relaxation bounds of (1.6) than Big-M method.

For an arbitrary branch *l*, the lower bound of (1.6) by McCormick linearization method is denoted as L_1^{lower}, yielding

$$L_1^{lower} = \boldsymbol{A} \cdot \boldsymbol{v} + (\overline{v} - \underline{v}) \cdot (\boldsymbol{u}^{l} - 1) - 2\boldsymbol{D}_r \boldsymbol{P}^{l} - 2\boldsymbol{D}_x \boldsymbol{Q}^{l} + \boldsymbol{D}_z \ell^{l} \tag{3.28}$$

However, in terms of DCHR, the lower bound of (1.6) for branch *l* denoted as L_2^{lower} is derived from the intersection set of first two inequality in (3.29), which is given by

$$L_2^{lower} = \boldsymbol{A} \cdot \boldsymbol{v} - 2\boldsymbol{D}_r \boldsymbol{P}^{l} - 2\boldsymbol{D}_x \boldsymbol{Q}^{l} + \boldsymbol{D}_z \ell^{l} \tag{3.29}$$

Hence, we can achieve the difference in algebra between L_1^{lower} and L_2^{lower} by $L_1^{lower} - L_2^{lower} = (\overline{v} - \underline{v}) \cdot (\boldsymbol{u}^{l} - 1)$ .Since $u^{l} \in \{0,1\}$, this clearly renders $L_1^{lower} - L_2^{lower} \leq 0$. Similarly, we can also achieve the upper bound of (1.6) by two methods are equal.

Moreover, this McCormick linearization method for (1.7) adopts a Lorentz cone ***L*** defined from (3.24). Let Φ_1 be the feasible set of this Lorentz cone ***L***, whereas DCHR has the feasible region

$$\Phi_2 = \{\Phi_1 \cap (v_m - v_n > 0)\} \cup \{\Phi_1 \cap (v_m - v_n < 0)\} \cup \{\Phi_1 \cap (v_m - v_n = 0)\} \tag{3.30}$$

This implies that Φ_2 is smaller than Φ_1 since $v_m - v_n$ only holds for either $v_m - v_n > 0$ or $v_m - v_n < 0$ or $v_m - v_n = 0$. In light of tighter bounds in (1.6) and (3.10), we have proved that DCHR has tighter relaxation bounds than the McCormick linearization method and Big-M method. ■

With tighter bounds, this DCHR approach can also converge at the optimal point with achieving SOC equality for a load oversatisaction assumption and radial networks as proved in Subsection 2.4. Making use of the above, the loss minimization of DNR is a nonconvex mixed-integer quadratically constrained programming (MIQCP) problem. Now we have enabled this MIQCP-based DNR model to a tractable MISOCP-based DNR reformulation with the set of optimization variables $\boldsymbol{x}^l := \left[\boldsymbol{P}^l, \boldsymbol{Q}^l, \ell^l, \boldsymbol{v}, \boldsymbol{Q}^{cr}, \boldsymbol{w}^l, \boldsymbol{m}^l, \boldsymbol{f}^l, \boldsymbol{\beta}^l_{mn}, \boldsymbol{\beta}^l_{nm}, \boldsymbol{u}^l\right]^T$, $\forall l \in \mathcal{E}$ subject to system operational constraints below. Leveraging Ω_1 and Ω_2 to represent (1.6) and (1.7), we have

$$
\min_{x^l} \quad P_0^l
$$

$$
s.t.\begin{cases}
P_{mn}^l + P_n^g - r_{mn}^l \ell_{mn}^l = \sum_{k\in\pi(n)} P_{nk}^l + P_n^d, \forall l \in \mathcal{E}, \forall m,n \in \mathcal{N} \\
Q_{mn}^l + Q_n^g - x_{mn}^l \ell_{mn}^l = \sum_{k\in\pi(n)} Q_{nk}^l + Q_n^d, \forall l \in \mathcal{E}, \forall m,n \in \mathcal{N} \\
\frac{1}{\overline{v}-\underline{v}} \cdot \boldsymbol{A} \cdot \boldsymbol{v} - \frac{1}{\overline{v}-\underline{v}} \cdot (2\boldsymbol{D_r P^l} + 2\boldsymbol{D_x Q^l} - |\boldsymbol{z^l}|^2 \ell^l) - \beta_{nm}^l \geq -1 \\
\frac{1}{\overline{v}-\underline{v}} \cdot \boldsymbol{A} \cdot \boldsymbol{v} - \frac{1}{\overline{v}-\underline{v}} \cdot (2\boldsymbol{D_r P^l} + 2\boldsymbol{D_x Q^l} - |\boldsymbol{z^l}|^2 \ell^l) - \beta_{mn}^l \geq -1 \\
\frac{1}{\overline{v}-\underline{v}} \cdot \boldsymbol{A} \cdot \boldsymbol{v} - \frac{1}{\overline{v}-\underline{v}} \cdot (2\boldsymbol{D_r P^l} + 2\boldsymbol{D_x Q^l} - |\boldsymbol{z^l}|^2 \ell^l) + u_{mn}^l \leq 1 \\
(1-\beta_{nm}^l)(\underline{v}-\overline{v}) \leq v_m - v_n \leq \beta_{nm}^l(\overline{v}-\underline{v}) \\
\beta_{mn}^l(\underline{v}-\overline{v}) \leq v_m - v_n \leq (1-\beta_{mn}^l)(\overline{v}-\underline{v}) \\
\ell^l = \ell_+^l + \ell_-^l,\ 0 \leq \ell_+^l \leq \beta_{mn}^l \overline{\ell}^l, 0 \leq \ell_-^l \leq \beta_{nm}^l \overline{\ell}^l \\
\left\| \begin{matrix} 2P_{mn}^l \\ 2Q_{mn}^l \\ w^l \end{matrix} \right\|_2 \leq m^l, \forall l \in \mathcal{E}, \forall m,n \in \mathcal{N} \\
w^l = \ell_{mn}^l - v_m,\ m^l = \ell_{mn}^l + v_m, \quad \forall l \in \mathcal{E}, \forall m,n \in \mathcal{N} \\
0 \leq 2D_r P^l + 2D_x Q^l - |z^l|^2 \ell^l \leq (\overline{v}-\underline{v}) \cdot \beta_{nm}^l \\
(\underline{v}-\overline{v}) \cdot \beta_{mn}^l \leq 2D_r P^l + 2D_x Q^l - |z^l|^2 \ell^l \leq 0 \\
-\overline{Q}_0^l \leq Q_0^l \leq \overline{Q}_0^l \\
\underline{Q}^{cr} \leq Q^{cr} \leq \overline{Q}^{cr} \\
\underline{v} \leq v \leq \overline{v} \\
\beta_{mn}^l + \beta_{nm}^l = u^l \\
\beta_{mn}^l = 0,\ \text{if}\ m = 0 \\
\sum_{n:(m,n)\in\mathcal{E}} \beta_{mn}^l = 1, \forall m \in \mathcal{N} \backslash 0 \\
\beta_{mn}^l \geq 0 \\
\boldsymbol{A}^T f = 1 \\
-N \cdot u^l \leq f^l \leq N \cdot u^l, \quad \forall l \in \mathcal{E} \\
1^T u^l = |\mathcal{N}| - 1, \quad u^l \in \{0,1\}
\end{cases} \tag{3.31}
$$

where P_0^l is the active power injection at the root node 0.

3.4 Case Study

3.4.1 Simple 6-node DN

The following simple 6-node DN is used to exemplify this polyhedral approximation of DNR model using Big-M relaxation method. The network is shown in Fig. 3.5. The node 1 is the PCC bus, while nodes 2-6 are PQ buses. In other words, $\mathcal{N}$ ={1,2,3,4,5,6} and $\mathcal{E}$ ={1,2,3,4,5}, where branch labels are displayed in yellow-filled square boxes. The impedance of each branch, the load demand of each node and the reactive power compensation capacity of installed capacitors are labeled in this figure. The voltage allowance band of each node is set to 0.97–1.07 p.u. The switch-off circuit breakers are marked with "□" and the rest are switch-on marked by "■". For a fixed topology, we focus on reactive power optimization on the active branches for the minimization of real power loss.

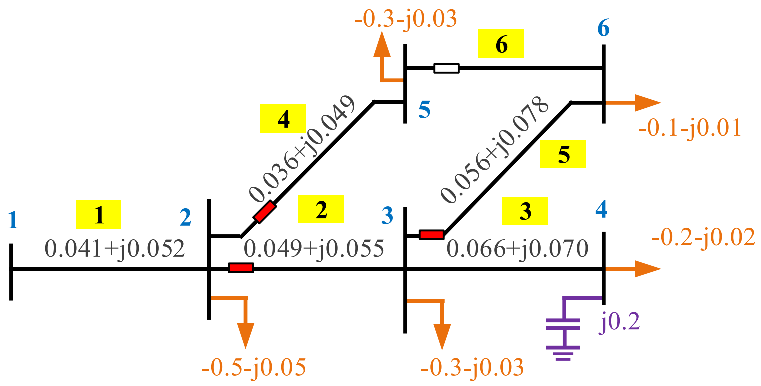

Fig. 3.5 Topology of a radial DN.

According to this DCHR-based DNR model (3.31), the size of $[P^l, Q^l, \ell^l, v, Q^{cr}]$ is 6·4+1=25; $[w^l, m^l, \ell^{l+}, \ell^{l-}]$ has the size 6·4=24 and $[f^l, \beta^l_{mn}, \beta^l_{nm}]$ has the size 3·6=18.The remaining u^l is a vector of $u^l = [u_{12}, u_{23}, u_{34}, u_{25}, u_{36}, u_{56}]$. Thus, the total number of variables is 25+24+18+6=73. The SCF constraints and spanning tree constraints are the same as the MISOCP-based DNR model with Big-M relaxation method. The tree-shaped voltage profiles before and after DNR operations are presented in Fig. 3.6. The output solutions are shown in Table 3.2 and Table 3.3 after running the above codes.

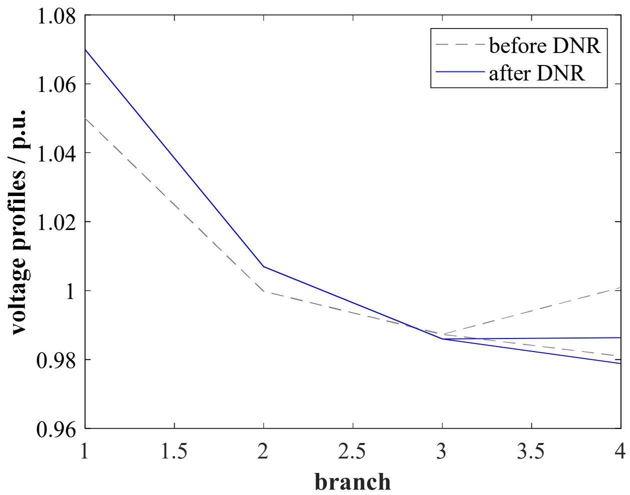

Fig. 3.6 Tree-shaped voltage profiles of simple 6-node DN.

Table 3.2 Optimal DNR objective of the 6-node DN.

Solvers	Minimal injected real power at PCC node (p.u.)	Real Power Loss (p.u.)	Algorithm Iterations	Computational Time (seconds)
MOSEK	1.504	0.1035	7	0.031
Baron	1.504	0.1035	6	0.030

Table 3.3 Optimal DNR solutions of the 6-node DN.

Solvers	Circuit breakers	
	Swicth-on status of Branch No.	Swicth-off status of Branch No.
MOSEK	5	1, 2 ,3, 4, 6
Baron	5	1, 2 ,3, 4, 6

3.4.2 Large-scale DNs

To validate the effectiveness of DCHR, we show the voltage profiles before and after DNR operations by this proposed DCHR approach. The tree-shaped voltage profiles are presented in Fig. 3.7 (a)-(d) for different DNs: (a) 16-node; (b) 33-node; (c) 123-node and (d) 1060-node. The voltage profiles before and after DNR operations are enhanced to reduce the power loss, where this phenomena can be observed by the blue lines as compared to grey dashed lines in Fig. 3.7 (a)-(d). This demonstrates that this proposed DCHR approach can successfully solve this DNR problem with voltage profile enhancements.

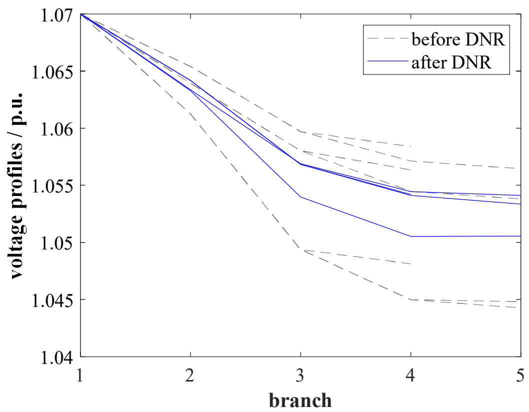

(a)

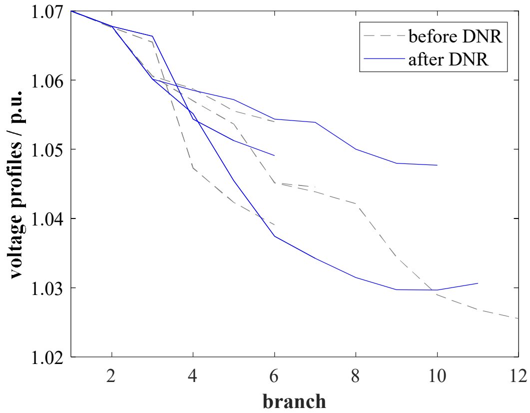

(b)

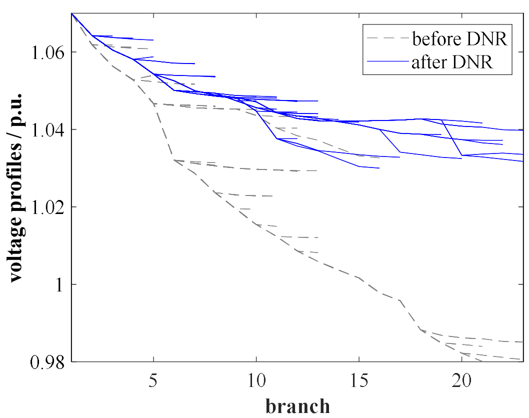

(c)

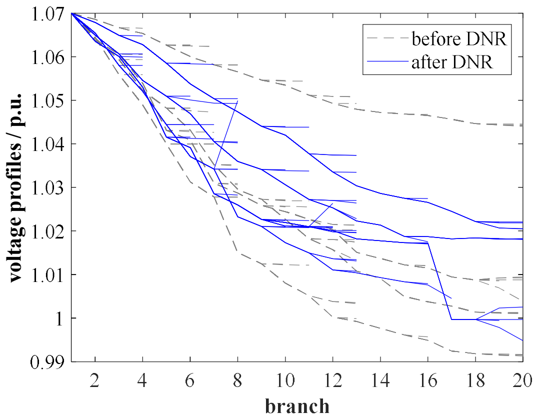

(d)

Fig. 3.7 Tree-shaped voltage profiles of different DNs: (a) 16-node; (b) 33-node; (c) 123-node and (d) 1060-node.

To compare the relaxation tightness of DCHR, we employ the DNR models using four methods: (*i*) the Big-M method for (1.6) and continuous SOC relaxation for (1.7) (M1) [14], (*ii*) the McCormick linearization method for (1.6) and continuous SOC relaxation for (1.7) (M2) [15], and (*iii*) the polyhedral approximation method with 32 segments of linearizations (M3) [17], and (*iv*) the proposed DCHR approach (M4). These comparable M1-M4 are implemented for the low and the high penetrations of reactive power capacitors and DERs for cases I and II, respectively. The computational performance in terms of CPU time in seconds and algorithm iterations are given in Table 3.3 for M1-M4. The convergence performance of duality gaps is presented in Fig. 3.8 by M1-M4.

Table 3.3 Computational Performance Among M1-M4.

Cases	Syst.	CPU Time (s)				Iterations			
		Convex	Relaxations		Approx.	Convex	Relaxations		Approx.
		M1	M2	M4	M3	M1	M2	M4	M3
I	16-node	0.281	0.250	0.234	0.297	202	172	113	99
	33-node	2.906	1.985	1.187	1.781	3452	2259	949	1290
	123-node	1.613	1.488	1.171	1.875	237	329	135	275
	1060-node	329.437	56.922	18.187	20.328	116663	16114	3764	4510
II	16-node	0.309	0.297	0.228	0.275	175	151	133	109
	33-node	3.703	2.141	1.432	1.890	2021	1432	635	1136
	123-node	1.703	1.641	1.218	1.918	237	329	179	152
	1060-node	686.813	97.969	39.094	46.938	127315	13929	5567	5936

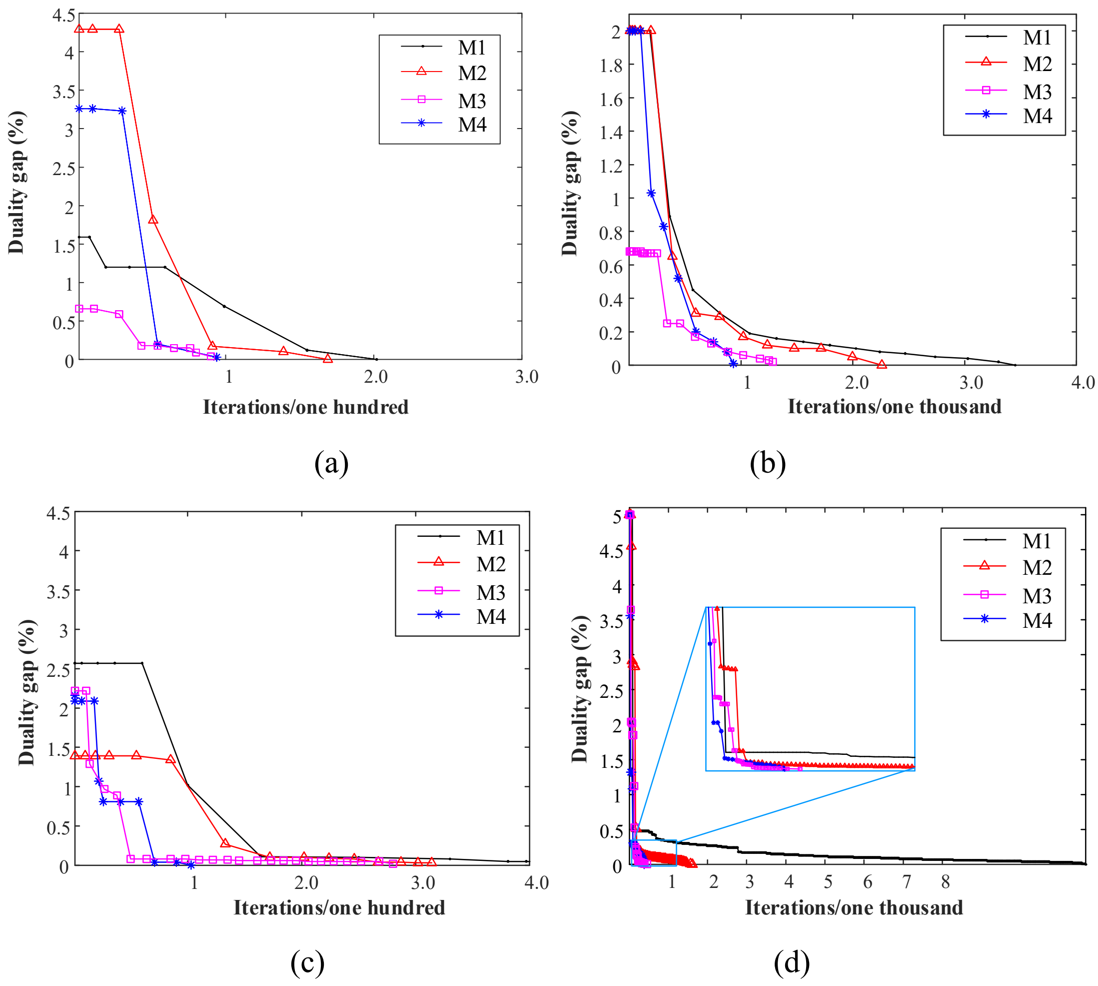

Fig. 3.8 Convergence performance: (a) 16-node; (b) 33-node; (c) 123-node; (d) 1060-node.

Table 3.3 shows that M4 significantly outperforms M1 and M2 with the less CPU running time and M4's solutions are more accurate than M3 in theory for all systems of two cases. Regarding the number of iterations, it suggests that the relaxation bounds of DNR models by M4 is more effective than M1-M3 as justified with the less running time. Since a large-enough positive scalar in M1 leads to loosing bounds, it is tricky for M1 to find the optimal configuration scheme quickly. Between M2 and M4, M4 can induce fast convergence with achieving SOC equality than M2, since SOC constraints in M4 are coupled with parent-child relationship variables. Additionally, M4 is superior for case I than case II, due to a larger number of branches that may have bi-directional power flows in case II. These conclusions are also justified by the fast convergence in two test systems in Fig 3.8 (a)-(d).

Moreover, we examine the relaxation bounds by M1, M2 and M4 to showcase the limitations of M1 and M2. For an arbitrary branch l, the bounds by M1 and by M4 are denoted as (3.28) and (3.29), respectively. For brevity, the number of integer-relaxed SOCP models solved in the B&B iterations can suggest this DNR model's boundary tightness. Thus, we display this number of SOCP-relaxations to represent the relaxation bounds during iterations in Fig. 3.9(a)-(d).

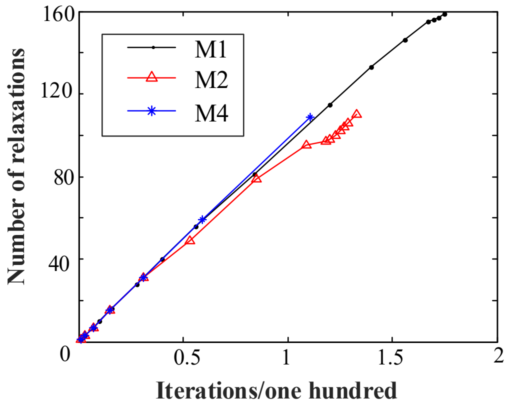

(a)

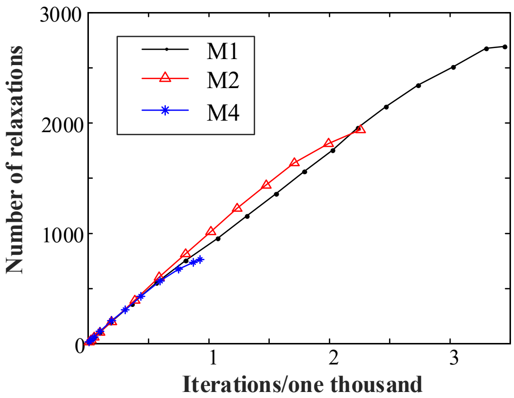

(b)

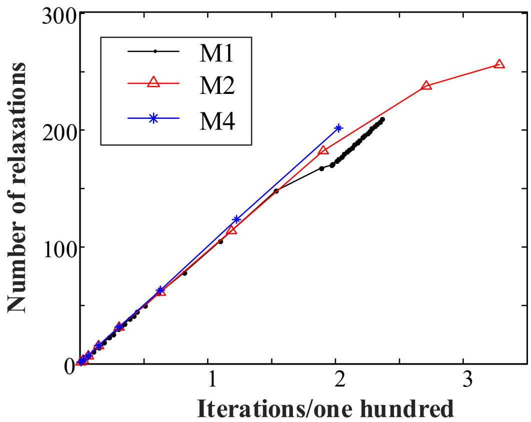

(c)

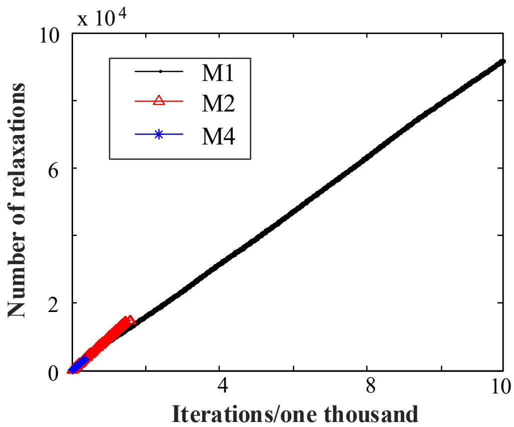

(d)

Fig. 3.9 Lower bounds of M1, M2 and M4: (a) 16-node; (b) 33-node; (c) 123-node; (d) 1060-node.

Clearly, the relaxation bounds by M1, M2 and M4 are significantly different, in which M4 has the tightest relaxation bounds as indicated in Fig. 3.9(a)-(d). This is because of the least numbers of relaxations in the B&B iterations. In theory, M4 has a tighter feasibility space for this DNR optimization due to $L_2^{lower} > L_1^{lower}$ in (3.28) and (3.29) and a tighter Lorentz cone $\boldsymbol{L}$ by (3.30). Based on these two aspects, M4 has tighter relaxation bounds than the M1 and M2.

3.5 Summary

This chapter proposes a DCHR approach to tackle the disjunctive nature of DNR problems. With continuous parent-child relationship variables as disjunctive variables, this DCHR approach is theoretically tighter than the McCormick linearization method and the Big-M method, and it is especially suitable for DNs with directional power flows. As demonstrated in case studies, the computing performance in terms of running time and iterations using a DCHR approach yields superior numerical performance than prior relaxation methods.

Chapter 4

Observability Defense-Constrained Topology Optimization of Active Distribution Networks for Cyber–Physical System Security Enhancement

The system observability is crucial for a sufficient level of controllability on ADNs, which provides the ability to understand the physical system states. This has proved to be extremely powerful, especially with the various grid operations that depend on the physical system's behavior, e.g., generator redispatch, fault location. Indeed, a huge number of feeders and nodes with limited metering points such as D-PMU units are essential to achieve this merit of observability. With D-PMU units, the full system observability for system-wide security operation in ADNs can be available with a good level of service continuity.

This chapter is focused on the defense level of cyber–physical security in the DNR model. Motivated by the minimum cost PMU placement model in a relaxed connected dominating set (RCDS) form [31], this chapter proposes a disjunctive RCDS formulation for reconfigurable DNs with the least defense cost in theory. Then, an observability defense-constrained DNR model can be cast as a mixed integer second-order conic programming problem (MISOCP). This observability defense-constrained DNR formulation will be elaborated and verified in case studies.

4.1 System Observability for Cyber–Physical Security Enhancement

D-PMUs are advanced grid measurements for security and economic operation, which measurement data are uploaded to dispatch centers via wireless/wired communication layers. From the perspective of cybersecurity, it is crucial to monitor the cyber interactions in cyber-physical DN entities against cyber attacks [35], where the relationship for physical DNs, cyber-physical DNs and cyber DNs is displayed in Fig. 4.1. If the some parts of DNs cannot be observed, then cyber attacks for these unobserved areas may not be easily detected. As such, we propose the term "observability defense" that can be used to describe the defense cost against cyber–physical threats subject to the full observability of DNs.

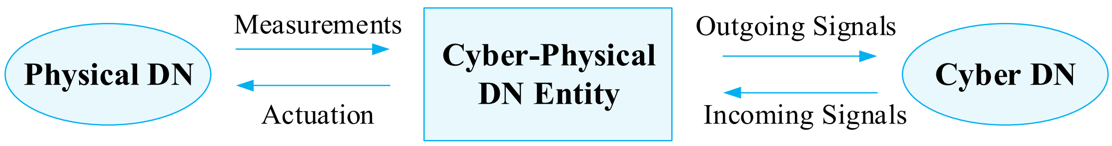

Fig. 4.1 Cyber-physical interactions in DNs

The observability defense cost is on the D-PMU measurement protection, which is very essential to prevent false data injection attacks (FDIAs) as common cyber–physical threats. If any measurements of D-PMUs are attackable by adversaries, corrupted measurements and/or load data can render improper DNR actions, then probably inducing physical security issues that cannot be observed. Accordingly, the effective cyber-physical system security defense, e.g., the full system observability guarantees, cannot be neglected. At present, the existing cyber-physical defense strategies focus on the full protection of D-PMU data for the entire DNs. However, a small number of D-PMU devices can actually cover the full observability of DNs, since some nodes have zero power injection. In other words, this observability defense strategy varies as the DNs change, which can be beneficial for reducing the defense cost. From this perspective, we study the defense issue of system observability in the DNR model.

Given that deployed D-PMUs and zero injection nodes are available in ADNs, power flow and nodal voltage phasor can be observable just based on a proper use combination of them. In terms of FDIAs during DNR operations, both zero injection nodes without having generation or loads and substation measurements cannot be attacked due to physical property and private communication networks [33]. Thus, load-side smart meters and unprotected D-PMU measurements may be attackable as displayed in Fig. 4.2. In this chapter, we only consider defensible D-PMUs and zero injection nodes as limited security resources for DNR operations. This system observability defense against FDIAs can be converted to seek a minimum number of protected D-PMUs for less channel resources and decryption service subject to the topological observability condition [34].

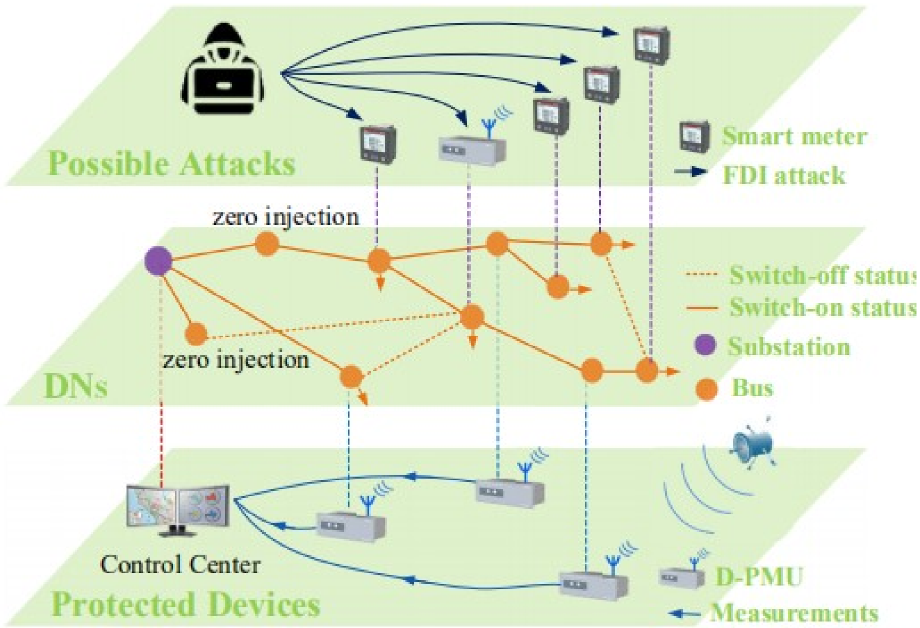

Fig. 4.2 Illustration of the system observability defense.

4.2 RCDS Formulation For Fixed ADNs

To begin with, we introduce the RCDS problem for fixed ADNs. Generally, ADNs are considered as a connected undirected tree $\mathcal{G}=(\mathcal{N},\mathcal{E})$, where $\mathcal{N}:=[1,2,\ldots,|\mathcal{N}|]$ is the set of nodes and $\mathcal{E}$ is the set of branches in the dimension $|\mathcal{E}|\times 1$. Suppose that an arbitrary branch $l:=(i,j), l\in\mathcal{E}$ is between nodes (i,j). For any RCDS solution $\mathcal{D}\subseteq\mathcal{N}$ under a fixed radial topology, we denote $\mathcal{E}[\mathcal{D}]:=\{l\in\mathcal{E}|(i,j)\cap\mathcal{D}\neq\phi\}$ as the set of edges connected to $\mathcal{D}$, where $\mathcal{E}[\mathcal{D}]$ is called a induced subgraph of $\mathcal{E}$. Following [31], this RCDS model is to seek a minimum node subset $\mathcal{D}$ via evaluating a minimum cardinality $|\mathcal{D}|$, such that subgraph $(\mathcal{N},\mathcal{E}[\mathcal{D}])$ is connected, yielding

$$\min_{\mathcal{D}\subseteq\mathcal{N}} \quad F=|\mathcal{D}| \tag{4.1a}$$

$$\text{s.t.} \quad (\mathcal{N},\mathcal{E}[\mathcal{D}]) \quad \text{connected} \tag{4.1b}$$

The minimum RCDS solution $\mathcal{D}^*$ for (4.1a)-(4.1b) is also called the perfect protection set in [30] and [31]. Mathematically, we can explain the constraint (4.1b) that (*i*) every node in $\mathcal{N}$ either belongs to $\mathcal{D}^*$ or is adjacent to a node in $\mathcal{D}^*$; and (*ii*) any node in $\mathcal{D}^*$ can reach any other node in $\mathcal{D}^*$ by a path that stays entirely within $\mathcal{D}^*$ or a "relaxed path" that there exists one node not in $\mathcal{D}^*$ along this path.

4.3 Disjunctive RCDS Formulation For Reconfigurable ADNs

From an operational perspective, ADNs are generally reconfigurable. Thereby, the RCDS solution $\mathcal{D}$ is dependent on a binary state vector of circuit breakers $\boldsymbol{u}^l$ for the graph $\mathcal{G}$ .Here, $\boldsymbol{u}^l$ is zero if the switch is open and one if closed, which $\psi(\boldsymbol{u}^l)=0$ denotes the spanning tree constraints for radiality and $h(\boldsymbol{u}^l)\leqslant 0$ denotes system-wide operational constraints. The subgraph induced by RCDS is then modified as $\mathcal{E}^u[\mathcal{D}] := \{l \in \mathcal{E}^u | (i,j) \cap \mathcal{D} \neq \phi\}$, where $\mathcal{E}^u := \{l \in \mathcal{E} | \ \psi(\boldsymbol{u}^l)=0, \boldsymbol{u}^l \in \mathbb{Z}\}$. Due to the disjunctive nature of DNR problems [9], we propose a disjunctive RCDS formulation for reconfigurable $\mathcal{E}^u$ in theory based on the existing RCDS model:

$$\min_{\mathcal{D}\subseteq\mathcal{N},\ \boldsymbol{u}^l\in\mathbb{Z}} \quad F = |\mathcal{D}| \tag{4.2a}$$

$$\text{s.t.} \quad (\mathcal{N}, \mathcal{E}^u[\mathcal{D}]) \quad \text{connected} \tag{4.2b}$$

$$\psi(\boldsymbol{u}^l)=0 \quad \text{and} \quad h(\boldsymbol{u}^l)\leqslant 0 \tag{4.2c}$$

It is evident that the minimum RCDS solution $\mathcal{D}^*$ for (4.2a)-(4.2c) is characterized by $\boldsymbol{u}^l$. The following Fig. 4.3(a) and (b) are two corresponding radial topologies for a 6-node network, where the root node 0 connects the substation. Suppose all nodes have loads and the D-PMUs at all nodes other than the root node 0 are eligible for defense.

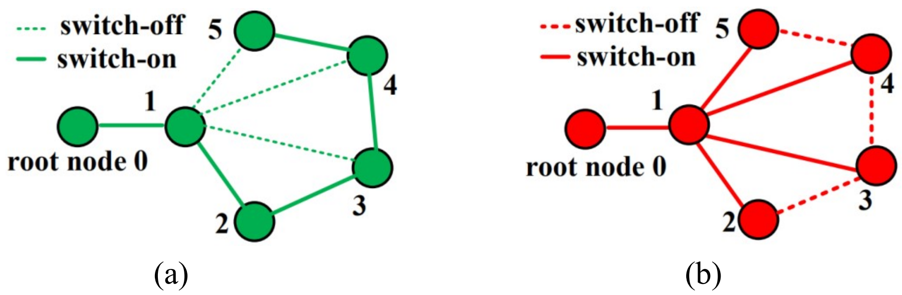

Fig. 4.3. (a) Topology $\mathcal{E}^u$ with two leaves; (b) topology $\mathcal{E}^u$ with five leaves.

By the observation, it is easily found that Fig. 4.2 (b) only employs one D-PMU at node 1, whereas Fig. 4.2 (a) must deploy two D-PMUs at nodes 2 and 4, respectively. The topology distinction is obvious since Fig. 4.2 (b) has four leaves but Fig. 4.2 (a) has one leaf, where a leaf refers to a terminal node with degree one for these two rooted trees.

This indicates that the topology determined by the optimal RCDS solution $\mathcal{D}^{t*}$ is equivalent to deal with a maximum leaf spanning tree problem (MLSTP) subject to $\psi(\boldsymbol{u}^l)=0$ in (4.2c). Without loss of generosity, if all non-leaf nodes have deployed D-PMU units, then the maximum leaf numbers determined by $\mathcal{D}^*$ and by the optimal MLSTP solution $\widetilde{\mathcal{D}}$ are equivalent, which can be proved below:

Proof: There exists an optimal MLSTP solution $\widetilde{\mathcal{D}}$ representing a spanning tree $\widetilde{\mathcal{G}}$ with n vertices and n-1 edges. Suppose that $\widetilde{\mathcal{G}}$ has s leaves such that $s \geq 1$ and $s < m$, where m is the number of leaves from the topology by the optimal RCDS solution $\mathcal{D}^{t*}$ if all non-leaf nodes have deployed D-PMU units. By the Handshake Lemma for all vertex v, the degree sum can be expressed as $\sum_{v=1}^{n} \deg v = \sum_{v=n-s+1}^{n} \deg v + s = \sum_{v=n-m+1}^{n} \deg v + m$. This further induces

$\sum_{v=n-s+1}^{n} \deg v > \sum_{v=n-m+1}^{n} \deg v$ since $s<m$. Recall that the total degree of non-leaf nodes represents the total number of edges that have these non-leaf nodes as endpoints. Thus, we have $\sum_{v=n-s+1}^{n} \deg v = 2(n-(n-s+1)) = 2s-2$ and $\sum_{v=n-m+1}^{n} \deg v = 2(n-(n-m+1)) = 2m-2$. By substitution, it is clear that $2s-2>2m-2$ can hold, i.e., $s>m$ stands, which contradicts the assumption $s<m$. This demonstrates that s should be equal to m. ■

It is assumed that $\mathcal{M}^P$ represents all nodes of D-PMUs other than the root node 0 and $\mathcal{M}^P \in \mathcal{N}$. Then, the decision vector is encoded by binary variables as z for D-PMUs in the dimension $|\mathcal{N}|\times 1$, i.e., $z_i \in \{0,1\}, \forall i \in \mathcal{M}^P$; otherwise, $z_i = 0$ for $i \notin \mathcal{M}^P$ .With $\mathcal{M}^P \neq \phi$ and the physical property of MLSTP, we can observe the minimum cardinality $|\mathcal{D}|$ has the maximum leaf spanning tree if $h(\boldsymbol{u}^l) \leq 0$ in (4.2c) is relaxed. This is essential for strengthening the lower bound of $\sum_{i\in\mathcal{M}^P} z_i$

$$\sum_{i\in\mathcal{M}^P} z_i \geq z^g \tag{4.3}$$

where z^g refers to the lower bound by solving (4.2a)-(4.2c) with relaxed $h(\boldsymbol{u}^l) \leqslant 0$. Since $\mathcal{M}^P \neq \phi$, then $z^g \geq 1$ holds, which indicates (4.3) should be tighter than $\sum_{i\in\mathcal{M}^P} z_i \geq 1$ in [30].

4.4 Linear Formulation of Disjunctive RCDS Constraint

Let $\mathcal{M}^l$ and $\mathcal{M}^k$ be the sets of zero injection nodes for non-leaf nodes and leaf nodes ($\mathcal{M}^l, \mathcal{M}^k \subseteq \mathcal{N}$), respectively. And $\boldsymbol{y}$ be the auxiliary binary-based decision variable vector for zero injection nodes in the dimension $|\mathcal{N}|\times 1$.

Namely, $y_i \in \{0,1\}, \forall i \in \mathcal{M}^I$ and $y_k = 1$ and $\forall k \in \mathcal{M}^k$; otherwise, $y_i = 0$ for $i \notin \mathcal{M}^I$. We denote $I(\boldsymbol{y}) := \{ i \in \mathcal{N} | \ y_i = 1 \ \text{ or } \ \exists j \in \mathcal{N} : y_j = 1, \forall l \in \mathcal{E}^u \}$ for all zero injection nodes and associated dominated nodes, where an associated dominated node for node *i* refer to a dominated non-zero injection node on a branch *l* := (*i*,*j*) whose the other side node *j* is a zero injection node with $y_i = 1$. And $P(\boldsymbol{z}) := \{ i \in \mathcal{N} | \ z_i = 1 \ \text{ or } \ \exists j \in \mathcal{N} : z_j = 1, \forall l \in \mathcal{E}^u \}$ for all D-PMU nodes and associated dominated nodes, where an associated dominated node for node *i* indicates a dominated node on a branch *l* := (*i*,*j*) whose the other side node *j* is a D-PMU node with $z_j = 1$.

In order to understand $P(\boldsymbol{z})$ and $I(\boldsymbol{y})$, the decision vector is encoded by binary variables as z for D-PMUs in the dimension $|\mathcal{N}| \times 1$. The vector y is the auxiliary binary-based decision variable vector for zero injection nodes in the dimension $|\mathcal{N}| \times 1$. Mathematically, we express as

$$z_i = 0, \quad \forall i \notin \mathcal{M}^P, \quad z_j \in \{0,1\} \quad \forall j \in \mathcal{M}^P \tag{4.4}$$

$$y_i = 0, \quad \forall i \notin \mathcal{M}^I, \quad y_k = 1, \quad \forall k \in \mathcal{M}^k, \quad y_j \in \{0,1\} \quad \forall j \in \mathcal{M}^I \tag{4.5}$$

For the graph $\mathcal{G}$, it is clear that $P(z) \cup I(y) = \mathcal{N}$ should hold, where

$$P(z) = \{ i \in \mathcal{N} || \, z_i = 1 \text{ or } \exists k \in \mathcal{N} : z_k = 1, (i,k) \in \mathcal{E} \} \tag{4.6}$$

$$I(y) = \{ i \in \mathcal{N} || \, y_i = 1 \text{ or } \exists j \in \mathcal{N} : y_j = 1, (i,j) \in \mathcal{E} \} \tag{4.7}$$

These two sets can be illustrated for node *i* in Fig. 4.4 (a) and (b).

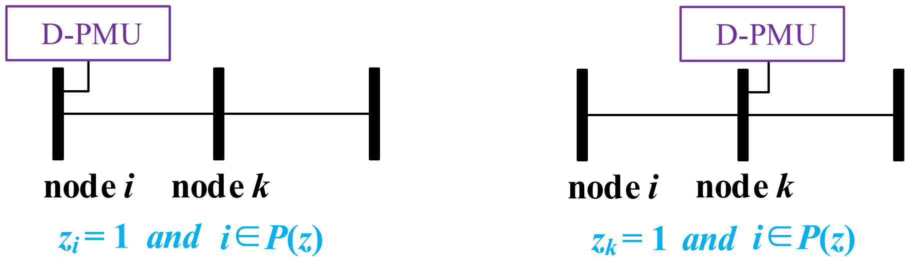

(a) Illustration of set $P(\boldsymbol{z})$

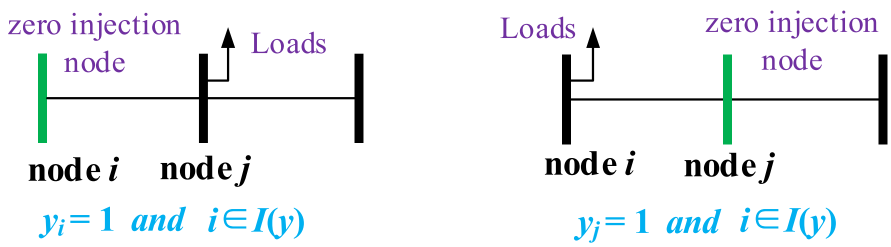

(b) Illustration of set $I(\boldsymbol{y})$

Fig. 4.4 Illustration of sets $P(\boldsymbol{z})$ and $I(\boldsymbol{y})$

For Fig. 4.4(a), $i \in P(z)$ holds according to (4.6) if a D-PMU unit is active at node i (i.e., $z_i = 1$) or a D-PMU unit is active at adjacent node k (i.e., $z_k = 1$). For Fig. 4.4(b), if node i has zero injection with $y_i = 1$, or adjacent node j as zero injection with $y_j = 1$, then $i \in I(y)$ according to (4.7).

Clearly, $P(\boldsymbol{z}) \cup I(\boldsymbol{y}) = \mathcal{N}$ should hold for arbitrary reconfiguration of ADNs; otherwise this topological observability condition does not stand [30]. This is becuase power flows of arbitrary node can be observed directly by a D-MPU unit or when an adjacent node is a zero injection bus. We illustrate this point from a 6-node system in Fig. 4.5 where node 1 has D-PMU unit and node 2 is a zero injection bus with y_2=1.

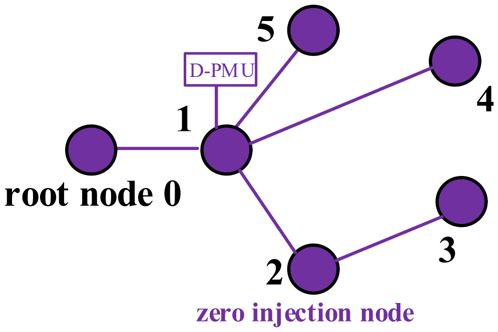

Fig. 4.5 Illustration of $P(z) \cup I(y) = \mathcal{N}$

In this example, it is clear that $P(z) = \{0,1,2,4,5\}$ and $I(y) = \{1,2,3\}$, and then $P(z) \cup I(y) = \{0,1,2,3,4,5\} = \mathcal{N}$. Under this condition $P(z) \cup I(y) = \mathcal{N}$, we incorporate an auxiliary binary variable $w_{ij}^l = 1$ for the branch l := (i,j) if the adjacent node *j* is dominated by the zero injection node *i*; otherwise $w_{ij}^l = 0$. Following [31], we express the connectivity constraints to formulate (4.2b):

$$z_i + \sum_{k:(i,k)\in\mathcal{E}^u} z_k + \sum_{j\in\mathcal{N}} \left(w_{ij}^l \cdot u_{ij}^l \right) \geq 1, \quad \forall i \in \mathcal{M}^P \tag{4.8a}$$

$$\sum_{i\in\mathcal{N}} \left(w_{ij}^l \cdot u_{ij}^l \right) \leq y_j, \quad \forall j \in \mathcal{M}^I \tag{4.8b}$$

where (4.8a) represents the connectivity constraint of the graph $\mathcal{G}$ such that $P(\boldsymbol{z}) \cup I(\boldsymbol{y}) = \mathcal{N}$; and (4.8b) states that among all active branches adjacent to an arbitrary zero injection node *i*, there is at most one adjacent branch whose other side node *j* can be dominated by node *i*.

Since (4.8a) and (4.8b) are established on reconfigurable ADNs marked by $\mathcal{E}^u$ and also have nonlinear terms w_{ij}^l u_{ij}^l, we equivalently relax them as a set of linear constraints with the auxiliary variables $m_{ij}^l = w_{ij}^l \cdot u_{ij}^l$ and $e_k = z_k \cdot u_{ik}^l$ using McCormick linearization method [100], where $m_{ij}^l, e_k \in \{0,1\}$:

$$m_{ij}^l \leq w_{ij}^l, \quad m_{ij}^l \leq u_{ij}^l, \quad e_k \leq z_k, \quad e_k \leq u_{ik}^l \tag{4.9a}$$

$$m_{ij}^l \geq w_{ij}^l + u_{ij}^l - 1, \quad e_k \geq z_k + u_{ik}^l - 1 \tag{4.9b}$$

Therefore, the linear formulation of disjunctive RCDS constraint consists of:

$$\begin{cases} z_i + \sum_{k:(i,k)\in\mathcal{E}} e_k + \sum_{j\in\mathcal{N}} m_{ij}^l \geq 1, \quad \forall i \in \mathcal{M}^P \\ \sum_{i\in\mathcal{N}} m_{ij}^l \leq y_j, \quad \forall j \in \mathcal{M}^I \\ \sum_{i\in\mathcal{M}^P} z_i \geq z^g \\ m_{ij}^l \leq w_{ij}^l, \quad m_{ij}^l \leq u_{ij}^l, \quad e_k \leq z_k, \quad e_k \leq u_{ik}^l \\ m_{ij}^l \geq w_{ij}^l + u_{ij}^l - 1, \quad e_k \geq z_k + u_{ik}^l - 1 \end{cases} \tag{4.10}$$

4.5 Observability Defense-Constrained DNR Formulation

For the sake of the minimal power loss in reconfigurable ADNs, the set of optimization variables involves a set of operation variables $\boldsymbol{x}_c^l := \left[\boldsymbol{P}^l, \boldsymbol{Q}^l, \ell^l, \boldsymbol{v}, \boldsymbol{Q}^{cr}, \boldsymbol{\beta}^l\right]^T, \boldsymbol{x}_c^l \in \mathbb{R}$, where $\boldsymbol{P}^l$ and $\boldsymbol{Q}^l$ refer to the vectors of sending-end active and reactive power flows; ℓ^l is the vector of squared current on branches; $\boldsymbol{v}$ is the vector of squared voltage profiles; $\boldsymbol{Q}^{cr}$ is the vector of nodal reactive power compensation; and $\boldsymbol{\beta}^l$ denotes the continuous parent-child relationship variable. For the proposed defense-constrained DNR model, a binary variable vector $\boldsymbol{x}_d^l := \left[\boldsymbol{u}^l, \boldsymbol{z}, \boldsymbol{y}, \boldsymbol{w}^l, \boldsymbol{m}^l, \boldsymbol{e}\right]^T, \boldsymbol{x}_d^l \in \mathbb{Z}$, is also included. Now, we express this DNR problem using the DCHR approach in the Chapter 3. By assuming that ADNs have sufficient D-PMUs, we can enable this defense-constrained DNR model as a MISOCP problem subject to system operational constraints $h(\boldsymbol{u}^l) \leqslant 0$ denoted by (4.11b)-(4.11l) and the disjunctive RCDS constraint denoted by (4.11m)-(4.11q) and spanning tree constraints for radiality $\psi(\boldsymbol{u}^l) = 0$ by (4.11r)-(4.11s).

It should be noted that the defense cost of zero injection nodes is zero. Hence, the minimum defense cost is with respect to D-PMUs. Since the number of D-PMUs is proportional to the consumption of decryption service and shared channel resources, this number of D-PMUs equivalently represents the minimum defense cost function. From the perspective of cyber-physical security, the minimum power loss P_{loss} can be subject to the distribution topology with the minimum cost of observability defense. To scale the physical units, we define c_1 and c_2 as coefficients with units \$ and \$/p.u. for defense cost $\sum_{i\in\mathcal{N}} z_i$ and power loss P_{loss}, respectively. In this study, we select c_1 = c_2 = 1, since P_{loss} per unit is generally less than 1 and $\sum_{i\in\mathcal{N}} z_i$ for positive integers starting from 1. Then, the weighted sum (4.11a) can be used to achieve the minimum $\sum_{i\in\mathcal{N}} z_i$ in priority, and then obtain the minimal power loss P_{loss}. With the observability defense constraint (4.10) and achievable z_g, the DNR model can be formulated as a MISOCP problem:

$$\min_{\boldsymbol{x}_c^l\in\mathbb{R},\boldsymbol{x}_d^l\in\mathbb{Z}} \quad P_{\text{loss}} + \sum_{i\in\mathcal{N}} z_i \tag{4.11a}$$

$$\text{s.t.} -\boldsymbol{P}^g + \boldsymbol{P}^d = \boldsymbol{A}^T\boldsymbol{P}^l - \boldsymbol{D}_r\ell^l \tag{4.11b}$$

$$-\boldsymbol{Q}^g - \boldsymbol{Q}^{cr} + \boldsymbol{Q}^d = \boldsymbol{A}^T\boldsymbol{Q}^l - \boldsymbol{D}_x\ell^l \tag{4.11c}$$

$$\frac{1}{\overline{v}-\underline{v}}\cdot\boldsymbol{A}\cdot\boldsymbol{v} - \frac{1}{\overline{v}-\underline{v}}\cdot(2\boldsymbol{D}_r\boldsymbol{P}^l + 2\boldsymbol{D}_x\boldsymbol{Q}^l - |\boldsymbol{z}^l|^2\,\ell^l) - \boldsymbol{\beta}_{ji}^l \geq -1 \tag{4.11d}$$

$$\frac{1}{\overline{v}-\underline{v}}\cdot\boldsymbol{A}\cdot\boldsymbol{v} - \frac{1}{\overline{v}-\underline{v}}\cdot(2\boldsymbol{D}_r\boldsymbol{P}^l + 2\boldsymbol{D}_x\boldsymbol{Q}^l - |\boldsymbol{z}^l|^2\,\ell^l) - \boldsymbol{\beta}_{ij}^l \geq -1 \tag{4.11e}$$

$$\frac{1}{\overline{v}-\underline{v}}\cdot\boldsymbol{A}\cdot\boldsymbol{v} - \frac{1}{\overline{v}-\underline{v}}\cdot(2\boldsymbol{D}_r\boldsymbol{P}^l + 2\boldsymbol{D}_x\boldsymbol{Q}^l - |\boldsymbol{z}^l|^2\,\ell^l) + \boldsymbol{u}_{ij}^l \leq 1 \tag{4.11f}$$

$$(1-\boldsymbol{\beta}_{ji}^l)(\underline{v}-\overline{v}) \leq \boldsymbol{A}\cdot\boldsymbol{v} \leq \boldsymbol{\beta}_{ji}^l(\overline{v}-\underline{v}),\ \boldsymbol{\beta}_{ij}^l(\underline{v}-\overline{v}) \leq \boldsymbol{A}\cdot\boldsymbol{v} \leq (1-\boldsymbol{\beta}_{ij}^l)(\overline{v}-\underline{v}) \tag{4.11g}$$

$$\ell^l = \ell_+^l + \ell_-^l,\ 0 \leq \ell_+^l \leq \boldsymbol{\beta}_{ij}^l\overline{\ell}^l, 0 \leq \ell_-^l \leq \boldsymbol{\beta}_{ji}^l\overline{\ell}^l \tag{4.11h}$$

$$0 \le 2\boldsymbol{D_r P^l} + 2\boldsymbol{D_x Q^l} - |\boldsymbol{z^l}|^2 \ell^l \le (\bar{v} - \underline{v}) \cdot \boldsymbol{\beta}_{ji}^l \tag{4.11i}$$

$$(\underline{v} - \bar{v}) \cdot \boldsymbol{\beta}_{ij}^l \le 2\boldsymbol{D_r P^l} + 2\boldsymbol{D_x Q^l} - |\boldsymbol{z^l}|^2 \ell^l \le 0 \tag{4.11j}$$

$$\left|\boldsymbol{P}^l\right|^2 + \left|\boldsymbol{Q}^l\right|^2 \le \boldsymbol{D}_v \cdot \ell^l, \quad -B \cdot \boldsymbol{u}^l \le \boldsymbol{P}^l, \boldsymbol{Q}^l \le B \cdot \boldsymbol{u}^l \tag{4.11k}$$

$$\underline{\boldsymbol{v}} \le \boldsymbol{v} \le \bar{\boldsymbol{v}}, \quad 0 \le \ell^l \le \bar{\ell}^l, \quad \underline{\boldsymbol{Q}}_{cr} \le \boldsymbol{Q}^{cr} \le \bar{\boldsymbol{Q}}_{cr} \tag{4.11l}$$

$$z_i + \sum_{k:(i,k)\in\mathcal{E}} e_k + \sum_{j\in\mathcal{N}} m_{ij}^l \ge 1, \quad \forall i \in \mathcal{M}^P \tag{4.11m}$$

$$\sum_{i\in\mathcal{N}} m_{ij}^l \le y_j, \quad \forall j \in \mathcal{M}^I \tag{4.11n}$$

$$\sum_{i\in\mathcal{M}^P} z_i \ge z^g \tag{4.11o}$$

$$m_{ij}^l \le w_{ij}^l, \quad m_{ij}^l \le u_{ij}^l, \quad e_k \le z_k, \quad e_k \le u_{ik}^l \tag{4.11p}$$

$$m_{ij}^l \ge w_{ij}^l + u_{ij}^l - 1, \quad e_k \ge z_k + u_{ik}^l - 1 \tag{4.11q}$$

$$\beta_{ij}^l + \beta_{ji}^l = u_{ij}^l, \quad \beta_{ij}^l = 0, \quad \text{if} \quad i = 0 \tag{4.11r}$$

$$\sum_{j:(i,j)\in\mathcal{E}} \beta_{ij}^l = 1, \forall i \in \mathcal{N} \setminus 0, \quad 0 \le \beta_{ij}^l \le 1, \forall l \in \mathcal{E} \tag{4.11s}$$

where P_{loss} is the active power loss of ADNs and the root node is 0. M is the big positive number. $\boldsymbol{P}^g$, $\boldsymbol{Q}^g$ and $\boldsymbol{P}^d$, $\boldsymbol{Q}^d$ indicate the vectors of given nodal active and reactive power injections and active and reactive loads at nodes. $\boldsymbol{A}$ is a $|\mathcal{E}|$ by $|\mathcal{N}|$ branch-node incidence matrix. $\boldsymbol{D}_r$, $\boldsymbol{D}_x$ and $\boldsymbol{D}_z$ indicate the diagonal matrices whose diagonal elements are the resistance vector, the reactance vector and the squared impedance modulus vector, respectively. $\boldsymbol{D}_v$ is the diagonal matrix whose diagonal elements are squared voltage profiles $\boldsymbol{v}$ of the sending nodes for all branches. B refers to the rated branch capacity. $\underline{\boldsymbol{Q}}_{cr}$, $\bar{\boldsymbol{Q}}_{cr}$, $\underline{\boldsymbol{v}}$, $\bar{\boldsymbol{v}}$, $\bar{\ell}^l$ represents the boundaries of $\boldsymbol{Q}^{cr}$, $\boldsymbol{v}$ and ℓ^l, respectively.

4.6 Case Study

The *IEEE* 16-node, 33-node, 123-node, and 1060-node distribution systems with a few DERs are used for tests. We have highlighted our RCDs solutions for the *IEEE* 33-node and 123-node DNs. With given zero injection nodes {3, 11, 18, 20, 24} for the *IEEE* 33-node system, the corresponding minimum RCDS solution $\mathcal{D}^*$ ={1, 2, 7, 10, 14, 16, 25, 28, 31} is displayed in Fig. 4.6, where solid and dashed lines refer to switch-on and switch-off status, respectively.

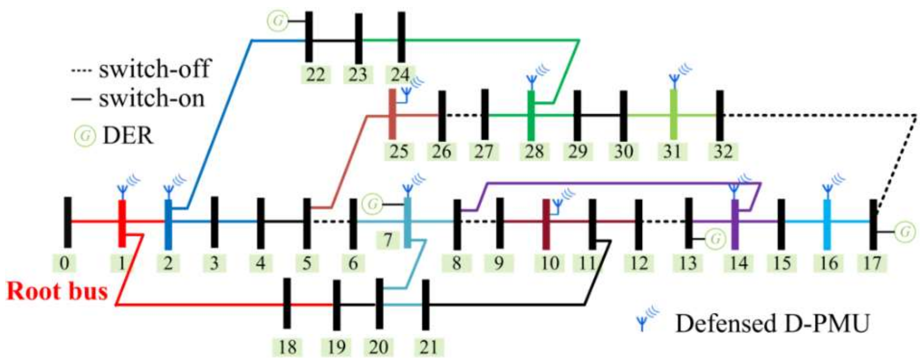

Fig.4.6. Minimal RCDS solution $\mathcal{D}^*$ of *IEEE* 33-node system

In terms of the *IEEE* 123-node ADN, the zero injection nodes are given as {3, 8, 14, 15,18, 21, 23, 25, 26 ,27, 44, 40, 54, 57, 61, 67, 72, 78, 81, 89, 91, 93, 97, 101, 105, 108, 110, 115, 116, 117, 119, 120, 121, 122} and the minimum RCDS solution $\mathcal{D}^*$ ={5, 8, 13, 14, 15, 19, 21, 25, 29, 31, 35, 38, 42, 47, 50, 52, 54, 55, 58, 60, 63, 65, 68, 70, 72, 74, 76, 78, 82, 84, 87, 89, 94, 95, 97, 99, 103, 106, 108, 110, 113, 123} as presented in Fig. 4.7.

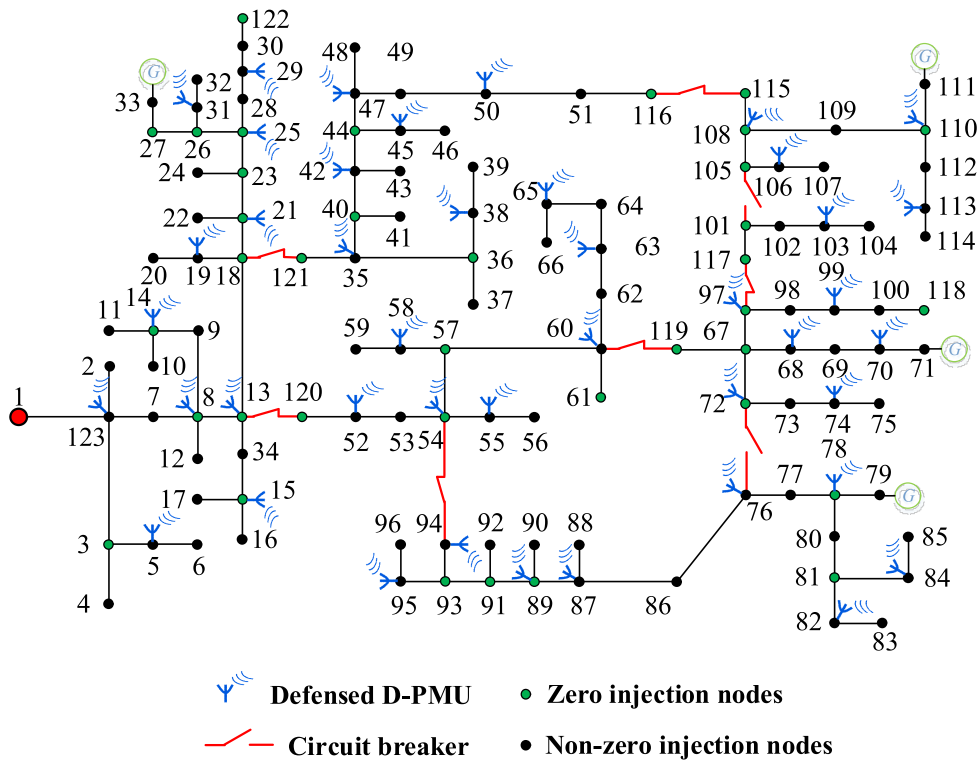

Fig. 4.7 Minimal RCDS solution $\mathcal{D}^{t*}$ of *IEEE* 123-node system.

In Fig. 4.6, the color-coded solid edges of $\mathcal{E}^{u}[\mathcal{D}^{*}]$ indicate that the graph ($\mathcal{N},\mathcal{E}^{u}[\mathcal{D}^{*}]$) is connected. Similarly to Fig. 4.6, Fig. 4.7 presents the optimal locations of defensed D-PMU units, which means every branch flow can be observable under defensed D-PMUs at dominated node set $\mathcal{D}^{*}$. These simulation results of two test systems demonstrate that our proposed observability defense-constrained DNR approach is effective for the power loss minimization subject to the full observability of ADNs.

To compare the total cost, we employ the DNR models with the low and the high penetrations of D-PMUs, respectively. Table 4.1 shows the power loss cost of the conventional DNR model without D-PMUs (p.u.), the observability defense cost and the corresponding power loss cost (p.u.), and CPU time (in seconds) for two penetration rates of D-PMUs.

Table 4.1 Optimal observability defense-constrained DNR solutions

DNs	DNR Loss	Cost of Low D-PMUs				Cost of High D-PMUs			
		z^g	Defense	Loss	Time	z^g	Defense	Loss	Time
16-node	0.0302	5	6	0.0323	0.521	5	5	0.0318	0.500
33-node	0.0542	9	11	0.0594	2.368	9	9	0.0586	1.719
123-node	0.0995	35	41	0.1029	175.542	35	35	0.0995	151.024
1060-node	0.1404	45	59	0.1823	225.032	45	45	0.1409	179.078

For these exhibited cases, our proposed observability defense-constrained DNR solution with the low and the high penetrations of D-PMUs successfully achieves the complete system observability status in four test systems. The distinction between them is the different total cost. The defense cost and power loss cost for the high penetration of D-PMUs is much lower than the one for the low penetration of D-PMUs. This is because more D-PMUs locations lead to a larger feasible space for the DNR optimization. For this reason, the defense cost is equal to z^g for test systems with the high penetration of D-PMUs. This demonstrates that the proposed DNR model seeks the minimum defense cost in priority and then pursues the minimal power loss cost. This is also why the minimal power loss cost is generally larger than the power loss cost of pure DNR model. In contrast, if the feasible space is minor, then the optimal cost would be larger for test systems with the low penetration of D-PMUs. Additionally, the proposed DNR model involves the tighter bound in (4.3), which induces the desirable computational efficiency in terms of CPU time for two case studies.

4.7 Summary

This chapter proposes a disjunctive RCDS formulation for reconfigurable networks with the least defense cost in theory. With this formulation, an observability defense-constrained DNR model can be constructed as a MISOCP problem. As demonstrated in case studies, this observability defense-constrained DNR model perfectly enables an observable DNR solution just with the minimal defense cost and active power loss for cyber–physical system security enhancement.

Chapter 5

A Consensus ADMM-based Differentially Private Topology Optimization Approach for Privacy Preservation Enhancement of Multi-Agent Active Distribution Networks

The topology switch for the loss minimization may expose the private load change information of an agent, e.g., transition from a light load to a heavy load, in interconnected ADNs managed by multiple agents. To address this issue, this paper proposes a DP-DNR mechanism based on the C-ADMM algorithm. This can tackle privacy leakage challenges on the agent's and customer's levels. To suppress private load change leakage as an agent's concern, this DP-DNR mechanism provides a mixture output of realistically optimal topology switch status and corresponding obfuscated-but-feasible load flows, part of which may have reverse load flow directions. On the customer's level, the C-ADMM-based decentralized DP-DNR approach can seek the optimal topology switch without customer's load datasets of agents, whilst exchanged communication signals in C-ADMM algorithm are also synthetic based on the proposed DP-DNR mechanism.

5.1 Differential Privacy Theory

Differential privacy protects statistical or real-time data by adding desirable amount of noise along with maintaining a healthy trade-off between privacy and accuracy. This process can be illustrated in Fig. 5.1. The protection of complete data from database can be achieved by DP; otherwise unprotected data can be analyzed or inferred by doing analyst query attacks.

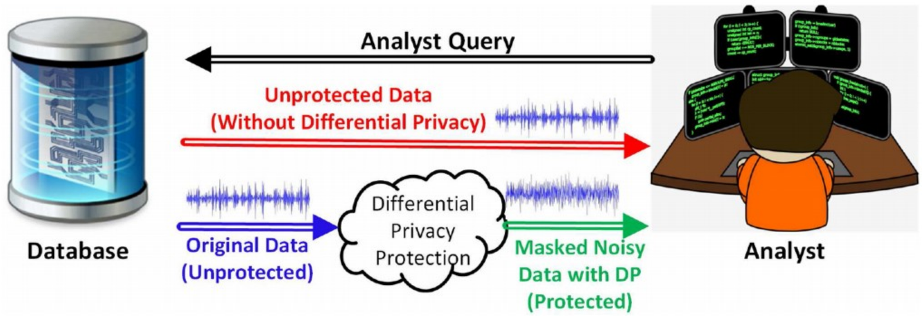

Fig. 5.1 Data output with DP preservation and without DP preservation.

Accoding to DP theory, DP guarantees for optimization datasets are achieved through randomization. Thus, when answering optimization queries, the DP-based mechnism is to make adjacent optimization datasets statistically similar. Suppose $\tilde{x}(d)$ be a randomized counterpart of optimization map $x(d)$, and two datasets d', d are adjacent with the Euclidean distance $\| d-d' \| \leqslant \alpha$ bounded by some prescribed parameter $\alpha \geq 0$. By [51], we have the formal definition of DP:

Definition 5.1 (*Differential privacy*). A random optimization map $\tilde{x}$: $\mathbb{D} \rightarrow \mathbb{X}$ is (ε, δ)−differentially private if $\forall \hat{x} \in \mathbb{X}$ and $\forall \boldsymbol{d}, \boldsymbol{d'} \in \mathbb{D}$ satisfying $\| d-d' \| \leqslant \alpha$ for some $\alpha > 0$, it holds that

$$\Pr[\tilde{x}(d)=\hat{x}] \leqslant \Pr\left[\tilde{x}(d')=\hat{x}\right]\exp(\varepsilon)+\delta \tag{5.1}$$

where probability **Pr** is taken over randomness of $\tilde{x}$.

According to this definition, the probabilities of observing the same optimization result on adjacent datasets are similar up to parameters $\varepsilon > 0$, termed *privacy loss*, and $\delta > 0$, termed *probability of failure*. Accordingly, $\tilde{x}(\boldsymbol{d})$ and $\tilde{x}(\boldsymbol{d'})$ are statistically similar if parameters ε and δ take smaller values. In other words, smaller parameters ε and δ can have the stronger privacy preservation.

Definition 5.2 (Output perturbation). For dataset universe $\mathbb{D} \subset \mathbb{R}^k$, the output perturbation is $x(\boldsymbol{d}) + \hat{\zeta}$ with perturbation $\hat{\zeta}$, where Δ_1 is the worst-case ℓ_1−sensitivity of the map to adjacent datasets.

Definition 5.3 (Input perturbation). For dataset universe $\mathbb{D} \subset \mathbb{R}^k$, the input perturbation is twofold: data perturbation $\tilde{d} = d + \zeta$ with perturbation ζ, where Δ_1 is the worst-case ℓ_1−sensitivity of an identity query to adjacent datasets, is followed by the map $x(\tilde{d})$.

Proposition 5.1 The output and input perturbation strategies are (ε, 0)-differentially private. Both strategies directly extend to (ε, δ)-differential privacy by choosing the Laplace distribution of random perturbations calibrated to ℓ_2−sensitivities.

5.2 Non-Private DNR Formulation

The DNs are considered as a connected undirected tree $\mathcal{G} = (\mathcal{N}, \mathcal{E})$, where $\mathcal{N}$ is the set of nodes and $\mathcal{E}$ is the set of branches and the set of root nodes is S. Suppose that an arbitrary branch $l := (m,n), \forall l \in \mathcal{E}$ is between nodes (m,n) and the root node is assumed as 0. The simplified DNR model is based on the linearized *DistFlow* equations, which is cast as a mixed-integer quadratic programming (MIQP) problem.

The set of optimization variables involves a set of operational variables $\boldsymbol{x}^l := \left[\boldsymbol{P}^l, \boldsymbol{Q}^l, \boldsymbol{Q}^{cr}, \boldsymbol{\beta}^l\right]^T$, switch status indicator variables $\boldsymbol{u}^l \in \mathbb{Z}^{|\mathcal{E}|}$. In this vein, $\boldsymbol{P}^l \in \mathbb{R}^{|\mathcal{E}|}$ and $\boldsymbol{Q}^l \in \mathbb{R}^{|\mathcal{E}|}$ refer to the vectors of sending-end active and reactive power flows. $\boldsymbol{Q}^{cr} \in \mathbb{R}^{|n_{cr}|}$ is the vector of nodal reactive power compensation and n_{cr} is the number of capacitors. $\boldsymbol{\beta}^l \in \mathbb{R}^{2|\mathcal{E}|}$ are continuous parent-child relationship variables. $\boldsymbol{\beta}^l$ are constructed with spanning tree constraints. For convenience, we express the MIQP-based DNR model in following form:

$$\min_{\boldsymbol{x}^l \in \mathbb{R}, \boldsymbol{u}^l \in \mathbb{Z}} \begin{bmatrix} \boldsymbol{P}^l \\ \boldsymbol{Q}^l \end{bmatrix}^T \begin{bmatrix} \boldsymbol{D}_r & \boldsymbol{0}_{|\mathcal{E}|\times|\mathcal{E}|} \\ \boldsymbol{0}_{|\mathcal{E}|\times|\mathcal{E}|} & \boldsymbol{D}_r \end{bmatrix} \begin{bmatrix} \boldsymbol{P}^l \\ \boldsymbol{Q}^l \end{bmatrix} \tag{5.3a}$$

$$\text{s.t.} \begin{bmatrix} \boldsymbol{A}^T & \boldsymbol{0}_{|\mathcal{E}|\times|\mathcal{E}|} & \boldsymbol{0}_{|\mathcal{E}|\times n_{cr}} \\ \boldsymbol{0}_{|\mathcal{E}|\times|\mathcal{E}|} & \boldsymbol{A}^T & \boldsymbol{A}_{cr} \end{bmatrix} \begin{bmatrix} \boldsymbol{P}^l \\ \boldsymbol{Q}^l \\ \boldsymbol{Q}^{cr} \end{bmatrix} = \begin{bmatrix} -\boldsymbol{P}^g + \boldsymbol{P}^d \\ \boldsymbol{Q}^g + \boldsymbol{Q}^d \end{bmatrix} \tag{5.3b}$$

$$2\boldsymbol{D}_r\boldsymbol{P}^l + 2\boldsymbol{D}_x\boldsymbol{Q}^l - (1-\boldsymbol{u}^l)M \le \boldsymbol{A}v \le 2\boldsymbol{D}_r\boldsymbol{P}^l + 2\boldsymbol{D}_x\boldsymbol{Q}^l + (1-\boldsymbol{u}^l)M \tag{5.3c}$$

$$-\boldsymbol{u}^l M \le \boldsymbol{P}^l, \boldsymbol{Q}^l \le \boldsymbol{u}^l M, \quad \underline{\boldsymbol{v}} \le \boldsymbol{v} \le \overline{\boldsymbol{v}}, \quad \underline{\boldsymbol{Q}}^{cr} \le \boldsymbol{Q}^{cr} \le \overline{\boldsymbol{Q}}^{cr} \tag{5.3d}$$

$$\beta^l_{mn} + \beta^l_{nm} = u^l_{mn}, \quad \beta^l_{mn} = 0, \text{ if } m = S \tag{5.3e}$$

$$\sum_{n:(m,n)\in\mathcal{E}} \beta^l_{mn} = 1, \quad \forall m \in \mathcal{N} \setminus S \tag{5.3f}$$

$$0 \leqslant \beta^l_{mn} \leqslant 1, \quad \forall l \in \mathcal{E} \tag{5.3g}$$

where (5.3a) states the quadratic active power loss of DNs under the assumption of flat voltage profiles for all nodes. M refers to the big positive number and Γ denotes the branch capacity. $\boldsymbol{P}^g, \boldsymbol{Q}^g$ and $\boldsymbol{P}^d, \boldsymbol{Q}^d$ indicate the vectors of given nodal active and reactive power injections and active and reactive loads at nodes. $\boldsymbol{A}$ is a $|\mathcal{E}|$ by $|\mathcal{N}|$ branch-node incidence matrix and $\boldsymbol{A}_{cr}$ is a diagonal matrix whose i-th diagonal element is equal to 1 if node i has the reactive compensation capacitors; otherwise it is zero. $\boldsymbol{D}_r$ and $\boldsymbol{D}_x$ indicate the diagonal matrices whose diagonal elements are the resistance and reactance vectors, respectively. Γ refers to the rated branch capacity. $\underline{\boldsymbol{Q}}_{cr}, \overline{\boldsymbol{Q}}_{cr}, \underline{v}$ and $\overline{v}$ represent the boundaries of $\boldsymbol{Q}^{cr}$ and $\boldsymbol{v}$, respectively.

Therefore, we can summarize $\boldsymbol{c},\boldsymbol{A},\boldsymbol{G}_v,\boldsymbol{d},\boldsymbol{G}_{cr},\boldsymbol{b}_v,\boldsymbol{b}_{cr},\boldsymbol{K}$ and $\boldsymbol{h}$ from (5.3e)-(5.3g). To avoid heavy notions, we express the general mathematical formulation of a non-private DNR model in the MIQP form with respect to operational variables $\boldsymbol{x}^l$ including active/reactive power flow variables and reactive power compensation variables, continuous parent-child relationship variables $\boldsymbol{\beta}^l$ and switch status indicator variables $\boldsymbol{u}^l$. We summarize this MIQP-based non-private DNR model below.

Non-Private DNR:
$$\min_{\boldsymbol{x}^l\in\mathbb{R},\boldsymbol{u}^l\in\mathbb{Z}} F_0=(\boldsymbol{x}^l)^T\boldsymbol{c}(\boldsymbol{x}^l) \tag{5.4a}$$
$$\text{s.t.}\mathcal{X}:=\left\{(\boldsymbol{x}^l,\boldsymbol{u}^l)\ \middle|\ \begin{array}{l}\tilde{\boldsymbol{A}}\boldsymbol{x}^l=\tilde{\boldsymbol{d}},\begin{bmatrix}\boldsymbol{G}_v\\ \boldsymbol{G}_u\end{bmatrix}\begin{bmatrix}\boldsymbol{x}^l\\ \boldsymbol{u}^l\end{bmatrix}\leqslant\begin{bmatrix}\boldsymbol{b}_v\\ \boldsymbol{b}_u\end{bmatrix},\boldsymbol{K}\begin{bmatrix}\boldsymbol{x}^l\\ \boldsymbol{u}^l\end{bmatrix}=\boldsymbol{h}\\ \boldsymbol{G}_{cr}\boldsymbol{x}^l\leq\boldsymbol{b}_{cr},\underline{\boldsymbol{x}}^l\leqslant\boldsymbol{x}^l\leqslant\overline{\boldsymbol{x}}^l\end{array}\right\} \tag{5.4b}$$

where $\mathcal{X}$ refers to the non-empty feasibility space and f denotes the approximate system power loss with a fixed diagonal matrix $\boldsymbol{c}$. The inequality in (5.4b) represents the voltage security constraints, physical ranges of reactive power compensation capacitors and topology-linked branch capacity constraints, which are marked by the subscripts v, cr and u for $\boldsymbol{G}$ and $\boldsymbol{b}$. The first and second equality denotes the system-wide load balance of DNs and radiality constraints.

5.3 Differentially Private DNR Formulation

5.3.1 Privacy Leakage Problem of Non-private DNR Model

Suppose that the realistic tie-switch status $\boldsymbol{u}^{l_t}$ and corresponding tie-line load flows $\boldsymbol{x}^{l_t}$ for an arbitrary tie-line l_t have to be shared with neighbor agents by a joint DSO. As stated, there exist agent's and customer's privacy concerns. As conflicting interests, different agents as stakeholders may bid for grid services such as demand response, which is dependent on operational topology as well as load flows of tie-lines. For agent's privacy concerns, sharing raw data of tie-lines between agents may cause privacy challenges, i.e., the private load change information may be exposed. On the customer's privacy-preserving level, since a joint DSO performs the DNR operation for the loss minimization of the entire interconnected ADNs, all load datasets from different agents are obliged to upload to the distribution dispatch center. This may increase the possibility of exposing sensitive load consumption of customers managed by an agent to adversaries who can further infer commercial behaviors or perform cyber-physical attacks.

We illustrate these two categories of privacy concerns in one example. For the agent's concerns, as shown in Fig. 5.2(a), four agents A-D with three normally-open tie-switches where each agent manages a specific ADN with one substation. If agent A has an heavily loading event while others have light loads displayed in the top layer of Fig. 5.2(a), an optimal DNR decision with the minimal power loss objective can be made to close on all tie-switches between agent A and others as shown in the middle layer. As observed, some heavy loads in agent A are transferred to neighborhood ADNs after switching off sectionalizing breakers, thus eliminating its overloading problem. However, these optimal DNR actions inadvertently exposes the substantial load increase of agent A, which can be easily inferred from this DNR actions and tie-line load flows. In energy market, suppose other agents such as B, C and D are malicious bidders against agent A, and it is inferred that some heavy loads in agent A have been transferred to other agents. Then, agents B, C and D can bid high prices for grid services, while agent A cannot win the contracts at the low price. Because they know that agent A has insufficient loads to respond this request. As such, a synthetic DNR solution with realistic tie-switch status can be against this load change information of agent A leaked by realistic DNR operations. As indicated in the third DP-DNR layer, as long as tie-line load flows and directions are obfuscated, the private load change information of agent A can be preserved. Moreover, for the customer's concerns, Fig. 5.2(b) exhibits that all agents' load datasets have to upload to the DSO who performs centralized DNR decisions. In contrast to centralized decisions, the decentralized mode can also seek optimal DNR decisions, but only with a few exchanged communication messages of boundary variables. Thus, the customer's privacy can be preserved.

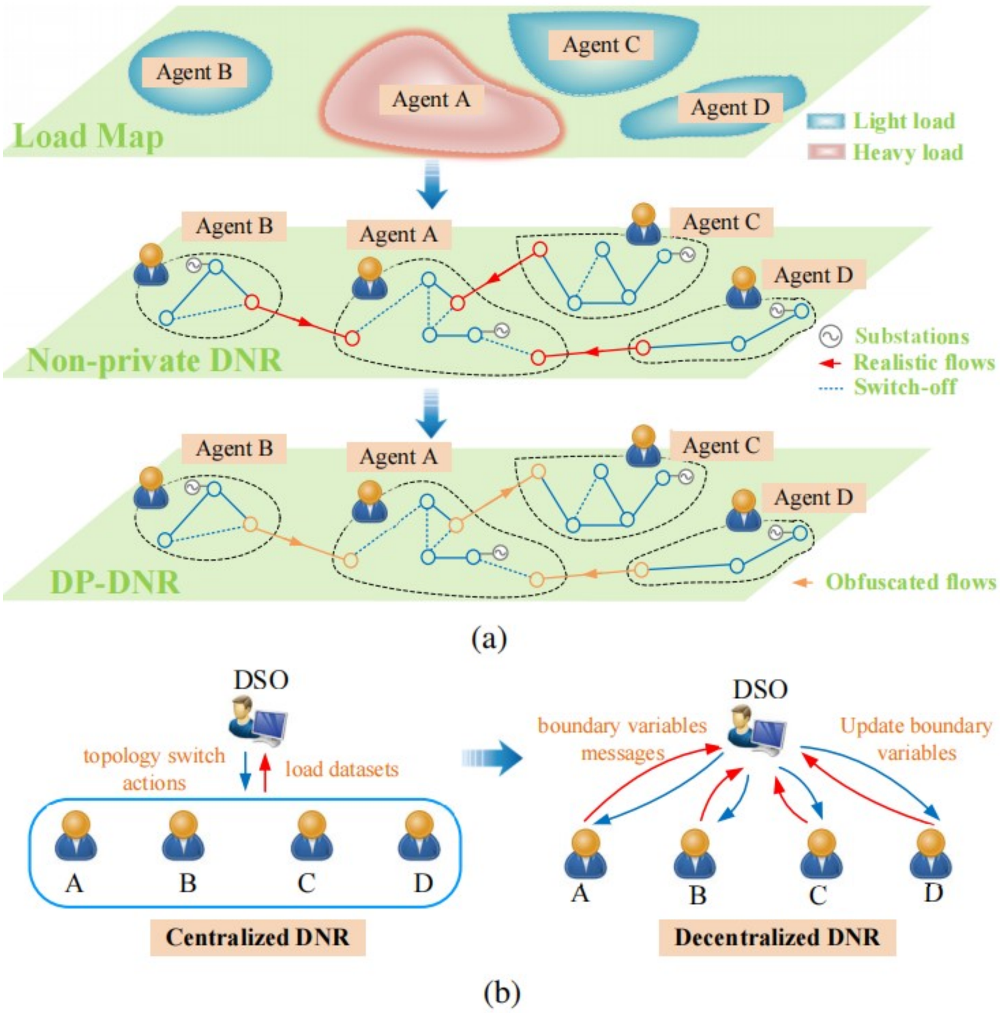

Fig. 5.2. (a) An exposure event of agent's privacy; (b) leakage of customer's privacy by centralized DNR model.

5.3.2 Privacy-Preserving Criteria For DP-DNR Mechanism

The well-known Laplace mechanism can be used to make queries over $\mathcal{X}$ differentially private via an effective DP-DNR mechanism $\tilde{\mathcal{M}}$ for $(\boldsymbol{x}^l, \boldsymbol{u}^l)$. This DP-DNR mechanism $\tilde{\mathcal{M}}$ should output obfuscated-but-feasible tie-line load flows $\boldsymbol{x}^{l_t}$ from $\boldsymbol{x}^l$ and realistically optimal topology variables $\boldsymbol{u}^l$. To do this, we aim to realize the following framework of this DP-DNR mechanism $\tilde{\mathcal{M}}$:

$$\min_{\boldsymbol{x}^l \in \mathbb{R}, \boldsymbol{u}^l \in \mathbb{Z}} F_1 = \left(\boldsymbol{x}^l\right)^T \boldsymbol{c}\boldsymbol{x}^l \tag{5.5}$$

$$\text{s.t.}\quad \text{optimality of topology variables } \boldsymbol{u}^{l} \tag{5.6}$$

$$\text{feasibility of operational variables for } \boldsymbol{x}^{l_t} \tag{5.7}$$

where the objective function (5.6) represents the system loss of the entire interconnected ADNs. Constraint (5.7) enforces $\tilde{\mathcal{M}}$ to output realistically optimal topology solutions $\boldsymbol{u}^{l*}$ equal to the ones by the non-private DNR model. Constraint (5.8) denotes the operational constraints involving random perturbations, which can enable $\tilde{\mathcal{M}}$ to provide obfuscated-but-feasible tie-line load flows $\boldsymbol{x}^{l_t^*}$.

According to this framework, this DP-DNR mechanism $\tilde{\mathcal{M}}$ can be an ε-differential private algorithm based on the following Theorem:

Theorem 5.1 (*DP-DNR Mechanism*): Suppose random perturbations obey Laplace distribution $\xi^{l_t} \sim \mathbb{P}_\xi,\ \mathbb{P}_\xi := Lap(\Delta_\rho / \varepsilon)$, for an arbitrary tie-line $l_t \in \mathcal{T}$. And $\left(\hat{\boldsymbol{x}}^{l}, \boldsymbol{u}^{l*}\right) \in \mathcal{X}$ is the optimal solution of non-private DNR model. Then, the DP-DNR mechanism $\tilde{\mathcal{M}}$ can output a mixture of obfuscated-but-feasible operational variable solution $\boldsymbol{x}^{l_t^*}$ and realistically optimal topology solution $\boldsymbol{u}^{l*}$, such that $\hat{\boldsymbol{x}}^{l_t} = \boldsymbol{x}^{l_t^*} + \boldsymbol{\alpha}^{l_t^*}\xi^{l_t}$ for this tie-line l_t. This can be an ε-differential private algorithm. The proof is as follows:

Proof: According to the definition of Laplace mechanism, let the query output answers be $\mathcal{O} = \boldsymbol{x}^{l_t^*}$, and we alternatively rewrite this theorem in the definition of ε-differential privacy.

$$\mathbb{P}_\xi[\tilde{\mathcal{M}}(\boldsymbol{d}) = \mathcal{O}] \leqslant \mathbb{P}_\xi\left[\tilde{\mathcal{M}}\left(\boldsymbol{d}'\right) = \mathcal{O}\right] e^{\varepsilon} \tag{5.8}$$

for any two ρ-neighborhood load datasets $\boldsymbol{d}$ and $\boldsymbol{d}'$ and output solutions $\mathcal{O}$.

For convenience, we define $\boldsymbol{\xi}^{l}=\left[\xi^{l_1},\ldots,\xi^{l_n}\right]$, $\left\{\boldsymbol{\alpha}^{l_t}\right\}=\left[\alpha^{l_1},\ldots,\alpha^{l_n}\right]$, $\left\{\boldsymbol{x}^{l_t}\right\}=\left[x^{l_1},\ldots,x^{l_n}\right]$, where n refers to the total number of tie-lines. Thus, the query output $\{\mathcal{O}^{l_t}\}$ for all tie-lines $\forall l_t \in \mathcal{T}$, $\forall t=1,\ldots,n$, with the vectors of $\boldsymbol{\xi}^{l}$, can be written as

$$\mathcal{O}^{l_t}=\boldsymbol{x}^{l_t^*}=\hat{\boldsymbol{x}}^{l_t}-\boldsymbol{\alpha}^{l_t^*}\xi^{l_t}, \quad \forall t\in[1,n] \tag{5.9}$$

Therefore, the ratio of probabilities on two ρ-indistinguishable load datasets $\boldsymbol{d}$ and $\boldsymbol{d}'$ can be bounded by

$$\frac{\mathbb{P}_{\xi}\left[\tilde{\mathcal{M}}(\boldsymbol{d})=\mathcal{O}^{l_t}\right]}{\mathbb{P}_{\xi}\left[\tilde{\mathcal{M}}(\boldsymbol{d}')=\mathcal{O}^{l_t}\right]}=\frac{\mathbb{P}_{\xi}\left[\begin{bmatrix}\hat{\boldsymbol{x}}^{l_1}(\boldsymbol{d})\\ \vdots\\ \hat{\boldsymbol{x}}^{l_n^*}(\boldsymbol{d})\end{bmatrix}-\begin{bmatrix}\boldsymbol{\alpha}^{l_1^*}\\ \vdots\\ \boldsymbol{\alpha}^{l_n^*}\end{bmatrix}\begin{bmatrix}\xi^{l_1}\\ \vdots\\ \xi^{l_n}\end{bmatrix}=\begin{bmatrix}\mathcal{O}^{l_1}\\ \vdots\\ \mathcal{O}^{l_n}\end{bmatrix}\right]}{\mathbb{P}_{\xi}\left[\begin{bmatrix}\hat{\boldsymbol{x}}^{l_1}(\boldsymbol{d}')\\ \vdots\\ \hat{\boldsymbol{x}}^{l_n}(\boldsymbol{d}')\end{bmatrix}-\begin{bmatrix}\boldsymbol{\alpha}^{l_1^*}\\ \vdots\\ \boldsymbol{\alpha}^{l_n^*}\end{bmatrix}\begin{bmatrix}\xi^{l_1}\\ \vdots\\ \xi^{l_n}\end{bmatrix}=\begin{bmatrix}\mathcal{O}^{l_1}\\ \vdots\\ \mathcal{O}^{l_n}\end{bmatrix}\right]}=\frac{\mathbb{P}_{\xi}\left[\begin{bmatrix}\boldsymbol{\alpha}^{l_1^*}\xi^{l_1}\\ \vdots\\ \boldsymbol{\alpha}^{l_n^*}\xi^{l_n}\end{bmatrix}=\begin{bmatrix}\mathcal{O}^{l_1}-\hat{\boldsymbol{x}}^{l_1}(\boldsymbol{d})\\ \vdots\\ \mathcal{O}^{l_n}-\hat{\boldsymbol{x}}^{l_n}(\boldsymbol{d})\end{bmatrix}\right]}{\mathbb{P}_{\xi}\left[\begin{bmatrix}\boldsymbol{\alpha}^{l_1^*}\xi^{l_1}\\ \vdots\\ \boldsymbol{\alpha}^{l_n^*}\xi^{l_n}\end{bmatrix}=\begin{bmatrix}\mathcal{O}^{l_1}-\hat{\boldsymbol{x}}^{l_1}(\boldsymbol{d}')\\ \vdots\\ \mathcal{O}^{l_n}-\hat{\boldsymbol{x}}^{l_n}(\boldsymbol{d}')\end{bmatrix}\right]}$$

$$\overset{(i)}{=}\frac{\prod_{t=1}^{n}\boldsymbol{\alpha}^{l_t^*}\exp\left\{-\frac{\varepsilon\left\|\mathcal{O}^{l_t}-\hat{\boldsymbol{x}}^{l_t}(\boldsymbol{d})\right\|_2}{\Delta_\rho}\right\}}{\prod_{t=1}^{n}\boldsymbol{\alpha}^{l_t^*}\exp\left\{-\frac{\varepsilon\left\|\mathcal{O}^{l_t}-\hat{\boldsymbol{x}}^{l_t}(\boldsymbol{d}')\right\|_2}{\Delta_\rho}\right\}}=\prod_{t=1}^{n}\exp\left(\frac{\varepsilon\left\|\mathcal{O}^{l_t}-\hat{\boldsymbol{x}}^{l_t}(\boldsymbol{d}')\right\|_2-\varepsilon\left\|\mathcal{O}^{l_t}-\hat{\boldsymbol{x}}^{l_t}(\boldsymbol{d})\right\|_2}{\Delta_\rho}\right)$$

$$\overset{(ii)}{\leqslant}\prod_{t=1}^{n}\exp\left(\frac{\varepsilon\left\|\hat{\boldsymbol{x}}^{l_t}(\boldsymbol{d})-\hat{\boldsymbol{x}}^{l_t}\left(\boldsymbol{d}'\right)\right\|_2}{\Delta_\rho}\right)=\exp\left(\frac{\varepsilon\left\|\hat{\boldsymbol{x}}^{l}(\boldsymbol{d})-\hat{\boldsymbol{x}}^{l}\left(\boldsymbol{d}'\right)\right\|_2}{\Delta_\rho}\right)\overset{(iii)}{\leqslant}\exp\left(\frac{\varepsilon\Delta_\rho}{\Delta_\rho}\right)=e^{\varepsilon} \tag{5.10}$$

where (i) comes from the definition of the probability density function of the Laplace distribution. In (ii) step, it is followed by the inequailty of norms, i.e., $|a|-|b|\le|a-b|$ for any real-valued numbers a and b. For the (iii) step, $\left\|\hat{\boldsymbol{x}}^{l_t}(\boldsymbol{d})-\hat{\boldsymbol{x}}^{l_t}\left(\boldsymbol{d}'\right)\right\|_2$ denotes the l_2-sensitivity on ρ-indistinguishable input datasets $\hat{\boldsymbol{x}}^{l}(\boldsymbol{d})$ and $\hat{\boldsymbol{x}}^{l}(\boldsymbol{d}')$ subject to

$\left\|\hat{\boldsymbol{x}}^l(\boldsymbol{d})-\hat{\boldsymbol{x}}^l(\boldsymbol{d}')\right\|_2 \le \Delta\rho$. Accordingly, it is clear that (5.8) holds based on (5.10), which proves this Theorem. ■

Please note that $\boldsymbol{\alpha}^l$ represents a vector of recourse variables by the DP-DNR mechanism $\tilde{\mathcal{M}}$. For tie-lines, $\boldsymbol{\alpha}^{l_t} \in \left[-\overline{\boldsymbol{\alpha}}^l, \overline{\boldsymbol{\alpha}}^l\right]$ and $\boldsymbol{\alpha}^{l_b}=0$ for other internal branches $\{l_b\}$ in each agent, where $\varepsilon=\{l_b\}\cup\mathcal{T}$ holds. Therefore, we can express $\boldsymbol{x}^l+\boldsymbol{\alpha}^l\xi^l$ to represent the load flows of an arbitrary line $l\in\varepsilon$. The recourse function of $\boldsymbol{\alpha}^l$ is to scale the random perpetuation ξ^l in the program of DP-DNR mechanism, which will be discussed in the later context. Regarding synthetic solutions, we further propose two privacy-preserving criteria for shared tie-line load flow data, i.e., load flow quantity and direction obfuscations.

(1) Load flow quantity obfuscation

To obfuscate $\boldsymbol{x}^{l_t}$ with quantities, we incorporate a virtual power injection variable vector $\boldsymbol{g}, \boldsymbol{g}\in\mathbb{R}$, at boundary nodes of tie-lines, which aims to balance the random perturbations in tie-line load flows. Let $\boldsymbol{g}_m$ and $\boldsymbol{g}_n$ represent the virtual power injections at boundary nodes m and n for an arbitrary tie-line $l_t = \{m, n\}$. In Fig. 5.3(a) and (b), this tie-line is switch-on and the realistically optimal power flow direction is supposed to be $m\rightarrow n$, i.e., $\hat{\boldsymbol{x}}^{l_t}=\boldsymbol{d}_n > 0$, and the obfuscated load flow directions are displayed with a blue arrow ($m\rightarrow n$ or $n\rightarrow m$). The power flow equality at boundary nodes m and n is then formulated:

$$\boldsymbol{A}_m\boldsymbol{x}^l=\boldsymbol{d}_m-\boldsymbol{g}_m, \quad \boldsymbol{A}_n\boldsymbol{x}^l=\boldsymbol{d}_n-\boldsymbol{g}_n \tag{5.11}$$

$$\boldsymbol{g}_m=-\boldsymbol{\alpha}^{l_t}\xi^{l_t}, \quad \boldsymbol{g}_n=\boldsymbol{\alpha}^{l_t}\xi^{l_t}, \quad \boldsymbol{g}\in\left[-\overline{\boldsymbol{g}},\overline{\boldsymbol{g}}\right] \tag{5.12}$$

$$-\boldsymbol{u}^{l_t}\overline{\boldsymbol{\alpha}}^{l} \le \boldsymbol{\alpha}^{l_t} \le \boldsymbol{u}^{l_t}\overline{\boldsymbol{\alpha}}^{l} \tag{5.13}$$

where $\boldsymbol{A}_m$ and $\boldsymbol{A}_n$ refer to the m-th and n-th row of matrix $\boldsymbol{A}$, respectively. And $-\overline{\boldsymbol{g}}$ and $\overline{\boldsymbol{g}}$ are the lower and upper boundaries of $\boldsymbol{g}$. By constraint (5.13), the recourse variable $\boldsymbol{\alpha}^{l_t}$ is enforced to a zero if this tie-line l_t is switch-off by $\boldsymbol{u}^{l_t}=0$; otherwise, $\boldsymbol{\alpha}^{l_t}$ can be in the range of $\left[-\overline{\boldsymbol{\alpha}}^{l},\overline{\boldsymbol{\alpha}}^{l}\right]$. For a switch-on tie-line l_t, $\boldsymbol{\alpha}^{l_t}$ is incorporated to scale the random perpetuation ξ^{l_t} in constraints (5.12).

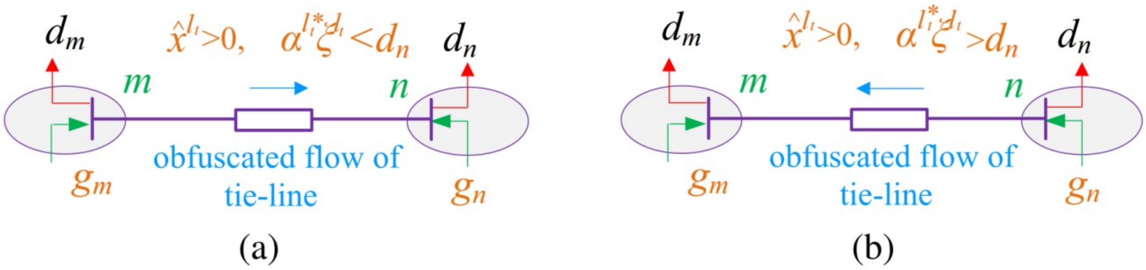

Fig. 5.3. (a) Realistic flow $m \rightarrow n$; (b) reversed flow $n \rightarrow m$.

Indeed, if $\boldsymbol{u}^{l_t^*}=1$ holds for tie-line l_t, then non-zero virtual injections $\boldsymbol{g}_m$ and $\boldsymbol{g}_n$ through constraints (5.11)-(5.13) can obfuscate the tie-line load flow $\boldsymbol{x}^{l_t^*}$. In Fig.5.3(a), it maybe smaller than the realistically optimal load flow $\hat{\boldsymbol{x}}^{l_t}$ if $0<\boldsymbol{\alpha}^{l_t^*}\boldsymbol{\xi}^{l_t}<\boldsymbol{d}_n$ with the direction $m \rightarrow n$, or larger than $\hat{\boldsymbol{x}}^{l_t}$ if $\boldsymbol{\alpha}^{l_t^*}\boldsymbol{\xi}^{l_t}<0$ with the direction $m \rightarrow n$. Reversing the flow direction $n \rightarrow m$ is just when $\boldsymbol{\alpha}^{l_t^*}\boldsymbol{\xi}^{l_t}>\boldsymbol{d}_n$ in Fig.5.3(b), which will be discussed in the load flow direction obfuscation. Even though this is achievable for load flow quantity obfuscation, it may enable a DP-DNR mechanism $\tilde{\mathcal{M}}$ to converge at a topology solution other than the realistic $\boldsymbol{u}^{l^*}$. Therefore, we propose the load flow quantity obfuscation criteria for $\boldsymbol{x}^{l_t}$ which can enable $\tilde{\mathcal{M}}$ to maintain the optimality of topology solution at $\boldsymbol{u}^{l^*}$.

Criteria 1(*Quantity Obfuscation of Tie-lines*): With virtual power injection $\boldsymbol{g}$ at boundary nodes of tie-lines, the proposed DP-DNR mechanism $\tilde{\mathcal{M}}$ with the modified objective function F_1

$$F_1 = \left(\boldsymbol{x}^l + \boldsymbol{\alpha}^l \boldsymbol{\xi}^l\right)^T \boldsymbol{c}\left(\boldsymbol{x}^l + \boldsymbol{\alpha}^l \boldsymbol{\xi}^l\right) \tag{5.14}$$

should converge at $(\boldsymbol{x}^{l*}, \boldsymbol{u}^{l*})$, if there $\exists \boldsymbol{\alpha}^{l_t^*} \neq 0$ for then switch-on tie-line l_t is true.

For the switch-on tie-line l_t, $\boldsymbol{\alpha}^{l_t^*}$ can be achieved as a non-zero number, which existence proof is as follows:

Proof: Suppose $(\hat{\boldsymbol{x}}^l, \boldsymbol{u}^{l*}) \in \mathcal{X}$ is the optimal solution of non-private DNR model. It is clear that the following constraints can stand

$$\boldsymbol{G}_v^{l_t} \begin{bmatrix} \hat{\boldsymbol{x}}^l \\ \boldsymbol{u}^{l*} \end{bmatrix} \leqslant \boldsymbol{b}_v^{l_t}, \quad \forall l_t \in \mathcal{T} \tag{5.15}$$

Since $\hat{\boldsymbol{x}}^{l_t} = \boldsymbol{x}^{l_t^*} + \boldsymbol{\alpha}^{l_t^*} \xi^{l_t}$ holds according to Theorem 2, we can find

$$\boldsymbol{G}_v^{l_t,*} \boldsymbol{\alpha}^{l_t} \boldsymbol{\xi}^{l_t} \leqslant \boldsymbol{b}_v^{l_t} - \boldsymbol{G}_v^{l_t} \begin{bmatrix} \boldsymbol{x}^{l_t^*} \\ \boldsymbol{u}^{l*} \end{bmatrix}, \quad \forall l_t \in \mathcal{T} \tag{5.16}$$

Where $\boldsymbol{G}_v^{l_t,*}$ is a real number on the l_t-th entry of the row vector $\boldsymbol{G}_v^{l_t}$.

When this DP-DNR model converges at $(\boldsymbol{x}^{l*}, \boldsymbol{u}^{l*})$, this inequality can be achieved at the equality according to the Karush–Kuhn–Tucker (KKT) conditions at the linear programming relaxation stage. Thus, with sampled $\xi^{l_t} \neq 0$, we have

$$\boldsymbol{\xi}^{l_t} \boldsymbol{G}_v^{l_t,*} \boldsymbol{\alpha}^{l_t^*} \leqslant \boldsymbol{b}_v^{l_t} - \boldsymbol{G}_v^{l_t} \begin{bmatrix} \hat{\boldsymbol{x}}^{l_t} \\ \boldsymbol{u}^{l*} \end{bmatrix}, \quad \forall l_t \in \mathcal{T} \tag{5.17}$$

If $\boldsymbol{G}_v^{l_t}\begin{bmatrix}\hat{\boldsymbol{x}}^{l_t}\\ \boldsymbol{u}^{l*}\end{bmatrix}<\boldsymbol{b}_v^{l_t}$ holds, then $\boldsymbol{b}_v^{l_t}-\boldsymbol{G}_v^{l_t}\begin{bmatrix}\hat{\boldsymbol{x}}^{l_t}\\ \boldsymbol{u}^{l*}\end{bmatrix}\neq 0$ can be achieved. This means $\boldsymbol{\alpha}^{l_t^*}\neq 0$ by (5.17). Otherwise, $\boldsymbol{\alpha}^{l_t^*}=0$ if and only if $\boldsymbol{G}_v^{l_t}\begin{bmatrix}\hat{\boldsymbol{x}}^{l_t}\\ \boldsymbol{u}^{l*}\end{bmatrix}=\boldsymbol{b}_v^{l_t}$. But as voltage security constraints are soft constraints, $\boldsymbol{\alpha}^{l_t^*}=0$ can be avoided as long as the range of voltage profiles can be minored for a little bit. This proof also demonstrates that $\boldsymbol{\alpha}^{l_t^*}$ cannot change the optimality of topology variables at $\boldsymbol{u}^{l_t^*}$.

■

With a proper $\boldsymbol{\alpha}^{l_t^*}$, we elaborate how the virtual power injection vector $\boldsymbol{g}$ in this proposed DP-DNR mechanism $\tilde{\mathcal{M}}$ maintains the optimality of topology solutions $\boldsymbol{u}^{l*}$. With an intuitive understanding, we discuss this criteria from the physical perspective. Fig.5.3(a) shows the realistically optimal load flow direction $m\rightarrow n$. If $\boldsymbol{g}_n$ injects $\boldsymbol{\alpha}^{l_t^*}\xi^{l_t}>0$ and $\boldsymbol{g}_m$ ejects $-\boldsymbol{\alpha}^{l_t^*}\xi^{l_t}<0$, then $\boldsymbol{x}^{l_t^*}+\boldsymbol{\alpha}^{l_t^*}\xi^{l_t}=\hat{\boldsymbol{x}}^{l_t}$. This means the minimization of F_1, denoted as F_1^*, is equal to the minimal F_0^* over $\mathcal{X}$. Conversely, if $\boldsymbol{g}_n=\boldsymbol{\alpha}^{l_t^*}\xi^{l_t}<0$ and $\boldsymbol{g}_m=-\boldsymbol{\alpha}^{l_t^*}\xi^{l_t}>0$, then $\boldsymbol{x}^{l_t^*}+\boldsymbol{\alpha}^{l_t^*}\xi^{l_t}=\hat{\boldsymbol{x}}^{l_t}$ clearly holds. This implies $F_1^*=F_0^*$ still holds. In a vein, this virtual power injection vector $\boldsymbol{g}$ does not increase or decrease the minimal value of objective function F_1^*. So the optimality of topology solution $\boldsymbol{u}^{l*}$ will not be influenced by this virtual power injection vector $\boldsymbol{g}$.

The convex formulation of $\tilde{\mathcal{M}}$ can be cast as a stochastic optimization problem with a sampled vector ξ^l for tie-lines as blow:

$$\min_{\boldsymbol{x}^l,\boldsymbol{\alpha}^l,\boldsymbol{g}\in\mathbb{R},\boldsymbol{u}^l\in\mathbb{Z}} F_1 \tag{5.18}$$

$$\text{s.t.}\mathcal{X}_{\mathrm{I}} := \left\{ (\boldsymbol{x}^l, \boldsymbol{\alpha}^l, \boldsymbol{g}, \boldsymbol{u}^l) \;\middle|\; \begin{array}{l} \tilde{\boldsymbol{A}}\boldsymbol{x}^l = \tilde{\boldsymbol{d}}, \begin{bmatrix} \boldsymbol{G}_v \\ \boldsymbol{G}_u \end{bmatrix} \begin{bmatrix} \boldsymbol{x}^l \\ \boldsymbol{u}^l \end{bmatrix} \leqslant \begin{bmatrix} \boldsymbol{b}_v \\ \boldsymbol{b}_u \end{bmatrix}, \boldsymbol{K} \begin{bmatrix} \boldsymbol{x}^l \\ \boldsymbol{u}^l \end{bmatrix} = \boldsymbol{h} \\ (5.11)-(5.13), \boldsymbol{G}_{cr}\boldsymbol{x}^l \le \boldsymbol{b}_{cr}, \underline{\boldsymbol{x}}^l \leqslant \boldsymbol{x}^l \leqslant \overline{\boldsymbol{x}}^l \end{array} \right\} \tag{5.19}$$

where the superscript symbol $\sim$ of $\boldsymbol{A}$ and $\boldsymbol{d}$ represent the matrices and vectors excluding boundary nodes, and $\mathcal{X}_{\mathrm{I}}$ refers to the non-empty feasibility space of this model.

(2) Load flow direction obfuscation

Obfuscating $\boldsymbol{x}^{l_t}$ with reversed directions can avoid the exposure event of private load change information as previously exemplified in Fig.5.3(a). Thus, the load flow direction obfuscation can be realized with the proper selection of $\boldsymbol{\alpha}^l$. For instance, as displayed in Fig.5.3(b), the obfuscated load flow $\boldsymbol{x}^{l_t^*}$ equals to $\hat{\boldsymbol{x}}^{l_t} - \boldsymbol{\alpha}^{l_t^*}\xi^{l_t} < 0$ if $\boldsymbol{\alpha}^{l_t^*}\xi^{l_t} > \boldsymbol{d}_n$ and $\hat{\boldsymbol{x}}^{l_t} = \boldsymbol{d}_n$. Consequently, the obfuscated load flow direction is reversed to $n \rightarrow m$. Now, we express the criteria of tie-line load flow direction obfuscation, yielding

Criteria 2(*Direction Obfuscation of Tie-lines*): Suppose $\mathcal{T}_i$ represents the set of tie-lines connected to the *i*-th agent where $\forall i \in \mathcal{A}$ and $\mathcal{A}$ is the set of agents. The *i*-th agent connects at least two switch-on tie-lines with the same load flow direction. If this agent has such a direction obfuscation request, then at least one load flow direction of $\boldsymbol{x}^{l_t^*}$ should be reversed to the realistic directions. For other agents who have less than one switch-on tie-line or do not have such requests, it is unnecessary for the load flow direction obfuscation. Mathematically, we have

$$\left(f_i-1\right)M \leqslant \tau_i \sum_{l_t \in \mathcal{T}_i} \boldsymbol{u}^{l_t} - \vartheta \leqslant f_i M \tag{5.20}$$

$$\left(f_i-1\right)M \leqslant \tau_i \sum_{l_t \in \mathcal{T}_i} \boldsymbol{x}^{l_t} \leqslant \left(1-f_i\right)M \tag{5.21}$$

where M is a big positive scalar. ϑ is the given constant and we select ϑ=1.5 in this chapter. And τ_i is a given parameter such that τ_i=1 if the i-th agent with heavy loads have a request of tie-line load flows direction obfuscations; otherwise τ_i=0.

This criteria can be elaborated here. Constraint (5.20) can explore the i-th agent who has at least two switch-on tie-lines, if an auxiliary binary variable f_i=1. Otherwise, f_i=0 refers to other agents with less than one switch-on tie-line. Then, for this i-th agent, we consider reversing one of tie-line load flows, when running into all optimal tie-lines' loads flow towards the same direction. Enforcing $\sum_{l_t \in \mathcal{T}_i} \boldsymbol{x}^{l_t}=0$ for this i-th agent can lead to $\boldsymbol{\alpha}^{l_t^*} \xi^{l_t} > \boldsymbol{d}_n$ as indicated in Fig.5.3 (b). Hence, $\sum_{l_t \in \mathcal{T}_i} \boldsymbol{x}^{l_t}=0$ can be coupled with f_i=1. Instead, f_i=0 induces that $\sum_{l_t \in \mathcal{T}_i} \boldsymbol{x}^{l_t}=0$ can be automatically relaxed, which forms the constraint (5.21). We exemplify two cases in Fig.5.4(a) and (b). In Fig.5.4 (a), there is only one switch-on tie-line for the i-th agent, i.e., $\sum_{t \in \mathcal{T}_i} \boldsymbol{u}^{l_t}=1$ and f_i=0 by constraint (5.20), which relaxes constraint (5.21) for free. In Fig.5.4 (b), this i-th agent may need the load flow direction obfuscation since there exist two switch-on tie-lines. According to constraint (5.20), we achieve $\sum_{l_t \in \mathcal{T}_i} \boldsymbol{u}^{l_t}=2$ and f_i=1, and then $\sum_{l_t \in \mathcal{T}_i} \boldsymbol{x}^{l_t}=0$ gets automatically activated by constraint (5.21) for the load flow direction obfuscation.

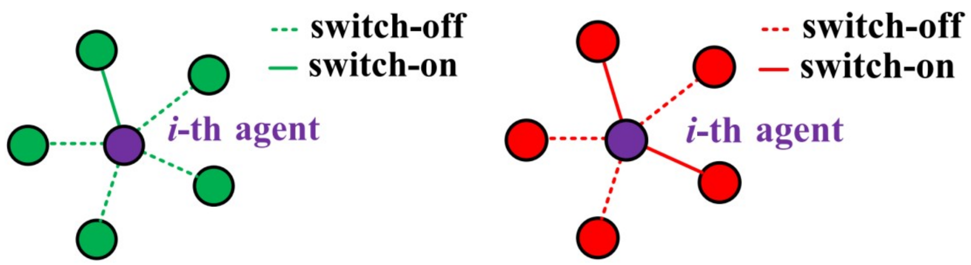

(a) (b)

Fig. 5.4. (a) One active tie-line; (b) two active tie-lines.

In light of the above, this proposed DP-DNR mechanism $\tilde{\mathcal{M}}$ can involve two privacy-preserving criteria, i.e., load flow quantity obfuscation and load flow direction obfuscation subject to the optimality of topology variables at $\boldsymbol{u}^{l*}$. Accordingly, with sampled $\boldsymbol{\xi}^{l}$ for tie-lines, the convex formulation of DP-DNR model with the objective function F_1 can be cast as

$$\mathbf{DP\text{-}DNR}: \quad \min_{\boldsymbol{x}^l, \boldsymbol{\alpha}^l, \boldsymbol{g} \in \mathbb{R}, \boldsymbol{f}, \boldsymbol{u}^l \in \mathbb{Z}} F_1 \tag{5.22}$$

$$\text{s.t.}\, \mathcal{X}_{\text{II}} := \left\{ (\boldsymbol{x}^l, \boldsymbol{\alpha}^l, \boldsymbol{f}, \boldsymbol{g}, \boldsymbol{u}^l) \;\middle|\; \begin{array}{l} \tilde{\boldsymbol{A}}\boldsymbol{x}^l = \tilde{\boldsymbol{d}}, \begin{bmatrix}\boldsymbol{G}_v \\ \boldsymbol{G}_u\end{bmatrix}\begin{bmatrix}\boldsymbol{x}^l \\ \boldsymbol{u}^l\end{bmatrix} \leqslant \begin{bmatrix}\boldsymbol{b}_v \\ \boldsymbol{b}_u\end{bmatrix}, \boldsymbol{K}\begin{bmatrix}\boldsymbol{x}^l \\ \boldsymbol{u}^l\end{bmatrix} = \boldsymbol{h} \\ (5.11)-(5.13), (5.20)-(5.21), \boldsymbol{G}_{cr}\boldsymbol{x}^l \le \boldsymbol{b}_{cr}, \underline{\boldsymbol{x}}^l \leqslant \boldsymbol{x}^l \leqslant \overline{\boldsymbol{x}}^l \end{array} \right\} \tag{5.23}$$

where $\mathcal{X}_{\text{II}}$ refers to the non-empty feasibility space of this DP-DNR model.

5.4 Consensus ADMM Algorithm

In this section, we reformulate this DP-DNR model (5.22)-(5.23) as a global consensus problem. We suppose the block variables $\boldsymbol{X}_i = \left[\boldsymbol{x}_i^l, \boldsymbol{\alpha}_i^l, \boldsymbol{u}_i^l, \boldsymbol{f}_i\right]^T$ for the i-th agent and $\forall i \in \mathcal{A}$, in which $\boldsymbol{X}_{i,b} = \left[\boldsymbol{x}_i^{l_t}, \boldsymbol{\alpha}_{i,b}^l, \boldsymbol{u}_{i,b}^l, \boldsymbol{f}_{i,b}^l\right]^T$ and voltage profile variables $\boldsymbol{v}_{i,b}$ are two vectors of boundary nodes of tie-line l_t who connects to the i-th agent. The consensus variables for tie-line l_t can be composed of $\boldsymbol{Z}_x = \left[\boldsymbol{x}_z^l, \boldsymbol{\alpha}_z^l, \boldsymbol{u}_z^l, \boldsymbol{f}_z\right]^T$ and squared voltage profiles $\boldsymbol{W}_v$. Accordingly, $\boldsymbol{X}_{i,b} - \boldsymbol{Z}_x = 0$ can hold for either $\boldsymbol{u}^{l_t} = 0$ or $\boldsymbol{u}^{l_t} = 1$. Please note that $\boldsymbol{g}$ can be achieved by sampled ξ^l and variables $\boldsymbol{\alpha}^l$, and thus it would be not regarded as consensus variables. And $\boldsymbol{v}_{i,b} - \boldsymbol{W}_v = 0$ can hold only if $\boldsymbol{u}^{l_t} = 1$; otherwise it should be relaxed when $\boldsymbol{u}^{l_t} = 0$.

Since the DP-DNR model can be represented by the block variables $\boldsymbol{X}_i$ and associated separable objective function $F_{1,i}(\boldsymbol{X}_i)$ for the i-th agent, the augmented lagrangian function $\mathcal{L}_\lambda$ can be expressed in the scaled form:

$$\mathcal{L}_\lambda = \sum_{i=1}^{n_\mathcal{A}} \left(F_i\left(\boldsymbol{X}_i\right) + \lambda/2 \left\| \boldsymbol{X}_{i,b} - \boldsymbol{Z}_x + \boldsymbol{\mu}_{i,b} \right\|_2^2 + \lambda/2 \left\| \boldsymbol{V}_{i,b} \right\|_2^2 \right) \tag{5.24}$$

where $n_\mathcal{A}$ is the number of agents, and $\boldsymbol{\mu}_{i,b}$ is the i-th agent's dual variables for the equality $\boldsymbol{X}_{i,b} - \boldsymbol{Z}_x = 0$. And λ is a given positive scalar. And $\boldsymbol{V}_{i,b}$ is an incorporated variable for $\boldsymbol{V}_{i,b} = \boldsymbol{u}^{l_t}(\boldsymbol{v}_{i,b} - \boldsymbol{W}v + \boldsymbol{\gamma}_{i,b})$ and $\boldsymbol{\gamma}_{i,b}$ is the associated dual variable. This equality can be further equivalent to

$$\boldsymbol{v}_{i,b} - \boldsymbol{W}_v + \boldsymbol{\gamma}_{i,b} - \left(1 - \boldsymbol{u}^{l_t}\right) M \leqslant \boldsymbol{V}_{i,b} \leqslant \boldsymbol{v}_{i,b} - \boldsymbol{W}_v + \boldsymbol{\gamma}_{i,b} + \left(1 - \boldsymbol{u}^{l_t}\right) M \tag{5.25}$$

Subsequently, we define $\mathcal{V}_i := \left\{\boldsymbol{V}_{i,b}, \boldsymbol{W}_v, \boldsymbol{v}_{i,b} \in \mathbb{R}, \boldsymbol{u}^{l_t} \in \mathbb{Z} \middle| (5.26)\right\}$ for the i-th agent. As the augmented Lagrangian function $\mathcal{L}_\lambda$ is separable over the $n_\mathcal{A}$ agents, each of the primal updates for the $(\boldsymbol{X}_i, \boldsymbol{V}_{i,b})$ can be performed independently.

This yields the decomposable ADMM steps:

$$\left(\boldsymbol{X}_{i,b}^{k+1}, \boldsymbol{V}_{i,b}^{k+1}\right) = \underset{\boldsymbol{X}_i \in \mathcal{X}_{\mathrm{II},i}, \boldsymbol{V}_{i,b} \in \mathcal{V}_i\left(\boldsymbol{W}_v^k\right)}{\operatorname{argmin}} F_i\left(\boldsymbol{X}_i\right) + \lambda/2 \left\| \boldsymbol{X}_{i,b} - \boldsymbol{Z}_x^k + \boldsymbol{\mu}_i^k \right\|_2^2 + \lambda/2 \left\| \boldsymbol{V}_{i,b} \right\|_2^2, \quad \forall i = 1, 2 \ldots, n_\mathcal{A} \tag{5.26}$$

$$\left(\boldsymbol{Z}_x^{k+1},\boldsymbol{W}_v^{k+1}\right)=\Pi_{\mathcal{C}}\left(\begin{bmatrix}\boldsymbol{X}_{i,b}^{k+1}+\boldsymbol{\mu}_i^k\\ \boldsymbol{v}_{i,b}^{k+1}+\boldsymbol{\gamma}_i^k\end{bmatrix}\right) \tag{5.27}$$

$$\boldsymbol{\mu}_{i,b}^{k+1}=\boldsymbol{\mu}_{i,b}^{k}+\boldsymbol{X}_{i,b}^{k+1}-\boldsymbol{Z}_x^{k+1},\boldsymbol{\gamma}_{i,b}^{k+1}=\boldsymbol{\gamma}_{i,b}^{k}+\boldsymbol{Z}_{x,u}^{k+1}\left(\boldsymbol{V}_{i,b}^{k+1}-\boldsymbol{W}_v^{k+1}\right) \tag{5.28}$$

where $\mathcal{C}$ is the Cartesian product of sets $\mathcal{C}_i, i=1,2,\ldots,n$ and $\Pi_{\mathcal{C}}$ stands for the projection over $\mathcal{C}$. For the consensus binary variables $\boldsymbol{Z}_{x,u}^{k+1}$ in the vector $\boldsymbol{Z}_x^{k+1}$, $\Pi_{\mathcal{C}}$ simply rounds each entry to 0 or 1 whichever is closer by [60], and $\mathcal{C}_i\in\mathbb{R}$ for the consensus continuous variables. Intuitively, the relationship between consensus variables $\left(\boldsymbol{Z}_x,\boldsymbol{W}_v\right)$ and optimization variables $\left(\boldsymbol{X}_{i,b},\boldsymbol{X}_{j,b},\boldsymbol{V}_{i,b},\boldsymbol{V}_{j,b}\right)$ from two adjacent agents *i* and *j* are explained in Fig.5.5.

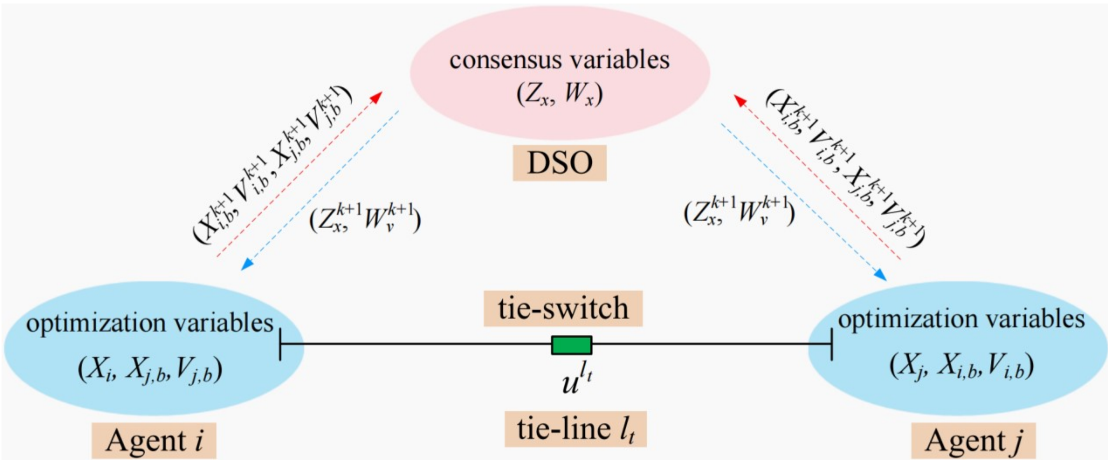

Fig. 5.5. Relationship between consensus variables and optimization variables.

Note that the optimal $\boldsymbol{V}_{i,b}^{k+1}=0$ can be achieved by (5.26) no matter if $\boldsymbol{u}^{l_t}=0$ or $\boldsymbol{u}^{l_t}=1$. This is because if $\boldsymbol{u}^{l_t}=0$, then $\boldsymbol{V}_{i,b}^{k+1}=0$ holds as minimizing $\left\|\boldsymbol{V}_{i,b}\right\|_2^2$ equals to zero. Alternatively, if $\boldsymbol{u}^{l_t}=1$, then $\boldsymbol{V}_{i,b}=\boldsymbol{v}_{i,b}-\boldsymbol{W}_v^k+\gamma_{i,b}^k$ stands which enables (5.26) as a standard form of the augmented Lagrangian function $\mathcal{L}_\lambda$ in the first step of C-ADMM algorithm. Of course, if $\boldsymbol{u}^{l_t}=0$, then $\boldsymbol{W}_v^{k+1}$ can be free in (5.27) $\gamma_{i,b}^{k+1}$ can be kept unchanged by (5.28). Moreover, by this C-ADMM iterations, (5.26) and

(5.28) are performed by each individual agent simultaneously and (5.26) is calculated by the proximal operator by the DSO. The convergence of C-ADMM is characterized in terms of the primal residual and the dual residual with predefined thresholds [60].

Next, we will exhibit the algorithmic pseudo-code for this proposed C-ADMM-based DP-DNR mechanism $\tilde{\mathcal{M}}$ with a random perpetuation vector ξ^l. As stated previously, the output of $\tilde{\mathcal{M}}$ can be a mixture of obfuscated-but-feasible tie-line load flows $\boldsymbol{x}^{l_t^*}$ and realistically optimal topology solution $\boldsymbol{u}^{l*}$ of the entire ADNs. The maximum iteration number is set to k_{max}, and then we can summarize this algorithm as below.

Algorithm 1 C-ADMM-based DP-DNR Mechanism $\tilde{\mathcal{M}}$

1: Initialization with input $\boldsymbol{c},\boldsymbol{A},\boldsymbol{G}_v,\boldsymbol{G}_{cr},\boldsymbol{b}_v,\boldsymbol{b}_{cr},\boldsymbol{b}_u,\boldsymbol{K},\boldsymbol{h}$ over $n_{\mathcal{A}}$ agents and input parameters $\varepsilon,\vartheta,\Delta_\rho,\tau,\overline{\boldsymbol{g}},\overline{\boldsymbol{\alpha}}^l$;

2: Sample a random perturbation vector ξ^l, i.i.d. $\xi^l \sim \mathbb{P}_\xi$;

3: **while** $k \leqslant k_{\max}$ **do**

4: Each agent distributively updates $\left(\boldsymbol{X}_{i,b}^{k+1},\boldsymbol{V}_{i,b}^{k+1}\right) \leftarrow \left(\boldsymbol{Z}_x^k,\boldsymbol{W}_v^k\right)$ by (5.26) and sends $\left(\boldsymbol{X}_{i,b}^{k+1},\boldsymbol{V}_{i,b}^{k+1}\right)$ to the DSO;

5: DSO updates $\left(\boldsymbol{Z}_x^{k+1},\boldsymbol{W}_v^{k+1}\right) \leftarrow \left(\boldsymbol{X}_i^{k+1},\boldsymbol{V}_{i,b}^{k+1}\right)$ by (5.27) and sends $\left(\boldsymbol{Z}_x^{k+1},\boldsymbol{W}_v^{k+1}\right)$ to all agents;

6: Each agent distributively updates $\left(\boldsymbol{\mu}_{i,b}^{k+1},\gamma_{i,b}^{k+1}\right) \leftarrow \left(\boldsymbol{\mu}_{i,b}^{k},\gamma_{i,b}^{k}\right)$ by (5.29) and $\mathcal{V}_i\left(\boldsymbol{W}_v^k\right) \leftarrow \mathcal{V}_i\left(\boldsymbol{W}_v^{k+1}\right)$;

7: **if** convergence condition is satisfied **then**

8: return optimal solution $\left(\boldsymbol{X}^*,\boldsymbol{u}^{l*}\right)$ for the entire ADNs;

9: **else**

10: $k \leftarrow k+1$

11: **end if**

12: **end while**

13: Release both obfuscated-but-feasible $\boldsymbol{x}^{l_t^*}$ and realistically optimal topology variables $\boldsymbol{u}^{l_t^*}$ for $\forall l_t \in \mathcal{T}$.

5.5 Case Study

To validate this C-ADMM-based DP-DNR mechanism $\tilde{\mathcal{M}}$, we have conducted simulation experiments on the *IEEE* RBTS-Bus 4 system with 68 nodes [101] and a modified real large-scale European distribution networks with 906 nodes [102]. The C-ADMM-based DP-DNR mechanism is calculated with MOSEK package [103].

5.5.1 IEEE RBTS-Bus 4 System

To validate this DP-DNR mechanism $\tilde{\mathcal{M}}$ about privacy preservation, we have conducted simulation experiments on the IEEE RBTS-Bus 4 system with 68 load points, 7 feeders and 6 distributed generators (DGs). This interconnected ADNs are managed by agents 1, 2 and 3 with 4 tie-lines {8, 10}, {28, 29}, {47, 45}, {28, 67}. We assume $\varepsilon = 1, \rho = 0.01\text{p.u.}, \tau = 1$ for agent 1 and $\tau = 0$ for agents 2 and 3, and $\bar{\alpha}^l = 20$. The sampled vector ξ^l is [0.3252, −0.7549, 1.3703, −1.7115]^T. We display the heat map of load distribution and associated optimal DNR solution with load flow arrows in Fig. 5.6(a). We further present the total loads of each agent before and after this optimal DNR operation as presented in Fig. 5.6(b) in the pie chart form, where the total loads is the algebra sum between the power flows from substations and tie-lines. The realistic and obfuscated tie-line load flows and voltage profiles are shown in Tab. 5.1. In this table, f and t refers to "from node" and "to node" in the column of nodes, and this is consistent with the columns of $\boldsymbol{P}^l$, $\boldsymbol{Q}^l$, $\boldsymbol{v}_f$ and $\boldsymbol{v}_t$, respectively.

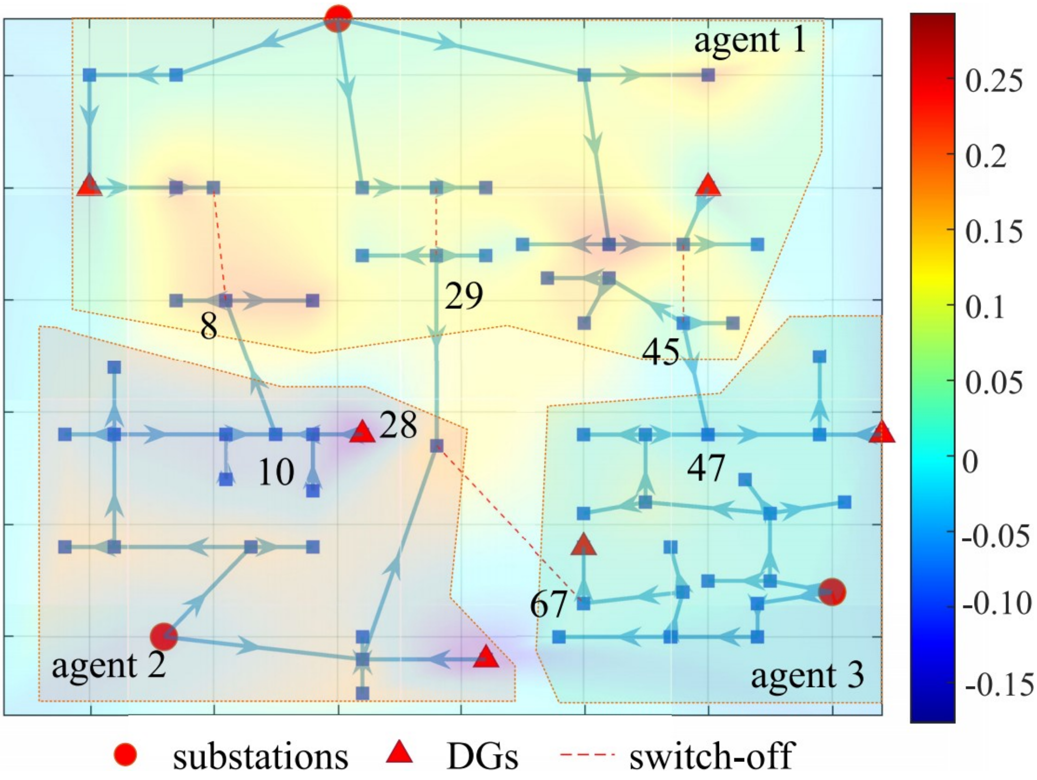

(a)

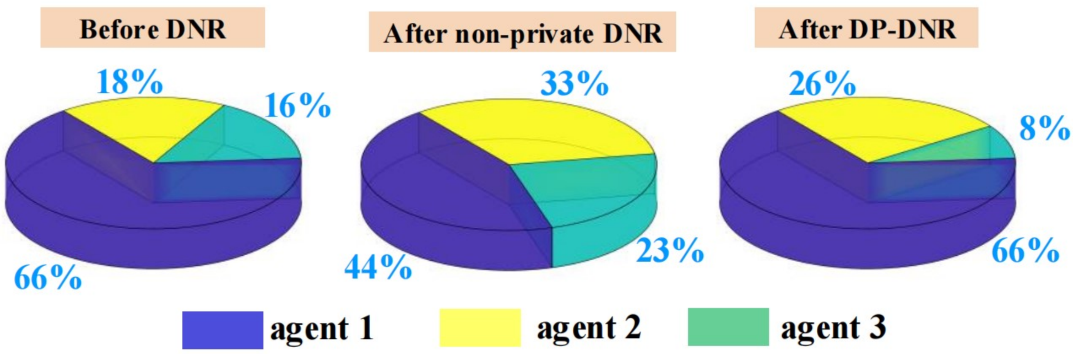

(b)

Fig. 5.6. (a) Obfuscated DP-DNR solutions for IEEE RBTS-Bus 4 System; (b) agent's load changes between different DNR models.

Table 5.1 Realistic and Synthetic Output under One Sampled Vector ξ^1

No.	Nodes	Obfuscated Values [p.u.]	Realistic Values [p.u.]

	f	t	$\boldsymbol{P}^l$	$\boldsymbol{Q}^l$	$\boldsymbol{v}_f$	$\boldsymbol{v}_t$	$\boldsymbol{P}^l$	$\boldsymbol{Q}^l$	$\boldsymbol{v}_f$	$\boldsymbol{v}_t$
1	47	45	-0.217	-0.134	1.026	1.031	0.615	0.165	1.014	1.011
2	10	8	0.336	0.223	1.027	1.007	0.095	0.225	1.014	1.013
3	28	29	-0.118	-0.089	1.021	1.026	0.205	0.090	1.020	1.018
4	28	67	0	0	1.026	1.032	0	0	1.020	1.032
Loss [p.u.]			0.0506				0.0506			

Fig. 5.6(a) exhibits some of load nodes in agent 1 are transferred to neighborhood agents 2 and 3, where the topology switch-off status is highlighted in red dashed lines. This is also the same optimal topology solution by solving the non-private DNR model. By observation, the tie-lines {47, 45} and {28, 29} have reversed the load flow directions. And the tie-line {8, 10} provides the obfuscated-but-feasible load flow in the realistic direction. The algebra sums of tie-line real and reactive flows for agent 1 equal to zero, as shown in the $\boldsymbol{P}^l$ and $\boldsymbol{Q}^l$ columns of Tab.5.1. This protects the load privacy of agent 1 and corresponding boundary voltage profiles are slightly obfuscated due to the feasibility of power flow equations.

As shown in Fig. 5.6(b), the proportions of three agent's loads have varied significantly by the DNR operation from the observation of the first two pie charts. However, as indicated in the third diagram of Fig. 5.6(b), this load proportions maintains quite similarly to the original load proportions in the first pie chart. It is concluded that no effective inference can be made about the loading levels of agent 1 if there is no internal topology information available. In summary, this DP-DNR solution not only guarantees the DSO's operational concerns with lossy interconnected ADNs, but also avoids exposing agent's load privacy in terms of tie-line load flow quantities and directions.

Moreover, we compare the feasibility and optimality of tie-line load flow obfuscations with the proposed DP-DNR mechanism $\tilde{\mathcal{M}}$ and the Laplace mechanism with the output perturbation (OP) strategy [50] and program perturbation (PP) strategy [49], respectively. We run 1000 random perturbations ξ^l for simulations as shown in Tab. 5.2. The first column refers to the number of tie-lines. The second column denotes the mean of active load flows of tie-lines, and the third column indicates the constraint violation percentage of the non-private DNR model. For the last column, we examine the optimality loss of output topology variables by the PP-based Laplace mechanism and $\tilde{\mathcal{M}}$.

Table 5.2 Syntneic Tie-line Load Flows under 1000 Samples

No.	Nodes		Mean of $\boldsymbol{P}^l$		Const. Violation (%)		Optimality Loss (%)	
	f	t	OP [50]	$\tilde{\mathcal{M}}$	OP [50]	$\tilde{\mathcal{M}}$	PP [49]	$\tilde{\mathcal{M}}$
1	47	45	0.615	0.244	1.651	0.0	86.251	0.0
2	10	8	0.095	0.103	1.625	0.0	98.124	0.0
3	28	29	0.090	0.154	1.647	0.0	97.632	0.0
4	28	67	0	0	1.664	0.0	95.121	0.0

As shown in Tab.5.2, the OP-based Laplace mechanism returns private solutions with a large number of violated constraints due to imbalances of load flows at boundary nodes; whereas the proposed DP-DNR mechanism $\tilde{\mathcal{M}}$ provides the formal guarantee for the individual constraint satisfaction. To compare the PP-based Laplace mechanism and $\tilde{\mathcal{M}}$, it is obvious that the PP-based Laplace mechanism cannot guarantee the realistic topology output, causing the large percentage of optimality loss. This hinders the practical applicability from the perspective of DSOs. This comparison verifies that $\tilde{\mathcal{M}}$ can achieve the optimality of topology variables $\boldsymbol{u}^l$ and the feasibility of operational variables $\boldsymbol{x}^l$ with a satisfactory operational and privacy-preserving performance.

5.5.2 Large-scale Practical European Distribution Networks

For the scalability analysis, the large-scale practical European distribution networks are adopted from reference [102], which operates at 0.416 kV and includes 906 nodes. To structure the interconnected ADNs, we have added 10 DGs and 9 points of common coupling (PCC) in this distribution networks, and then the number of tie-lines is 8. The parameter τ = 1 for agents 2 and 5, and τ = 0 for other agents. We visualize the heat map of load distribution and associated optimal DNR solution with different agents in Fig. 5.7. To be a clear exhibition, we display the realistic load flows of tie-lines and associated boundary voltage profiles and the mean of these obfuscated values under 1000 samples of random perturbations ξ^l in Tab.5.3. In this table, f and t refers to "from agent" and "to agent" in the column of agents, and this is applied for $\boldsymbol{P}^l$, $\boldsymbol{Q}^l$, $\boldsymbol{v}_f$ and $\boldsymbol{v}_t$, respectively.

Fig. 5.7 exhibits some of load nodes in agent 5 are switched to neighborhood agents by observing the switch-off branches marked in red dashed lines. The tie-line numbers marked in yellow box {1, 2, 3, 5, 6, 7} provide the obfuscated-but-feasible load flow in the realistic direction, whilst only the tie-line numbers {4, 8} have reversed the load flow directions, as reported in Tab. 5.3. Since agent 2 has the heavy loads as seen in Fig. 5.7, partial heavy loads can be transferred to agents 1 and 3 after this optimal DNR operation. Agents 1 and 3 inject the power via tie-line numbers 5 and 2, but agent 1 still supplies several loads in agent 5 via tie-line number 6. Since the agent 5 is heavily loaded, neighborhood agents 1, 4, 6 and 7 provide the power to supply loads in this area. To avoid agent's heavy load information leakage, the sums of all connected tie-lines for agents 2 and 5 are zero in Tab.5.3. For agent 5, some of connected tie-lines 4 and 8 have reversed load flow directions by applying this DP-DNR mechanism $\tilde{\mathcal{M}}$. Overall, this DP-DNR mechanism $\tilde{\mathcal{M}}$ performance for agents 2 and 5.

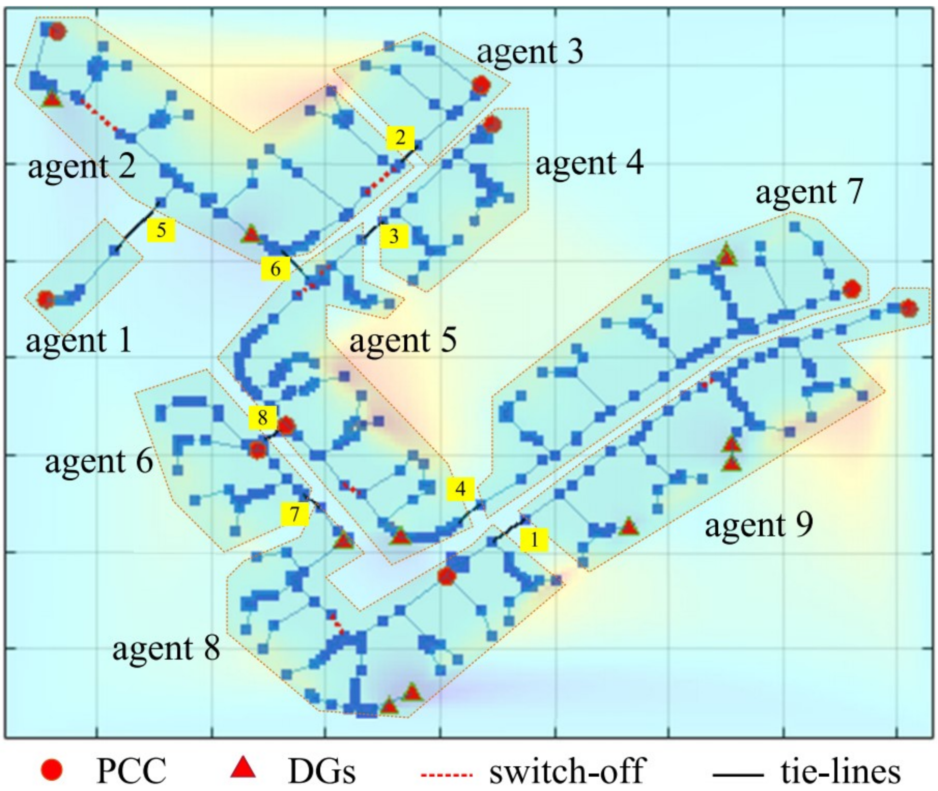

Fig. 5.7. Obfuscated DNR solutions for practical European distribution networks.

Table 5.3 Realistic and Synthetic Solutions under 1000 Samples

No.	Agents		Mean of Obfuscated Values				Realistic Values			
	f	t	$\boldsymbol{P}^l$	$\boldsymbol{Q}^l$	$\boldsymbol{v}_f$	$\boldsymbol{v}_t$	$\boldsymbol{P}^l$	$\boldsymbol{Q}^l$	$\boldsymbol{v}_f$	$\boldsymbol{v}_t$

1	8	9	0.091	0.022	1.021	1.013	0.078	0.011	1.016	1.008
2	2	3	-0.117	-0.125	1.001	1.013	-0.342	-0.094	1.005	1.018
3	5	4	-0.109	-0.056	1.021	1.017	-0.381	-0.264	1.024	1.021
4	5	7	0.168	0.018	1.013	1.016	-0.203	-0.216	1.012	1.014
5	2	1	-0.016	-0.035	1.029	1.034	-0.198	-0.064	1.026	1.031
6	2	5	0.085	0.048	1.016	1.014	0.034	0.011	1.013	1.011
7	6	8	0.335	0.160	1.026	1.014	0.213	0.089	1.026	1.015
8	5	6	0.192	0.122	1.067	1.061	-0.013	-0.001	1.065	1.062
Loss [p.u.]				0.2036				0.2036		

We compare the load proportion of each agent before and after this DNR operation as highlighted by blue and red radar forms in Fig. 5.8. With 1000 samples of random perturbations ξ^l, this figure depicts the possible range of this agent's loads by $\tilde{\mathcal{M}}$ in the pink-colored range. It is found that there is no load variations for agents 2 and 5 because of the load flow direction obfuscation criteria, while the possible ranges of other agent's loads are all similar to the original load distribution before the DNR operation. Accordingly, this figure validates the privacy-preserving effectiveness of our proposed $\tilde{\mathcal{M}}$ by the similar load proportion map.

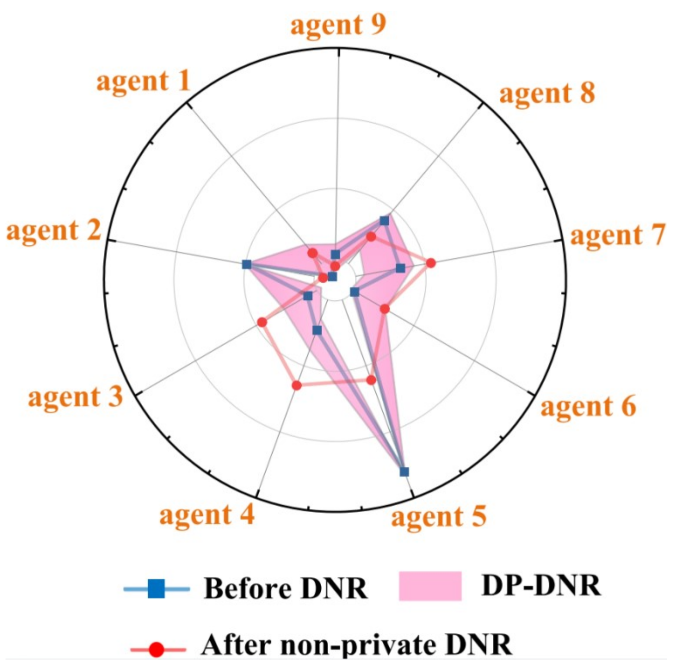

Fig. 5.8. Agent's load changes between different DNR models under 1000 samples.

Moreover, this C-ADMM algorithm, we suppose that the parameter λ is set to 100. The initial dual variables $\boldsymbol{\mu}_{i,b}$ and $\boldsymbol{\gamma}_{i,b}$ are zeros vectors and a good warm start $\boldsymbol{Z}_x$ and $\boldsymbol{W}_v$ is predefined for the iteration k = 1. With a sampled ξ^l, the convergence condition of primal residual and the dual residual norms should be less than $10^{-4}\sqrt{|\mathcal{N}|}$. The convergence performances of this C-ADMM algorithm for residuals of primal variables, dual variables and consensus variables are illustrated in Fig. 5.9(a), (b) and (c). It can be observed that norms of primal residual, dual and consensus residuals converge to stationary values at 180 iterations.

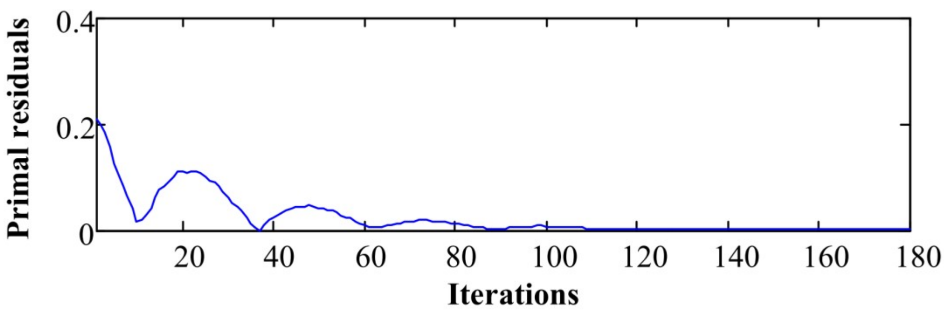

(a)

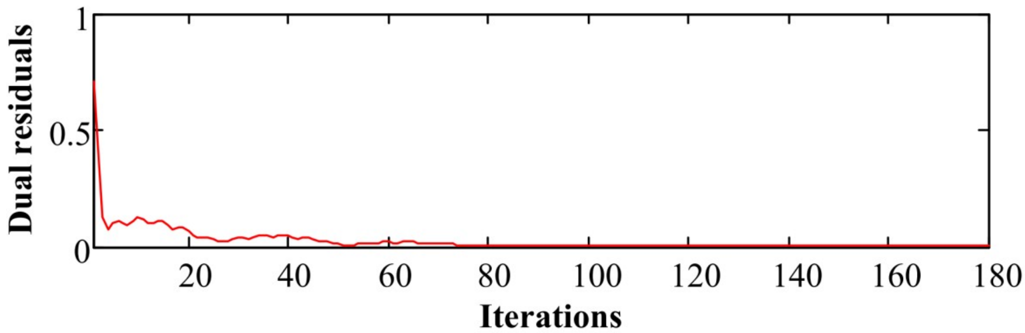

(b)

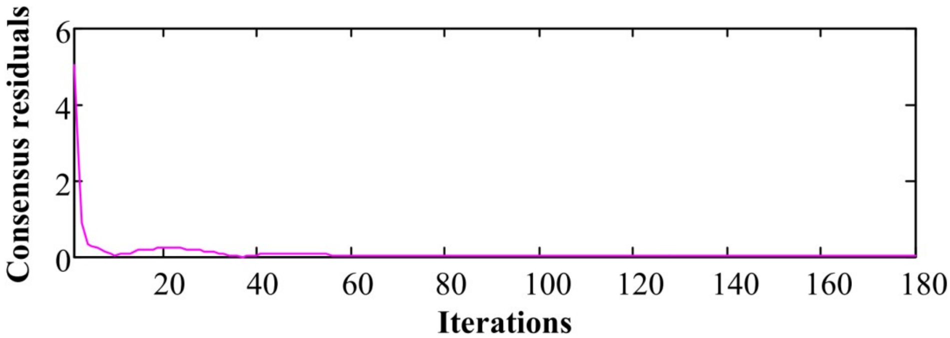

(c)

Fig. 5.9. Convergence performance of C-ADMM algorithm: (a) norms of primal residuals; (b) norms of dual residuals; (c) norms of consensus residuals

We discuss the privacy-preserving performance for our proposed C-ADMM-based DP-DNR mechanism $\tilde{\mathcal{M}}$ as compared to the C-ADMM-based non-private DNR approach. To exemplify this privacy-preserving performance, we can observe the different convergence performances of the active load flow $\boldsymbol{P}^{l_t}$ as boundary continuous variables $\boldsymbol{x}^{l_t}$ of the DP-DNR and non-private DNR models per twenty iterations in Fig. 5.10(a) and (b) where each color-coded line represents the tie-line's active load flow. It is clear that the C-ADMM algorithm can exchange privacy-preserving information $\boldsymbol{x}^{l_t^*} = \hat{\boldsymbol{x}}^{l_t} - \boldsymbol{\alpha}^{l_t^*} \xi^{l_t}$ based on Theorem 2 in Fig 5.10 (a), instead of realistic boundary continuous variables $\hat{\boldsymbol{x}}^{l_t}$ from each agent as shown in Fig 5.10(b). Hence, this ability of C-ADMM-based DP-DNR mechanism justifies the formation of protecting the boundary continuous variables $\boldsymbol{x}^{l_t^*}$.

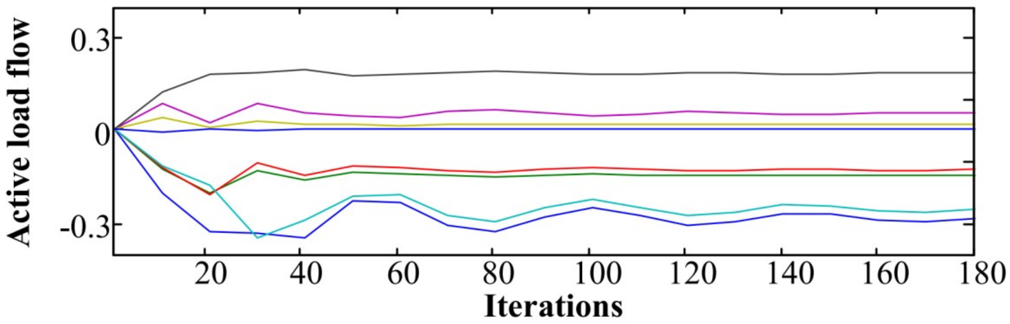

(a)

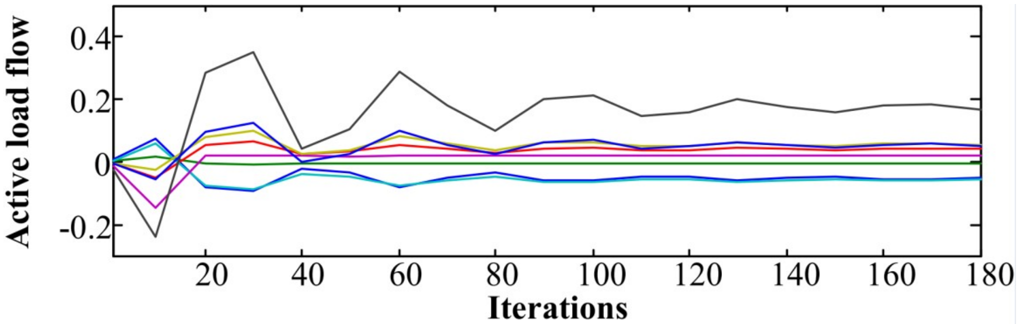

(b)

Fig. 5.10. Convergence performance of C-ADMM algorithm: (a) $\boldsymbol{x}^{l_t^*}$ by DP-DNR; (b) $\hat{\boldsymbol{x}}^{l_t}$ by non-private DNR

5.6 Summary

This chapter proposes a DP-DNR mechanism based on a C-ADMM approach for interconnected multi-agent ADNs. This query mechanism provides a mixture output of both realistically optimal tie-switch status and corresponding obfuscated-but-feasible tie-line load flows, part of which may have reverse directions. Moreover, the C-ADMM-based DP-DNR mechanism can seek the optimal topology switch without realistic communication signals and customer's load data from other agents, which maximally protects the agent's and customer's privacy. In the future energy-sharing market with mutual trust, this well-designed C-ADMM-based DP-DNR management will be much applicable for privacy-preserving grid operation of multi-agent ADNs, especially for agents with conflicting interests.

Chapter 6

Distribution-Level Topology Optimization in Economic Dispatch of Wind-Thermal-Bundled Power System for Operational Flexibility Enhancement

With a wind-thermal-bundled power system (WTBPS) under high wind penetration levels, the sharp power fluctuations of tie-lines for interconnected grids trigger a significant challenge of security-constrained power system operation. Smoothing power fluctuations with economic dispatch is widely concerned against this challenge.

This chapter proposes a distribution-level topology optimization contributing to the flexibility enhancement of a look-ahead rolling economic dispatch of WTBPS. The contributions of this paper are three-fold: 1) This study derives a new family of tightened ramping constraints of retrofitted coal-fired units. The proposed tightened constraints can be formulated in the linear or second-order conic (SOC) forms. The SOC constraints can be more accurate than the linear constraints due to minor inner-approximated errors between tightened and untightened ramping margins. 2) We construct the SOC constraints with minimal inner-approximated errors and the distribution-level topology optimization model to offset the insufficient ramping margins of retrofitted coal-fired units. A rolling economic dispatch model including

LTS-based strategy is then reformulated as a mixed-integer second-order cone programming (MISOCP) problem for a long look-ahead period, which has not been studied to date. 3) For this established MISOCP-based model, it is highly desirable to combine the Multi-cut Benders Decomposition (MBD) and Generalized Benders Decomposition (GBD) as the devised Multi-cut GBD (MGBD) to tackle this MISOCP problem, which can enhance overall computational efficiency and be suitable for online rolling economic dispatch.

6.1 Modeling of WTBPS and Associated Constraints

For the rapid growth of wind farms only with a fixed capacity of coal-fired plants, there are two ways to avoid suffering from wind curtailment. *i*) The one option is to upgrade coal-fired units, e.g. retrofitted coal-fired units have faster ramp rates. Herein, they can be used to rapidly track changes with unexpected ramp down of wind power. *ii*) Various alternatives such as distribution-side load transfer and energy storage can be used to increase the flexibility of wind-thermal-bundled transmission system further. In this paper, we discuss the flexible load transfer strategy (LTS) via reconfigurable topology of high voltage distribution networks (HVDNs) as a more realistic manner. In the near term, compared to total costs of energy storage, incorporating the flexible LTS and improving the flexibility of existing generators may be the most cost-effective means to accommodate more wind power generation. In this study, integrating wind-thermal-bundled transmission system with retrofitted coal-fired units and LTS-based HVDNs together forms a more flexible WTBPS.

There are quite a few coastal cities in the world suitable for constructing this WTBPS for other countries, where these places accommodate abundant dispatchable loads, and also are equipped with long-distance transporting coals by sea as well as off-shore wind resources. Towards this flexible control objective, we concentrate on its look-ahead economic dispatch problem in a rolling window, considering the dynamic ramping of retrofitted coal-fired units and the LTS via HVDNs.

6.1.1 Static Modeling of WTBPS

The 110kV dispatchable load resources from substations in HVDNs are generally in the range of 0 and 480 MW or even larger, accounting for nearly 5%-30% capacity of WTBPS. This flexibility indicates the better quick-response capacity than that of any coal-fired units. Consequently, integrating HVDNs to a wind-thermal generation system with connected AC/DC tie-lines to other grids forms a WTBPS, which produces more steady output power. Due to this flexibility, multiple independent agents of WTBPS can integrate with the same large-scale HVDNs, each of which connects tie-lines to other grids, as displayed in Fig. 6.1.

For the u-th agent of WTBPS, wind power $P_{\mathrm{W},u}^{t}$ is bundled with several retrofitted coal-fired units of total output power $P_{\mathrm{G},u}^{t}=\sum_{i=1}^{N_{\mathrm{G}}} r_{i,u}^{t} P_{\mathrm{G}i,u,\max}$, where $r_{i,u}^{t}=P_{\mathrm{G}i,u}^{t} / P_{\mathrm{G}i,u,\max}$ and N_{G} is the total number of retrofitted coal-fired units in the u-th agent of WTBPS. Meanwhile, $P_{\mathrm{G},u}^{t}$ can simultaneously coordinate with dispatchable loads $P_{\mathrm{D},u}^{t}$ with reconfigurable HVDNs. For every $t \in T_{\mathrm{s}}$, constraint (6.1) can be cast at bus i_{h} subject to transmission power $P_{\mathrm{T},u} \in\left[(1-\delta \%) P_{\text{base}},(1+\delta \%) P_{\text{base}}\right] \frac{1}{2}$ on tie-lines.

$$P_{W,u}^{t}+P_{G,u}^{t}-P_{D,u}^{t}=P_{T,u}^{t}, \quad (1-\delta\%)P_{\text{base}} \le P_{T,u}^{t} \le (1+\delta\%)P_{\text{base}} \tag{6.1}$$

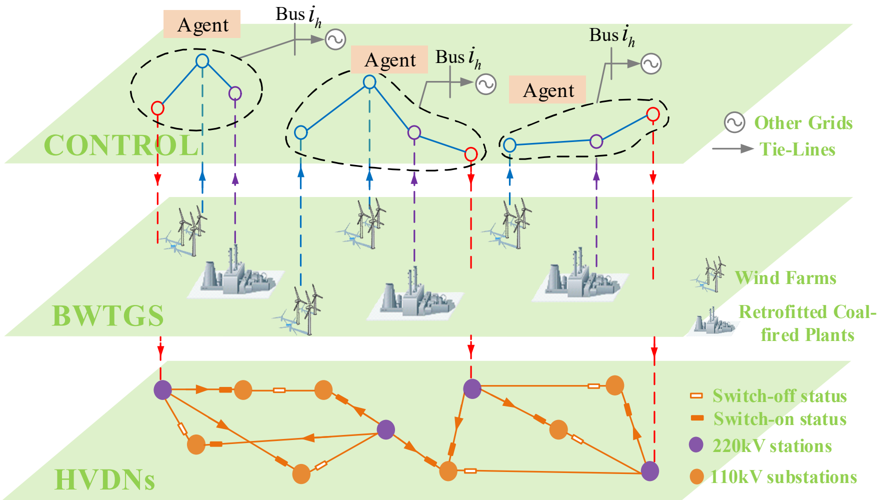

Fig. 6.1 An illustration of WTBPS consisting of the HVDNs layer (bottom), a wind-thermal-bundled layer (medium) and a control layer (top). In the bottom HVDNs layer, load flows are indicated with arrows. The vertical dashed lines connect the nodes in the bottom and medium layers, and to nodes in the top layer, which aggregate at bus i_h by different agents. Also, bus i_h in each agent is a starting node of tie-lines to connect other grids.

6.1.2 Operational Constraints of Retrofitted Coal-fired Units

Retrofitting flexibility measures consist of upgrading the control system, reducing the wall thickness of key components, auxiliary firing with dried lignite ignition burner in booster operation, and so forth [77]. These measures to increase flexibility have been widely employed in coal-fired plants in recent years. Table 6.1 shows the main differences between conventional coal-fired plants without retrofits and retrofitted coal-fired plants. Note that the ramp rate is equal to the ramping margin per minute dividing the corresponding rated capacity. In this chapter, we also declare that the ramp rate is on a minute level, whereas operational, untightened and tightened ramping (ramp-up/down) margins or boundaries or constraints between t-1 and t are on a dispatch period ΔT level.

As clearly shown in Table 6.1, conventional coal-fired plants without retrofits are inherently less flexible than retrofitted coal-fired plants in the minimum load level, ramp rate utilization, and hot and cold start-up time. As merits, the minimum load level of retrofitted coal-fired plants can be reduced to 15–35% of the rated power, and the ramp rate can be enhanced to 2–6% per minute of rated power, any of which contributes to a flexible rolling dispatch of WTBPS. The ramping limit is a linear function of the unit's generating output [78].

Table 6.1. Differences between conventional and retrofitted coal-fired plants

Items	Conventional power plants (without retrofits)	Retrofitted coal-fired power plants
Minimum load level (%)	50-60	15-35
Ramp rate (min/%)	0.6–2	2–6
Hot start-up time (h)	3-5	1.5-4
Cold start-up time (h)	5-8	5-6

However, experimentally measuring ramping limits with respect to each output power point is very tough in practice. In this regard, we adopt the upper envelope to approximate the ramping limits per minute so as to capture the dynamic ramp rates with respect to different output power points. Fig. 6.2 displays the historical ramp rates (%/min) of the retrofitted coal-fired plant rated in 600 MW capacity in northern China. The x-axis refers to the percentage of the output power of this coal-fired unit, while the y-axis denotes the operational ramp rates between two consecutive periods (%/min). Before retrofits, the ramp rate of this 600MW coal-fired plant is the designed 1.1%/min, and the minimum load level is 60% of the rated capacity.

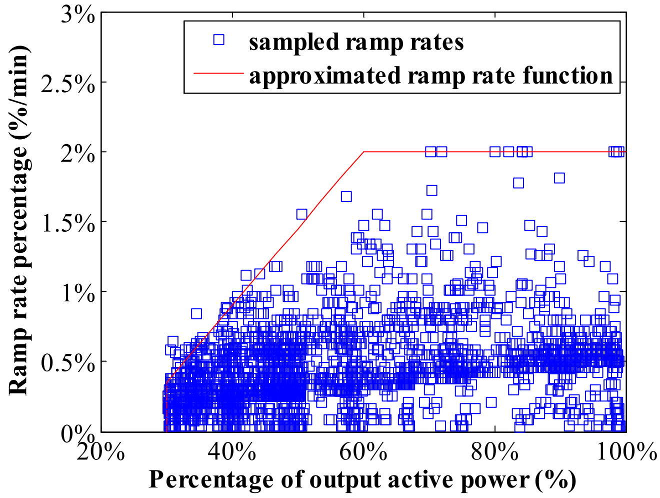

Fig.6.2. Historical ramp rates for the retrofitted coal-fired unit.

Fig. 6.2 shows 2, 500 samples of operational ramp rates with respect to different output power points, where the minimum load level is reduced to 30% and the ramp rate is improved to 2%. For these sampled points, a linear function in the red line segment is the upper envelope as the dynamic ramp rates. It is observed that the operational ramp rate is fixed to 2% when the output power exceeds 60%. Between 30% and 60%, the ramping limit is an approximated linear function of the unit's generating output. Therefore, the appropriate dynamic ramp rates $v_{i,u}^{t}$ (%/min) at time t can be reasonably treated as a linear function of output generation power, which yields

$$v_{i,u}^{t} = \begin{cases} a \cdot r_{i,u}^{t} - b, & r_{i,u}^{t} \le d \\ c, & r_{i,u}^{t} > d \end{cases} \tag{6.2}$$

where parameter c is determined by the enhanced ramp rate of retrofitted coal-fired units, while parameters a, b, and d are estimated from historical ramping data, minimum load level and d=(c+b)/a; and $r_{i,u}^{t}$ refers to the percentage of

$P^t_{\mathrm{G}i,u} / P_{\mathrm{G}i,u,\max}$.

Three kinds of models can be used to describe dynamic ramp rates: approximated linear model by Eq. (6.2), piecewise linear model by approximated thresholds [78], and stepwise linear model by given thresholds [78]. For their main differences, the first kind of ramp-rate expressions is a continuous function, whereas the rest two are a discrete function of thresholds. Since retrofitted coal-fired units can output more stable and accurate power in minutes, our proposed linear model of dynamic ramp rates can capture available operational ramp rates. However, the other two models of dynamic ramp rates cannot provide fast-tracking ability because of their fixed thresholds. For example, to distinguish between proposed and piecewise linear models, Fig. 6.3(a) reveals the ramp rate $v^t_{i,u}$ in a solid blue line using Eq. (6.2) with parameters a=0.055, b=0.013, c=0.02, and d=0.6 and using the piecewise linear model [78] in the dashed green line for a retrofitted coal-fired unit, respectively. The minimum load level is set to 30% of $P_{\mathrm{G}i,u,\max}$. The piecewise linear model is denoted as three fixed thresholds indicated by green line segments in Fig. 6.3(a), which depend on the slopes of segments and the interval ranges between two consecutive periods.

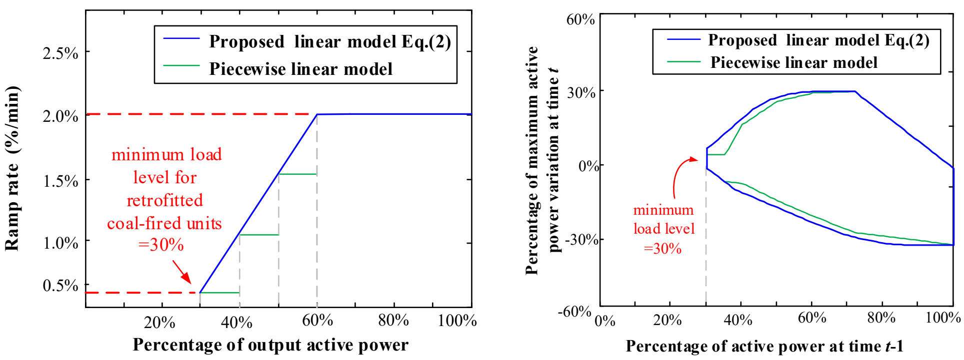

(a) (b)

Fig. 6.3. (a) Proposed and piecewise linear models of dynamic ramp rates per minute, and (b) percentage of maximum active power variations for fifteen minutes using the proposed and piecewise linear models of dynamic ramp rates.

Fig. 6.3(b) presents the maximum active power variations of a retrofitted coal-fired unit under a dispatchable period ΔT=15 minutes by the proposed and piecewise linear models of dynamic ramp rates, where *x*-axis refers to $y_{i,u}^{t-1}$ and *y*-axis indicates the percentage of maximum active power variations $y_{i,u}^{t}$ at time *t*. In this figure, $\Delta y_{i,u}^{t}$ can be sketched out by blue curves and several green line segments, which correspond to the proposed and piecewise linear models shown in Fig. 6.3(a), respectively. The maximum active power variations in blue line segments surround the area enclosed by green line segments, showing that its area is smaller than the blue one, especially when $r_{i,u}^{t} \leq 60\%$. In other words, Eq. (6.2) is a more adaptable solution to the tremendous wind power fluctuation challenges, especially during peak shaving stages. Moreover, the gaps between these two areas in Fig. 6.3(b) clearly indicate that using the piecewise linear model can result in suboptimal dispatch solutions. Thus, it can be concluded that the piecewise linear model cannot be used to output ramp-up/down margins of retrofitted coal-fired units during a dispatch period ΔT=15 min accurately.

Without loss of generality, $r_{i,u}^{t}$ can be analytically deduced as (6.3a)-(6.3d) for upper boundaries as ramp-up margins and (6.4a)-(6.4d) for lower boundaries as ramp-down margins under a dispatchable period ΔT in the ($r_{i,u}^{t-1}$, $r_{i,u}^{t}$)-space. Therefore, the operational ramping constraints are expressed as:

$$r_{i,u}^{t} \leq r_{i,u}^{t-1} + c \cdot (\Delta T - 1) \quad if\ r_{i,u}^{t-1} \geq d \tag{6.3a}$$

$$r_{i,u}^{t} \le (r_{i,u}^{t-1} - b/a)(a+1)^{\Delta T-1} + b/a \quad if\ r_{i,u}^{t-1} \le \xi_{i,u} \tag{6.3b}$$

$$r_{i,u}^{t} \le 1 \tag{6.3c}$$

$$r_{i,u}^{t} \le (r_{i,u}^{t-1} - b/a)(a+1)^{\eta-1} + b/a + c\cdot(\Delta T - \eta)\ if\ \xi_{i,u} < r_{i,u}^{t-1} < d \tag{6.3d}$$

$$r_{i,u}^{t} \ge r_{i,u}^{t-1} - c\cdot(\Delta T - 1) \quad if\ r_{i,u}^{t-1} \ge \chi_{i,u} \tag{6.4a}$$

$$r_{i,u}^{t} \ge (r_{i,u}^{t-1} - b/a)(1-a)^{\Delta T-1} + b/a \quad if\ r_{i,u}^{t-1} \le d \tag{6.4b}$$

$$r_{i,u}^{t} \ge 0.3 \tag{6.4c}$$

$$r_{i,u}^{t} \ge (r_{i,u}^{t-1} - c\cdot(\omega_{i,u} - 1) - b/a)(1-a)^{\Delta T-\omega_{i,u}} + b/a\ if\ d < r_{i,u}^{t-1} < \chi_{i,u} \tag{6.4d}$$

where $\xi_{i,u} = \dfrac{d - b/a}{(a+1)^{\Delta T-1}} + \dfrac{b}{a}$, $\chi_{i,u} = d + c(\Delta T - 1)$, and $d = (c+b)/a$, $\eta_{i,u} = round\ (\ln(c/(a\cdot r_{i,u}^{t-1} - b))/\ln(a+1) + 1)$, and $\omega_{i,u}$ $=round((r_{i,u}^{t-1} - d)/c+1)$, in which $round(\cdot)$ refers to a function of round towards negative infinity.

An intuitive explanation for ramping margins is given under different dispatch periods ΔT scaled in 60 minutes, 30 minutes, 15 minutes, and 5 minutes in 2-dimensional Fig. 6.4 with the above-mentioned parameters. This figure shows that a longer dispatch period ΔT has larger ramp-up/down margins than a shorter dispatch period. For instance, when ΔT=15min and $r_{i,u}^{t-1} = 60\%$, the ramp-up band lies in [60%, 88%], while the ramp-down range varies from 60% to 37%; whereas when ΔT=60min, the ramp-up and ramp-down bands can reach 100% and 30% for any $r_{i,u}^{t-1}$. This also uncovers that conventional ramping constraints, namely generation level changes between two consecutive dispatch periods below fixed ramping margins, are approximate if ΔT<60min and are redundant when ΔT=60 min.

Since some retrofitted coal-fired plants have more than 2% ramp rate, we depict ramp-up/down boundaries under ΔT=15min with the fixed parameters a=0.055 and d=0.6 and different sets of parameters c and $b = a\cdot d - c$ in Fig. 6.5. Fig. 6.5

suggests that larger parameter c results in larger ramp-up/down margins under ΔT =15min for the better quick-response capacity of coal-fired plants.

With the loss of generality, we depict (6.3a)-(6.4d) for boundaries as shown in Fig. 6.6, where all line segments $\overline{CD}$, $\overline{AB}$,and $\overline{DE}$ refer to three linear constraints (6.3a)-(6.3c); $\overline{FG}$, $\overline{HI}$ and $\overline{IJ}$ refer to another three linear constraints (6.4a)-(6.4c), and two green curves $\overset{\frown}{BC}$ and $\overset{\frown}{HG}$ indicate nonlinear constraints indicated in (6.3d) and (6.4d).

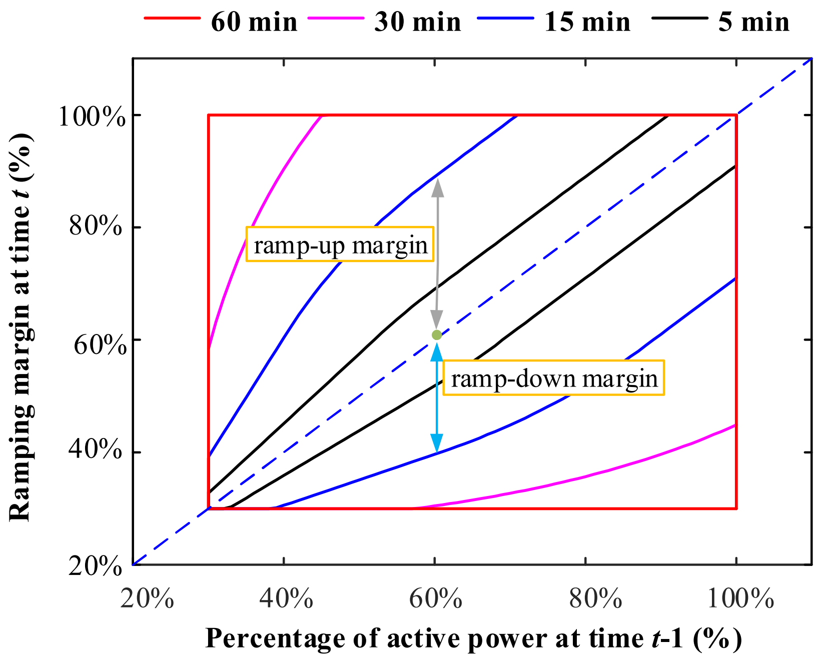

Fig. 6.4. Two-dimensonal ramping boundaries under different dispatch periods.

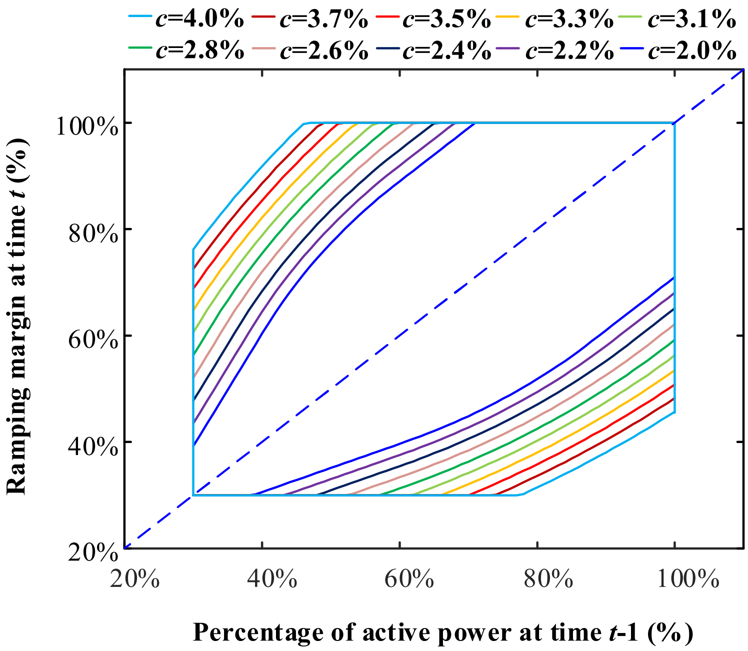

Fig. 6.5 Ramping boundaries under ΔT=15 minutes with different sets of parameters c and b.

We can prove these two nonlinear constraints as a convex function and a concave function, respectively.

Proof: For (6.3d) and (6.4d), it is assumed that the $\widehat{BC}$ and $\widehat{HG}$ functions are continuous and η *and* ω are continuous variables. In terms of (6.3d), let $f(x)=(x-b/a)(a+1)^{\eta-1}+b/a+c\cdot(\Delta T-\eta)$ where $x=r_{i,u}^{t-1}$, we can deduce the following equations:

$$\begin{cases} f'=(a+1)^{\eta-1}+(x-b/a)[(a+1)^{\eta-1}]'-c\cdot\eta' \\ [(a+1)^{\eta-1}]'=(a+1)^{\eta-1}\ln(a+1)\cdot\eta' \\ [(a+1)^{\eta-1}]''=(a+1)^{\eta-1}\ln(a+1)(\ln(a+1)\cdot(\eta')^2+\eta'') \\ \eta'=-a/[(ax-b)\ln(a+1)], \quad \eta''=a^2/[(ax-b)^2\ln(a+1)] \end{cases} \tag{6.5}$$

Based on the above, the resultant second derivative of $f(x)$ can be given by

$$f''=2[(a+1)^{\eta-1}]'+(x-b/a)[(a+1)^{\eta-1}]''-c\cdot\eta'' \tag{6.6}$$

Notably, $\eta'<0, \eta''>0$ hold for $\forall x\in(b/a,d)$. With (6.5), we obtain

$$[(a+1)^{\eta-1}]'<0, \quad [(a+1)^{\eta-1}]''>0 \tag{6.7}$$

From Eq.(6.6), we calculate $\Delta h = [(a+1)^{\eta-1}]' + \varepsilon \cdot [(a+1)^{\eta-1}]''$, where $\varepsilon = x - b/a > 0$.

$$\Delta h = (a+1)^{\eta-1} \ln(a+1) \{ \eta' - \varepsilon \ln(a+1)(\eta')^2 - \varepsilon \eta'' \} \tag{6.8}$$

We substitute $\eta'' = c \ln(a+1)(\eta')^2$ from Eq. (6.5) into Eq. (6.8), and obtain

$$\Delta h = \eta'(a+1)^{\eta-1} \ln(a+1) \{ 1 - \varepsilon \ln(a+1) \eta'(1-c) \} \tag{6.9}$$

It is clear that $\Delta h<0$ due to $\eta' < 0$, $\{1 - \varepsilon \ln(a+1)\eta'(1-c)\} > 0$. Consider $\Delta h<0$ and $[(a+1)^{\eta-1}]'<0$, thus causing $f''=\Delta h+[(a+1)^{\eta-1}]' - c\cdot\eta''<0$. This proves that $f(x)$ is a convex function for $\forall x \in (b/a, d)$.

For (6.4d), let $g(x) = (x - c\cdot(\omega-1) - b/a)(1-a)^{\Delta T-\omega} + b/a$ where $x = y_{i,u}^{t-1}$, and we similarly yield the following equations:

$$\begin{cases} g' = (1-a)^{\Delta T-\omega}(1 - c\cdot\omega') + (x - c\cdot(\omega-1) - b/a)[(1-a)^{\Delta T-\omega}]' \\ [(1-a)^{\Delta T-\omega}]' = -(1-a)^{\Delta T-\omega} \ln(1-a)\cdot\omega' \\ [(1-a)^{\Delta T-\omega}]'' = -(1-a)^{\Delta T-\omega} \ln(1-a)\cdot(\omega'' - \ln(1-a)\cdot(\omega')^2) \\ \omega' = 1/c, \quad \omega'' = 0 \end{cases} \tag{6.10}$$

Based on the above, we further achieve the second derivative of $g(x)$

$$\begin{aligned} g'' = -\omega'(1-a)^{\Delta T-\omega} \ln(1-a)(1 - c\cdot\omega') + (x - c\cdot(\omega-1) - b/a)[(1-a)^{\Delta T-\omega}]'' \\ + [(1-a)^{\Delta T-\omega}]' \end{aligned} \tag{6.11}$$

Notably, $\omega' > 0$, $\omega'' = 0$ hold for $\forall x \in (d, d + c\cdot(\Delta T - 1))$. Regarding $c\cdot(\omega-1) = x - d$, $d=(b+c)/a$, and $\ln(1-a)<0$, we obtain $g''>0$. This proves that $g(x)$ is a concave function for $\forall x \in (d, d + c\cdot(\Delta T - 1))$. ■

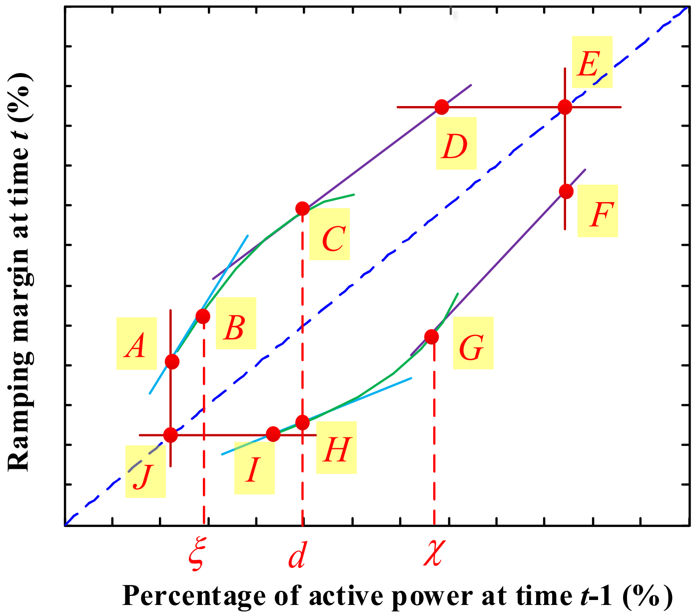

Fig. 6.6. General ramping boundaries of retrofitted coal-fired units.

Moreover, the spinning reserve requirement of WTBPS should be considered before performing an economic dispatch. The spinning reserve capacity provided by retrofitted coal-fired units should not exceed the system spinning reserve capacity:

$$\sum_{i=1}^{N_{\mathrm{G}}}(1-r_{i,u}^{t})P_{Gi,u,\max} \geq P_{u}^{\mathrm{spin}} \tag{6.12}$$

where P_u^{spin} refers to system spinning reserve capacity for the u-th agent of WTBPS and u=1,2,…,N_u. Considering wind turbines have no contribution to the spinning reserve, P_u^{spin} is assumed to be 10% of the transmission power minus the wind power rated capacity [101].

6.1.3 Distribution-Level Topology Optimization for HVDNs

The load switch-over operations imposed on HVDNs can help mitigate wind curtailment and moderate generation costs for WTBPS for a look-ahead rolling economic dispatch task. Direct supply connection (DSC) and serial supply connection

(SSC) are typical grid-scale structures for 110kV HVDNs as shown in Fig. 6.7, where P_c^t and P_d^t are active loads at 110kV substations C and D, respectively; P_{A1}^t and P_{A2}^t refer to the total active dis-patchable loads in 220kV stations A1 and A2, respectively.

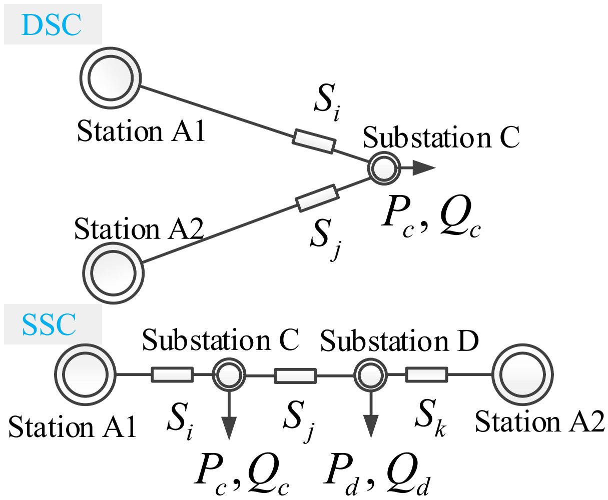

Fig. 6.7. Two typical HVDNs of DSC and SSC.

Thanks to simple topological units of HVDNs just with one or two buses, the well-known simplified *DistFlow* equations with negligible power loss can achieve acceptable accuracy. As reference [90] reported, nonlinear terms are negligible compared to linear terms, typically on the order of 1% error introduced. Distribution systems generally have relatively flat voltage profiles due to voltage automatic control devices with a small approximation error at about ±1%. In this regard, we develop simplified power balance equalities as linear matrix equalities [82] for which the complexity of HVDN reconfiguration acting as non-convex and nonlinear problems [102] can be greatly reduced.

As indicated in Fig. 6.8, the general form of (6.13a) and (6.13b) can be reformulated as $\boldsymbol{P}_{\mathrm{S},j}^{t}=\boldsymbol{L}_{j}^{t}\boldsymbol{S}^{t}+\boldsymbol{b}_{j}^{t}$, $\forall j\in N_{\mathrm{T}},\forall t\in T_{\mathrm{s}}$, where $\boldsymbol{P}_{\mathrm{S},j}^{t}$ denotes total active power on transformers in the j-th station and $\boldsymbol{L}_{j}^{t}$ and $\boldsymbol{b}_{j}^{t}$ refer to vectors of load coefficients at time t whose j-th element indicates the j-th station. Specifically, when the connected bus for the u-th agent of WTBPS belongs to 220kV station j, then $\boldsymbol{P}_{\mathrm{D},u}^{t}=\boldsymbol{P}_{\mathrm{S},j}^{t}$ holds at time t; for other stations, $\boldsymbol{P}_{\mathrm{S},j}^{t}$ should satisfy (6.13a). In addition, branch capacity constraints (6.14b) for cables and overhead lines in HVDNs are also considered in LTS model.

$$\begin{bmatrix} P_{\mathrm{A1}}^{t} \\ P_{\mathrm{A2}}^{t} \end{bmatrix} = \boldsymbol{L}^{t}\begin{bmatrix} S_{1}^{t} \\ S_{2}^{t} \end{bmatrix} + \boldsymbol{b}^{t} = \begin{bmatrix} P_{\mathrm{c}}^{t} & 0 \\ 0 & P_{\mathrm{c}}^{t} \end{bmatrix}\begin{bmatrix} S_{1}^{t} \\ S_{2}^{t} \end{bmatrix} + \boldsymbol{0} \tag{6.13a}$$

$$\begin{bmatrix} P_{\mathrm{A1}}^{t} \\ P_{\mathrm{A2}}^{t} \end{bmatrix} = \boldsymbol{L}^{t}\begin{bmatrix} S_{3}^{t} \\ S_{4}^{t} \\ S_{5}^{t} \end{bmatrix} + \boldsymbol{b}^{t} = \begin{bmatrix} P_{\mathrm{c}}^{t}+P_{\mathrm{d}}^{t} & P_{\mathrm{d}}^{t} & 0 \\ 0 & P_{\mathrm{c}}^{t} & P_{\mathrm{c}}^{t}+P_{\mathrm{d}}^{t} \end{bmatrix}\begin{bmatrix} S_{3}^{t} \\ S_{4}^{t} \\ S_{5}^{t} \end{bmatrix} + \begin{bmatrix} -P_{\mathrm{d}}^{t} \\ -P_{\mathrm{c}}^{t} \end{bmatrix} \tag{6.13b}$$

$$0 \le P_{\mathrm{S},j}^{t} \le (n_{\mathrm{s},j}\cdot S_{\mathrm{N},j}),\ \forall j\in N_{\mathrm{T}} \tag{6.14a}$$

$$0 \le P_{\mathrm{S},j}^{t} \le S_{\mathrm{L},j},\ \forall j\in N_{T} \tag{6.14b}$$

where $n_{\mathrm{s},j}$ refers to the number of transformers in the j-th station; $S_{\mathrm{N},j}$ denotes the single transformer rated capacity in the j-th station; $S_{\mathrm{L},j}$ indicates the branch capacity which branch connects to the j-th station.

Moreover, the approximate voltage drop for a branch section $\{m,k\}$ can be summarized based on simplified *DistFlow* equations. According to $v_m^2 - v_k^2 = 2(R_{mk}P_{mk}^{t} + X_{mk}Q_{mk}^{t})$ in simplified *DistFlow* equations, we rewrite this equation:

$$\begin{aligned} R_{mk}P_{mk}^{t} + X_{mk}Q_{mk}^{t} &= (v_m^2 - v_n^2)/2 = \frac{(v_m - v_n)^2}{2} + v_n(v_m - v_n) \\ &= \frac{(\Delta v_{mk}^{t})^2}{2} + v_n\Delta v_{mk}^{t} \le \frac{(\Delta \bar{v})^2}{2} + \bar{v}\cdot\Delta\bar{v} \end{aligned} \tag{6.15}$$

where R_{mk} and X_{mk} refer to resistance, reactance of branch (m,k), and P_{mk}^{t} and Q_{mk}^{t} denote active and reactive power flow on branch (m,k), $\overline{v}$ is the maximum voltage profile, and $\Delta\overline{v}$ refers to the allowable voltage drop, e.g. $\Delta\overline{v}=0.1$ p.u. for DNs [82].

Let allowable squared voltage drop be $\Delta\overline{V}=\frac{(\Delta\overline{v})^2}{2}+\overline{v}\cdot\Delta\overline{v}$, and since DSC has a fixed directional power flow, we can construct linear voltage security constraints with the allowable ranges of voltage profiles:

$$\begin{bmatrix} R_{\text{A1-C}}P_c^t+X_{\text{A1-C}}Q_c^t & R_{\text{A2-C}}P_c^t+X_{\text{A2-C}}Q_c^t \end{bmatrix}\begin{bmatrix} S_1^t \\ S_2^t \end{bmatrix}\leq\Delta\overline{V} \tag{6.16}$$

The power flow between substations C and D in SSC depends on the circuit switching status of circuit breakers among S_3^t, S_4^t and S_5^t. Given that this bi-directional power flow for different circuit switching variables among S_3^t, S_4^t and S_5^t, we can establish two linear equivalent voltage security constraints:

$$\begin{bmatrix} \lambda_1 & 0 & R_{\text{C-D}}P_{\text{d}}^t+X_{\text{C-D}}Q_{\text{d}}^t \\ 0 & \lambda_2 & R_{\text{C-D}}P_{\text{c}}^t+X_{\text{C-D}}Q_{\text{c}}^t \end{bmatrix}\begin{bmatrix} S_3^t \\ S_4^t \\ S_5^t \end{bmatrix}-\begin{bmatrix} R_{\text{C-D}}P_{\text{d}}^t+X_{\text{C-D}}Q_{\text{d}}^t \\ R_{\text{C-D}}P_{\text{c}}^t+X_{\text{C-D}}Q_{\text{c}}^t \end{bmatrix}\leq\begin{bmatrix} \Delta\overline{V} \\ \Delta\overline{V} \end{bmatrix} \tag{6.17}$$

Where $\lambda_1=R_{\text{A1-C}}P_c^t+X_{\text{A1-C}}Q_c^t+R_{\text{C-D}}P_{\text{d}}^t+X_{\text{C-D}}Q_{\text{d}}^t$, $\lambda_2=R_{\text{A2-D}}P_{\text{d}}^t+X_{\text{A2-D}}Q_{\text{d}}^t+R_{\text{C-D}}P_{\text{c}}^t+X_{\text{C-D}}Q_{\text{c}}^t$; other symbols in (6.16) and (6.17) can be found in *Nomenclature*.

It can be perceived that rearranging voltage profile expressions from simplified *DistFlow* equations leads to a more compact matrix form (6.16) and (6.17). Compared to [82], (6.16) and (6.17) have the same accuracy in the optimal circuit switch scheme yet with a small number of power flow variables. Additionally, frequent circuit switching will reduce the remaining useful life of circuit breakers. Thus, limiting the switching times of each circuit breaker over a rolling window is of importance [103].

Accordingly, this constraint is bounded by

$$\sum_{t=1}^{N_{Ts}} (S_j^t - S_j^{t-1})^2 = \sum_{t=1}^{N_{Ts}} ((S_j^t)^2 + (S_j^{t-1})^2 - 2 \cdot S_j^t S_j^{t-1}) \le N_w \tag{6.18}$$

where N_{Ts} refers to the number of time-horizons in a rolling window and N_w denotes the number of allowable switching actions.

Consider the property of binary number operations $(S_j^t)^2 = S_j^t$, and let $z_j^t = S_j^t + S_j^{t-1}$ that satisfy $z_j^t \in \{0,1\}$. By using piecewise McCormick envelopes [100], we exactly replace $z_j^t = S_j^t + S_j^{t-1}$ with

$$z_j^t \ge S_j^t + S_j^{t-1} - 1,\ z_j^t \le S_j^t,\ z_j^t \le S_j^{t-1} \tag{6.19}$$

Due to $z_j^t = S_j^t + S_j^{t-1}$, constraint (6.18) can be subsequently rearranged as

$$\sum_{t=1}^{N_{Ts}} (S_j^t + S_j^{t-1} - 2 \cdot z_j^t) \le \tau \tag{6.20}$$

As stated in Subsection 6.1.1, the maximum amount of dis-patchable loads only accounts for nearly 5%-30% capacity of WTBPS, which directly indicates retrofitted coal-fired units play a major role and load transfer operations only play a secondary role in tracking wind power of WTBPS. Thus, the substantial switching times of circuit breakers cannot be realistic for economic dispatch problems.

Alternatively, the radial operation requirement for HVDNs is essential to mesh topological units. Radial structures of DSC and SSC can be held from the observation of Fig. 6.7:

$$\text{DSC:}\quad S_1^t + S_2^t = 1 \qquad \text{SSC:}\quad S_3^t + S_4^t + S_5^t = 2. \tag{6.21}$$

Hereby, a more simplified LTS model (6.13)-(6.21) can be constructed for the following rolling economic dispatch model in Subsection 6.3.

6.2 Tightened Ramping Constraints

6.2.1 Linear Ramping Constraints

As displayed in Fig. 6.7(a), to simplify convex constraints (6.3d) and (6.4d), we replace arcs $\widehat{BC}$ and $\widehat{HG}$ by connecting a line between B and C and a line from H to G. Clearly, $\widehat{BC}$ and $\widehat{HG}$ are strictly tighter than arcs $\widehat{BC}$ and $\widehat{HG}$, which ramping area is a decagon whose vertexes are ABCDEFGHIJ. We approximate convex and concave constraints in (6.3d) and (6.4d) as (6.22), forming the linear ramp-up/down constraints of retrofitted coal-fired units.

$$\begin{bmatrix} 1 & -A_{\text{upper}} \\ -1 & A_{\text{lower}} \end{bmatrix} \begin{bmatrix} r_{i,u}^{t} \\ r_{i,u}^{t-1} \end{bmatrix} + \begin{bmatrix} -B_{\text{upper}} \\ B_{\text{lower}} \end{bmatrix} \le 0 \tag{6.22}$$

where A_{upper}, B_{upper}, A_{lower} and B_{lower} are obtained constants calculating from linear equations $\overline{BC}$ and $\overline{HG}$, given as:

$$\begin{cases} A_{\text{upper}} = \dfrac{a(\Delta T-1)\,(a+1)^{\Delta T-1}}{(a+1)^{\Delta T-1}-1} \\ A_{\text{lower}} = \dfrac{1-(1-a)^{\Delta T-1}}{a(\Delta T-1)} \end{cases}, \quad \begin{cases} B_{\text{upper}} = d - \dfrac{\Delta T-1}{(a+1)^{\Delta T-1}-1}\cdot\left(c+b(a+1)^{\Delta T-1}\right) \\ B_{\text{lower}} = d - \dfrac{(1-(1-a)^{\Delta T-1})d}{a(\Delta T-1)} - \dfrac{c(1-(1-a)^{\Delta T-1})}{a} \end{cases} \tag{6.23}$$

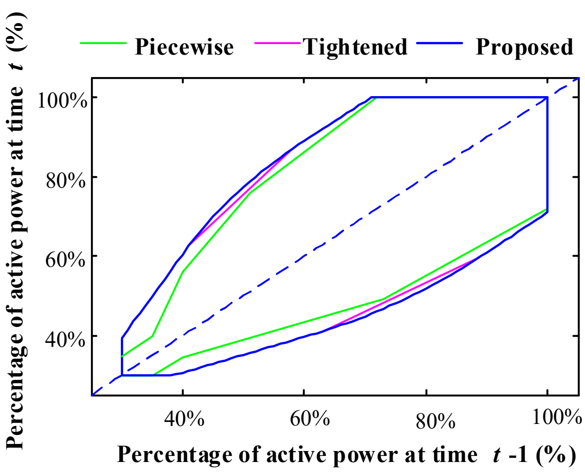

(a)

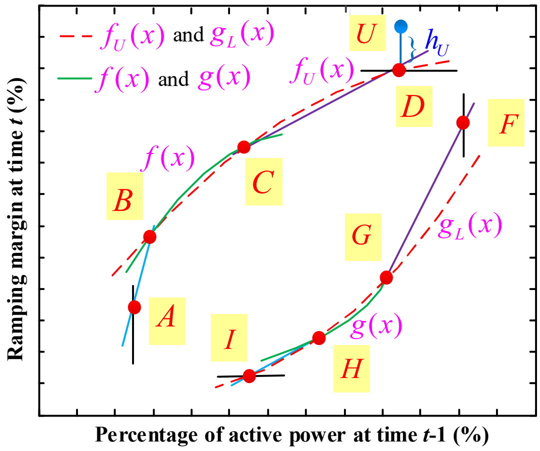

(b)

Fig. 6.8. (a) Ramping boundaries of a retrofitted coal-fired unit; (b) quadratic functions for $f(x)$ and $g(x)$.

Fig. 6.8(a) compares the ramping boundaries using the piecewise and proposed linear models, and tightened ramp-up/down margins by linear ramping constraints (6.22) under ΔT=15 minutes, respectively. As suggested in Fig. 6.8(a), the tightened ramping boundaries in pink line are very close to ramping boundaries using the proposed linear model in blue line, and also are more accurate than ramping boundaries using the piecewise linear model in green line, especially during peak shaving stages.

Let us derive the maximum inner-approximated errors Δe_U and Δe_L between linear and untightened ramp-up/down margins. We can write the maximum error of the linear retrofitted ramp-up constraint (6.22) as

$$\Delta f_{upper}(x) = f(x) - A_{\text{upper}} x - B_{\text{upper}} \tag{6.24}$$

where A_{upper}, B_{upper} can be found in (6.23).

Herein, d$\Delta f_{upper}(x)$/dx=0, yielding

$$-c \cdot \eta' - A_{\text{upper}} = 0 \tag{6.25}$$

Substituting $\eta' = -a / [(ax-b)\ln(a+1)]$ from Eq. (6.26), we can obtain the optimal x^* as

$$x^* = \frac{c}{A_{\text{upper}} \ln(a+1)} + \frac{b}{a} \tag{6.26}$$

Consequently, the maximum error between tightened and untightened ramp-up margins can be calculated in

$$\begin{aligned} \Delta f_{upper}(x^*) &= f(x^*) - A_{\text{upper}} x^* - B_{\text{upper}} \\ &= (\frac{c}{A_{\text{upper}} \ln(a+1)})(a+1)^{\eta^*-1} + \frac{b}{a}(1 - A_{\text{upper}}) + c \cdot (\Delta T - \eta^*) - \frac{c}{\ln(a+1)} - B_{\text{upper}} \end{aligned} \tag{6.27}$$

where $\eta^* = round(-\ln(\frac{a}{A_{\text{upper}} \ln(a+1)}) / \ln\left(a+1\right) + 1)$.

Moreover, the maximum error of the linear ramp-down constraint (6.22) can be summarized as

$$\Delta f_{lower}(x) = A_{\text{lower}} x + B_{\text{lower}} - g(x) \tag{6.28}$$

where A_{lower}, B_{lower} can be found in (6.23).

According to d$\Delta f_{lower}(x)$/dx=0 and $c(\omega$-1)=(x-d), we express

$$A_{\text{lower}} - (1-a)^{\Delta T - \omega} \frac{-\ln(1-a)}{a} = 0 \tag{6.29}$$

As a result, we can obtain the optimal x^* as

$$x^* = c(\Delta T - \frac{\ln(-\frac{aA_{\text{lower}}}{\ln(1-a)})}{\ln(1-a)} - 1) + d \tag{6.30}$$

The maximum error between linear and untightened ramp-down margins can be calculated in

$$\Delta f_{lower}(x^*) = A_{\text{lower}}x^* + B_{\text{lower}} - g(x^*) \tag{6.31}$$

where $\omega^* = round(\Delta T - \ln\left(-\frac{aA_{\text{lower}}}{\ln(1-a)}\right)/\ln(1-a))$.

6.2.2 SOC Ramping Constraints

As mentioned above, we simplify convex constraints (6.3d) and (6.4d) as linear constraints; However, it may induce approximations, which confine actual ramp-up/down margins of retrofitted coal-fired units. We consider drawing a tightened quadratic curve to replace arcs $\overset{\frown}{BC}$ and $\overset{\frown}{HG}$. For convenience, we define $x = r_{i,u}^{t-1}$ and then ramp-up/down margin functions *f*(*x*) and *g*(*x*) for arcs $\overset{\frown}{BC}$ and $\overset{\frown}{HG}$ are

$$\begin{cases} f(x) = (x - b/a)(a+1)^{\eta-1} + b/a + c\cdot(\Delta T - \eta) \\ g(x) = (x - c\cdot(\omega-1) - b/a)(1-a)^{\Delta T-\omega} + b/a \end{cases} \tag{6.32}$$

where $f(x)$ and $g(x)$ are defined as Lipschitz continuous functions. Let $f_U(x) = a_{f,\text{upper}}\cdot x^2 + b_{f,\text{upper}}\cdot x + c_{f,\text{upper}}$ and $g_L(x) = a_{f,\text{lower}}\cdot x^2 + b_{f,\text{lower}}\cdot x + c_{f,\text{lower}}$ represent the quadratic functions to approximate *f*(*x*) and *g*(*x*), where $a_{f,\text{upper}}$, $b_{f,\text{upper}}$, $c_{f,\text{upper}}$ and $a_{f,\text{lower}}$, $b_{f,\text{lower}}$, $c_{f,\text{lower}}$ are quadratic coefficients of $f_U(x)$ and $g_L(x)$, respectively.

As displayed in Fig. 6.8(b), let us prove the quadratic constraint $f_U(x)$ in red dashed lines as arc $\overset{\frown}{BCD}$ in dashed lines has the minimal inner-approximated error that can be used to approximate $f(x)$. We assume that our initial point is an arbitrary U on the vertical line of point D subject to $x_{\text{U}} = x_{\text{D}}$ and $v_{\text{U}} = v_{\text{D}} + h_{\text{U}}$. With this specified point U and fixed points B and C, we can determine a specific quadratic function to represent arc $\overset{\frown}{BCU}$. Consequently, we have

$$\begin{bmatrix} x_B^2 & x_B & 1 \\ x_C^2 & x_C & 1 \\ x_U^2 & x_U & 1 \end{bmatrix} \begin{bmatrix} a_{f,\text{upper}} \\ b_{f,\text{upper}} \\ c_{f,\text{upper}} \end{bmatrix} = \Gamma \begin{bmatrix} a_{f,\text{upper}} \\ b_{f,\text{upper}} \\ c_{f,\text{upper}} \end{bmatrix} = \begin{bmatrix} y_B \\ y_C \\ y_D + h_U \end{bmatrix} \tag{6.33}$$

where Γ is the coefficient matrix of $f_U(x)$, and x_B, x_C, x_D and x_U refer to x-coordinates of points B, C, D and U and y_B, y_C, y_D and y_U refer to y-coordinates of points B, C, D and U, respectively.

Since Γ is invertible, the quadratic coefficients $a_{f,\text{lower}}$, $b_{f,\text{lower}}$ and $c_{f,\text{lower}}$ can be expressed as,

$$\begin{bmatrix} a_{f,\text{upper}} \\ b_{f,\text{upper}} \\ c_{f,\text{upper}} \end{bmatrix} = \Gamma^{-1} \begin{bmatrix} y_B \\ y_C \\ y_D \end{bmatrix} + \Gamma^{-1} \begin{bmatrix} 0 \\ 0 \\ h_U \end{bmatrix} = \Gamma^{-1} \begin{bmatrix} y_B \\ y_C \\ y_D \end{bmatrix} - \frac{1}{|\Gamma|} \begin{bmatrix} x_C - x_B \\ x_B^2 - x_C^2 \\ x_C^2 x_B - x_B^2 x_C \end{bmatrix} \cdot h_U \tag{6.34}$$

where $|\Gamma|$ is the moduli of Γ and Γ is only with respect to the x-coordinates of points B, C, and U. By (6.34), we express $f_U(x)$ as

$$\begin{aligned} f_U(x) &= \begin{bmatrix} x^2 & x & 1 \end{bmatrix} \begin{bmatrix} a_{f,\text{upper}} \\ b_{f,\text{upper}} \\ c_{f,\text{upper}} \end{bmatrix} = \begin{bmatrix} x^2 & x & 1 \end{bmatrix} \left(\Gamma^{-1} \begin{bmatrix} y_B \\ y_C \\ y_D \end{bmatrix} - \frac{x_C - x_B}{|\Gamma|} \begin{bmatrix} 1 \\ -x_C - x_B \\ x_C x_B \end{bmatrix} \cdot h_U \right) \\ &= \left(\Gamma^{-1} \begin{bmatrix} y_B \\ y_C \\ y_D \end{bmatrix} \right)^T \begin{bmatrix} x^2 \\ x \\ 1 \end{bmatrix} + h_U \cdot \Upsilon^T \cdot \begin{bmatrix} x^2 \\ x \\ 1 \end{bmatrix} \end{aligned} \tag{6.35}$$

where $\Upsilon = -\frac{x_C - x_B}{|\Gamma|} \begin{bmatrix} 1 & -x_C - x_B & x_C x_B \end{bmatrix}^T$.

Observing Eq. (6.35), $[x^2\ x\ 1] \cdot \Gamma^{-1} \cdot [y_B\ y_C\ y_D]^T$ is the quadratic function for arc $\widehat{BCD}$. If h_U=0, arc $\widehat{BCD}$ overlaps arc $\widehat{BCD}$. Moreover, for any $\forall x \geq x_C$, we rearrange $\Upsilon^T \cdot \begin{bmatrix} x^2 & x & 1 \end{bmatrix}^T$ as

$$\Upsilon^T \cdot \begin{bmatrix} x^2 & x & 1 \end{bmatrix}^T = -\frac{x_C - x_B}{|\Gamma|} (x^2 - (x_C + x_B)x + x_C x_B) \tag{6.36}$$

where $x_C > x_B$ and $|\Gamma|$<0.

It is clear that $x^2-(x_C+x_B)x+x_Cx_B$ is a quadratic function where the parabola opens upward. The minimization achieves at $x^*=(x_B+x_C)/2$, but $x>x_C>x^*$, so the minimization must be at x_C. The minimal value of Eq. (6.36) yields $-\frac{x_C-x_B}{|\Gamma|}(x_C^2-(x_C+x_B)x_C+x_Cx_B)=0$. Therefore, $\Upsilon^T\cdot\begin{bmatrix}x^2 & x & 1\end{bmatrix}^T\geq 0$ is proven.

With $\Upsilon^T\cdot\begin{bmatrix}x^2 & x & 1\end{bmatrix}^T\geq 0$, if $h_U\neq 0$ means that point U is higher than point D, then we can perceive that $f_U(x)$ can be a monotonically increasing function with respect to h_U for any fixed $\boldsymbol{x}$ from (6.35). If and only if $h_U=0$, then the minimization of $f(x)$-$f_U(x)$ can be achieved, which indicates that the quadratic constraints $\overset{\frown}{BCD}$ has the minimal inner-approximated error for arc $\overset{\frown}{BC}$. It should be noted that $f_U(x_A)$ can be higher than $(0.3-b/a)(a+1)^{\Delta T-1}+b/a$ where $x_A=0.3$. This indicates arc $\overset{\frown}{BCD}$ can envelop point A. Analogously, the quadratic constraint $f_L(x)$ can be justified as arc $\overset{\frown}{IHG}$, which can envelop the point F.

The maximum inner-approximated errors Δs_U and Δs_L between arcs $\overset{\frown}{BCD}$ and $\overset{\frown}{BC}$ and between arcs $\overset{\frown}{IHG}$ and $\overset{\frown}{HG}$ can be obtained by establishing $\mathrm{d}f(x)/\mathrm{d}x = \mathrm{d}f_U(x)/\mathrm{d}x$ and $\mathrm{d}g(x)/\mathrm{d}x = \mathrm{d}g_L(x)/\mathrm{d}x$, respectively. The solutions yield:

$$\frac{a\cdot c}{(a\cdot x_+^*-b)\ln(a+1)}=2a_{f,\mathrm{upper}}x_+^*+b_{f,\mathrm{upper}} \tag{6.37a}$$

$$2a_{f,lower}x_-^*+b_{f,lower}=(1-a)^{\Delta T-\frac{x_-^*-d}{c}-1}\cdot\frac{-\ln(1-a)}{a} \tag{6.37b}$$

where x_+^* and x_-^* denotes the x-coordinates of the maximum inner-approximated errors for arcs $\overset{\frown}{BCD}$ and $\overset{\frown}{IHG}$.

Eq. (6.37a) is a quadratic equation and Eq. (6.37b) is a transcendental equation. Eq. (6.37b) can be dealt with Newton method [104]. With achieved roots x_+^* and x_-^*, the maximum inner-approximated errors Δs_U and Δs_L between quadratic and untightened ramp-up/down margins can be calculated in

$$\Delta s_U = f(x_+^*) - f_U(x_+^*) \ , \ \Delta s_L = g_L(x_-^*) - g(x_-^*) \tag{6.38}$$

Based on the above, the quadratic ramping constraints with minimal inner-approximated errors are given as

$$a_{f,\text{upper}} \cdot (r_{i,u}^{t-1})^2 + b_{f,\text{upper}} \cdot r_{i,u}^{t-1} + c_{f,\text{upper}} \geq r_{i,u}^t \tag{6.39a}$$

$$a_{f,\text{lower}} \cdot (r_{i,u}^{t-1})^2 + b_{f,\text{lower}} \cdot r_{i,u}^{t-1} + c_{f,\text{lower}} \leq r_{i,u}^t \tag{6.39b}$$

where $a_{f,\text{upper}}$, $b_{f,\text{upper}}$, $c_{f,\text{upper}}$, $a_{f,\text{lower}}$, $b_{f,\text{lower}}$, and $c_{f,\text{lower}}$ can be obtained by arcs $\overset{\frown}{BCD}$ and $\overset{\frown}{IHG}$.

To convert this quadratic constraint (6.39a) and (6.39b) in the rotated SOC form, we have

$$\begin{cases} 2 \cdot m_{\text{upper}} \cdot 1/2 \geq \| J_{\text{upper}} \|^2, m_{\text{upper}} = -r_{i,u}^t - \dfrac{b_{f,\text{upper}}^2}{4a_{f,\text{upper}}} + c_{f,\text{upper}} \\ J_{\text{upper}} = \sqrt{-a_{f,\text{upper}}} \cdot r_{i,u}^{t-1} - \dfrac{1}{2} b_{f,\text{upper}} \sqrt{-1/a_{f,\text{upper}}} \end{cases} \tag{6.40a}$$

$$\begin{cases} 2 \cdot m_{\text{lower}} \cdot 1/2 \geq \| J_{\text{lower}} \|^2, m_{\text{lower}} = r_{i,u}^t + \dfrac{b_{f,\text{lower}}^2}{4a_{f,\text{lower}}} - c_{f,\text{lower}} \\ J_{\text{lower}} = \sqrt{a_{f,\text{lower}}} r_{i,u}^{t-1} + \dfrac{1}{2} b_{f,\text{lower}} \sqrt{1/a_{f,\text{lower}}} \end{cases} \tag{6.40b}$$

Making use of the above, we can summarize that linear and SOC operational constraints of retrofitted coal-fired units can be characterized by (6.3a)-(6.3c), (6.4a)-(6.4c), (6.12), (6.27)-(6.28) and (6.3a)-(6.3c), (6.4a)-(4c), (6.12), (6.40a)-(6.40b), respectively.

6.3 Distribution-Level Topology Optimization for Flexibility Enhancement in Look-ahead Rolling Economic Dispatch Approach

6.3.1 Rolling Economic Dispatch Model

With the day-ahead unit commitment scheme and forecasted wind power data, we can establish the economic dispatch model over a rolling window, during which WTBPS maintains steady transmission power within specified bands. Each dispatch involves several look-ahead hours. In general, the wind power forecast for 4–6 hours has relatively low forecast errors [73]. In this study, the look-ahead period is thus set as 5 hours including the current hour and the remaining look-ahead hours in the intra-day stage. This rolling economic dispatch aims to reach the minimum thermal production cost and switch-over operational cost subject to operational constraints of WTBPS. Specifically, the thermal production cost for a horizon of length N_{Ts} is produced by retrofitted coal-fired units; whereas switch-over operational cost is associated with optimal load transfer solutions via HVDNs. In summary, we depict the following look-ahead rolling economic dispatch framework and associated rolling process:

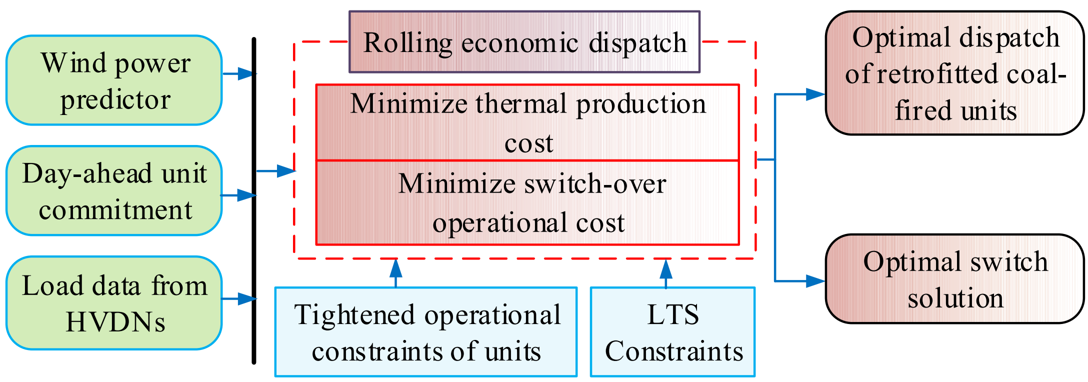

(a)

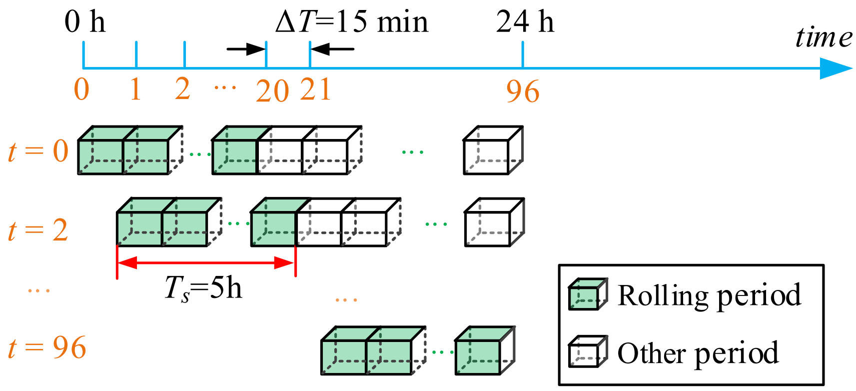

(b)

Fig. 6.9. (a) Look-ahead rolling economic dispatch framework; (b) rolling process.

Since different y_i^t have similar production cost coefficients, we approximately express the coal-fired generation cost F_{o1} as

$$\min_{r_{i,u}^t \in \mathbb{R}} F_{o1} = \sum_{t=1}^{N_{T_s}} \sum_{u=1}^{N_u} \sum_{i=1}^{N_{G,u}} [c_{2i,u}(r_{i,u}^t P_{Gi,u,\max})^2 + c_{1i,u} r_{i,u}^t P_{Gi,u,\max} + c_{0i,u}] \tag{6.41}$$

where $c_{2i,u}$, $c_{1i,u}$ and $c_{0i,u}$ refer to production cost coefficients for the i-th retrofitted coal-fired unit in the u-th agent of WTBPS; $N_{G,u}$ and N_u indicate the total number of retrofitted coal-fired units in the u-th agent and the total number of agents, respectively.

Moreover, addressing the operational cost minimization issue in an LTS task is to seek the smallest number of total circuit switching operation times and the minimum amount of dispatchable loads during a rolling window. This chapter adopts circuit switching service cost $c_{H,u}$ to multiply switching operation times plus purchasing costs of dispatchable loads as $c_{D,u} \cdot (P_{D,u}^t)^2$. As a result, $F_{o2} = \sum_{t=1}^{N_{T_s}} \sum_{u=1}^{N_u} \left\{ c_{D,u} \cdot (P_{D,u}^t)^2 + c_{H,u} \sum_{j=1}^{N_s} (S_j^t - S_j^{t-1})^2 \right\}$. After applying $z_j^t = S_j^t S_j^{t-1}$ to F_{o2}, F_{o2} can be rearranged as

$$F_{o2} = \sum_{t=1}^{N_{T_s}} \sum_{u=1}^{N_u} \left\{ c_{D,u} \cdot (P_{D,u}^t)^2 + c_{H,u} \sum_{j=1}^{N_s} (S_j^t - S_j^{t-1})^2 \right\} \tag{6.42}$$

In light of all these facts, we consider that two objectives are assumed to have equal priorities and weighting coefficients are selected as $\mu_1 = \mu_2 = 1/2$. Thus, a look-ahead rolling economic dispatch model is the minimization of F_o subject to the power balance of tie-lines (6.1), operational limits of retrofitted coal-fired units (6.3a)-(6.3c), (6.4a)-(6.4c) and (6.12), and linear ramping constraints of retrofitted coal-fired units (6.22)-(6.23) or SOC ramping constraints of retrofitted coal-fired units (6.41a) and (6.41b), plus simplified voltage-constrained LTS via HVDNs (6.13)-(6.21).

P1: Rolling economic dispatch model with linear ramping constraints

$$\begin{aligned} &\min_{r_{i,u}^t, P_{D,u}^t, P_{T,u}^t \in \mathbb{R}, S_i^t, z_j^t \in \mathbb{N}} F_o = \mu_1 F_{o1} + \mu_2 F_{o2} \\ &\text{s.t.} \quad (6.1), (6.3a)\text{-}(6.3c), (6.4a)\text{-}(6.4c), (6.12)\text{-}(6.23), \forall t \in T_s \end{aligned} \tag{6.43}$$

P2: Rolling economic dispatch model with SOC ramping constraints

$$\begin{aligned} &\min_{r_{i,u}^t, P_{D,u}^t, P_{T,u}^t, m_{\text{upper}}, m_{\text{lower}}, J_{\text{upper}}, J_{\text{lower}} \in \mathbb{R}, S_i^t, z_j^t \in \mathbb{N}} F_o = \mu_1 F_{o1} + \mu_2 F_{o2} \\ &\text{s.t.} \quad (6.1), (6.3a)\text{-}(6.3c), (6.4a)\text{-}(6.4c), (6.5)\text{-}(6.14), (6.25a), (6.25b)\ \forall t \in T_s \end{aligned} \tag{6.44}$$

Since this proposed rolling economic dispatch model (6.43) or (6.44) has different groups of variables, we can express (6.43) or (6.44) in a more compact model form. To avoid heavy notion, one group of continuous variables is defined as $\boldsymbol{y}_{1,\boldsymbol{u}} := \{(\boldsymbol{r}_{\boldsymbol{u}}^{\boldsymbol{t}}, \boldsymbol{P}_{\boldsymbol{D,u}}^{\boldsymbol{t}}, \boldsymbol{P}_{\boldsymbol{T,u}}^{\boldsymbol{t}}) \in \mathbb{R}, t \in T_s\}$ and $\boldsymbol{Y}_1 =: \{\boldsymbol{y}_{1,\boldsymbol{u}}\}$, u=1,2,…, N_u for (6.43) and $\boldsymbol{y}_{2,\boldsymbol{u}} := \{(\boldsymbol{r}_{\boldsymbol{u}}^{\boldsymbol{t}}, \boldsymbol{P}_{\boldsymbol{D,u}}^{\boldsymbol{t}}, \boldsymbol{P}_{\boldsymbol{T,u}}^{\boldsymbol{t}}, m_{\text{upper}}, m_{\text{lower}}, J_{\text{upper}}, J_{\text{lower}}) \in \mathbb{R}, t \in T_s\}$ and $\boldsymbol{Y}_2 =: \{\boldsymbol{y}_{2,\boldsymbol{u}}\}$, u=1, 2,…,N_u for (6.44) for all retrofitted coal-fired units in the u-th agent of WTBPS. The other category of discrete variables refers to $\boldsymbol{X} := \{(\boldsymbol{S}^{\boldsymbol{t}}, \boldsymbol{z}^{\boldsymbol{t}}) \in \mathbb{N}, t \in T_s\}$. Without loss of generality, we further modify (6.43) and (6.44) in more general forms as (6.35a)-(6.45e) and (6.46a)-(6.46f), respectively.

Compact P1 subject to linear constraints:

$$\min_{\boldsymbol{X}\in\mathbb{N},\, \boldsymbol{Y}_1\in\mathbb{R}} \mu_1(\boldsymbol{Y}_1^{\mathrm{T}} D_{q_1}^{y} \boldsymbol{Y}_1 + (D_{l_1}^{y})^T \boldsymbol{Y}_1) + \mu_2(\boldsymbol{X}^T D_q^x \boldsymbol{X} + (D_l^x)^T \boldsymbol{X}) \tag{6.45a}$$

$$s.t. \quad \boldsymbol{A}_l \cdot \boldsymbol{X} + \boldsymbol{B}_l \cdot \boldsymbol{Y}_1 \le \boldsymbol{b}_l \tag{6.45b}$$

$$\boldsymbol{E}_l \cdot \boldsymbol{Y}_1 \le \boldsymbol{h}_l \tag{6.45c}$$

$$\boldsymbol{F}_l \cdot \boldsymbol{X} \le \boldsymbol{r}_{le} \tag{6.45d}$$

$$\boldsymbol{G}_l \cdot \boldsymbol{X} = \boldsymbol{r}_{ls} \tag{6.45e}$$

where $\boldsymbol{Y}_1^{\mathrm{T}} D_{q_1}^{y} \boldsymbol{Y}_1 + (D_{l_1}^{y})^T \boldsymbol{Y}_1 = \sum_{t=1}^{N_{T_S}} \sum_{u=1}^{N_u} \sum_{i=1}^{N_{G,u}} [c_{2i,u}(r_{i,u}^t P_{\mathrm{G}i,u,\max})^2 + c_{1i,u} r_{i,u}^t P_{\mathrm{G}i,u,\max}]$ and $D_{q_1}^{y}$, D_q^x, $D_{l_1}^{y}$ and D_l^x in (6.45a) are constant matrices summarizing from (6.41) and (6.42). Constraint (6.45b) refers to constraint (6.1) which $\boldsymbol{A}_l$, $\boldsymbol{B}_l$ and $\boldsymbol{b}_l$ are constant vectors drawn from constraint (6.1). Constraint (6.45c) includes constraints (6.3a)-(6.3c), (6.4a)-(6.4c) and (6.12), (6.22)-(6.23) where $\boldsymbol{E}_l$ and $\boldsymbol{h}_l$ can be deduced as constant matrices. Constraint (6.45d) and (6.45e) encompass inequalities and equalities for LTS-based network operational constraints (6.13)-(6.21) for the LTS-based HVDNs with deduced constant matrices $\boldsymbol{F}_l$, $\boldsymbol{r}_{le}$, $\boldsymbol{G}_l$,and $\boldsymbol{r}_{ls}$.

According to minor inner-approximated errors for rotated SOC constraints (6.40a) and (6.40b), this compact **P2** is more accurate than **P1**, expressed as

Compact P2 subject to SOC constraints:

$$\min_{\boldsymbol{X}\in\mathbb{N}, \boldsymbol{Y}_2\in\mathbb{R}} \mu_1(\boldsymbol{Y}_2^{\mathrm{T}} D_{q_2}^{y} \boldsymbol{Y}_2 + (D_{l_2}^{y})^T \boldsymbol{Y}_2) + \mu_2(\boldsymbol{X}^T D_q^x \boldsymbol{X} + (D_l^x)^T \boldsymbol{X}) \tag{6.46a}$$

$$s.t. \quad \boldsymbol{A}_l \cdot \boldsymbol{X} + \boldsymbol{B}_l \cdot \boldsymbol{Y}_2 \le b_l \tag{6.46b}$$

$$\boldsymbol{E}_l \cdot \boldsymbol{Y}_2 \le \boldsymbol{h}_l \tag{6.46c}$$

$$\boldsymbol{F}_l \cdot \boldsymbol{X} \le \boldsymbol{r}_{le} \tag{6.46d}$$

$$\boldsymbol{G}_l \cdot \boldsymbol{X} = \boldsymbol{r}_{ls} \tag{6.46e}$$

$$\boldsymbol{Y}_2^T \boldsymbol{Q}_r \boldsymbol{Y}_2 + \boldsymbol{l}_r{}^T \boldsymbol{Y}_2 \le \boldsymbol{g}_r \tag{6.46f}$$

where $\boldsymbol{Y}_2{}^{\mathrm{T}} D_{q_2}^{y} \boldsymbol{Y}_2 + (D_{l_2}^{y})^T \boldsymbol{Y}_2 = \sum_{t=1}^{N_{T_S}} \sum_{u=1}^{N_u} \sum_{i=1}^{N_{G,u}} [c_{2i,u} (r_{i,u}^t P_{\mathrm{G}i,u,\max})^2 + c_{1i,u} r_{i,u}^t P_{\mathrm{G}i,u,\max}]$, and $D_{q_2}^{y}$ and $D_{l_2}^{y}$ in (6.46a) are constant matrices. Quadratic constraints in constraint (6.46f) can automatically convert to standard rotated SOC constraints with the auxiliary variables (J_{upper}, m_{upper}, J_{lower}, m_{lower}). The constant matrices $\boldsymbol{Q}_r$, $\boldsymbol{l}_r$ and $\boldsymbol{g}_r$ are symbols of $a_{f,\mathrm{upper}}$, $b_{f,\mathrm{upper}}$, $c_{f,\mathrm{upper}}$, $a_{f,\mathrm{lower}}$, $b_{f,\mathrm{lower}}$ and $c_{f,\mathrm{lower}}$.

6.3.2 Multi-cut Generalized Benders Decomposition

As observed in compact **P1 and P2,** this look-ahead economic dispatch model is a MISOCP problem. This MISOCP-based optimization problem is established on large-scale HVDNs and multiple agents of WTBPS, which contains a substantial number of continuous and integer variables during the look-ahead period. Running this large-scale optimization model mixed with the LTS-based network operation model is inevitably time-consuming. Fortunately, the compact **P1** and **P2** can be decomposed into a relaxed master problem (***MP***) with respect to $\boldsymbol{X}$ and many sub-problems with respect to $\boldsymbol{Y}_1$ or $\boldsymbol{Y}_2$, which perfectly suits GBD decomposition framework.

Given discrete variables $\hat{\boldsymbol{X}}$ from ***MP***, we can develop the sub-problem on continuous variables $\boldsymbol{Y}_1 =: \{\boldsymbol{y}_{1,u}\}$ and $\boldsymbol{Y}_2 =: \{\boldsymbol{y}_{2,u}\}$, u=1, 2,…, N_u. By observation on the block matrices $\boldsymbol{B}_{l,u}$ and $\boldsymbol{E}_{l,u}$ of constraints (6.45b) and (6.45c) for **P1** and constraints (6.46b) and (6.46c) for **P2**, we can find that the structure of compact **P1** and **P2** has a special "block-angular" form on variables $\boldsymbol{y}_{1,u}$ and $\boldsymbol{y}_{2,u}$ in the sub-problem ($\boldsymbol{SP}_u$) for the u-th agent of WTBPS. In other words, any agent of WTBPS does not interfere with other agents of variables. In general, $\boldsymbol{y}_u$ refers to $\boldsymbol{y}_{1,u}$ for **P1** or $\boldsymbol{y}_{2,u}$ for **P2**.

$$\begin{array}{c} \text{Agent 1} \\ \text{Agent 2} \\ \vdots \\ \text{Agent } N_u \end{array} \begin{bmatrix} \boldsymbol{B}_{l,1} & & & \\ & \boldsymbol{B}_{l,2} & & \\ & & \ddots & \\ & & & \boldsymbol{B}_{l,N_u} \end{bmatrix} \cdot \begin{bmatrix} \boldsymbol{y}_1 \\ \boldsymbol{y}_2 \\ \vdots \\ \boldsymbol{y}_{N_u} \end{bmatrix} \le \begin{bmatrix} \boldsymbol{b}_{l,1} \\ \boldsymbol{b}_{l,2} \\ \vdots \\ \boldsymbol{b}_{l,N_u} \end{bmatrix} - \begin{bmatrix} \boldsymbol{A}_{l,1} \\ \boldsymbol{A}_{l,2} \\ \vdots \\ \boldsymbol{A}_{l,N_u} \end{bmatrix} \cdot \hat{\boldsymbol{X}} \tag{6.47}$$

We summarize this special "block-angular" decomposable structure in (6.47) with three characteristics as convexity, linear separability and linear independence.

i) **Convexity**: **P2** is all convex on continuous variables $\boldsymbol{y_u}$ with given the discrete variables $\hat{\boldsymbol{X}}$;

ii) **Linear separability**: constraints (6.45b)-(6.45e) and (6.46b)-(6.46e) are all linear on discrete variables $\boldsymbol{X}$ with given the continuous variables $\hat{\boldsymbol{y}}_{\boldsymbol{u}}$;

iii) **Linear independence**: with given discrete variables $\hat{\boldsymbol{X}}$, different groups of continuous variables $\boldsymbol{y_u}$ are linearly independent. Under these three characteristics, it is highly desirable to utilize the GBD method with multiple cuts as MGBD. MGBD can decompose the sub-problem of GBD into multiple independent smaller optimization models by (6.47), which sub-problems engender multiple feasibility cuts and optimality cuts at each iteration. Recall that classical GBD only generates one feasibility cut for each iteration, whereas the number of feasibility cuts and optimality cuts is equal to N_u in each iteration in MGBD. Thus, MGBD enables faster convergence of the large-scale MP model and then save more running time, as compared to the single-cut GBD method.

Following MGBD approach, we formulate the sub-problem ($\boldsymbol{SP_u}$) for the u-th agent of WTBPS for **P2** at the k-th iteration as a SOCP-based model with given discrete variables $\hat{\boldsymbol{X}}^{k-1}$:

$$\min_{\boldsymbol{y}_{2,u}\in\mathbb{R}} \mu_1(\boldsymbol{y}_{2,u}^T D_{q_2}^y \boldsymbol{y}_{2,u} + (D_{l_2}^y)^T \boldsymbol{y}_{2,u}) + \mu_2((\hat{\boldsymbol{X}}^{k-1})^T D_q^x \hat{\boldsymbol{X}}^{k-1} + (D_l^x)^T \hat{\boldsymbol{X}}^{k-1}) \tag{6.48a}$$

$$\text{s.t.} \quad \boldsymbol{B}_{l,u} \cdot \boldsymbol{y}_{2,u} \le \boldsymbol{b}_{l,u} - \boldsymbol{A}_{l,u} \cdot \hat{\boldsymbol{X}}^{k-1} \tag{6.48b}$$

$$\boldsymbol{E}_{l,u} \cdot \boldsymbol{y}_{2,u} \leq \boldsymbol{h}_{l,u} \tag{6.48c}$$

$$\boldsymbol{y}_{2,u}^T \boldsymbol{Q}_{r,u} \boldsymbol{y}_{2,u} + \boldsymbol{l}_{r,u}^T \boldsymbol{y}_{2,u} \leq \boldsymbol{g}_{r,u} \tag{6.48d}$$

where $\boldsymbol{A}_l = \{\boldsymbol{A}_{l,u}\}$, $\boldsymbol{l}_r = \{\boldsymbol{l}_{r,u}\}$, $\boldsymbol{B}_l = \{\boldsymbol{B}_{l,u}\}$, $\boldsymbol{b}_l = \{\boldsymbol{b}_{l,u}\}$, $\boldsymbol{E}_l = \{\boldsymbol{E}_{l,u}\}$, $\boldsymbol{h}_l = \{\boldsymbol{h}_{l,u}\}$, $\boldsymbol{Q}_r = \{\boldsymbol{Q}_{r,u}\}$ and $\boldsymbol{g}_r = \{\boldsymbol{g}_{r,u}\}$ for u=1, 2,…, N_u.

If this $\boldsymbol{SP_u}$ problem is optimal with $\hat{\boldsymbol{y}}_{2,u}^k$, the upper bound is

$$UB_k = \min\{UB_{k-1}, \mu_1 \sum_{u=1}^{N_u} ((\hat{\boldsymbol{y}}_{2,u}^k)^T D_{q_2}^y \hat{\boldsymbol{y}}_{2,u}^k + (D_{l_2}^y)^T \hat{\boldsymbol{y}}_{2,u}^k) + \mu_2 ((\hat{\boldsymbol{X}}^{k-1})^T D_q^x \hat{\boldsymbol{X}}^{k-1} + (D_l^x)^T \hat{\boldsymbol{X}}^{k-1})\}$$

; otherwise it is infeasible, we turn to solve an l_1-minimization feasibility check problem with the relaxed variable $\sigma_u \geq 0$ where for u=1, 2,…, N_u as follows:

$$\min_{\boldsymbol{y}_u, \sigma_u \in \mathbb{R}} \sigma_u \tag{6.49a}$$

$$\text{s.t.} \quad \boldsymbol{B}_{l,u} \cdot \boldsymbol{y}_{2,u} - \sigma_u \leq \boldsymbol{b}_{l,u} - \boldsymbol{A}_{l,u} \cdot \hat{\boldsymbol{X}}^{k-1} \tag{6.49b}$$

$$\boldsymbol{E}_{l,u} \cdot \boldsymbol{y}_{2,u} - \sigma_u \leq \boldsymbol{h}_{l,u} \tag{6.49c}$$

$$\boldsymbol{y}_{2,u}^T \boldsymbol{Q}_{r,u} \boldsymbol{y}_{2,u} + \boldsymbol{l}_{r,u}^T \boldsymbol{y}_{2,u} - \sigma_u \leq \boldsymbol{g}_{r,u} \tag{6.49d}$$

On the one hand, if the $\boldsymbol{SP_u}$ problem is feasible at k-th iteration as indicated in (6.48a)-(6.48d), we substitute the obtained continuous variables $\hat{\boldsymbol{y}}_{2,u}^k$ and Lagrange multiplier vectors $\hat{\boldsymbol{\lambda}}_{u,1}^k$, $\hat{\boldsymbol{\lambda}}_{u,2}^k$, and $\hat{\boldsymbol{\lambda}}_{u,3}^k$ for constraints (6.48a)-(6.48d), which enforces the optimality cut as:

$$\begin{aligned}&(\hat{\boldsymbol{\lambda}}_{u,1}^k)^T \boldsymbol{A}_{l,u} \boldsymbol{X} + (\hat{\boldsymbol{\lambda}}_{u,1}^k)^T (\boldsymbol{B}_{l,u} \cdot \hat{\boldsymbol{y}}_{2,u}^k - \boldsymbol{b}_{l,u}) + (\hat{\boldsymbol{\lambda}}_{u,2}^k)^T (\boldsymbol{E}_{l,u} \cdot \hat{\boldsymbol{y}}_{2,u}^k - \boldsymbol{h}_{l,u}) + \\ &(\hat{\boldsymbol{\lambda}}_{u,3}^k)^T ((\hat{\boldsymbol{y}}_{2,u}^k)^T \boldsymbol{Q}_{r,u} \hat{\boldsymbol{y}}_{2,u}^k + \boldsymbol{l}_{r,u}^T \hat{\boldsymbol{y}}_{2,u}^k - \boldsymbol{g}_{r,u}) + \mu_1 \sum_{u=1}^{N_u} ((\hat{\boldsymbol{y}}_{2,u}^k)^T D_{q_2}^y \hat{\boldsymbol{y}}_{2,u}^k + (D_{l_2}^y)^T \hat{\boldsymbol{y}}_{2,u}^k) \leq q_u\end{aligned} \tag{6.50}$$

where q_u is an auxiliary variable from the $\boldsymbol{SP_u}$ for the $\boldsymbol{MP}$.

On the other hand, provided that the $\boldsymbol{SP_u}$ problem is infeasible at the k-th iteration, by solving l_1-minimization feasibility check problem as indicated in (6.49a)-(6.49e), and then we substitute continuous variables $\hat{\boldsymbol{y}}_{\boldsymbol{u}}^{f,k}$ and Lagrange multiplier vectors $\hat{\boldsymbol{\gamma}}_{\boldsymbol{u},1}^{\boldsymbol{k}}$, $\hat{\boldsymbol{\gamma}}_{\boldsymbol{u},2}^{\boldsymbol{k}}$,and $\hat{\boldsymbol{\gamma}}_{\boldsymbol{u},3}^{\boldsymbol{k}}$ for constraints (6.49b)-(6.49d) to form the feasibility cut:

$$\begin{aligned}(\hat{\boldsymbol{\gamma}}_{\boldsymbol{u},1}^{\boldsymbol{k}})^T A_{l,u}\boldsymbol{X}+(\hat{\boldsymbol{\gamma}}_{\boldsymbol{u},1}^{\boldsymbol{k}})^T(\boldsymbol{B}_{\boldsymbol{l},\boldsymbol{u}}\cdot\hat{\boldsymbol{y}}_{2,\boldsymbol{u}}^{f,k}-\boldsymbol{b}_{\boldsymbol{l},\boldsymbol{u}})+(\hat{\boldsymbol{\gamma}}_{\boldsymbol{u},2}^{\boldsymbol{k}})^T(\boldsymbol{E}_{\boldsymbol{l},\boldsymbol{u}}\cdot\hat{\boldsymbol{y}}_{2,\boldsymbol{u}}^{f,k}-\boldsymbol{h}_{\boldsymbol{l},\boldsymbol{u}})+\\(\hat{\boldsymbol{\gamma}}_{\boldsymbol{u},3}^{\boldsymbol{k}})^T((\hat{\boldsymbol{y}}_{2,\boldsymbol{u}}^{f,k})^T\boldsymbol{Q}_{\boldsymbol{r},\boldsymbol{u}}\hat{\boldsymbol{y}}_{2,\boldsymbol{u}}^{f,k}+\boldsymbol{l}_{\boldsymbol{r},\boldsymbol{u}}^{\boldsymbol{T}}\hat{\boldsymbol{y}}_{2,\boldsymbol{u}}^{f,k}-\boldsymbol{g}_{\boldsymbol{r},\boldsymbol{u}})\le 0\end{aligned} \tag{6.51}$$

After imposing the optimality cuts (6.50) and the feasibility cuts (6.51) for u=1, 2,…, N_u, we establish the relaxed ***MP*** model at k-th iteration for all agents:

$$\min_{\boldsymbol{X},q_u\in\mathbb{R}}\sum_{u=1}^{N_u}q_u+\mu_2(\boldsymbol{X}^T D_q^x\boldsymbol{X}+(D_l^x)^T\boldsymbol{X}) \tag{6.52a}$$

$$\text{s.t.}\quad F_l\cdot\boldsymbol{X}\le r_{le},\ \ G_l\cdot\boldsymbol{X}=r_{ls}\text{, and (6.50)-(6.51)} \tag{6.52b}$$

The lower bound is obtained as $LB_k=\mu_2((\boldsymbol{X}^k)^T D_q^x\boldsymbol{X}^k+(D_l^x)^T\boldsymbol{X}^k)+\sum_{u=1}^{N_u}q_u^k$, where $\boldsymbol{X}^{\boldsymbol{k}}$ and q_u^k are optimal solutions from (6.52a)-(6.52b). Until $\|LB_k-UB_k\|$ is less than the given tolerance, this MGBD algorithm can be converged.

This MGBD can generally be solved by servers at the dispatch center, while $\boldsymbol{SP_u}$ can be individually and simultaneously tackled by each agent. Traditionally, the centralized rolling economic dispatch enforces each agent to upload sensitive local data to the dispatch center, such as power outputs, power capacities, utilization levels, without privacy protection [105]. However, with this MGBD computation framework, agents can only share the dispatchable loads and Lagrange multiplier vectors with the dispatch center, which preserves the privacy of sensitive information. In summary, the entire computation procedure on multiple paralleled CPU cores is implemented in Fig. 6.10.

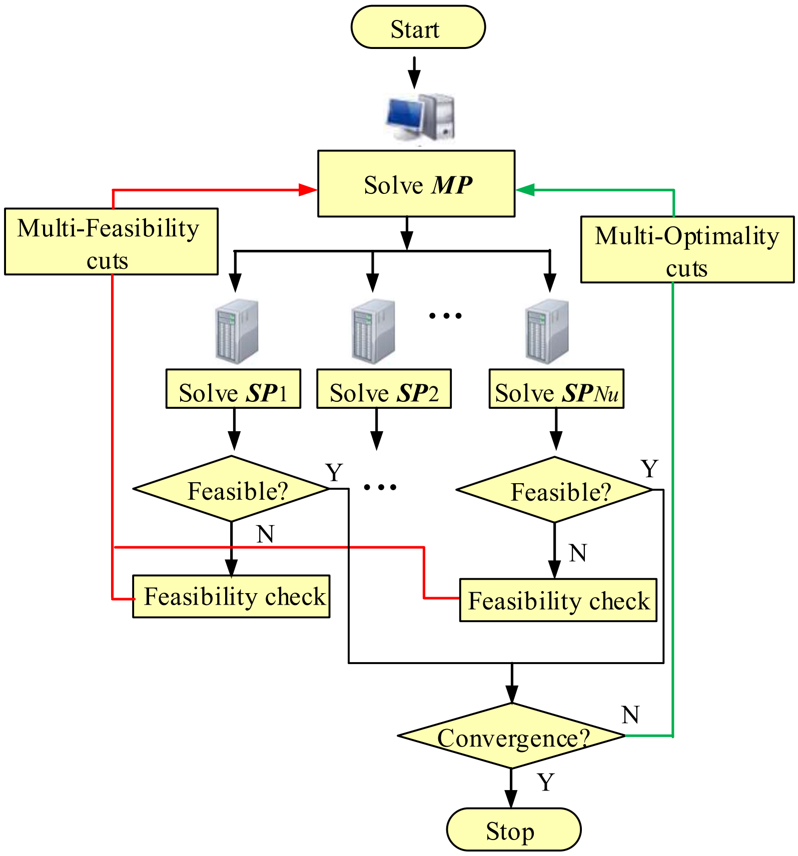

Fig. 6.10. Computation procedure of MGBD for **P1** and **P2**.

6.4 Case Studies

A real modified HVDN system with 220kV and 110kV voltage levels in central China as shown in Fig. 6.11 [82]. Four agents A_1-A_4 of WTBPS are integrated in four different 220kV stations, namely stations TH, ZJS, HTC and SQZ, with tie-lines PT1-PT4. This integrated practical system is used for case studies to validate the proposed look-ahead rolling economic dispatch approach.

Assume that four agents have the same installed capacities of wind power and coal-fired power generation. In each agent, there are five retrofitted coal-fired units satisfying $5\cdot P_{\mathrm{G,max}}=P_{base}$=1500 MVA, ΔT =15min, T_{s}=5h, N_{Ts}=20, P_u^{spin} =37.5 MVA, δ%=5% and P_{wind}=1200MVA. The $c_{2i,u}$, $c_{1i,u}$, and $c_{0i,u}$ for all agents are set to 0.00049

(\$/MW^{2}h), 18.23 (\$/MWh) and 35.54 (\$). The $c_{D,u}$ and $c_{H,u}$ are set to 4.17 (\$/MWh) and 10 (\$/p.u.) respectively for all agents. This HVDN system has 17 units of 220kV stations labeled with long rectangle boxes and rated capacities in light yellow color and 57 units of 110kV substations marked with black-filled circles. The status of switch breakers is shown in Fig. 6.11 for the initial period. The number of allowable switch actions during a rolling window is set to 6 times [103]. Load data for each substation and wind power data for four agents are forecasted for T_s=5h ahead. The voltage profiles of all nodes are bounded in [0.95, 1.05] p.u., and the thermal capacities of branches are less than 0.126 p.u., and other network parameters can be found in [82], where the base power is set to 1000 MW. And given tolerance for MGBD is set to $\varepsilon = 10^{-3}$ in this study. In addition, conventional coal-fired units without retrofits and retrofitted coal-fired units with dynamic ramping are compared. These three categories of coal-fired plants with installed wind power capacity P_{wind} participate in the following simulation experiments, as shown in Table 6.2.

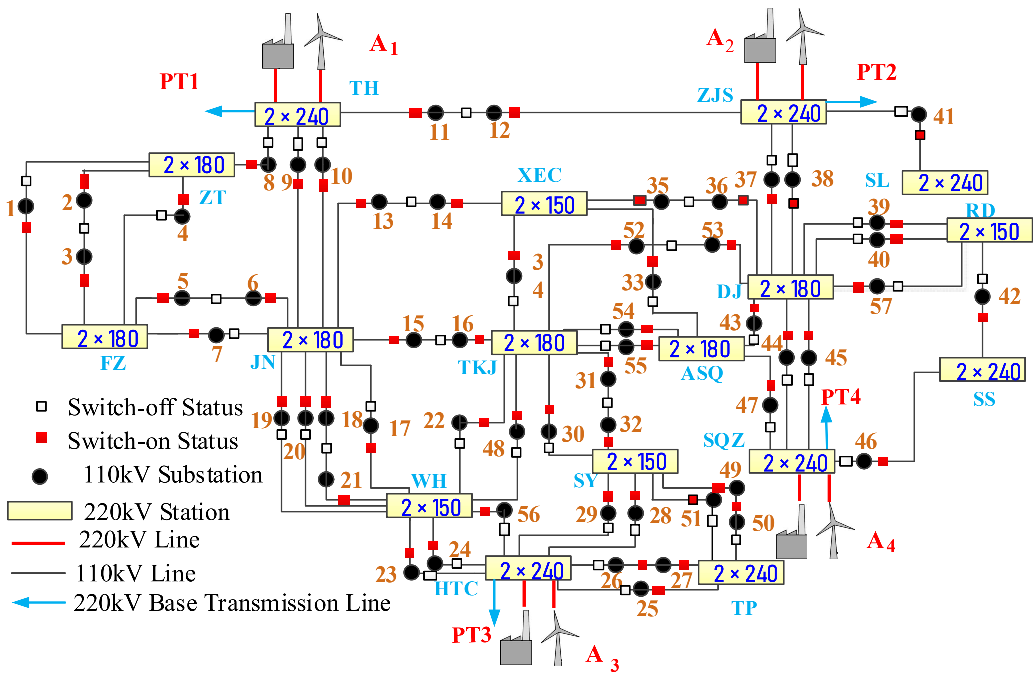

Fig. 6.11. A real modified HVDNs in central China.

Table 6.2. Comparative coal-fired plants

Types of coal-fired plants	Minimum load level (%)	Ramp rate (min/%)
Conventional coal-fired units with normal ramp rate	60	1.1%
Retrofitted coal-fired units with piecewise linear model of dynamic ramp rates [78]	30	$v_{i,u}^{t}=\begin{cases}0.35\%, & r_{i,u}^{t}\in[0.3,0.4]\\ 1.0\%, & r_{i,u}^{t}\in[0.4,0.5]\\ 1.5\%, & r_{i,u}^{t}\in[0.5,0.6]\\ 2\%, & r_{i,u}^{t}\in[0.6,1.0]\end{cases}$
Retrofitted coal-fired units with proposed dynamic ramp rates Eq.(6.2)	30	$v_{i,u}^{t}=\begin{cases}a\cdot r_{i,u}^{t}-b, & r_{i,u}^{t}\le d\\ c, & r_{i,u}^{t}>d\end{cases}$ where a=0.055, b=0.013, c=0.02, d=0.6.

In this study, we adopt the following comparative rolling economic dispatch (ED) models for agent A_1 in Table 6.3. We mainly divide two categories of factors for economic dispatch models: dispatchable loads and ramp rate. For dispatchable loads, reference [77] adopts a load-shedding variable in the look-ahead rolling economic dispatch model instead of a network-based model, namely unrestricted dispatchable loads. The second column refers to unrestricted dispatchable loads. In contrast, the LTS-based HVDN operation model only outputs discrete dispatchable loads which are indicated in the third column. For ramp rates, we consider conventional and retrofitted coal-fired units into ED models where types of coal-fired units are introduced in Table II. The fourth and fifth columns refer to conventional coal-fired units with the normal ramp rate and retrofitted coal-fired units with the piecewise linear model of dynamic ramp rates, respectively. The sixth and seventh columns denote linear- and SOC-based tightened ramping constraints of retrofitted coal-fired units. Parameters of the normal ramp rate and dynamic ramp rates are taken from Table 6.2.

Table 6.3 Comparative rolling economic dispatch models for agent A1

ED models	Dispatchable loads		Normal ramp rate	Dynamic ramp rates		
	unrestricted	HVDNs		piecewise	linear	SOC
ED1	√				√	
ED2	√					√
ED3	√		√			
ED4	√			√		
ED5	√					√
ED6	√					√
ED7		√				√
ED8		√			√	

6.4.1 Maximum Inner-Approximated Errors of Tightened Ramping Constraints

We present accuracy discussions for maximum inner-approximated errors between the untightened and linear and SOC ramping constraints. Fig. 6.13(a)-(c) present the maximum inner-approximated errors between the untightened and linear ramping constraints, i.e. Δe_U and Δe_L, and between the untightened and SOC ramping constraints, i.e. Δs_U and Δs_L, with respect to different ranges of experimental parameters a, b, c. In this experiment, we define the following sets of parameters a, b and c where $d=(b+c)/a$.

- In Fig. 6.12(a), parameters a and b vary from 0.0467 to 0.06 and 0.001 to 0.015, and parameter c is fixed to 0.02.
- In Fig. 6.12(b), parameters a and c vary from 0.0467 to 0.06 and 0.020 to 0.025, and parameter b is fixed to 0.013.
- In Fig. 6.12(c), parameters b and c vary from 0.011 to 0.015 and 0.020 to 0.025, and parameter a is fixed to 0.055.

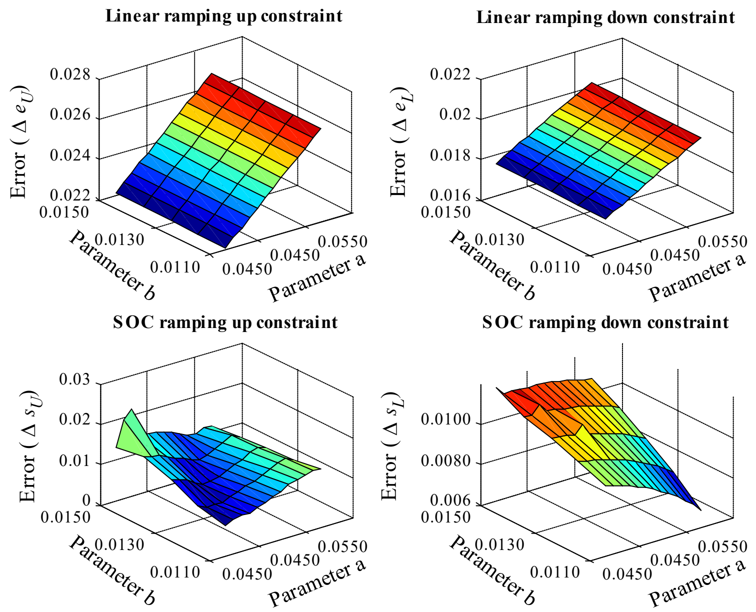
Linear ramping up constraint
Error (Δ e_U)
0.028
0.026
0.024
0.022
0.0150
0.0130
0.0110
Parameter b
0.0450
0.0450
0.0550
Parameter a
Linear ramping down constraint
Error (Δ e_L)
0.022
0.02
0.018
0.016
0.0150
0.0130
0.0110
Parameter b
0.0450
0.0450
0.0550
Parameter a
SOC ramping up constraint
Error (Δ s_U)
0.03
0.02
0.01
0
0.0150
0.0130
0.0110
Parameter b
0.0450
0.0450
0.0550
Parameter a
SOC ramping down constraint
Error (Δ s_L)
0.0100
0.0080
0.006
0.0150
0.0130
0.0110
Parameter b
0.0450
0.0450
0.0550
Parameter a

(a)

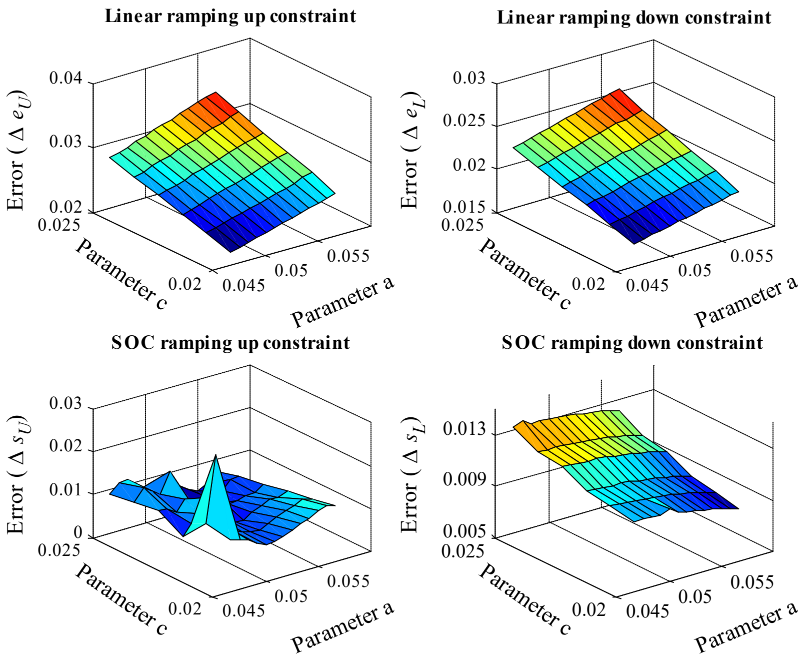
Linear ramping up constraint
Error (Δ e_U)
0.04
0.03
0.02
0.025
Parameter c
0.02
0.045
0.05
0.055
Parameter a
Linear ramping down constraint
Error (Δ e_L)
0.03
0.025
0.02
0.015
0.025
Parameter c
0.02
0.045
0.05
0.055
Parameter a
SOC ramping up constraint
Error (Δ s_U)
0.03
0.02
0.01
0
0.025
Parameter c
0.02
0.045
0.05
0.055
Parameter a
SOC ramping down constraint
Error (Δ s_L)
0.013
0.009
0.005
0.025
Parameter c
0.02
0.045
0.05
0.055
Parameter a

(b)

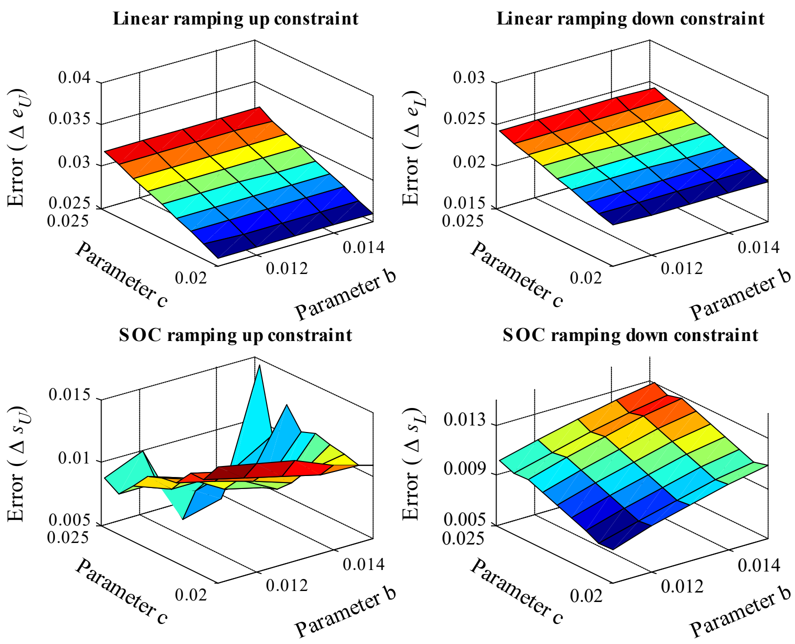

(c)

Fig. 6.12 Maximum inner-approximated errors using linear and SOC ramping constraints with different sets of parameters

From Fig. 6.12(a)-(c), it should be noted that the maximum inner-approximated errors Δe_U, Δe_L, Δs_U and Δs_L are quantified below 3.21%, 2.45%, 2.84%, and 1.36% with different sets of parameters. Following $\Delta e_U > \Delta s_U$ and $\Delta e_L > \Delta s_L$, this suggests that the SOC ramping constraints are more accurate than corresponding linear ramping constraints. For SOC ramping constraints, the maximum inner-approximated errors are specified with 2.84%$\cdot P_{base}/5$=8.52 MW and 1.36%$\cdot P_{base}/5$=4.08 MW for ramp-up/down margins under ΔT=15min, respectively.

6.4.2 Boundaries of Wind Power Fluctuations

The allowable ramping margin of wind power turbines (WPTs) can be quantified with three kinds of ramping constraints using normal ramp rate, the piecewise, and proposed linear models of dynamic ramp rates from Table 6.2. The corresponding allowable ramping margins caused by three kinds of ramping constraints are drawn in black, pink and blue lines in Fig. 6.13. The ramping boundary of this installed wind power capacity is depicted in green lines, and three forecasted sets of wind power data are also included in Fig. 6.13.

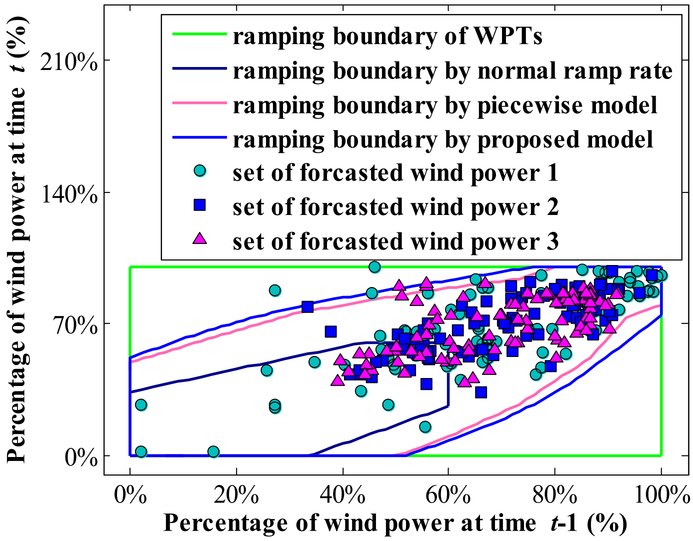

Fig. 6.13 Different allowable ramping margins of WPTs.

Fig. 6.13 suggests that the allowable ramping margin of WPTs can be enlarged as long as coal-fired plants are retrofitted, as justified by ramping areas with boundaries in black lines, blue lines, and pink lines. Moreover, the theoretical ramping area in green lines is determined by installed wind power capacities. For WTBPS, feasible wind power fluctuations of WPTs have boundaries with blue, pink or black lines between adjacent periods. This is the reason why only the set of forecasted wind power 2 is completely located in the allowable ramping margin of WPTs, whereas the other two sets 1 and 3 of wind power data cannot be completely accommodated by WTBPS. In this case, wind curtailment or load transfer is inevitable for these two sets.

Fig. 6.13 depicts the untightened and tightened allowable ramping margins of WPTs under ΔT =15min. The blue line indicates the untightened boundary by the proposed operational ramping constraints. The red and black lines refer to tightened ramping boundary of WPTs caused by linear and SOC ramping constraints. It is shown that one point of forecasted wind power dataset 2 remarked in the blue-filled square box lies on the SOC ramping constraint. The linear constraints lead to purchasing dispatchable loads via a few switch-over operations of HVDNs if linear ramping constraints are involved. Instead, adopting tightened SOC ramping constraints can accommodate this problem.

6.4.3 Linear Versus SOC Ramping Constraints

After the feasibility-check procedure for wind power data using tightened ramping margin of WPTs from Fig. 6.14(a), we can carry out the simulation experiments to validate the dispatch solution accuracy for ED1and ED2. To clearly distinguish between ED1 and ED2, we compare the optimal generation power solutions of ED1 and ED2 over the rolling window from 8:30 to 13:30, subject to linear and SOC ramping constraints as shown in Fig. 6.14(b).

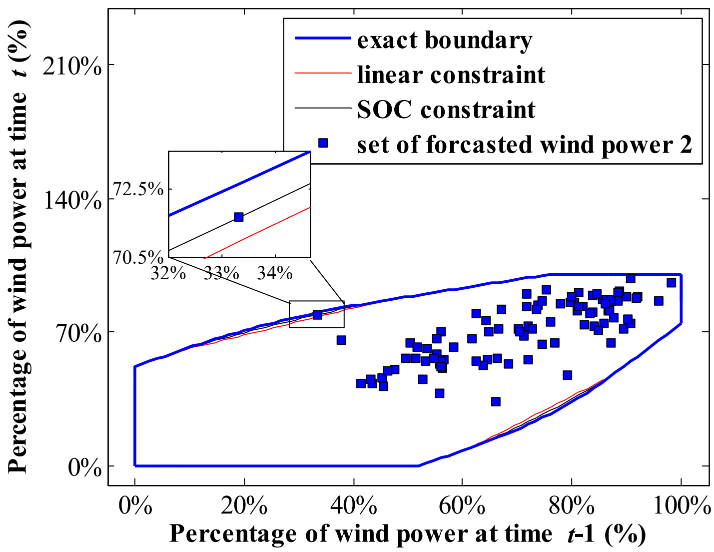

(a)

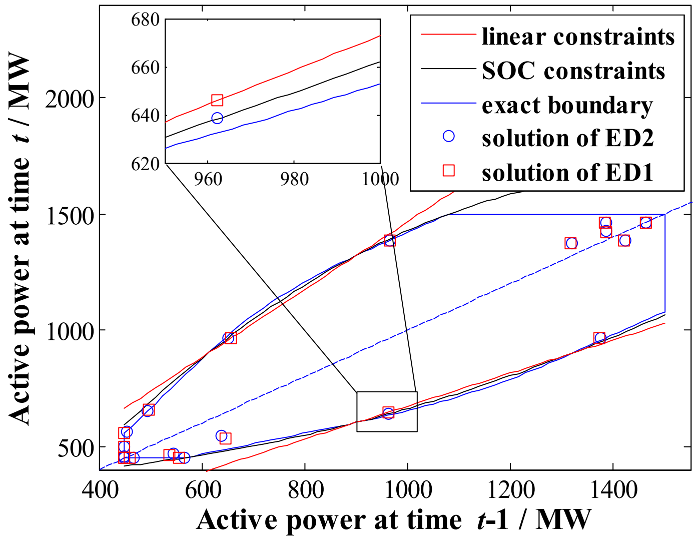

(b)

Fig. 6.14. (a) Untightened and tightened ramping margins of WPTs under ΔT =15min; (b) Optimal rolling ED solutions between ED1 and ED2.

Remarkable differences can be inferred from Fig. 6.15(b) between optimal solutions of ED1and ED2. The optimal solutions of ED2 is more accurate than the ones obtained by ED1 shown in the embedded graph, since the optimal solution of ED2 is closer to the untightened ramping margin in blue line. With acceptable errors indicated by maximum error analysis in Fig. 6.15(a)-(c), the optimal rolling economic dispatch solution of ED2 can be deemed as accurate, regardless of how wind power changes during these periods. Thus, SOC constraints in ED2 can replace nonlinear untightened constraints with acceptable errors for optimal economic dispatch solutions.

6.4.4 Normal, Piecewise Versus SOC Ramping Constraints

To exemplify the quick-response, we compare the optimal generation power solutions and optimal dispatchable loads over the rolling window from 8:30 to 13:30 by ED3, ED4 and ED5, as shown in Fig. 6.15(a) and (b). Note that optimal ED solutions of ED3, ED4 and ED5 are compared under the typical load demands and the mean of wind power data in 100 random scenarios in Fig. 6.15(a), and optimal dispatchable loads are collected under 100 random wind power scenarios in Fig. 6.15(b). Table 6.4 contains the average objective costs of ED3, ED4 and ED5 in 100 wind power scenarios. The second column refers to the generation cost F_{o1}; and the third column indicates the operational cost F_{o2}; and the last column F_o is the total cost of this rolling economic dispatch.

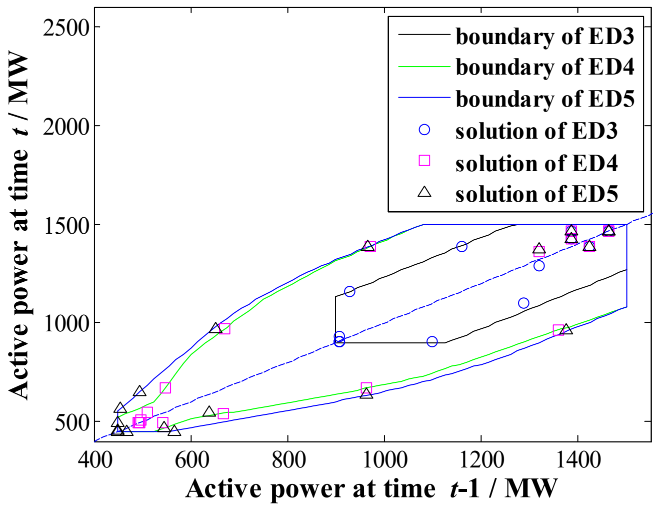

(a)

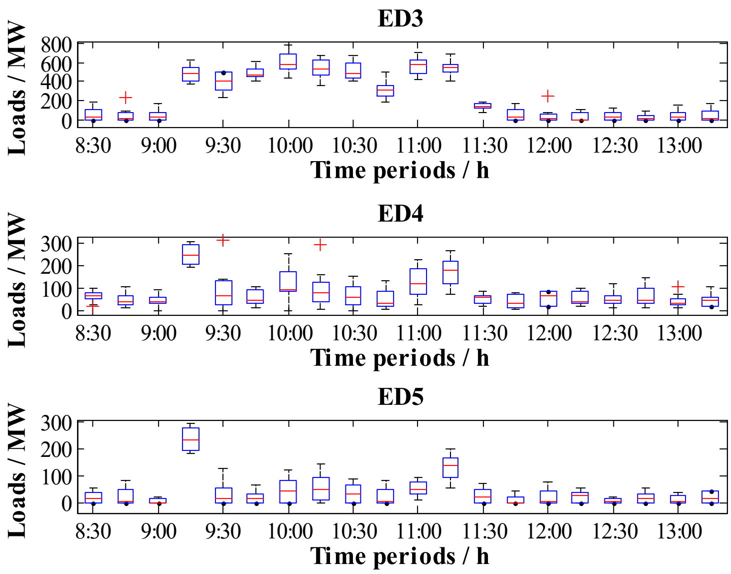

(b)

Fig. 6.15. (a) optimal ED solutions under typical load demands and mean of wind power data; (b) optimal dispatchable loads in 100 wind power scenarios.

Fig. 6.15(a) reveals that ED4 and ED5 can quickly react to wind power fluctuations with multiple output power below 600MW, while ED3 is incapable of accommodating these wind power variations. This suggests that retrofitted coal-fired units are more flexible than conventional coal-fired plants. To compare ED4 and ED5, ED5 is superior to ED4 since ED5 can seek many optimal output solutions that are smaller than 600MW whereas ED4 cannot do so. Moreover, Fig. 6.15(b) presents that ED5 seeks the least dispatchable loads from HVDNs than the quantities obtained by ED3 and ED4 in each dispatch period. These results also validate ED5's superiority in the quick-response to unexpected wind power fluctuations, as also reflected in the smallest total cost F_{o1}, F_{o2}, and F_o for ED5 in Table 6.4.

Table 6.4. Average costs of 100 wind power scenarios

ED Models	F_{o1} ($\times 10^5$\$)	F_{o2} ($\times 10^5$\$)	F_o ($\times 10^5$\$)
ED3	10.40	82.420	46.41
ED4	8.67	5.400	7.01
ED5	8.49	3.031	5.75

6.4.5 Unrestricted Versus LTS-based HVDNs

Fig. 6.16(a) and (b) show the rolling ED differences between ED6 and ED7 with the wind power data extracted from the sets of forecasted wind power 2 and 3, respectively. Fig. 6.16(a) shows that ED7 and ED8 have the same solution since there are no circuit switching actions. When wind power fluctuates sharply between adjacent intervals, ED6 and ED7 may have different schemes of purchasing dispatchable loads from HVDNs. Fig. 6.16(b) interprets that the switched load 213.27

MW is essential at 09:30, since the wind power varies by 614.72 MW, which is larger than the maximum ramp-down margin 251.67 MW of retrofitted coal-fired units at that time. Otherwise, it has to conduct load transfer operations. For ED6 and ED7, ED7 purchases more dispatchable loads from the LTS-based network than that solved by ED6, such as 09:30, 11:15, and 11:30. This is caused by the continuous circuit switching variable instead of the network-constrained discrete circuit switching variable.

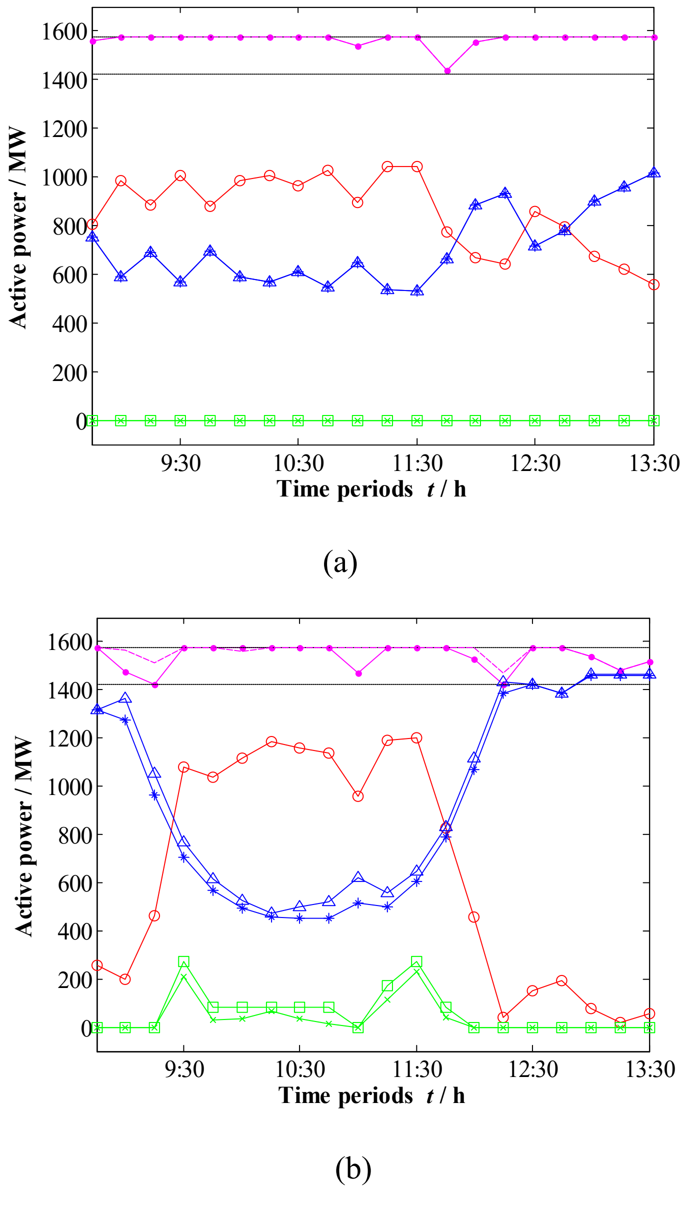

(a)

(b)

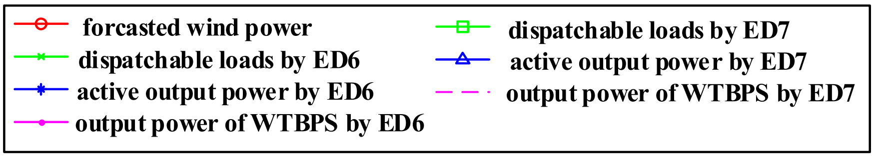

(c)

Fig. 6.16. Optimal ED solutions between ED6 and ED7: (a) set of forecasted wind power 2; (b) set of forecasted wind power 3; and (c) legends for (a) and (b).

6.4.6 Centralized Versus Decentralized MBGD Methods

We conduct simulation experiments to validate the computational efficiency between the centralized MILP- and MISOCP-based methods and the proposed decentralized MGBD-based method for ED7 and ED8 in case studies. Four methods are compared: Centralized MILP programming solver for ED8 (**M1**); Centralized MISOCP programming solver for ED7 (**M2**); Centralized MISOCP programming solver embedded in a GBD framework for ED7 (**M3**); Decentralized MISOCP programming solver embedded an MGBD framework for ED7(**M4**).

These four methods are implemented by using CPLEX tools and MOSEK in the MATLAB environment with an AMD Ryzen 75800X 8-core CPU 3.80GHz processor. Three kinds of stochastic wind power scenarios for four agents are generated where the maximum power fluctuation accounting for wind power rated capacity between two consecutive periods is set to ΔP =0.3, 0.5, and 0.8. Note that all forecasted wind power data satisfy tightened ramping margin of WPTs under ΔT =15min and load transfer boundaries.

Table 6.5. Computing performance of four methods

Cases	Methods	Iterations	Entire CPU Time (s)	CPU Time (s) TMP	TSP
I	M1	/	5.34	/	/
ΔP =0.3	M2	/	12.11	/	/

N_u=4	M3	4	12.89	9.85	3.04
	M4	2	6.05	4.43	1.62
I ΔP =0.5 N_u=4	M1	/	4.11	/	/
	M2	/	11.29	/	/
	M3	5	13.12	10.05	3.07
	M4	2	5.85	4.23	1.62
I ΔP =0.8 N_u=4	M1	/	5.44	/	/
	M2	/	12.89	/	/
	M3	7	12.42	10.06	2.36
	M4	3	5.96	4.11	1.85
II ΔP =0.3 N_u=8	M1	/	5.34	/	/
	M2	/	15.11	/	/
	M3	8	18.42	14.22	4.20
	M4	4	7.56	5.54	2.02
II ΔP =0.5 N_u=8	M1	/	5.41	/	/
	M2	/	16.36	/	/
	M3	9	20.08	15.75	4.33
	M4	5	7.47	5.12	2.35
II ΔP =0.8 N_u=8	M1	/	5.02	/	/
	M2	/	16.81	/	/
	M3	15	21.73	15.24	6.49
	M4	5	7.51	5.40	2.11

Table 6.5 displays the numerical results for case studies in different wind power scenarios. For case II, we consider involving eight agents of WTBPS connecting to 220kV stations FZ, RD, XEC, and SY. The number of constraints and variables is twice as many as case I. The first column indicates case numbers with different ranges of wind power fluctuations. The second column denotes four methods. The third column shows the total number of iterations required to reach the optimum only for GBD and MGBD approaches. The fourth column presents the entire CPU time (in seconds) required to solve the overall problem. The fifth column includes the sum of CPU running time (in seconds) of the master problem (TMP) and sub-problems (TSP) in M3 and M4, respectively.

For M1 and M2, M1 converges more rapidly than M2, with a smaller amount of CPU time for the two cases. With the larger system sizes as indicated in case II, M1 outperforms M2 with superior advantages in CPU time. This outperformance of M1 stems from the MILP-based ED8, whereas M2 is applied to address the MISOCP-based ED7 with a more accurate solution than the MILP-based ED8. Compared to M3, M4 shows a remarkably smaller amount of CPU time and a less number of iterations in two cases. And the CPU processing time for M3 substantially increases with larger system sizes. However, the effectiveness of the proposed M4 can be ensured within less than 8 seconds of CPU processing time, which saves more than 65% of computation time compared with M3.

Based on the above, M4 outperforms M2-M3 in the least CPU time and outperforms M1 in the accuracy of the solution. Provided that M4 is performed on multiple distributed computing servers, it can be certainly expected that the computing performance of M4 can bring better computational efficiency to this decomposition–coordination computing framework, especially for a large-scale optimization problem.

6.5 Summary

The chapter proposes a look-ahead rolling economic dispatch approach of WTBPS considering the variable ramp rate of retrofitted coal-fired units and flexible voltage-constrained LTS via HVDNs. The SOC ramping constraints are validated with acceptable inner-approximated error (at most 2.84%) when ΔT =15 min. Results from the case studies demonstrate that this proposed rolling economic dispatch approach is applicable for multiple WTBPS agents to accommodate wind power fluctuations with the minimization of production cost, purchasing cost, and switch-over operation cost. Moreover, the proposed MGBD-based decentralized method enables many subproblems to be solved in parallel, which facilitates this large-scale rolling economic dispatch model to be quickly solved, saves around 65% computational time and releases more computational resources. Therefore, the computing performance for the proposed MGBD-based method is proved to be satisfactory with higher efficiency.

Chapter 7

Conclusions and Future Work

7.1 Conclusions

DNs can adaptively maintain load balancing and loss reduction at the voltage security-constrained operation level, and to coordinate real-time transactive dispatch tasks between supply and demand at the market level of DNs.

On system-wide operation level, with the proliferation of diverse power entities (e.g. renewable generation, electric vehicles and storage) into smart DNs, adaptive reconfiguration of the electrical topology of DNs may run into physical security issues, i.e., over-voltage and under-voltage excursions. Moreover, on cyber-physical system security level, massive D-PMU devices are connected into smart DNs for the full system observability in recent years. The cyber-physical nature of DNs facilitates the exchange of crafted D-PMU signals amongst actuating and monitoring power entities in DNs. This renders that an effective defense of observability plays a crucial role in the cyber-physical security of DNs against cyber-attacks. Additionally, to keep a fairly transactive energy market, DSOs have to share sensitive power flow datasets with different participants, which may leak the sensitively private data including nodal load and generation data of residential customers. Obfuscating sensitive datasets up to some quantity but preserve their statistic values is essential for customer's privacy guarantees.

Thereby, in order to proactively mitigate these problems, this thesis proposes several advanced topology optimization methods to achieve a DNR solution for cyber-physical security, privacy-preserving and dispatch flexibility enhancement. The primary conclusions and contributions of this thesis are summarized as follows:

(1) The proposed DCHR approach can tackle the disjunctive nature of DNR problems. With continuous parent-child relationship variables as disjunctive variables, this DCHR approach is theoretically tighter than the McCormick linearization method and the Big-M method, and it is especially suitable for DNs with directional power flows. As demonstrated in case studies, the computing performance in terms of running time and iterations using a DCHR approach yields superior numerical performance than prior relaxation methods.

(2) The proposed disjunctive RCDS formulation can be applicable for reconfigurable networks with the least defense cost in theory. With this formulation, an observability defense-constrained DNR model can be constructed as a MISOCP problem, which perfectly enables an observable DNR solution just with the minimal defense cost and active power loss for cyber–physical security enhancement.

(3) For multi-agent ADNs, we proposes a DP-DNR mechanism based on a C-ADMM approach for interconnected multi-agent ADNs. This query mechanism provides a mixture output of both realistically optimal tie-switch status and corresponding obfuscated- but-feasible tie-line load flows, part of which may have reverse directions. Moreover, the C-ADMM-based DP-DNR mechanism can seek the optimal topology switch without realistic communication signals and customer’s load data from other agents, which maximally protects the agent’s and customer’s privacy.

In the future energy-sharing market with mutual trust, this well-designed C-ADMM-based DP-DNR management will be much applicable for privacy-preserving grid operation of multi-agent ADNs, especially for agents with conflicting interests.

(4) The proposed distribution-level topology optimization contributes to the flexibility enhancement of a look-ahead rolling economic dispatch of WTBPS, which offsets the insufficient ramping margins of retrofitted coal-fired units. The proposed SOC ramping constraints of retrofitted coal-fired units are validated with acceptable inner-approximated error (at most 2.84%) when ΔT =15 min. Results from the case studies demonstrate that this proposed rolling economic dispatch approach is applicable for multiple WTBPS agents to accommodate wind power fluctuations with the minimization of production cost, purchasing cost, and switch-over operation cost. Moreover, the proposed MGBD-based decentralized method enables many subproblems to be solved in parallel, which facilitates this large-scale rolling economic dispatch model to be quickly solved, saves around 65% computational time and releases more computational resources. Therefore, the computing performance for the proposed MGBD-based method is proved to be satisfactory with higher efficiency.

7.2 Future Work

This thesis proposes several advanced topology optimization methods to achieve a DNR solution for cyber-physical security, privacy-preserving and dispatch flexibility enhancement. To enrich the current work, the following topics should be investigated in the future.

1) Under the digital transformation of the energy industry, power electronic-based circuit breakers are gradually upgraded with high-speed switching properties. Thanks to smart (remotely controlled) circuit breakers, the real-time topology optimization technology can be a promising load transition event via network reconfiguration, which can be used to relieve stress on a primary energy sources when demand for electric is greater than the primary power source can supply. At the operation level, DSOs perform the topology optimization strategy for load balancing and/or loss reduction by the means of choosing optimal status of sectionalizing switches and tie-switches in energy-intensive ADNs on different voltage levels, i.e., HVDNs, medium-voltage DNs (MVDNs) and low-voltage DNs (LVDNs). This also facilitates interacting with transmission system operators with the provision of grid services at the transmission-distribution interface. In other words, doing this topology optimization task on multi-voltage level ADNs actually responds to multiple operational requests by DSOs, e.g., quick load balance, system loss minimization and/or virtual power plants, as a load transition event towards operational requests for system-level operational flexibility enhancement. Therefore, it is necessary to develop the tailored topology optimization model via the coordinated maneuvers of circuit breakers in multi-voltage level ADNs on different time-scales in the future.

2) In terms of reconfigurable topologies, multi-voltage level ADNs, i.e., HVDNs, MVDNs and LVDNs. According to *IEEE* guidelines, LVDNs are low-voltage networks whose voltages are up to 380V, and MVDNs contain networks with

voltages from 10kV up to 35kV, and HVDNs are operated on 110kV as developed in Finland, China, and Spain, etc. Different categories of ADNs have different graph characterizations. As reported, LVDNs or MVDNs generally have single-meshed network structures with depth but non-width properties. In contrast to LVDNs or MVDNs, HVDNs are sub-transmissions constructed in multi-meshed topology (closed loop) but operated in radial structures (open loop), where network structures normally develop wide but non-deep around each station. It is clear that the physical properties of graph characterizations between HVDNs, LVDNs and MVDNs can be significant distinct, i.e, topology structures of HVDNs are more simplified than general DNs. In the future, we wonder how physical network properties of certain ADNs can be utilized to reduce the computational complexity of topology optimization. This is very crucial for a fast computation, as the general DNR formulation may not be helpful for efficient solvability, especially for large-scale networks, e.g., the DNR computational time of 1060-node DNs benchmark spends more than 600 seconds. To address this issue, we will concentrate on graph characterizations for multi-voltage level DNs with specific graphs on multi-voltage level ADNs.

References

[1] E. Ghiani, F. Pilo and G. Celli, “Definition of smart distribution networks,” Operation of Distributed Energy Resources in Smart Distribution Networks, Academic Press, pp.1-23, 2018.

[2] O. Inderwildi, C. Zhang, X. Wang, and M. Kraft, “The impact of intelligent cyber-physical systems on the decarbonization of energy,” *Energy & Environmental Science*, vol. 13, no. 3, pp. 744-771, 2020.

[3] S. Grijalva and M. Costley, “Decentralized Energy Management Architecture for Service-Oriented Cyber-Physical Electric Grids”, *Advanced Computational Electricity Systems* (ACES), 2016.

[4] C. Liu, J.C. Bedoya, N. Sahani, et al., “Cyber–Physical System Security of Distribution Systems,” *Foundations and Trends® in Electric Energy Systems*, vol. 4, no. 4, pp. 346-410, 2021.

[5] H. Song, G.A. Fink and S. Jeschke, Security and privacy in cyber-physical systems: foundations, principles, and applications, John Wiley & Sons, 2017.

[6] M. Z. Jacobson et al., “100% Clean and Renewable Wind, Water, and Sunlight All-Sector Energy Roadmaps for 139 Countries of the World,” *Joule*, vol. 1, no. 1, pp. 108-121, 2017.

[7] N. Liu, C. Li and L. Chen, “Hybrid data-driven and model-based distribution network reconfiguration with lossless model reduction,” *IEEE Trans. on Industr. Inform.*, vol. 18, no. 5, pp. 2943-2954, 2022.

[8] X. Jiang, Y. Zhou, W. Ming, P. Yang and J. Wu, “An Overview of Soft Open Points in Electricity Distribution Networks,” *IEEE Trans. on Smart Grid*, vol. 13, no. 3, pp. 1899-1910, May 2022.

[9] C. Lei, S. Bu, J. Zhong, Q. Chen and Q. Wang, "Distribution Network Reconfiguration: A Disjunctive Convex Hull Approach," *IEEE Trans. on Power Syst.*, 2023.

[10] M. E. Baran and F. F. Wu, "Network reconfiguration in distribution systems for loss reduction and load balancing," *IEEE Trans. Power Deli*, vol. 4, no. 2, 1989.

[11] H.D. Chiang and R. Jean-Jumeau, "Optimal network reconfigurations in distribution systems: a new formulation and a solution methodology," *IEEE Trans. Power Deli.*, vol. 5, no. 4, 1990.

[12] S. Toune, H. Fudo, T. Genji, Y. Fukuyama, and Y. Nakanishi, "Comparative study of modern heuristic algorithms to service restoration in distribution systems," *IEEE Trans. Power Syst.*, vol. 17, no. 1, 2002.

[13] S. Mishra, D. Das, and S. Paul, "A comprehensive review on power distribution network reconfiguration," *Energy Syst.*, vol. 8, no. 2, pp. 227–284, 2017

[14] J. A. Taylor and F. S. Hover, "Convex models of distribution system reconfiguration," *IEEE Trans. on Power Syst.*, vol. 27, no. 3, pp. 1407– 1413, 2012.

[15] M. K. Singh, V. Kekatos, S. Taheri, K. P. Schneider, and C.-C. Liu, "Enforcing radiality constraints for der-aided power distribution grid reconfiguration," *arXiv preprint arXiv:1910.03020*, 2019.

[16] M. Lavorato, J. F. Franco, M. J. Rider, and R. Romero, "Imposing radiality constraints in distribution system optimization problems," *IEEE Trans. Power Syst.*, vol. 27, no. 1, pp. 172–180, Feb. 2012

[17] R. A. Jabr, R. Singh, and B. C. Pal, "Minimum loss network reconfiguration using mixed-integer convex programming," *IEEE Trans. on Power Syst.*, vol. 27, no. 2, pp. 1106–1115, 2012.

[18] J.-P. Chiou, C.-F. Chang, and C.-T. Su "Variable scaling hybrid differential evolution for solving network reconfiguration of distribution systems," *IEEE Trans. Power Syst.*, vol. 20, no. 2, pp. 668–674, May 2005.

[19] A. Asrari, T. Wu, and S. Lotfifard, "The impacts of distributed energy sources on distribution network reconfiguration," *IEEE Trans. Power Electron.*, vol. 31, no. 2, pp. 606–613, Jun. 2016

[20] J. F. Franco, M. J. Rider, M. Lavorato, and R. Romero, "A mixed integer LP

model for the reconfiguration of radial electric distribution systems considering distributed generation," *Elect. Power Syst. Res.*, vol. 97, pp. 51–60, Apr. 2013.

[21] Q. Li and V. Vittal, "Convex hull of the quadratic branch ac power flow equations and its application in radial distribution networks," *IEEE Trans. on Power Syst.*, vol. 33, no. 1, pp. 839–850, 2017.

[22] S. Wang, J. Liu, R. Bo, and Y. Chen, "Approximating input-output curve of pumped storage hydro plant: A disjunctive convex hull method," *IEEE Trans. on Power Syst.*, 2022.

[23] A. Cardenas, "Cyber-physical systems security knowledge area," The Cyber Security Body of Knowledge (cybok). Boca Raton, FL, USA: CRC, 2021.

[24] H. Sandberg, "Cyber-Physical Security," in Encyclopedia of Systems and Control. Berlin, Germany: Springer, 2020.

[25] O. Kosut, L. Jia, R. J. Thomas, and L. Tong, "Malicious data attacks on smart grid state estimation: Attack strategies and countermeasures," *in Proc. IEEE 1st Int. Conf. Smart Grid Commun.*, 2010, pp. 220–225.

[26] Z. Guo, D. Shi, K. H. Johansson, and L. Shi, "Worst-case innovation-based integrity attacks with side information on remote state estimation," *IEEE Trans. Control Netw. Syst.*, vol. 6, no. 1, pp. 48–59, Mar. 2019.

[27] Q. Dai, L. Shi, and Y. Ni, "Risk assessment for cyberattack in active distribution systems considering the role of feeder automation," *IEEE Trans. Power Syst.*, vol. 34, no. 4, pp. 3230–3240, Jul. 2019.

[28] S. A. Desilva, J. Kim, E. Cotilla-Sanchez, and T. Hagan, "On PMU data integrity under GPS spoofing attacks: A sparse error correction framework," *IEEE Trans. Power Syst.*, vol. 36, no. 6, pp. 5317–5332, Nov. 2021

[29] S. Bu, L. G. Meegahapola, D. P. Wadduwage and A. M. Foley, "Stability and Dynamics of Active Distribution Networks (ADNs) With D-PMU Technology: A Review," *IEEE Trans. on Power Syst.*, vol. 38, no. 3, pp. 2791-2804, May 2023.

[30] K. C. Sou, “Protection placement for power system state estimation measurement data integrity,” *IEEE Trans. Control. Netw. Syst.*, vol. 7, no. 2, pp. 638–647, 2019.

[31] K. C. Sou and J. Lu, “Relaxed connected dominating set problem for power systemcyber–physical security,” *IEEE Trans. Control. Netw. Syst.*, vol. 9, no. 4, pp. 1780–1792, 2022.

[32] A. Akrami, M. Doostizadeh, and F. Aminifar, “Optimal reconfiguration of distribution network using μ pmu measurements: A data-driven stochastic robust optimization,” *IEEE Trans. on Smart Grid*, vol. 11, no. 1, pp. 420–428, 2020.

[33] G. S. Dua, B. Tyagi, and V. Kumar, “Deploying micro-pmus with channel limit in reconfigurable distribution systems,” *IEEE Syst. J.*, vol. 16, no. 1, pp. 832–843, 2022

[34] J. Zhao, G. Zhang, and R. A. Jabr, “Robust detection of cyber attacks on state estimators using phasor measurements,” *IEEE Trans. on Power Syst.*, vol. 32, no. 3, pp. 2468–2470, 2016.

[35] N. Jacobs, S. Hossain-McKenzie, A. Summers, C. B. Jones, B. Wright and A. Chavez, “Cyber-physical observability for the electric grid,” *2020 IEEE Texas Power and Energy Conference (TPEC)*, 2020.

[36] B. Zargar, A. Angioni, F. Ponci and A. Monti, “Multiarea Parallel Data-Driven Three-Phase Distribution System State Estimation Using Synchrophasor Measurements,” *IEEE Trans. Instrum. Meas.*, vol. 69, no. 9, pp. 6186-6202, Sept. 2020.

[37] C. Lei, S. Bu and Q. Wang, "Observability Defense-Constrained Distribution Network Reconfiguration for Cyber-Physical Security Enhancement," *IEEE Trans. on Power Syst.*, 2023 (Early Access).

[38] J. Xiao, T. Zhang, G. Zu, F. Li, and C. Wang, “Tsc-based method to enhance asset utilization of interconnected distribution systems,” *IEEE Trans. on Smart Grid*, vol. 9, no. 3, pp. 1718–1727, 2018.

[39] C. Véliz and P. Grunewald, “Protecting data privacy is key to a smart energy

future," *Nature Energy*, vol. 3, no. 9, pp. 702–704, 2018.

[40] J. Wang, F. Gao, Y. Zhou, Q. Guo, C.-W. Tan, J. Song, and Y. Wang, "Data sharing in energy systems," *Adv. Appl. Energy*, vol. 10, pp. 1–18, 2023.

[41] Y. Chen, C. Zhao, S. H. Low, and A. Wierman, "An energy sharing mechanism considering network constraints and market power limitation," *IEEE Trans. on Smart Grid*, vol. 14, no. 2, pp. 1027–1041, 2023.

[42] M. B. Gough, S. F. Santos, T. AlSkaif, M. S. Javadi, R. Castro, and J. P. Catalo, "Preserving privacy of smart meter data in a smart grid environment," *IEEE Trans. on Industr. Inform*., vol. 18, no. 1, pp. 707– 718, 2022.

[43] M. U. Hassan, M. H. Rehmani, and J. Chen, "Differential privacy techniques for cyber physical systems: a survey," *IEEE Commun. Surv*. Tut., vol. 22, no. 1, pp. 746–789, 2020.

[44] R. Kaviani and K. W. Hedman, "An enhanced energy management system including a real-time load-redistribution threat analysis tool and cyber-physical sced," *IEEE Trans. on Power Syst*., vol. 37, no. 5, pp. 3346–3358, 2022.

[45] T. Wu, C. Zhao, and Y.-J. A. Zhang, "Privacy-preserving distributed optimal power flow with partially homomorphic encryption," *IEEE Trans. on Smart Grid*, vol. 12, no. 5, pp. 4506–4521, 2021.

[46] C. Dwork, A. Roth et al., "The algorithmic foundations of differential privacy," *Foundations and Trends in Theoretical Computer Science*, vol. 9, no. 3–4, pp. 211–407, 2014.

[47] Q. Hu, S. Bu, W. Su, and V. Terzija, "A privacy-preserving energy management system based on homomorphic cryptosystem for iot-enabled active distribution network," *J. Modern Power Syst. Clean Energy*, 2023.

[48] V. Dvorkin, F. Fioretto, P. Van Hentenryck, P. Pinson, and J. Kazempour, "Differentially private optimal power flow for distribution grids," *IEEE Trans. on Power Syst*., vol. 36, no. 3, pp. 2186–2196, 2021.

[49] T. W. Mak, F. Fioretto, L. Shi, and P. Van Hentenryck, "Privacy-preserving power system obfuscation: A bilevel optimization approach," *IEEE Trans. on Power*

Syst., vol. 35, no. 2, pp. 1627–1637, 2020.

[50] F. Fioretto, T. W. Mak, and P. Van Hentenryck, “Differential privacy for power grid obfuscation,” *IEEE Trans. on Smart Grid*, vol. 11, no. 2, pp. 1356–1366, 2020.

[51] V. Dvorkin, F. Fioretto, P. Van Hentenryck, J. Kazempour, and P. Pinson, “Differentially private convex optimization with feasibility guarantees,” *arXiv preprint arXiv*:2006.12338, 2020.

[52] V. Dvorkin, F. Fioretto, P. Van Hentenryck, P. Pinson, and J. Kazempour, “Privacy-preserving convex optimization: When differential privacy meets stochastic programming,” *arXiv preprint arXiv:2209.14152, 2022*.

[53] F. Ding and K. A. Loparo, “Hierarchical decentralized network recon-figuration for smart distribution systems—part i: Problem formulation and algorithm development,” *IEEE Trans. on Power Syst.*, vol. 30, no. 2, pp. 734–743, 2015.

[54] A. S. Kahnamouei and S. Lotfifard, “Enhancing resilience of distribution networks by coordinating microgrids and demand response programs in service restoration,” *IEEE Syst. J.*, vol. 16, no. 2, pp. 3048–3059, 2021.

[55] W. Li, Y. Li, C. Chen, Y. Tan, Y. Cao, M. Zhang, Y. Peng, and S. Chen, “A full decentralized multi-agent service restoration for distribution network with dgs,” *IEEE Trans. on Smart Grid*, vol. 11, no. 2, pp. 1100–1111, 2020.

[56] R. R. Nejad and W. Sun, “Enhancing active distribution systems re-silience by fully distributed self-healing strategy,” *IEEE Trans. on Smart Grid*, vol. 13, no. 2, pp. 1023–1034, 2022.

[57] S. Konar, A. K. Srivastava, and A. Dubey, “Distributed optimization for autonomous restoration in der-rich distribution system,” *IEEE Trans. on Power Deli.*, 2023.

[58] S. Boyd, N. Parikh, E. Chu, B. Peleato, J. Eckstein et al., “Distributed optimization and statistical learning via the alternating direction method of multipliers,” *Foundations and Trends® in Machine learning*, vol. 3, no. 1, pp. 1–122, 2011.

[59] C. Zhang, M. Ahmad, and Y. Wang, “Admm based privacy-preserving decentralized optimization,” *IEEE Trans. Inf. Forensics Secur*., vol. 14, no. 3, pp. 565–580, 2019.

[60] R. Takapoui, N. Moehle, S. Boyd, and A. Bemporad, “A simple effective heuristic for embedded mixed-integer quadratic programming,” *Int. J. Control*, vol. 93, no. 1, pp. 2–12, 2020.

[61] Q. Yang, et al, “Prospective contributions of biomass pyrolysis to China’s 2050 carbon reduction and renewable energy goals,” *Nat Commun*., vol.12, pp. 1-12, 2021.

[62] G. He, J. Lin, F. Sifuentes, X. Liu, N. Abhyankar, and A. Phadke, “Rapid cost decrease of renewables and storage accelerates the decarbonization of China’s power system,” *Nat Commun.*, vol.11, pp. 1-9, 2020.

[63] S. Mallapaty, “How China could be carbon neutral by mid-century”, *Nature*, vol. 586, pp. 482-483, 2020.

[64] C. Figueres, et al, “Emissions are still rising: ramp up the cuts”, *Nature,* vol. 564, pp. 27-30, 2018.

[65] Impram S, Nese S V, and Oral B, “Challenges of renewable energy penetration on power system flexibility: A survey,” *Energy Strategy Reviews*, vol. 31, pp.1-12, 2020.

[66] C. Lei, S. Bu, Q. Wang, Q. Chen, L. Yang, and Y. Chi, "Look-ahead Rolling Economic Dispatch Approach for Wind-Thermal-Bundled Power System Considering Dynamic Ramping and Flexible Load Transfer Strategy," *IEEE Trans. on Power Syst.*, 2023 (Early Access).

[67] D. J. Olsen and D. S. Kirschen, "Profitable emissions-reducing energy storage," *IEEE Trans. on Power Syst*., vol. 35, no. 2, pp. 1509-1519, Mar. 2020.

[68] M. Zhou, J. Y. Zhai, G. Y. Li, and J. W. Ren, "Distributed dispatch approach for bulk AC/DC hybrid systems with high wind power penetration," *IEEE Trans. on Power Syst.*, vol. 33, no. 3, pp. 3325-3336, 2017.

[69] Z. Chen, J. Zhu, H. Dong, W. Wu, and H. Zhu, "Optimal dispatch of WT/PV/ES combined generation system based on cyber-physical-social Integration," *IEEE Trans. on Smart Grid*, vol. 13, no. 1, pp. 342-354, Jan. 2022.

[70] V. P.Sakthivel and P. D. Sathya, "Single and multi-area multi-fuel economic dispatch using a fuzzified squirrel search algorithm," *Protection and Control of Modern Power Systems*, vol. 6, no. 2, pp. 147-159, 2021.

[71] Z. Zhang, C. Wang, S. Chen, Y. Zhao, X. Dong, and X. Han, "Multi-time scale co-optimized dispatch for integrated electricity and natural gas system considering bidirectional interactions and renewable uncertainties," *IEEE Trans. Ind. Appl,* 2022 (Early Access).

[72] C. Z. Shao, Y. Ding, P. Siano, and Y. H. Song, "Optimal scheduling of the integrated electricity and natural gas systems considering the integrated demand response of energy hubs, " *IEEE Syst. J.*, vol. 15, no. 3, pp. 4545-4553, 2020.

[73] Y. Wang, S. Lou, Y. Wu, and S. Wang, "Flexible operation of retrofitted coal-fired power plants to reduce wind curtailment considering thermal energy storage," *IEEE Trans. on Power Syst.*, vol. 35, no. 2, pp. 1178-1187, Mar. 2020.

[74] Z. Zhang, J. Shi, W. Yang, Z. Song, Z. Chen, and D. Lin, "Deep reinforcement learning based bi-layer optimal scheduling for microgrid considering flexible load control, " *CSEE J. Power Energy Syst.*, 2021 (Early Access).

[75] United Nations Economic Commission For Europe. Opportunities for coupling wind and coal based generation in the electricity sector. Available Online: https://unece.org/fileadmin/DAM/energy/se/pdfs/CES/ge12_WS/CEP-12_2016_INF.3v2.pdf.

[76] C. Na, et al, "Economic decision-making for coal power flexibility retrofitting and compensation in China," *Sustainability*, vol.10, no.348, 2018.

[77] F. Ess, F. Peter, and Dr. F. Klummp, "Flexibility in thermal power plants-with a focus on existing coal-fired power plants," *Agora Energiewende*, Berlin, Germany, Tech. Rep. 115/04-S-2017/EN, Jun. 2017.

[78] T. Li and M. Shahidehpour, “Dynamic ramping in unit commitment,” *IEEE Trans. Power Syst.*, vol. 22, no. 3, pp. 1379–1381, Aug. 2007.

[79] C. M. Correa-Posada, G. Morales-España, P. Dueñas, and P. Sánchez-Martín, “Dynamic Ramping Model Including Intraperiod Ramp-Rate Changes in Unit Commitment,” *IEEE Trans. on Sustain. Energy*, vol. 8, no. 1, pp. 43-50, Jan. 2017.

[80] Z. Jin, K. Pan, L. Fan and T. Ding, “Data-driven look-ahead unit commitment considering forbidden zones and dynamic ramp rate,” *IEEE Trans. Ind. Inf*, vol. 15, no. 6, pp. 3267-3276, June 2019.

[81] X. Li et al., “Wind-Thermal-CSP bundling model with an adjustable heat storage strategy for CSP stations, ” *IEEE Access*, vol. 9, pp. 25984-25992, 2021.

[82] C. Lei, S. Bu, Q. Wang, N. Zhou, L. Yang, and X. Xiong, “Load transfer optimization considering hot-spot and top-oil temperature limits of transformers, ” *IEEE Trans. on Power Deli.*, vol. 37, no. 3, pp. 2194-2208, June 2022.

[83] “IEEE Draft Guide for Overhead AC Transmission Line Design, ” *IEEE P1863/D10*, pp. 1-96, 25 July 2019.

[84] "Distributed Generation in Europe – Physical Infrastructure and Distributed Generation Connection," KEMA, Inc., pp. 26, 2011.

[85] Mikko Laaja, "General planning principles of high voltage distribution networks including wind power," Master of Science Thesis, Department of Computing and Electrical Engineering, Tampere University of Technology, Finland, 2012. [Online]. Available: https://trepo.tuni.fi/handle/123456789/21124.

[86] A. M. Geoffrion, “Generalized benders decomposition,” *J. Optim. Theory Appl.*, vol. 10, no. 4: pp. 237-260, 1972.

[87] F. Q. You, I. E. Grossmann, “Multicut benders decomposition algorithm for process supply chain planning under uncertainty,” *Ann. Oper. Res.*, vol. 210, pp. 191–211, 2013.

[88] M. Farivar and S. Low, "Branch flow model: Relaxations and convexification – Part I, " *IEEE Trans. Power Syst.*, Vol. 28, No. 3, Aug. 2013.

[89] S. H. Low, "Convex relaxation of optimal power flow part I: Formulations and equivalence," *IEEE Trans. Control Netw. Syst.*, vol. 1, no. 1, pp. 15–27, Mar. 2014.

[90] H. Zhu and H. J. Liu, "Fast Local Voltage Control Under Limited Reactive Power: Optimality and Stability Analysis," *IEEE Trans. Power Syst.*, vol. 31, no. 5, pp. 3794-3803, Sept. 2016.

[91] Ben-Tal and A. Nemirovski, "On polyhedral approximations of the second-order cone," *Math. Oper. Res.*, vol. 26, no. 2, pp. 193–205, May 2001

[92] C. Lei. MATDNR Toolbox v1.0. [Online]. Available: https://github.com/honolulufishing/MATDNR/releases /tag/Matlab.

[93] MOSEK Aps Website. [Online]. Available: https://www.mosek.com.

[94] N.V. Sahinidis, "BARON: A general purpose global optimization software package," *J Glob Opti.,* no.8, pp. 201–205, 1996.

[95] J. F. Sturm, "Using SeDuMi 1.02, a MATLAB toolbox for optimization over symmetric cones," *Optimization Methods and Software*, no. 11, vol. 1–4, pp. 625–653, 1999.

[96] W. Yan, J. Yu, D. C. Yu and K. Bhattarai, "A new optimal reactive power flow model in rectangular form and its solution by predictor corrector primal dual interior point method," *IEEE Trans. Power Syst*, vol. 21, no. 1, pp. 61-67, Feb. 2006.

[97] M. K. Singh, V. Kekatos, S. Taheri, K. P. Schneider, and C.-C. Liu, "Enforcing radiality constraints for DER-aided power distribution grid reconfiguration," *arXiv preprint arXiv:1910.03020*, 2019.

[98] Y. Wang, Y. Xu, J. Li, J. He and X. Wang, "On the Radiality Constraints for Distribution System Restoration and Reconfiguration Problems," *IEEE Trans. Power Syst.*, vol. 35, no. 4, pp. 3294-3296, July 2020.

[99] H. Ahmadi and J. R. Martí, "Mathematical representation of radiality constraint in

distribution system reconfiguration problem," *Int. J. Electr. Power Energy Syst.*, vol. 64, pp. 293-299, 2015.

[100] G. McCormick, "Computability of global solutions to factorable nonconvex programs: Part I convex underestimating problems," *Math. Program.*, vol. 10, pp. 146–175, 1976.

[101] R. Billinton, S. Kumar, N. Chowdhury, K. Chu, K. Debnath, L. Goel, E. Khan, P. Kos, G. Nourbakhsh, and J. Oteng-Adjei, "A reliability test system for educational purposes-basic data," *IEEE Trans. on Power Syst*., vol. 4, no. 3, pp. 1238–1244, 1989.

[102] K. P. Schneider, B. Mather, B. C. Pal, C.-W. Ten, G. J. Shirek, H. Zhu, J. C. Fuller, J. L. R. Pereira, L. F. Ochoa, L. R. de Araujo et al., "Analytic considerations and design basis for the ieee distribution test feeders," *IEEE Trans. on Power Syst*., vol. 33, no. 3, pp. 3181–3188, 2017.

[103] M. ApS, "Mosek optimization toolbox for matlab," *User's Guide and Reference Manual*, *Version*, vol. 4, p. 1, 2022.

[104] J. Dong, K. Xie , C. Singh, and B. Hu, "Optimal capacity and type planning of generating units in a bundled wind–thermal generation system," *Applied Energy*, pp. 200-210, 2016.

[105] X. Zhang, Y. Liu, H. Gao, L. Wang, and J. Liu, "A bi-level corrective Line switching model for urban power grid congestion mitigation," *IEEE Trans. on Power Syst.*, vol. 35, no. 4, pp. 2959-2970, July 2020.

[106] J. Wang, et al. "Cooperative overload control strategy of power grid-transformer considering dynamic security margin of transformer in emergencies," *Int. J. Electr. Power Energy Syst.*, vol. 140, pp. 108098, 2022.

[107] N. I. Muskhelishvili, *Singular Integral Equations*, Netherlands: Groningen, 1953.

[108] B. Fan and X. Wang, "Distributed privacy-preserving active power sharing and frequency regulation in microgrids," *IEEE Trans. on Smart Grid*, vol. 12, no. 4, pp. 3665-3668, July 2021.

[109] IBM CPLEX® Optimizer Website. [Online]. Available: https://www.ibm.com/analytics/cplex-optimizer.